

**Synthesis and characterization of Pt/TiO₂/C
composite catalysts for fuel cells prepared using a
glucose modifier**

by

Christopher Odetola

A Thesis Submitted in Partial Fulfillment of the Requirements for the Degree of

Doctor of Philosophy

University of Ontario Institute of Technology
Faculty of Science
Materials Chemistry

March, 2017

© Christopher Odetola, 2017

Certificate of Approval

Abstract

Catalysts in the electrodes of polymer exchange membrane fuel cells (PEMFCs) serve a critical function in reactions which can be used to generate electrical energy from chemical fuels. Pt nanoparticles are commonly dispersed on a conductive support and used as electrode materials in these devices because of their exceptional catalytic activity and electrochemical active surface area. The performance and stability of these electrodes strongly depend on the characteristics of the support.

Catalysts supported on high surface area carbon black are widely used in low-temperature fuel cells. In PEMFCs, these catalyst materials can be exposed to high potential and low pH values, resulting in irreversible loss of activity that will limit the useful lifetime of the cell, ultimately leading to its failure. Pt is a noble metal which has good intrinsic stability, but carbon is not thermodynamically stable resulting in the corrosion of the catalyst support under these conditions. The design of more resilient platinum catalyst supports to carry out the successful reaction in a fuel cell's catalyst layer is required to extend the lifetime of PEMFCs degradation.

In this thesis, two approaches were used to synthesize robust catalyst support materials for fuel cell applications. In the first case, carbon surfaces were functionalised to enhance their interactions with the catalyst and secondly, stable metal oxide was combined with modified carbon substrates, to maximise contacts within the composite electrocatalysts and to prevent carbon corrosion of a single phase carbon support catalyst. TiO₂ NPs, were first chemically bonded to the surfaces of Vulcan carbon to help anchor the Pt catalyst nanoparticles through strong metal-support interactions. Validation of a dual phase catalyst support is an important goal of this research. Each material phase offers a unique advantage that can only be recognized by the preparation of a composite electrocatalyst. Pristine Vulcan (PV) was functionalised with glucose hydroxyl functional groups that react with the base titanium metal alkoxide in a sol-gel reaction and then calcined to form a more chemically crystalline surface. This is followed by impregnation reduction process to deposit the nanostructured Pt catalyst.

Material characterization data of synthesized materials were used to correlate the effects of support structure and composition on resilient performance. Advantages from the TiO₂/C supports toward performance and durability were contrasted against a set of control samples and demonstrated *ex situ*. The prepared composite catalysts showed substantial enhancements toward oxygen reduction reaction (ORR) and methanol oxidation reaction (MOR) as well as improved stability of the Pt-TiO₂ heterogeneous interface formed between catalyst and support. The enhanced performance and durability of these composite catalysts is improved by applying the science of materials and interfaces to the synthesis of composite supports, thus serving as an example for further progress and optimization.

Irradiation of these composite catalysts with UV-visible light also showed ~ 171 % photo enhanced activity for MOR, which clearly demonstrates a synergistic effect between the photo- and electrocatalysts. The comparison between the prepared catalysts indicates that there is an appropriate ratio of carbon and TiO₂ to obtain the best performance of these photoelectroactive materials. These results demonstrate that methanol oxidation is achieved by electro- and photoelectrocatalysis using a simple and affordable method. This procedure can be conveniently exploited to enhance the response of direct methanol fuel cell electrodes.

Keywords: Vulcan carbon, glucose, TiO₂, Sol-gel, photoelectrocatalysis, electrochemical impedance spectroscopy.

Acknowledgements

The last five years have been a rollercoaster ride and I have learned not only about electrochemistry but also about people and life. I would like to thank my supervisors, Dr. Liliana Trevani and Dr. Bradley Easton for sponsoring me to complete my PhD while working at their respective research labs. Thank you for your technical guidance, for widening my horizons and encouraging throughout my PhD thesis. It was difficult at times to meet both the family demands and keep up with the thesis work but I was always encouraged to do my best. I do really appreciate every single invitation for lunch, Christmas dinner and summer barbeque meetings. Thanks you Liliana for investing in several coffee sessions and describing science on the coffee receipts. I will be eternally grateful to you both for the numerous feedbacks and constructive criticism throughout my PhD thesis.

My sincere gratitude goes to my supervisory committee: Dr. Andrew Vreugdenhil and Dr. Franco Gaspari for your valuable contributions with this project. Thank you for making it comfortable to discuss challenges and approach research with a new outlook. My sincere gratitude goes to Dr. Aicheng Chen, my external examiner, and to Dr. Fedor Naumkin, my internal examiner, for agreeing to be a part of this process. To my lab mates, both past and present, you have kept me motivated and have made the last 5 years a truly enjoyable experience. You all have contributed positively in one way or the other to my time in UOIT, thank you all.

I am grateful for the support and funding provided by NSERC which made performing this research possible.

I would like to thank my family, friends and well-wishers for their unwavering love and support in the pursuit of this project. I am encouraged, thanks for being part of my life.

Lastly, but certainly not least, I will like to appreciate my wife, Olawande, for all of your support, patience, and encouragement which enabled me to have the persistence I needed to do my research and to complete the writing of this thesis.

Table of Contents

Certificate of Approval	ii
Abstract	iii
Acknowledgements	v
Table of Contents	vi
List of Tables	xi
List of Figures	xiii
List of Abbreviations and Symbols	xxii

Chapter 1 – Introduction and literature review	1
1.1 Background to fuel cell	2
1.2 Types of fuel cell	4
1.3 Structure and mode of operation of Proton exchange membrane fuel cells	5
1.4 Oxygen reduction reaction (ORR) Catalyst	8
1.5 Pt Catalyst Stability	9
1.6 Catalyst Support Corrosion	13
1.7 Mitigation strategies for carbon corrosion	17
1.7.1 Alternative carbon support materials	17
1.7.1.1 Carbon Nanotubes	18
1.7.1.2 Graphene and graphene oxide	19
1.7.1.3 Ordered mesoporous carbon	20
1.7.2 Non carbon support: Metal oxides	22
1.7.3 Crystal lattice, electronic structures and application of TiO _x	24
1.7.4 TiO ₂ catalyst support	26
1.7.5 TiO ₂ /carbon composite catalyst support	29
1.8 Thesis Objectives	31
1.9 Thesis Organization	32

1.10 References	33
Chapter 2 – Experimental (Materials and Methods)	42
2.1 Chemicals and materials	43
2.2 Synthesis of catalyst materials	43
2.2.1 Carbon functionalization	43
2.2.2 Glucose pre-adsorption on carbon substrate	44
2.2.3 TiO ₂ Deposition: Synthesis of TiO ₂ /G-PV, TiO ₂ /G-ATV and /TiO ₂ /ATV composite supports	44
2.2.4 Pt deposition on TiO ₂ /C substrates	45
2.3 Electrochemical measurements and sample preparations	46
2.3.1 Electrochemical cell cleaning	46
2.3.2 Glassy carbon electrode cleaning	46
2.3.3 Catalyst ink preparation and casting procedure	47
2.3.4 Half-Cell Electrochemical Measurements	47
2.4 Materials characterization techniques	49
2.4.1 Scanning electron microscope (SEM)	49
2.4.2 Transmission electron microscope (TEM)	50
2.4.3 Thermogravimetric analysis (TGA)	51
2.4.4 Raman spectroscopy analysis	53
2.4.5 X-ray diffraction (XRD)	54
2.4.6 X-ray photoelectron spectroscopy (XPS)	55
2.4.7 Brunauer Emmett Teller (BET) surface area analysis	57
2.5 Electrochemical characterization techniques	60
2.5.1 Cyclic voltammetry (CV) and electrochemical surface area (ECSA) determination	60
2.5.2 Stripping Voltammetry	62

2.5.3 Rotating disc electrode (RDE) and Oxygen reduction reaction	62
2.5.4 Methanol oxidation reaction (MOR)	63
2.5.5 Electrochemical impedance spectroscopy	65
2.6 References	70
Chapter 3 – Physicochemical characterizations of modified carbon and TiO₂/C composite catalyst supports for fuel cell application	74
3.1 Introduction	75
3.2 Physical characterization of modified carbon and composite	77
3.3 Electrochemical measurement and support durability study	79
3.4 Results and Discussion	79
3.4.1 Material Characterizations	79
FTIR Analysis	79
Thermogravimetric Analysis	82
BET Analysis	85
Morphological characterization by electron microscopy	90
XRD Analysis	94
Raman Spectroscopy Analysis	97
XPS Analysis	98
3.5 Electrochemical activity	108
3.6 Discussion of sol-gel derived TiO ₂ /C composite supports	115
3.7 Conclusions.....	116
3.8 References	118
Chapter 4 – Study of glucose doped acid treated composite catalyst and comparative analysis	123
4.1 Introduction	124
4.2 Experimental	126
4.2.1 Synthesis of composite catalysts.....	126

4.2.2 Material characterization.....	127
4.2.3 Electrochemical characterization	128
4.3 Results and discussion	129
4.3.1 Material characterization.....	129
4.3.2 Electrochemical characterization	138
4.4 Impact of catalyst loading and electrolyte effect on rotating disc electrode measurements	147
4.5 Conclusion and Summary	152
4.6 References.....	152
Chapter 5 – Oxygen reduction reaction and electrochemical stability of Pt/TiO₂/Carbon fuel cell electrocatalysts prepared using a glucose modifier ...	
5.1 Introduction	159
5.2 Experimental	161
5.3 Physical characterization results and discussion	161
5.3.1 Thermal analysis and samples composition determination	161
5.3.2 The impact of carbon pre-treatment on the properties of TiO ₂ /ATV and TiO ₂ /G-PV substrates	164
5.3.3 Physical Properties of Pt on TiO ₂ /ATV and TiO ₂ /G-PV	166
5.4 Electrochemical characterization results	173
5.4.1 Ex-situ and In-situ Addition of TiO ₂ NPs on standard Pt/C catalyst	173
5.4.2 Electrochemical characterization of Pt/TiO ₂ /ATV catalysts	178
5.4.3 Electrochemical characterization of Pt/TiO ₂ /G-PV catalysts and comparison analysis with Pt/TiO ₂ /ATV catalysts	181
5.5 Conclusion and summary.....	191
5.6 References	193

Chapter 6 – Photo-enhanced methanol oxidation and electrochemical stability: understanding the impacts of Pt and TiO₂ nanoparticles on the electrode performances	195
6.1 Introduction to methanol oxidation reaction	196
6.2 Materials characterization	201
6.3. Electrochemical and photoelectrochemical measurements	201
6.4 Results and Discussion	202
6.4.1 Materials Characterization	202
6.4.2 Electrocatalytic Activity of supported catalysts toward Methanol Oxidation...	206
6.4.3 Photo-Electrocatalytic Activity toward Methanol Oxidation with and without UV-Visible Light	211
6.4.4 CO Oxidation and Stripping Experiments with and without UV-Visible Light	219
6.4.5 Influence of Pt surface area on photo-enhancement	224
6.5 Conclusion	228
6.6 References	229
Chapter 7 – Summary and Future Directions.....	234
7.1 Summary and Future Directions	235
7.2 References	240
Chapter 8 – Appendices.....	242

List of Tables

Chapter 1

Table 1.1. Main fuel cell types	5
Table 1.2. Operating modes and possible causes of catalyst layer degradation	11

Chapter 3

Table 3.1. Summary of TiO ₂ contents on the modified carbon supports	85
Table 3.2: BET surface area data for reference and composite materials	89
Table 3.3: Atomic surface compositions of different elements through XPS analysis.....	101
Table 3.4 States of elements detected by surface analysis through XPS.....	102
Table 3.5: Summary of XPS analysis of C1s, O1s and Ti peaks of the reference material and composite supports.....	108

Chapter 4

Table 4.1: Physical Properties of TiO ₂ / C and Pt Catalysts	130
Table 4.2: XPS Analysis of Pt/TiO ₂ / G-ATV and Pt/TiO ₂ / ATV Catalysts	134
Table 4.3: Summary of electrochemical properties of prepared catalysts.....	138

Chapter 5

Table 5.1: TGA showing weight % of TiO ₂ and Pt in the synthesized catalyst materials.....	164
Table 5.2: XRD average crystalline size of Pt in the synthesized catalyst materials.....	170
Table 5.3: XPS data for reference materials and prepared Pt/TiO ₂ /ATV and Pt/TiO ₂ /G-PV samples.....	173
Table 5.4: ECSA values of Pt/TiO ₂ /ATV catalysts.....	181
Table 5.5: Summary of electrocatalytic activity and stability.....	183
Table 5.6: Limiting capacitance BOL and EOL data following stability study	189

Chapter 6

Table 6.1: Total peak current density and current contributions for methanol oxidation at 0.8 V vs NHE with and without illumination.....	214
Table 6.2: Charge Transfer Resistance (R_{CT}) and exchange current density (j_o) obtained from EIS data for Pt/PV and Pt/TiO ₂ /G-PV catalysts.....	218
Table 6.3: Activation energies (E_a) obtained from methanol oxidation at differential potentials for Pt/PV and Pt/TiO ₂ /G-PV catalysts with and without illumination.....	223

List of Figures

Chapter 1

Figure 1.1: Schematic of PEMFC mode of operation.....	6
Figure 1.2: Schematic of the electrode and porous active layer.....	7
Figure 1.3: Sketch of catalyst layer triple phase boundaries (TPBs)	14
Figure 1.4: Most stable materials under the typical PEMFC cathode condition at 80°C, derived from pH-potential diagrams thermodynamically calculated	22
Figure 1.5: crystal structures of titanium dioxide (a) Rutile and (b) Anatase	24
Figure 1.6: Mechanism of TiO ₂ photocatalysis process	25
Figure 1.7: Glucose doped composite catalysts synthetic approach.....	31

Chapter 2

Figure 2.1: Synthesis of Pt based composite catalyst materials	46
Figure 2.2: A three electrode electrochemical cell set up schematic	48
Figure 2.3: TGA curve of Vulcan carbon in air	52
Figure 2.4: Photoionization of an atom by the ejection of a 1s electron by x-ray radiation.....	56
Figure 2.5: Half cell CV of Pt supported on carbon black in 0.5 M H ₂ SO ₄ electrolyte solution	60
Figure 2.6: ORR polarization curves Pt supported on carbon black in oxygen saturated 0.5 M H ₂ SO ₄ electrolyte solution.....	62
Figure 2.7: CV of methanol oxidation reaction in 0.5 M CH ₃ OH + 0.5 M H ₂ SO ₄ Electrolyte solution.....	65
Figure 2.8: Diagram of simple circuit to model electrode/ Electrolyte interface.....	68
Figure 2.9: Transmission line model	69
Figure 2.10: Equivalent circuit used in modeling methanol oxidation reaction.....	70

Chapter 3

Figure 3.1: FTIR spectra of Pristine Vulcan (PV) acid treated Vulcan (ATV) and glucose doped Vulcan (G-PV).....	81
Figure 3.2: The (A) TGA and (B) DSC curves obtained under argon and (C) and (D) in air for Pristine Vulcan (PV) and Acid treated Vulcan (ATV).....	83
Figure 3.3: (A) TGA and (B) DSC curves of TiO ₂ /ATV and TiO ₂ /G-PV supports in air (C) TGA and (D) DSC curves of TiO ₂ /G-PV supports under air.	84
Figure 3.4: Nitrogen adsorption–desorption isotherms (A) at 77 K for pristine and modified Vulcan carbon with respective pore size distribution (B) and for composite supports after calcination (C) as well as pore size distribution curves (D).	87
Figure 3.5: Scanning electron micrographs of PV, (A) ATV (B) and G-PV (C) carbon supports.....	91
Figure 3.6: Transmission electron micrographs of PV, (A) ATV (B) and G-PV (C) carbon supports.....	92
Figure 3.7: Transmission electron micrographs of TiO ₂ /ATV, (A) and TiO ₂ /G-PV (B) composite supports	93
Figure 3.8: XRD patterns for PV, ATV and G-PV (A) as well as the anataseTiO ₂ (SA) and rutile phase of SA following heat treatment (B).	95
Figure 3.9: XRD patterns for TiO ₂ /ATV and TiO ₂ /G-PV composites after calcination at two different temperature in nitrogen	96
Figure 3.10: Raman spectra carbon supports (A), commercial TiO ₂ (SA) with composite support materials, TiO ₂ /ATV and TiO ₂ /G-PV (B)	97
Figure 3.11: XPS analysis C1s spectra pristine Vulcan carbon (PV)	99
Figure 3.12: XPS analysis C1s spectra glucose doped pristine Vulcan carbon (G-PV)	99
Figure 3.13: XPS analysis O1s spectra pristine Vulcan carbon (PV)	100
Figure 3.14: XPS analysis O1s spectra G-PV.....	100

Figure 3.15: XPS analysis C1s spectra of TiO ₂ /ATV (A) and TiO ₂ /G-PV (B) composite supports	103
Figure 3.16: XPS analysis Ti (A) and O1s (B) spectra of commercial TiO ₂ (SA).....	104
Figure 3.17: XPS analysis O1s spectra of TiO ₂ /ATV (A) and TiO ₂ /G-PV (B) composite supports.....	106
Figure 3.18: XPS analysis Ti spectra of TiO ₂ /ATV (A) and TiO ₂ /G-PV (B) composite supports	107
Figure 3.19: Cyclic voltammetry of carbon supports carried out in N ₂ -saturated 0.5M H ₂ SO ₄ at 25 °C a scan rate of 50mV/s.	109
Figure 3.20: Cyclic voltammetry of unplatnized supports: (A) PV, (B) TiO ₂ and (C) TiO ₂ /G-PV carried out in N ₂ saturated 0.5 M H ₂ SO ₄ at 25 °C and 50 mV/s scan rate.	110
Figure 3.21: Cyclic voltammetry of carbon TiO ₂ /G-PV supports with varied TiO ₂ content in N ₂ -saturated 0.5M H ₂ SO ₄ at 25 °C	111
Figure 3.22: CVs TiO ₂ (A), pristine Vulcan (PV) and TiO ₂ /G-PV (C) supports under aging conditions in N ₂ -saturated 0.5M H ₂ SO ₄ solution at 25 °C	112
Figure 3.23: Electrochemical impedance spectroscopy (EIS) plots of TiO ₂ electrode at 0.60V showing Nyquist plot (a), capacitance plot (b) and normalised capacitance plot (c) in N ₂ - saturated 0.5M H ₂ SO ₄ solution scan rate of 50 mV/s, test temperature: 25 °C.....	113
Figure 3.24: Electrochemical impedance spectroscopy (EIS) plots of PV support at 0.60V showing Nyquist plot (a), capacitance plot(b) and normalised capacitance plot (c) in nitrogen saturated 0.5M H ₂ SO ₄ solution scan rate of 50 mV/s, test temperature: 25 °C.....	114
Figure 3.25: Electrochemical impedance spectroscopy (EIS) plots of TiO ₂ /G-PV electrode at 0.60V showing Nyquist plot (a), capacitance plot(b) and normalised capacitance plot (c) in nitrogen saturated 0.5M H ₂ SO ₄ solution scan rate of 50 mV/s, test temperature: 25 °C.....	115
Figure 3.26: Possible configurations of carbon and TiO ₂ particles in the synthesized TiO ₂ /C composite supports.....	116

Chapter 4

Figure 4.1: Synthesis of Pt/TiO ₂ /G-ATV catalyst.....	127
Figure 4.2: Thermogravimetric analysis under air for compositional analysis: ATV, G-ATV, Pt/ 14 wt% TiO ₂ / G-ATV and Pt/ 14 wt% TiO ₂ / G-ATV catalyst. Experimental conditions: average sample mass: 10 mg, gas flow rate: 50 ml/min, and heating rate 20 °C/min.....	130
Figure 4.3: TEM characterization: (a-b) 14wt% TiO ₂ /G-ATV and (c-d) 5wt%TiO ₂ / ATV composite supports.	131
Figure 4.4: TEM characterization: (a) Pt/14 wt% TiO ₂ / G-ATV and particle size distribution (b) 5wt% TiO ₂ / ATV and particle size distribution.	132
Figure 4.5: XPS characterization: O1s Scan: (a) Pt/14 wt% TiO ₂ / G-ATV and (b) Pt/5 wt% TiO ₂ / ATV.....	133
Figure 4.6: XRD patterns of: (a) acid treated Vulcan (ATV), Anatase (SA) and SA annealed at 500 ⁰ C for 6 hours in N ₂ , 14 wt% TiO ₂ /G-ATV and 5wt%TiO ₂ /ATV (b) 14 wt% TiO ₂ /G-ATV and 5wt%TiO ₂ /ATV (c) Pt/ ATV, Pt/14 wt% TiO ₂ / G-ATVand Pt/ 5wt%TiO ₂ /ATV.....	135
Figure 4.7: Raman spectra of: (a) acid treated Vulcan (ATP), Anatase TiO ₂ (SA), 14 wt% TiO ₂ /G-ATV and 5wt%TiO ₂ /ATV	137
Figure 4.8: Half-cell CVs of : (a) Pt/ ATV (b) Pt/ 14 wt% TiO ₂ / G-ATV (c) Pt/ 5 wt% TiO ₂ / ATV catalysts under aging conditions in argon-saturated 0.5M H ₂ SO ₄ solution at a scan rate of 50 mV s ⁻¹ test temperature: 25 °C for 4000 potential cycles. Pt loading 0.1 ± 0.01 mg cm ⁻²	139
Figure 4.9: Relationship of different catalysts under aging conditions: (a) ECSA vs potential cycle number (b) Normalized ECSA under the catalyst stability assessment period.....	141
Figure 4.10: Nyquist plots for: (a) Pt/ ATV, (b) Pt/ 14 wt% TiO ₂ / G-ATV and (c) Pt/ 5 wt% TiO ₂ / ATV at beginning of life (BOL) and after 4000 potential cycles (EOL).....	142
Figure 4.11 : Capacitance plots for : (a)Pt/ ATV , (b) Pt/ 14 wt% TiO ₂ / G-ATV and (c) Pt/ 5 wt% TiO ₂ / ATV at beginning of life (BOL) and after 4000 potential cycles (EOL).....	142

Figure 4.12: ORR activities of each catalyst at beginning of life (a, b, c) corresponding Koutecky-Levich plots are shown in (d, e, and f). Measurements were carried out in O ₂ -saturated 0.5M H ₂ SO ₄ at 25 °C, Pt loading 0.1 ± 0.01 mg cm ⁻²	144
Figure 4.13: Mechanisms of Oxygen reduction reaction on platinum based electrode surface	145
Figure 4.14: Comparison of the ORR activities of each catalyst at (a) beginning of life (BOL) and (b) end of life (EOL, 4000 potential cycles. Measurements were carried out in O ₂ -saturated 0.5M H ₂ SO ₄ at 25 °C, using an electrode rotation rate of 1600 RPM.....	146
Figure 4.15: Comparison of the ORR activities of each catalyst 20µgcm ⁻² Pt loading on all catalysts. Measurements were carried out in O ₂ -saturated in 0.1M HClO ₄ (left) and 0.5M H ₂ SO ₄ (right) at 25 °C a scan rate of 5 mVs ⁻¹ using electrode rotation rates 400-1600 RPM.....	148
Figure 4.16: Comparison of the ORR activities of each catalyst at 1600RPM in O ₂ -saturated (a) 0.1M HClO ₄ and (b) 0.5M H ₂ SO ₄ . Measurements were carried out at 25 °C a scan rate of 5 mV s ⁻¹ with 20µgcm ⁻² Pt loading on all catalysts.....	149
Figure 4.17: Comparison of levich's plots for kinetic analysis of each catalyst at 0.2V under different rotation rates in O ₂ -saturated (a) 0.1M HClO ₄ and (b) 0.5M H ₂ SO ₄ . Measurements were carried out at 25 °C a scan rate of 5 mV s ⁻¹ with 20µgcm ⁻² Pt loading on all catalysts.....	150
Figure 4.18: Normalized ECSA of catalysts under stability assessment in (a) 0.1M HClO ₄ and (b) 0.5M H ₂ SO ₄ . Measurements were carried out at 25 °C a scan rate of 50 mV s ⁻¹	151

Chapter 5

Figure 5.1: The (a) TGA and (b) DSC curves obtained under argon for Glucose (G), Pristine Vulcan (PV), Acid treated Vulcan (ATV) and synthesized TiO ₂ . Experimental conditions: sample mass ~ 10 mg, gas flow rate: 50 mL/min, and heating rate of 20 °C/min.....	162
Figure 5.2: (a) TGA and (b) DSC curves obtained under air for 14% TiO ₂ / G-PV,	

and Pt/14% TiO ₂ / G-PV. Experimental conditions: sample mass ~ 10 mg, gas flow rate: 50 mL/min, and heating rate 20 °C/min.....	163
Figure 5.3: BET surface areas of glucose (G), pristine vulcan (PV), acid treated Vulcan (ATV), glucose doped Vulcan (G-PV) and composite supports (TiO ₂ /ATV and TiO ₂ /G-PV) following heat treated at 500 °C for 2 hours.....	165
Figure 5.4: Transmission electron micrograph (a) and (b) Pt particle size distri- bution of Pt/PV Catalyst.....	167
Figure 5.5: Transmission electron micrographs and Pt particle size distribution for: (a) and (b) 14 wt% TiO ₂ /GPV, (c) and (d) 14 wt% TiO ₂ /ATV.....	168
Figure 5.6: XRD patterns: (a) Pt on carbon supports(b) Pt/ wt%TiO ₂ /ATV (c) Pt/ wt%TiO ₂ /G-PV.....	170
Figure 5.7: (a) XPS surface scan of C, Ti, O1s and Pt (b) Ti ₂ peaks (c) O1s peaks and (d) Pt peaks scans for TiO ₂ , TiO ₂ /G-PV and Pt/TiO ₂ /G-PV catalyst materials.....	172
Figure 5.8: (a) Half-cell CV of mechanically mixed TiO ₂ on Pt/C catalyst at different concentrations in N ₂ -saturated 0.5M H ₂ SO ₄ solution at a scan rate of 50 mV/s, test temperature: 25 °C (b) Expansion of the hydrogen adsorption/ desorption regions (c) Change in ECSA as a function of TiO ₂ wt% loading.....	175
Figure 5.9: EIS characterization of mechanised mixed TiO ₂ on Pt/C catalyst at 0.425V biased potential in N ₂ -saturated 0.5M H ₂ SO ₄ solution (a) Nyquist plots (b) Limiting capacitance plots. (c) Normalised capacitance plot.....	176
Figure 5.10: Half-cell CV of <i>in situ</i> deposited TiO ₂ on Pt/C catalyst at different concentrations in N ₂ -saturated 0.5M H ₂ SO ₄ solution at a scan rate of 50 mV/s, test temperature: 25 °C.....	177
Figure 5.11: Half-cell CVs of Pt/TiO ₂ /ATV catalysts in N ₂ -saturated 0.5M H ₂ SO ₄ solution at a scan rate of 50 mV/s test temperature: 25 °C.....	179
Figure 5.12: EIS characterization of Pt/TiO ₂ /ATV catalysts at 0.425V biased potential in N ₂ -saturated 0.5M H ₂ SO ₄ solution (a) Nyquist plots (b) Limiting capacitance plots. (c) Normalised capacitance plots.....	180
Figure 5.13: Half-cell CVs for: (a) Pt/ ATV, (b) Pt/ G-PV, (c) Pt/ 14 wt% TiO ₂ / ATV,	

and (d) Pt/ 14 wt% TiO ₂ / G-PV catalysts in argon-saturated 0.5M H ₂ SO ₄ solution at a scan rate of 50 mV/s. Aging conditions: 4000 potential cycles at 25 °C.....	182
Figure 5.14: Beginning of Life (BOL) Electrochemical cell surface areas as a function of TiO ₂ loadings for Pt/TiO ₂ /ATV and Pt /TiO ₂ /G-PV.....	183
Figure 5.15: ECSA loss and normalized Electrochemical cell surface areas for different catalysts under stability assessment aging conditions.....	185
Figure 5.16: EIS characterization of Pt/G-PV catalyst at 0.425V biased potential in N ₂ -saturated 0.5M H ₂ SO ₄ solution at various intervals under durability study (a) Nyquist plots (b) Limiting capacitance plots. (c) Normalised capacitance plots.....	186
Figure 5.17: EIS characterization of Pt/ 14 wt% TiO ₂ / ATV catalyst at 0.425V biased potential in N ₂ -saturated 0.5M H ₂ SO ₄ solution at various intervals under durability study (a) Nyquist plots (b) Limiting capacitance plots. (c) Normalised capacitance plots.....	187
Figure 5.18: EIS characterization of Pt/ 14 wt% TiO ₂ / G-PV catalyst at 0.425V biased potential in N ₂ -saturated 0.5M H ₂ SO ₄ solution at various intervals under durability study (a) Nyquist plots (b) Limiting capacitance plots. (c) Normalised capacitance plots.....	188
Figure 5.19: ORR curves: for different rotation speeds (400-2500RPM) at a scan rate of 5 mV/s for prepared catalysts (a) Pt/ATV (b) Pt/14 wt% TiO ₂ /ATV (c) Pt/14 wt% TiO ₂ /G-PV (d) Comparison at 900 RPM for tested catalysts (e) Koutecky-Levich plots at 0.65V vs. NHE. Measurements were carried out in O ₂ -saturated 0.5M H ₂ SO ₄ at 25 °C.	191

Chapter 6

Figure 6.1: Network of reactions for methanol oxidation.....	197
Figure 6.2: Schematic mechanism of methanol photo oxidation enhancement on (A) Pt/PV, and (B) Pt/TiO ₂ /G-PV catalysts.....	199
Figure 6.3: HR-STEM image of TiO ₂ /G-PV composite support and elemental mapping images of C, O and Ti.....	203

Figure 6.4: HR-STEM image of Pt/ TiO ₂ /G-PV catalyst and elemental mapping of Pt and Ti nanoparticles.....	204
Figure 6.5: XPS spectra. High resolution spectra of O1s for (A) TiO ₂ , (B) TiO ₂ /G-PV catalyst supports. High resolution spectra of Pt4f for(C) Pt/PV and (D) Pt/ TiO ₂ /G-PV. Experimental data are represented by symbols.....	206
Figure 6.6: Methanol Oxidation Reaction (A) Mass normalized current density CVs and (B) Forward peak current density in N ₂ - saturated 0.5M CH ₃ OH + 0.5M H ₂ SO ₄ solution scan rate of 50 mV/s test temperature: 25 °C.....	207
Figure 6.7: Methanol oxidation at electrolyte concentrations on Pt/TiO ₂ /G-PV (A) CVs (B) forward reaction in nitrogen saturated 0.5M CH ₃ OH +0.5M H ₂ SO ₄ solution scan rate of 50 mV/s test temperature: 25 °C.....	209
Figure 6.8: Methanol oxidation (A) Peak current vs onset potential and (B) Peak currents vs electrolyte concentration Activity.....	211
Figure 6.9: Methanol oxidation activity at 25 °C of (A) PV, (B) TiO ₂ (synthesized) and (C) TiO ₂ /G-PV supports with and without irradiation in N ₂ saturated 0.5 M CH ₃ OH + 0.5 M H ₂ SO ₄ solution at a scan rate of 50 mV/s. Currents normalized by glassy carbon electrode area = 0.196 cm ²	212
Figure 6.10: Methanol oxidation on platinized supports at 25 °C. (A) Mass activity and (B) Specific activity with and without irradiation in N ₂ - saturated 0.5 M CH ₃ OH + 0.5 M H ₂ SO ₄ solution.....	213
Figure 6.11: Chronoamperometry intermittent irradiation of catalyst materials at 25 °C and 0.85V in N ₂ saturated 0.5 M CH ₃ OH + 0.5 M H ₂ SO ₄ solution.....	216
Figure 6.12: Nyquist plots at 25 °C and 0.55V for (A) Pt/PV and (B) Pt/TiO ₂ /G-PV with corresponding fittings from the equivalent circuit; (C) Equivalent circuit for fitting impedance data, in nitrogen saturated 0.5 M CH ₃ OH + 0.5 M H ₂ SO ₄ solution; (D) Charge transfer resistance with and without irradiation from fitting impedance data to equivalent circuit.....	217
Figure 6.13: (A) CO oxidation and stripping without illumination and (B) CO oxidation with and without illumination in 0.5 M H ₂ SO ₄ solution at a scan rate of 50 mV/s and 25 °C. Currents normalized by glassy carbon electrode area = 0.196 cm ²	220

Figure 6.14: Methanol oxidation platinized supports (A) Pt/PV and (B) Pt/TiO ₂ /G-PV catalysts at different temperature without irradiation in N ₂ - saturated 0.5 M CH ₃ OH + 0.5 M H ₂ SO ₄ solution at 50 mV/s. Insets show methanol oxidation currents with and without irradiation at 25°C. Corresponding Arrhenius plots of methanol oxidation at various temperatures with and without illumination for (C) Pt/PV and (D) Pt/TiO ₂ /G-PV catalysts.....	222
Figure 6.15: Durability study (A) CVs of Pt/TiO ₂ /G-PV based on the electrode geometric area (0.196cm ²), and (B) Pt active area as a function of cycle number carried out in N ₂ -saturated 0.5 M H ₂ SO ₄ at 25 °C and a scan rate of 50 mV/s.....	225
Figure 6.16: (A) Pt surface area as a function of methanol oxidation peak currents in N ₂ - saturated 0.5 M CH ₃ OH + 0.5 M H ₂ SO ₄ at different cycling intervals following during durability study in 0.5 M H ₂ SO ₄ and (B) Normalized data for the catalysts with and without illumination.....	226

List of Abbreviations and Symbols

AC – Ampere

AC – Alternating current

ADT– Accelerated durability test

AST– Accelerated stress test

ATV – Acid Treated Vulcan

BET – Brunauer-Emmett-Teller

BJH – Barret-Joyner-Halenda

BOL – Beginning of life

°C– Celsius

C – Capacitance

CB – Conduction Band

C_{DL} – Double layer capacitance

CL – Catalyst layer

CNT – Carbon nanotube

CPE – Constant phase element

CV – Cyclic voltammetry or cyclic voltammogram

DC – Direct current

DMFC – direct methanol fuel cell

DOE- Department of energy

DSC – Differential scanning thermogravimetry

E – Potential

E_a^{app} – Apparent activation energy

ECSA – electrochemically active surface area or electrochemical surface area

EELS – electron energy loss spectroscopy

E_F– Fermi Energy

E_G– Energy (Band) Gap

EIS – electrochemical impedance spectroscopy

E_{max} – Peak potential

EOL – End of life

eV– Electron Volts
 FTIR – Fourier Transform Infrared spectroscopy
 GC – glassy carbon
 G-ATV – Glucose doped acid treated Vulcan
 G-PV – Glucose Doped Vulcan
 HOR – Hydrogen oxidation reaction
 ICEs – Internal combustion engines
 I_{\max} – Peak current
 $h\nu$ - UV-visible irradiation
 JM – Johnson Matthey
 j_0 – Current density
 KL – Koutecky-Levich
 L – Inductance
 MEA – Membrane electrode assembly
 M_{N_2} – Molar mass of N_2
 MOR – Methanol oxidation
 MO_x – Metal Oxide
 MWCNT – Multi-Wall Carbon Nanotube
 n– Number of Electrons
 n– Amount adsorbed at relative pressure P/P_0 ,
 n_m – Monolayer capacity (Surface coverage of adsorbate)
 NPs– Nanoparticles
 ORR – Oxygen reduction reaction
 P – Adsorption pressure
 PEMFC – Proton exchange membrane fuel cell
 P_0 – Saturation pressure
 PV– Pristine Vulcan
 N_A – Avogadro’s constant
 R – Resistance
 R_2 – A form of resistance in the equivalent circuit
 R_{CT} – Charge transfer resistance

R_s – Solution resistance

R_Σ – Total electrode resistance

ω – Angular frequency

Z' – Real impedance

Z'' – Imaginary impedance

Φ -Phase angle

CHAPTER ONE

Introduction and Literature Review

1.1 Background

Population growth and improvement in the standard of living conditions demand for new clean and sustainable energy sources since the combustion of fossil fuels such as coal, natural gas, and oil releases a significant amount of greenhouse gases with a devastating effect on the environment [1-3]. The non-renewable nature of fossil fuel reserves and political instability are also major factors to this renewed interest in alternative energy sources [3] mainly taking into account that total energy demand is expected to double in 2050 unless cogent steps are implemented to moderate energy use [1-2].

On top of those problems, current energy systems suffer from poor efficiency via conversion of stored energy to useful energy. For instance, automobile internal combustion engines (ICEs) have a theoretical maximum efficiency of approximately 50% which rarely exceed 30% in practice due to operational constraints [4]. In this scenario, hydrogen fuel cells are considered a leading contender to replace internal combustion engines, since renewable energy sources, such as wind, solar and biomass can be used to generate clean hydrogen, and fuel cells are not exposed to the limitations imposed by internal combustion engines. In addition, hydrogen fuel cells can continuously provide electrical energy as long as the reactant are supplied from outside the cell [1] which is an advantage over lithium and other battery systems.

For mobile application, the transition from ICEs to a zero emission energy fuel cells, such as proton exchange membrane fuel cells (PEMFCs) that readily convert hydrogen and oxygen into water with electricity, would have a great impact on minimizing greenhouse gas emissions in densely populated areas. Although this primary energy source is not readily available in its pure molecular state, recent advances in technology has made it easier to produce from renewable sources such as electrolyzers, powered by wind turbines or solar photovoltaics [5].

PEMFCs in comparison to ICEs can readily convert primary energy source (hydrogen) with a higher theoretical efficiency that is not restricted by Carnot cycles at low temperature. PEMFCs produce less friction with no moving parts that make them more reliable and durable. PEMFCs are produced in modular forms that allow independent

power scaling for various applications such as 1 W for mobile phones all the way up to the megawatt range (power plants). PEMFCs devices operate in continuous energy flow and can easily be refueled, unlike batteries that need to be recharged periodically or thrown away [6].

There are several challenges that face current fuel cell technology and impede its wider implementation. Two critical aspects are the slow kinetics of the oxygen reduction reaction (ORR), acting as a bottleneck for the overall reaction and Pt corrosion and dissolution under the cathode conditions where the ORR takes place. At the root of both cost and stability issues is the catalyst layers used in the anode and cathode, consisting of expensive Pt-based materials. According to a study completed for the Department of Energy (DOE), approximately 55% of the overall fuel cell cost stems from the Pt-based catalyst layers [7]. The kinetics of the ORR is inherently much more sluggish than the hydrogen oxidation reaction (HOR) occurring at the anode, and this is often considered the primary factor limiting the overall fuel cell performance. This results in extensive reliance on Pt loading catalyst materials in order to facilitate the ORR at a reasonable rate.

Catalyst durability is one of the key issues limiting widespread use of PEMFCs. Platinum which is by far the most efficient catalyst for PEMFC thermodynamically dissolves in the vicinity of 1.0 V (vs. Normal Hydrogen Electrode; NHE) in acid environments. During the normal operation, rapid idle to peak power cycles result in cathode potential variations from 0.6 to 1V (vs. NHE) causing catalyst degradation. The carbon on which platinum is supported also corrodes at high electrode potentials above 1.0 V which is common in PEMFC operation, during start-stop cycles voltage spike occurs which can be as high as 1.5 V (vs. NHE). Surface area losses of platinum nanoparticles supported on carbon during cycling conditions need to be reduced. Robust electrodes with minimal Pt loading, enhanced activity, improved stability and less susceptibility to fuel impurities needs to be addressed prior to PEMFC commercialization.

Fuel cell devices must be widely produced in mass-market applications to meet automotive and domestic sectors demand. This will require an overhaul of the current energy system with infrastructural development for generating, distributing and storing fuel. For automotive applications, PEMFC technology must compete favourably with the market leader, conventional ICEs both in terms of cost and reliability. For example, the

approximated operational cost of automotive ICE is approximately 25-35 \$/kW with a lifespan of more than 5000 hours [8]. The current Pt loading in a typical PEMFC electrode uses a high Pt loadings of 0.4 mg_{Pt}/cm² on the cathode and 0.3 mg_{Pt}/cm² on the anode [9]. Thus, there is need to reduce Pt loadings to maximise cost of the fuel cell stack. However this should be approach with almost care as significant reduction in metal loading may affect mass transport in the catalyst layer with performance loss [10]. The performance target of 0.125 mg_{Pt}/cm² Pt loading has been proposed for PEMFC electrodes [10-11]. With this proposed loading, the total Pt needed in a fuel cell vehicle will be around 8 g, which will be similar to what internal combustion engines vehicles have today [9]. Another important challenge facing current fuel cell technology is corrosion of the catalyst support. A stable support is required to maintain its performance. Thus, finding a means of reducing the platinum content or replacing it entirely, as well as the development of more robust catalyst support materials are areas of great interest.

1.2 Types of fuel cell

Fuel cells are classified into six major groups based on the nature of the electrolyte material that each system uses [12-13]. As shown in Table 1, the electrolyte material determines the operating conditions and their performance characteristic, making each type of cell suitable for specific applications. The first four fuel cells are characterised by their moderate temperature of operation (50-120 °C) well below the temperature range of molten carbonate and solid oxide fuel cells (600-1000 °C) [12, 14].

Phosphoric acid fuel cells (PAFCs), molten carbonate fuel cells (MCFCs) and solid oxide fuel cells (SOFCs) are all primarily used for stationary power applications while PEMFCs and DAFCs are used for smaller power applications such as vehicles and even electronics. MCFCs and SOFCs are generally heavy because they require dense layers of ceramic electrolytes to operate. On the other hand, PEMFC and DAFC are lighter with a solid electrolyte (Proton exchange membrane, PEM), hence are more advantageous to use in transportation devices and small electronics. The use of a solid membrane in the latter can minimise corrosion from the electrolyte solutions without the need to contain and circulate fluid. The low temperature operation with quick start up of PEMFCs and DAFCs are necessary for their applications in vehicles and small devices.

Table 1.1: Main fuel cell types

Fuel cell type	Operating Temperature (°C)	Output Range (kW)	Efficiency (%)	Primary use
PEMFC	50-100	<250	50-60	Portable Power Transportation
DAFC	60-90	1-100	50-60	Portable Power Transportation
Alkaline FC	90-100	10-100	60-70	Military, Space
Phosphoric Acid FC	150-200	50-1000	80-85	Distributed Generation
Molten Carbonate FC	600-700	<1000	85	Large Distributed Generation
Solid Oxide FC	650-1000	5-3000	85%	Large Distributed Generation

1.3 Structure and mode of operation of proton exchange membrane fuel cells (PEMFCs)

The mode of operation of PEMFCs involves inlet injection of hydrogen gas at the anode side of the fuel cell and pure oxygen gas or air at the cathode side concurrently. These gases at their respective sides flow through channels in plates and migrate through gas diffusion layers to the catalyst surface. The resultant electrochemical reactions are depicted in Figure 1.1. The positively charge carriers (protons) pass through the membrane (usually Nafion) to the cathode compartment for subsequent ORR. On the other hand, negatively charge electrons go through an external circuit resulting in an electric current with a link to the cathode side. At the cathode, the electrons combine with protons and oxygen to produce water as reaction by-product. These processes are shown in Figure 1.1 for complete direct electrochemical energy conversion.

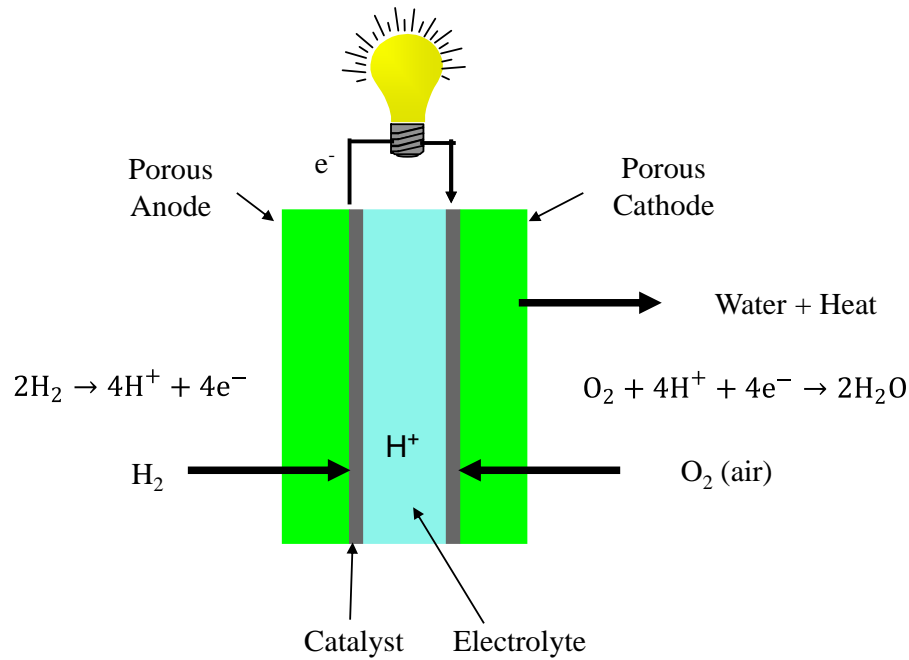


Figure 1.1: Schematic of PEMFC mode of operation

The two electrochemical reactions in a fuel cell take place within three layers known as the membrane electrode assembly (MEA). In a typical MEA, two porous electrodes, anode and cathode are present; each of which is catalyzed on one side and bonded to either side of a thin membrane. The porous electrode has an active layer sandwiched between the gas diffusion layer and the electrolyte. This allows the electrode to be interpenetrated with both the gas and the electrolyte. This is important, as the reaction must occur at what is known as a triple phase boundary, in which an active site on the catalyst is exposed to both the gas and the electrolyte, so that all the reactants may be present. The standard catalyst/support structure is platinum on carbon black. The main catalyst driving the chemical reaction can be applied either directly to the porous electrodes or to the membrane.

Pt and Pt alloy materials constitute the commonly used PEMFC electrode materials with a polymer membrane that prevents gas mixing and crossover between the two cell compartments. Ideally, the membrane is composed of a polymer capable of conducting protons through an aqueous network. This membrane material determines to a large extent the operating temperature of the PEMFC. Despite significant research interest dedicated to studying different polymer materials for PEMFCs, Nafion[®] remains the best performing membrane for this application. Precious metal catalysts are needed to facilitate the electrode reactions with temperature sensitive polymer membrane. The two electrochemical reactions on these electrodes occur primarily at certain region in the catalyst layer called triple phase boundaries (TPB), which is the common meeting point of the catalyst, reactants and electrolyte. Figure 1.2 shows the simplified schematic diagram of TPB. PEMFCs are extremely versatile with energy supply ranging from < 10 W up to 1 MW and have been successful demonstrations for low and high energy application requirements such as in stationary power, portable and automotive applications [15].

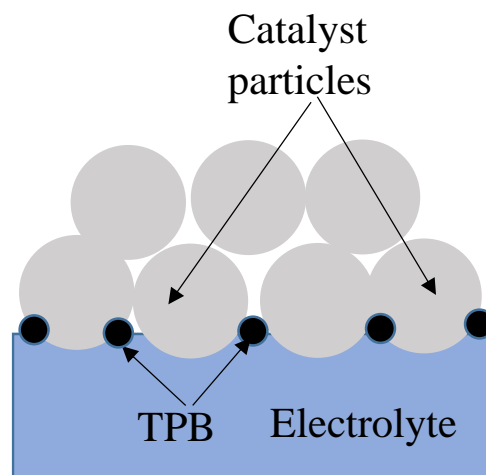


Figure 1.2: Sketch of catalyst layer triple phase boundaries (TPBs) [16].

1.4 Oxygen reduction reaction (ORR) Catalysts

Most of the performance losses in a PEMFC is due to the limitations of the ORR catalyst at the cathode electrode [17]. The ORR is kinetically sluggish in PEMFCs and is even more so for the cathode of a DMFC, as the cathode catalyst layer experiences the cross-over of methanol, making the cathode electrocatalyst having to simultaneously catalyse the oxygen reduction and the undesired methanol oxidation reactions. This results in mixed potentials at the cathode and leads to a loss of fuel efficiency. ORR is also a challenging reaction to catalyse, in the sense that it requires catalyst material to be: 1) stable under the extreme corrosive conditions PEMFC; 2) chemically active so as to be able to activate O-O bond; and 3) noble enough to be able to release the oxygen from the surface in the form of water [17].

At the moment, Pt, a precious metal, is the best metal catalyst for the reduction of oxygen. It is widely used and known to be the state of the art cathode catalyst for low temperature fuel cells [18]. The ORR has been shown to proceed through two parallel pathways in aqueous electrolytes according to the following reactions [19]:



The first pathway (Eq. 1.1) involves the direct four-electron pathway, where oxygen adsorbs to the surface of Pt to generate intermediate species that will subsequently undergo further steps such as accepting protons and electrons and cleaving the oxygen-oxygen bond to eventually produce water [20-21]. In Eq. 1.2, the second possible pathway, it is often referred to as the indirect two-electron pathway, where oxygen combines with two-protons and two electrons to give hydrogen peroxide (H_2O_2). The formed peroxide will get reduced to water (Eq. 1.3). It is commonly accepted that the 4-electron pathway is faster than the 2-electron pathway hence, it is the most preferred pathway reaction in fuel cells [19, 22]. The two electron pathway reaction is highly

undesired in fuel cells because not only reduces the efficiency of the system, but also the H_2O_2 can degrade the catalytic activity of the catalysts and membrane, thereby resulting in significant fuel cell degradation or even failure.

1.5 Pt Catalyst stability

Pt-based catalysts dissolve when the cathode is subjected to potential cycles during fuel cell operation. Pt dissolution can occur at low pH, in a narrow potential near 1 V vs. NHE [23- 24]. Pt will dissolve above this potential according to the surface oxidation and oxide reduction processes below:



The Pt ion dissolution and solubility in the electrolyte determine the diffusive capability of the Pt particles. This includes the dissolution of Pt, diffusion through the electrolyte, and the growth of crystallites. These induce adverse effects on fuel cell performance should be mitigated [25]. Pt cation solubility increases with potential, temperature, and low pH.

Different mechanisms for Pt dissolution and redeposition on the catalyst surface and Pt migration through the surface have been suggested to explain the increase of the catalyst particle size over exposure time. The thermodynamic driving force for agglomeration/sintering and Ostwald ripening is the reduction in surface energy accompanying particle growth [26]. This phenomenon leads to dissolution of smaller particles and growth of larger particles [27]. When Pt dissolves in the electrolyte, it can diffuse and grow into larger crystals which offer lower surface tension and minimizes their electronically strained lattice configurations and reactive surface sites [28]. This causes a loss of ECSA and platinum deposition in the polymer electrolyte, contributing to its degradation.

Accelerated Stress Tests (ASTs) have been used to evaluate the stability of Pt catalysts in a three-electrode cell. This procedure usually allows degradation in the catalyst activity to be observed within several days, rather than several weeks as otherwise required before any significant decrease in fuel cell performance is noticed [29]. Cycling the electrode potential between two extreme values can accelerate Pt corrosion and also induce Pt dissolution because it can contribute to remove the protective oxide and hydroxide layer formed on the surface of Pt and speeds up corrosion when the electrode is exposed to high positive potentials in the following cycle before the surface can be passivated again [30].

As highlighted in a classic paper by Kinoshita, Lunquist, and Stonehart, potential cycling had historically been known to increase corrosion processes in phosphoric acid fuel cells where carbon corrosion is also a significant problem [31]; the paper showed how the cycling profile could accelerate corrosion rates. They varied cycling parameters and ran profiles of square and triangular waves of the supported Pt electrodes. Detached Pt particles (from carbon support) are ineffective in the fuel cell reaction. Pt cations diffusing into the membrane can reduce proton conductivity and lead to more degrading mechanisms of the ionomer. Pt reduction in the ionomer poses a major risk to the material. The rate and location of Pt^{2+} reduction and nucleation in the ionomer was found to depend on the partial pressure of both hydrogen and oxygen [32].

The stability of the Pt catalyst nanoparticles also depends on the mode of operation. For instance, in stationary mode, the common practice is to operate the cell stacks at a constant current density ($200 - 300 \text{ mA/cm}^2$). In such a mode, a significant decrease of about 50% in ECSA was observed for the initial 1000-2000 hours and remains constant up to 40,000 hours. On the contrary, PEMFCs for automobile applications undergo a continual substantial decrease in ECSA during their operation due to harsh operating modes such as frequent potential or load cycling, start/stop, high load and idling [33]. Fuel cell operation modes corresponding to vehicle operating conditions are classified as load cycling (acceleration/deceleration while driving), start-stop (stack start up/shutdown), and high load operation (steady high speed driving) and low load operation (continued idling). In addition, the weather condition where the vehicle will be used plays a major role in ECSA loss.

Automobile drive cycles are the test procedures used to emulate the typical usage of a vehicle on the road. These driving cycles are categorized into two types: (i) transient and modal driving cycles [34] and (ii) transient driving cycles with frequent changes in speed, typical of real driving patterns whereas modal driving cycles involve prolonged periods at a constant speed. Fuel cell in automobile transient operation includes 1,200,000 load cycles, 17,000 start/stop cycles and 1650 freeze cycles [35]. The decrease in voltage from the theoretical voltage of 1.23 V is due to the activation, ohmic and crossover losses. In normal operation, the cathode potential varies in a range of 1.2 to 0.6 V caused by cycling between idle and peak load which includes ohmic losses. Higher potentials up to 1.4 V (or even higher) are encountered in start/stop cycling.

During idling constant potential high voltages (~ 0.90 V vs. NHE) are observed, where minimal currents are drawn from the fuel cell [36]. Fuel cell vehicles will operate a significant amount of time at idling conditions of about 40% in its service lifetime [37]. An overview of operating modes and possible causes of cathode catalyst degradation are briefly listed below in Table 1.2. Evaluation of performance loss under each operating mode by imposing loads on a fuel cell vehicle has been documented [38]. This was simulated during real world driving by mirroring how internal combustion engines are typically operated. It was observed that potential cycling and idling accounts for 56% of the total degradation whereas start-up/stop-down accounts for 44% even though, the role of operating conditions and their relation to relevant mechanisms of ECSA loss is well not understood [38]

Table 1.2: Operating modes and possible causes of catalyst layer degradation [39]

Operating mode	Causes	Degradation
Potential cycling	<ul style="list-style-type: none"> • Pt/C degradation 	<ul style="list-style-type: none"> • ECSA loss
Start-up/shut-down	<ul style="list-style-type: none"> • Carbon support corrosion by high potential 	<ul style="list-style-type: none"> • ECSA loss • Catalyst layer water accumulation
Idling(low current)	<ul style="list-style-type: none"> • Pt/C degradation • Catalyst poisoning (membrane) • Chemical decomposition by H_2O_2 formation 	<ul style="list-style-type: none"> • ECSA loss • Membrane proton conductivity loss

A systematic study on the impact of Pt particle size and operating conditions on PEMFC cathode catalyst durability was carried out by Yang et al. [40] using MEAs with 0.2 mg/cm² Pt loading on both the anode and the cathode. The results indicated that ~ 12 nm particles resulted in practically no change ECSA or mass activity up to 10, 000 cycles with low fuel cell performance at high current density regions. The smaller Pt particles (~2 nm) showed very good initial performance and high losses of ECSA, mass activity, and potential loss at high current densities. On the other hand, the MEA prepared with ~7 nm Pt particles showed very good initial performance and slow electrode decay characteristics. On the other hand, the fuel cell performance under constant flow of H₂ and air at 80 °C and 150 kPa back pressure showed potential loss of 25-30 mV at 0.8 and 1.5 A/cm² after 30,000 cycles between 0.6 and 1.0 V (vs. NHE). A very stable H₂-air fuel cell performance with less than 30 mV loss at 0.8 and 1.5 A/cm² was achieved when the MEA was cycled at low relative humidity. (RH) conditions (30% RH) up to 10,000 cycles. The slow decay for the 7 nm particle size catalyst was attributed to the particle stability.

Arisetty et al. [41] investigated the effect of Pt loading on Pt catalyst durability using commercial MEAs having 0.15 mg/cm² Pt loading at the cathode and 0.05 mg/cm² Pt at the anode. The authors observed high ECSA loss for the MEA with 0.15 mg/cm² Pt when compared to the MEA having 0.4 mg/cm² Pt. It was further observed that 70% of the 54 mV cell voltage loss at 1.0 A/cm² after 30,000 cycles resulted from the reduced mass transfer coefficient in the catalyst layer of the MEA with 0.15 mg/cm² Pt.

The durability of a 40% Pt/graphitic carbon catalyst under simulated fuel cell automotive operating conditions i.e. potential cycling under H₂/air atmosphere, as well as the effect of Pt dissolution at different temperatures have been investigated by Dhanushkodi et al. [42]. A significant loss in ECSA was observed during the first 1000 cycles at all the temperatures. Cell potential loss of ~ 30, 35, and 90 mV were observed at 1.7 A/cm² after 20,000 cycles at 40, 60, and 80 °C, respectively. The authors used a diagnostic expression to estimate the kinetic activity losses using effective platinum surface area from the cyclic voltammograms which indicated that the performance loss is mainly due to Pt loss.

1.6 Catalyst Support Material

Another significant challenge facing current fuel cell technology is corrosion of the catalyst support and is being addressed independently by organizations such as the US DOE Office of Energy Efficiency and Renewable Energy's Hydrogen Fuel Cells and Infrastructure (HFCIT) program in close association with national laboratories, universities, and industry [43]. The electrocatalyst on either electrode (anode and cathode) is usually dispersed onto the porous structure of a carbon support material. The nature of electrocatalyst support materials is a deciding factor on performance and durability of low-temperature fuel cells. If ideally designed, the catalyst support can help promote the electrocatalytic reaction by facilitating charge transfer, mass transport of reactant fuels, and removal of products. Carbonaceous materials (chemically or physically activated carbons, carbon blacks, and graphitized carbons) are still considered the state-of-the-art and the most commercially successful catalyst support. The role of the catalyst support is to: (i) provide high surface area over which metallic particles can be dispersed and stabilized, (ii) guarantee an adequate electronic conductivity to support electrochemical processes, and (iii) facilitate mass transport of reactants and products to and from the active sites.

Existing literature data show that support corrosion is [more predominant](#) in (PAFCs) [44], but degradation in performance due to catalyst support corrosion has been also observed in PEMFCs during duty cycling despite the lower operating temperature range. Even though, the rate of carbon corrosion is lower in the case of PEMFCs, it is still thermodynamically favourable and cannot be avoided [45]. Electrochemical oxidation produces microstructural degradation and surface chemical changes, which lead to lost catalytic activity or even disastrous electrode failure. Carbon oxidation can impair catalyst microstructure, producing changes in surface hydrophobicity that may lead to gas transport difficulties [46].

The carbon support in a PEMFC is susceptible to corrosive conditions such as high water content, low pH, high oxygen concentration, temperatures ranging from 50-90°C, and high potential (0.6-1.2 V) [47]. Despite being the most widely used catalyst support for PEMFC, carbon support is actually thermodynamically unstable at PEMFC operating conditions. Electrochemical carbon support corrosion proceeds as in:



The standard electrode potential for this reaction at 25 °C is 0.207 V vs. NHE. Carbon is therefore thermodynamically unstable above this potential. Although carbon can also undergo combustion under PEMFC conditions, the electrochemical oxidation is observed. As carbon support corrodes, Pt nanoparticles agglomerate into larger particles and/or detach from the support material, consequently reducing the electrochemical surface area (ECSA) and catalytic activity. In the case of severe corrosion, the porous structure of the catalyst layer can be destroyed, increasing the mass transport resistance due to the blockage of gas access paths. Figure 1.3 shows Pt supported on electrically conducting carbon support and in contact with proton conducting ionomer in a normal electrode. However, after carbon oxidation, the Pt loses the electrical conductivity pathway, leading to inactive catalyst sites. The loss in Pt activity decreases the fuel cell performance significantly.

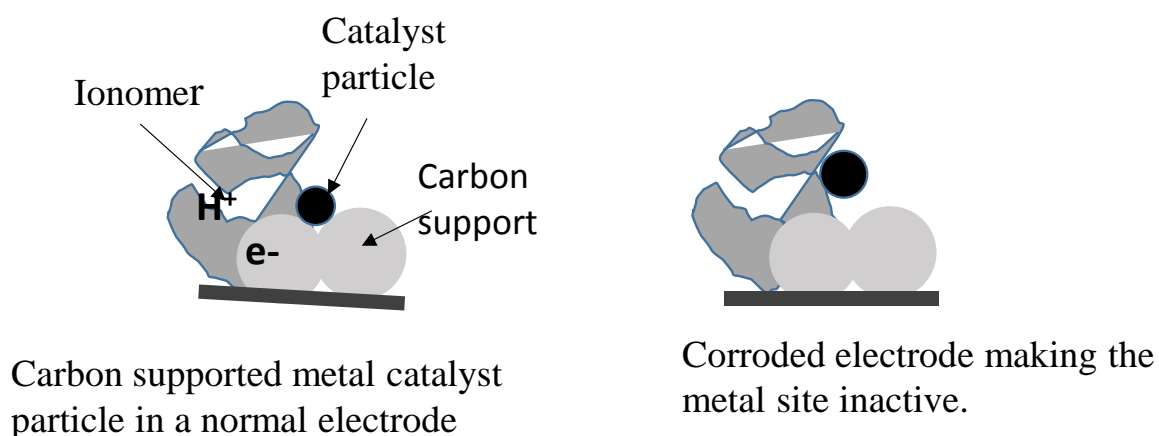


Figure 1.3: Schematic showing carbon support oxidation and loss of Pt activity [49] (Reprinted from García, B. L. *et al*, Low-Temperature Synthesis of a PtRu/Nb_{0.1}Ti_{0.9}O₂ Electrocatalyst for Methanol Oxidation. *Electrochemical and Solid-State Letters*, 10(7), B108-B110. Reproduced by permission of The Electrochemical Society

In automotive applications, the electrode can be exposed to potentials greater than 0.8V vs. NHE. This condition is experienced during low electric power demand, which corresponds to a significant portion of the fuel cells' operating time [48]. Carbon corrosion

can occur in both cathode and anode of a PEM fuel cell. During the start-up and shut down of the fuel cell, local cathode potential excursions as high as 1.5V (vs. NHE) can be observed [49], resulting in significant carbon oxidation. Anode carbon corrosion can also happen when there is a complete fuel starvation of one or more cells in a working stack [50]. The starved cells are driven into a reversed operation with the anode potential becoming higher than the cathode potential. This state triggers water electrolysis and carbon oxidation on the fuel cell anode to provide the required protons and electrons for the reduction of oxygen at the cathode. A potential drop in the starved anode region accelerates carbon corrosion by raising the potential difference at the cathode to extreme values up to ~1.5 V vs. NHE.

Carbon corrosion causes many adverse effects in the cathode which directly affect the demise of performance and operational lifetime of the fuel cell. The structure of the electrode is altered and permanently degraded. This leads to a change in material properties of carbon, surface bonding characteristics, decrease in surface area, and an increase in electronic resistivity [51-52]. The cathode layer thins and also becomes more compact which limits mass transport of fuel and product.

The structure and properties of the carbon play a significant role in carbon corrosion. Amorphous carbons with only short range ordering show poor corrosion resistance in comparison to long range order. Electrochemical degradation is slowed significantly by carbon graphitization. Graphite is composed of sp^2 carbon atoms bonded to three adjacent carbons in planar hexagonal rings also referred to as graphene sheets. These graphitized carbons show greater hydrophobicity and lower oxygen adsorption which also correlates with corrosion resistance. Corrosion is preferred at surface defects and disorder in the carbon lattice [53]. The process can also start at edges and corners of basal planes where free electrons are present [53]. These sites offer lower activation energy of electron transfer and surface oxide formation. This hydrophilic nature of the catalyst layer is more susceptible to corrosion for these reasons and can also create transport problems, causing water to accumulate in the electrode.

The interaction between Pt and carbon supports is of great importance when studying their corrosion. Metal-support interfaces are best described by Pt bonding to carbon by different Fermi energy levels and electron donation from the carbon support to

Pt [54]. This bonding nature has been revealed by XPS [55]. Electronic modifications of the metal by electron donating supports like graphite have been identified by a technique coupling infrared spectroscopy with carbon monoxide sorption calorimetry measurement. It also permitted an identification of the type, number, strength, and energy distribution of the surface sites on the catalyst as a function of the metallic interaction with the catalyst support [56]. Enhancing the interaction through strong anchoring sites improves the catalytic properties by bond disorder in the adsorbed metal clusters. However, the bond interaction between Pt and carbon is weak which ultimately contributes in large part to the enhanced dissolution between the two materials. The presence of Pt on carbon alone is enough to accelerate the reaction.

Qualitative experimental results using differential electrochemical mass spectroscopy (DEMS) has shown that CO₂ emission was directly proportional to the Pt surface area of carbon in 0.5 M sulphuric acid [49]. Experiments performed at 30 °C, 50 °C, and 70 °C showed that Pt catalyzed support can be easily oxidized compared to the non-catalyzed supports. The catalyst particles generate oxygen atoms, which react with carbon atoms, generating CO₂, and causing a significant loss of active catalyst surface area, thereby decreasing the performance. The Pt catalyst thereby plays a role in accelerating the corrosion of carbon.

Several practical approaches have evolved over time to carbon corrosion induced by erratic operation cycle, for instance the application of an external load to reduce voltage generated by the H₂/air segment and an increase in gas flow rate during start-up/shutdown to reduce the H₂/air front time. While these approaches look promising in minimising catalyst support corrosion, their practicability depends strongly on the application of the PEMFC. Therefore, a combination of system operation mitigation strategies and corrosion resistant support material is required to meet the DOE durability targets, especially under very dynamic automotive fuel cell operation strategies.

1.7 Mitigation strategies for carbon corrosion

1.7.1 Alternative carbon support materials

A practical mitigation strategy concerning carbon corrosion will involve the use of more durable support materials. These materials could be classified as: *i*) alternative carbon materials that are able to better sustain corrosion, for example high graphitic and nanostructured carbon materials and *ii*) development of non-carbon and modified carbon materials as support for the catalyst, such as using non-carbonaceous and/or inorganic oxide/carbide supports, nanostructured thin films (NSTFs) or un-supported catalysts. Advanced carbon based materials such as carbon nanotubes (CNT), carbon nanofibers (CNF), graphene, and mesoporous carbon have been investigated as catalyst supports for PEMFCs. These materials have desirable properties such as high surface area, good electrical conductivity, and more electrochemically stable due to their graphitic nature. The following subsections summarise recent progress in these alternative carbon and hybrid materials for applications in PEMFCs.

1.7.1.1 Carbon Nanotubes.

Carbon nanotubes are 3-D cylindrical nanostructures made up by ~~single~~ sheets of hexagonally arranged carbon atoms. They can be classified into single-walled (SWCNTs) or multi-walled (MWCNTs). SWCNTs are typically semiconductors with a band gap inversely proportional to the nanotube diameter. MWCNTs consist of a concentric set of cylinders with a spacing of 0.34 nm between the cylindrical walls resulting in a structure with relatively larger diameter than SWCNTs. Due to their high electrical conductivity, multiwalled carbon nanotubes present as excellent candidates for fuel cell electrode supports and many studies have shown enhanced catalytic ability for H_2/O_2 or the oxidation of alcohols when using CNTs as the support [57-60] These studies have shown that CNTs are superior to carbon black as catalyst supports in PEMFCs. In one study, it was shown that show that CNT based catalyst gave a 10% higher fuel cell voltage and twice the power density than those supported on carbon black [61]. The higher performance was attributed to the unique structure of CNTs which enhances the transport of gas

reactants to the catalysts, as well as its high surface area which allows good dispersion of Pt particles on the surface. It has also been shown that lower Pt loadings are required in CNT composites compared to other supports to achieve similar performance. This has the potential to significantly lower the amount of Pt necessary for catalysts and therefore lower production costs.

Although there are very few reports regarding the durability of CNTs as a catalyst support for PEMFC, Wang and co-workers found almost 90% loss of ECSA for Pt/C, while only 37% loss was observed for Pt/CNT after 168 h of oxidation treatment [62]. Shao et al. found that Pt/CNT degrades by 26.1% in terms of ECSA, compared to 49.8% for conventional Pt/C during an accelerated degradation test [63]. In another study using voltammetry and XPS analysis, Shao et al. found that CNTs are more resistant to electrochemical oxidation than carbon black, which they attributed to the unique closed structure of the CNTs. Although further investigations are needed, these studies suggest that CNTs could potentially provide much higher durability than carbon black.

1.7.1.2 Graphene and graphene oxide

Graphene is also an interesting candidate for applications in fuel cell composite electrodes. Its high conductivity and surface area make this material ideally suited for electrochemical application. Graphene is a flat monolayer of a hexagonal network of carbon atoms. Due to its unique structural properties such as thinness, mechanical strength, transparency, conductivity and high surface area, graphene has become the focus of intense research efforts for many applications including DAFCs, supercapacitors, sensors, and transistors. Studies also shown that Pt/graphene exhibited high CO tolerance and electrochemical stability compared to a commercial catalyst [64-65].

Graphene oxide (GO) has also drawn a lot of interest and attention due to its hydrophilicity and mechanical strength. GO has lower conductivity compared to graphene but it is chemically ‘tunable’, making it attractive for applications as catalyst support in fuel cells. The oxygen functional groups on the graphene structure create defects and edge planes on the surface which act as nucleation and anchoring sites for metal nanoparticles.

This results in small particle size and good particle distribution leading to high ECSA and mass activity [66-68]. The enhanced CO tolerance was attributed to the presence of covalently bonded oxygen functional groups and possibly a bifunctional mechanism between Pt and the GO support. Recently many research groups have also started investigating the electrochemical reduction of GO [69-70].

Studies have shown that graphene films can be formed on the surface of electrodes by the electrochemical reduction of GO. When sufficiently negative potentials are applied, the reduced graphene deposits on the surface of a working electrodes forming multiple layers of graphene. These films can be used as supports for metal nanoparticles in PEMFCs [71-72]. The hydrophilicity of GO promotes water activation, which readily oxidizes the adsorbed CO on Pt. Unfortunately, surface oxygen functional groups on carbon are also known to reduce the durability of fuel cell catalysts by promoting carbon corrosion [73]. Additionally, the complex synthesis methods mean that it is not yet suitable for large scale productions.

1.7.1.3 Ordered mesoporous carbon

Ordered mesoporous carbon (OMC) materials have well-ordered porous structure, providing high surface area and conductivity. OMCs are prepared either by using ordered mesoporous silica templates or by templating triblock copolymer structures and the structure can be tailored by the control of synthesis parameters. For example, the BET surface area can be altered from 200 to 2000 m²/g by changing the carbon precursor and synthesis conditions. More importantly, the three-dimensional porous structure has been shown to improve the diffusion of reactants and by-products, making it attractive as a catalyst support material [74]. The authors found that Pt supported on OMC with a BET surface area of 2000 m²/g exhibited superior electrocatalytic mass activity toward oxygen reduction compared to Pt supported on conventional carbons. Since then, a large number of studies followed. Generally, all OMC supported catalysts presented higher metal dispersion and higher catalytic activity, both for oxygen reduction and methanol oxidation, than carbon black supported catalysts [75-78]. Pore morphology was found to play an important role on the electrochemical performance. Song et al. prepared two kinds of

mesoporous carbon materials; one is a highly ordered structure mesoporous carbon and the other is wormhole-like mesoporous carbon with a disordered three-dimensional nano-network structure. Both materials have similar pore volume, BET surface area and mesopore size but it was found that Pt on ordered structure mesoporous carbon has higher electrocatalytic activity than Pt on wormhole-like mesoporous carbon [79].

Limited reports have been made on the durability of OMC-based electrode. Due to the high surface area of OMC, it is expected that it is more susceptible to corrosion. One strategy is by increasing the graphitization degree of OMC. A highly graphitic ordered mesoporous carbon synthesised using a soft template was found to have better corrosion resistance than Vulcan [80]. However, graphitization decreases the porosity and surface area of carbon materials. In summary, some general conclusions can be drawn:

- 1) Several studies have shown that better fuel cell performance could be achieved with the use of nanostructured carbon as catalyst support with reduced Pt loadings in comparison to conventional carbon black and the improved performance were ascribed to better catalyst utilization and/or support-catalyst interactions [81-82].
- 2) The purification of these carbon materials, especially nanostructured carbons, is usually complex and time consuming than the fabrication process of carbon black, this will invariably have cost implication in the catalyst development
- 3) These advanced carbon materials are thermodynamically stable over the entire ORR operating window and have been shown to be more corrosion resistant than conventional carbon black [85]
- 4) It can be challenging depositing metal nanoparticles on these carbon supports due to inherent inert surface and the highly ordered (sp^2). Thus metal deposition often involves a pre-treatment through surface functionalization [83]. Extensive surface treatment is often required to achieve well dispersed catalyst loadings on CNT and CNF can in effect make these materials less stable in fuel cell [84].
- 5) Half-cell experiments have shown complications arising from mass transport losses are encountered when converting these catalysts to porous fuel cell electrodes with the addition of a proton-conducting ionomer [86].

- 6) The interaction of Pt with these support materials mostly occurs through van der Waals forces and electrostatic interaction at sp^2 sites, though some weak covalent bonding is possible, this limits the ability to improve the intrinsic activity of Pt nanoparticles.

Based on some of these shortcomings, significant research work has been done to replace carbon supports with electrically conducting ceramic materials that have the ability to undergo strong covalent metal–metal bonding with the Pt clusters. It has been hypothesized the enhanced interaction will further improve Pt nanoparticle dispersion and stability as well as improve their ORR activity. Several supports have been proposed in the literature, though only a few have been studied with enough detail to make reasonable conclusions regarding their potential application as supports for Pt ORR electrocatalysts. Within the oxide category, nanostructured TiO_2 is studied in this work.

1.7.2 Non carbon support: Metal oxides

Metal oxides possess unique characteristics to be used as fuel cell catalyst support materials as stated below:

- 1) They have much higher corrosion resistance in the electrochemical environment of PEMFCs compared with carbon, because metal oxides can exist in a high oxidation state and do not readily lose further electrons to become further oxidized.
- 2) Some metal oxide supports can enhance the catalytic activity of precious metal nanocatalysts. The strong metal-metal oxide interaction could prevent the agglomeration of metal particles and contribute to maintain small metal particle sizes [87].
- 3) Due to the presence of hydroxyl groups on the metal oxide surface, the support could function as co-catalyst of noble metal nanoparticles catalysts in the oxidation of liquid fuels such as methanol and ethanol (bifunctional mechanism) [88].

Because of these desirable features, metal oxides have been used as independent electrocatalysts, co-catalysts and supports PEMFCs in aqueous acidic and alkaline electrolytes. There are some reviews about metal oxides in PEMFCs [89], binary metal oxides such as titanium oxide (TiO_x), tungsten oxide (WO_x), molybdenum oxide (MoO_x),

For PEMFC applications, it is important that a metal oxide material meets the following requirements:

- 1) ***High stability in acidic media under fuel cell operating conditions.*** Titanium oxide, tungsten oxide, molybdenum oxide and ruthenium oxide, etc. are stable in acidic media, while manganese oxide and perovskite oxides are stable in alkaline media.
- 2) ***Resistance to electrochemical corrosion.*** Metal oxides should also be electrochemically stable under PEMFCs operating conditions, or metal nanoparticles supported on them will peel off from them and agglomerate, leading to the degradation of the catalyst layer. For example, there was no oxidation peak observed between 0 and 2.0 V vs. NHE in 1 M sulfuric acid for titanium oxides [91].
- 3) ***Reasonable electrical conductivity.*** In the case of metal oxides, the electrical conductivity can be improved by doping with other metal ions or mixing with conductive carbon black to form oxide–carbon nanocomposites.
- 4) ***High specific surface area for an appropriate dispersion of noble metal nanoparticles on the metal oxides substrate to potentially allow for ultra-low Pt loading on the surface.*** This can also be achieved by supporting metal oxide nanoparticles on carbon materials with a large specific surface area as composite support.
- 5) ***Adequate porosity to ensure easy mass transfer of liquid fuels or oxygen gas and prevent water flooding in the electrodes.***
- 6) ***Compatibility with other electrode materials.*** In the case of metal oxide/carbon substrates, the noble metal nanoparticles should be able to form good three-phase boundary junctions with the carbon and metal oxide to minimize Pt loss.

1.7.3 Crystal lattice, electronic structures and applications of TiO₂

TiO₂ is thermodynamically stable under fuel cell operating conditions and exists naturally in three common crystal structures: anatase, brookite, and rutile. Evidence suggests that at the nanoscale, the anatase form is more stable than the rutile phase [92].

However all crystal structures of TiO_2 are semiconductors with a wide band gap (E_g) ~ 3 eV (3.2 eV for anatase and 3.02 eV for rutile). Titania is most commonly found in its +4 valence state at STP because of its $[\text{Ar}] 4s^2 3d^2$ electron configuration. Altering the Ti:O stoichiometry can be an effective way to increase the electron carrier concentration and improve the conductivity. Other stoichiometric ratios like TiO , Ti_2O_3 , Ti_3O_5 , and Ti_4O_7 have resulted in lower band gaps and higher electrical conductivities. Some of the best combinations for stability and conductivity values have been measured in Ti_4O_7 [93-94]. This material is sold commercially by the Atraverda Corporation and known as Ebonex® with resistivity as low as $10^{-3} \Omega \cdot \text{cm}$ at 298 K [95-96]. More generally, these are known as Magnéli phases with chemical formula $\text{Ti}_n\text{O}_{2n-1}$ (where n is between 4 and 10) [97]. They are formed at high temperatures under low oxygen atmosphere. Magnéli phases and other sub-stoichiometric ratios are stable, have good corrosion resistance, and are often used in acidic environments.

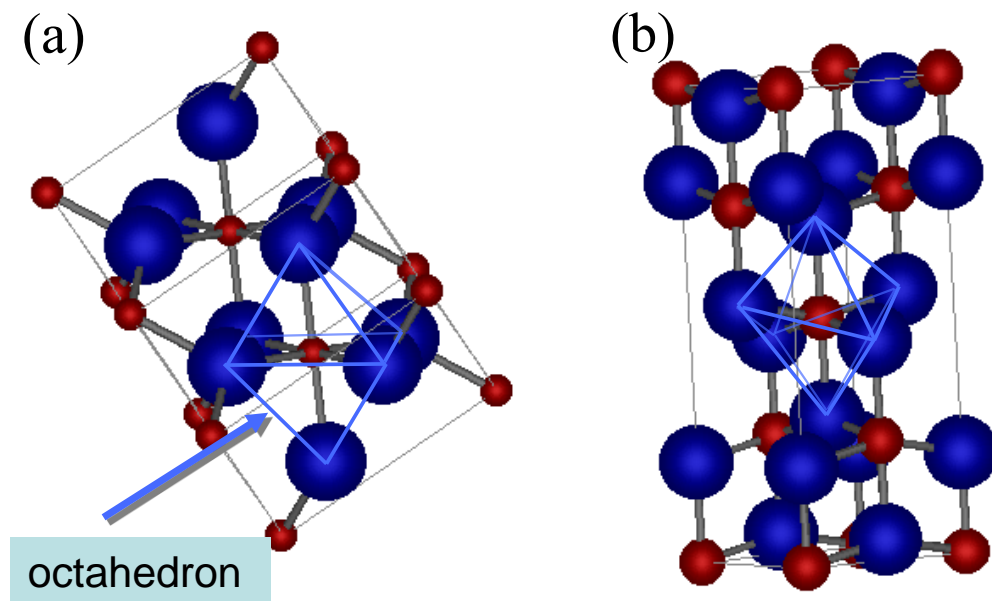


Figure 1.5: Crystal structures of titanium dioxide (a) Rutile and (b) Anatase [96]

Magnéli phases with low resistivity have been prepared and tested as catalyst supports [98-99]. However, they have several properties which make them unsuitable for application to PEMFC. They have some corrosion resistance in acidic environments, but

could be further oxidized to TiO_2 at higher potentials [100]. Also, the high temperature required for the synthesis of Magnéli phases results in very low surface areas materials $\sim 1 \text{ m}^2/\text{g}$.

TiO_2 has a refractive index of 2.5 - 2.9 range which is one of the highest known indices for all materials and its brightest white comes from ability to refract visible light when particle size is optimized to about half its wavelength (200~350 nm). The bright white material is commonly used as a pigment in make-up, paint, food coloring, dyes, textiles, and many other purposes requiring an opaque dispersion of the visible electromagnetic spectrum. However, its optical properties vary depending on the nature of crystal and defects found within it. The high dielectric constant of TiO_2 gives result to its widespread use in capacitive devices and other related technical applications such as television and radio where it is critical to store high charges in small volumes [101].

TiO_2 exhibits strong absorbance in the UV region. Photoexcitation occurs when photons with energy greater than the bandgap, $E_{h\nu} > E_g$, of TiO_2 are absorbed, thus creating mobile electron-hole pairs in the near surface region of the substrate (Figure 1.6). This phenomenon is of primary importance for applications in photocatalysis and photovoltaics [102]. Free electrons on the surface bond with H_2O and can electrolyze the splitting of water molecules. This process can also form reactive intermediates like $\cdot\text{OH}$ radicals which have very high oxidative potential. This field of research has produced the greatest number of journal articles on TiO_2 material in recent times.

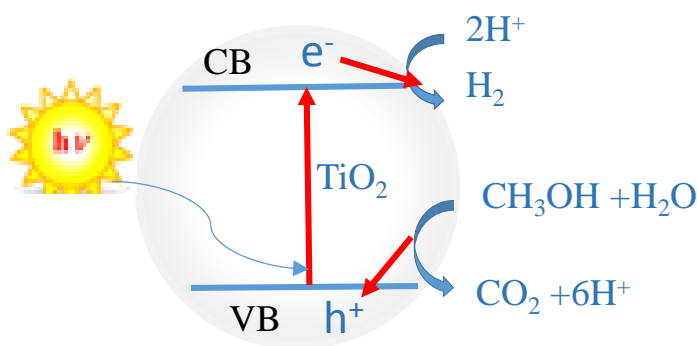


Figure 1.6: Mechanism of TiO_2 photocatalysis process. ($h\nu$ is the UV-visible irradiation)

1.7.4 TiO₂ catalyst support

Many efforts have been made to alter the electrical properties of titania by doping it with transition metals, introducing defects, and formation of TiO₂ composites. Most of the pioneering work was done to enhance photo-response to perform more efficient redox reactions when excited by photons of lower energy in the visible region. The new materials have demonstrated many different effects and properties of charge transfer, electron-hole recombination rates, lower band gap(s), adsorption capacity, morphology, phase stability, intermetallic and interionic bonding, and more. Some interesting results from the metal coating of titania with GroupVIII metals like Pt and carbon modified titania as well as carbon-titania supports are reviewed.

When platinum is reduced on n-type titania semiconductors, a Schottky junction can be formed. This results from the energy band bending and alignment of Fermi levels. Metals with low work functions like platinum can cause electrons to accumulate at the interface of titania due to a barrier formed between the two materials. When electrons are excited in the oxide and they can cross the barrier into conductive metal, recombination is prevented with a reactive electron-hole left behind [103]. The separation of charge may be influential in the role of TiO₂ supported catalysts used in the electrode. In fact, the electrochemical potential can control its reactivity by a similar way to stimulation of photochemical reactions as was famously reported by Honda and Fujishima [104].

The most attractive advantage of TiO₂ based supports is the electronic interaction with Pt catalyst nanocrystals. Some surface cations in oxides can be reduced to lower states which facilitate a strong metal-support interaction (SMSI) with group VIII noble metals like Pt when supported on TiO₂, a term notoriously dubbed by S. J. Tauster [105]. Pt particles on the surface of oxides formed a strong bond and appeared as flattened “raft-like particles” to Tauster. An intermetallic interaction exists between reduced Ti atoms and the noble metals on their surface. Later, it was discovered that actually the Ti cations from the oxide had diffused around its surfaces and physically encapsulated the catalysts. Bonnani et al. [106] also realized the encapsulation was at least semi-reversible and dependent upon the preparation conditions. This description of SMSI has since been broadened to encompass support-induced changes in the catalytic activity and selectivity of the base metal catalyst because this metal–support is closely linked to the catalytic behavior of the

latter. SMSI has been found to play significant roles in many catalytic reactions, such as alcohol oxidation, CO oxidation and ORR [107-109].

There are several proposed mechanisms that intent to explain the primary function of the metal oxide on the catalytic behavior of supported metal nanoparticles. However, these mechanisms are not mutually exclusive and each focus on explaining a slightly different observation related to supported metal catalysts as different experimental observations are often involved. Together, these various experimental observations as a whole describe a complex series of interactions showing how the metal–support interface can strongly influence surface chemistry and selectively amplify specific reaction pathways. Some mechanism pathways have been proposed to explain the observed metal–support interactions: (1) formation of active sites when the support wets (or decorates) the metal particle [110], (2) activation and spillover from chemically active sites in the support [111], and (3) electronic mediation through charge transfer [112]. It is also important to know that substantial difference in adsorption energies metal and oxide molecules with oxide–metal interface could can also bring together reactants that would not co-adsorb on either an oxide or a metal alone [113]. In a separate study, John Robertson in 2010 showed that these intermetallic interactions are much stronger than those directly between carbon and platinum and could serve to anchor the catalyst and prevent dissolution [114].

Hepel et al. applied quantum mechanical calculations to study the support–catalyst cluster interactions and surface diffusivity of adsorbed intermediates on bimetallic catalysts supported on nanoporous TiO_2 [115]. The simulation shows the electron cloud to be evenly spread over all the surface atoms when Pt atom forms bonds with the Ti atoms of TiO_2 . This SMSI effect lowers the activation energy for CO_{ad} surface mobility, and leads to a more facile diffusion of CO_{ad} from Pt sites to TiO_2 , and thus a lower poisoning effect on a TiO_2 support compared with unsupported Pt and Pt alloy catalysts.

Gustavsson et al. prepared Pt / TiO_2 catalyst film on a Nafion membrane and observed that a thin layer of TiO_2 between Pt and Nafion increases the ORR performance compared with a Pt film deposited directly on Nafion [116]. This improved performance was attributed to better dispersion of Pt on TiO_2 and substantial proton conduction through the thin TiO_2 layer. In another study, Pt/ TiO_2 catalyst was shows better thermal stability and electrochemical activity than Pt/C [117]. The TiO_2 in the electrode material minimised

Pt particles agglomeration and enhanced dispersion of the Pt atoms in the clusters hence the observed stability.

Huang et al. performed in situ fuel cell measurements using a Pt/TiO₂ electrocatalyst [118]. The catalyst showed polarization curves, which were similar even after 200 h corrosion time compared with a significant performance decrease of commercial Pt/C catalyst after 50 h corrosion time exposure. However, TiO₂ like other transition metal oxides is non-conductive at room temperature. Significant improvement strategies were needed to synthesize stable and conductive form of this oxide as novel catalytic support material. This is partially solved by reduction of TiO₂ to sub-stoichiometric forms at high temperatures and doping with appropriate metal cations [119-120], but such treatments often lead to decreasing support surface area for catalyst dispersion.

1.7.5 TiO₂ /carbon composite catalyst support

The common strategy to improve the poor electronic conductivity of TiO₂ support for energy application is to combine with carbon materials that have excellent conductivities such as carbon black, graphene, and carbon nanotubes. Apart from producing smaller of TiO₂ particles and introducing nanostructures, combining TiO₂ with carbon substrates have been effective at increasing the electrochemical performance of TiO₂ [121]. TiO₂ /carbon combinations are also of interest because component materials can be recovered after use in a wide range of applications [122], and synergistic effects of oxide/carbon interface are present between TiO₂ and carbon [123]. Various combinations are in the literature. More common configurations include TiO₂ nanoparticles in a carbon matrix, carbon coated with TiO₂, and mechanical mixtures of TiO₂ and carbon, which are referred to in the literature as impregnated/supported catalysts, or doped, hybrid, or composite materials.

Ideally the deposition of TiO₂ on carbon would result in a new class of hybrid support material that blends the excellent electrical conductivity and mesoporous structure of carbon black with the corrosion resistance of TiO₂. However, most of the preparation methods of carbon/TiO₂ composites in use was in the context of physical mixing, either in

solution [124-125] or via mechanical routes [126], and thus, catalytic performance of TiO_2 could only be limitedly improved due to the insufficient electronic contact between the TiO_2 and the carbon particles. Therefore, in order to further increase the catalytic performance, it is necessary to improve the contact between carbon nanomaterials and TiO_2 , which requires more delicately designed preparation strategies. The synthesis of TiO_2 /carbon composite structure in a single step would facilitate application development; since most reported preparations of TiO_2 /carbon composites involved several steps [127-129].

There is some contradicting evidence in a few reports over the phase necessary to achieve acceptable conductivity for electrochemical applications [130-131]. The discrepancy may come as a result of the preparation technique used. Huang et al. used a sol-gel procedure to prepare a conductive rutile phase by reducing the oxide at higher temperature [118]. The transformation temperature for the densely-packed rutile phase with ($\sim 550^\circ\text{C}$) is higher than that of the metastable anatase phase. The greater temperatures required for the rutile transformation also limits the porosity of titania and decreases the surface area substantially.

Pt/C+ TiO_2 materials were investigated for fuel cell performance following hydrolysis of TiO_x on Pt/C catalyst and its durability rivaled the commercial Pt/C in a real PEMFC during cyclic voltammetry degradation tests, but did not improve cell performance or catalyst activity [132]. In other study, Kraeme *et al* shows improvement in catalytic activity following Pt deposition on ultrasonically mixed TiO_2 /carbon black [133]. But this approach does not offer the optimum performance improvement due to the lack of material synthesis control and the structural ordering required for the dual benefit.

Very recently, there have been reports on the design and synthesis of oxide–carbon hybrid support materials with Pt nanoparticles deposited at the interfaces between metal oxides and carbon [134-135]. Jiang et al prepared carbon riveted Pt/ TiO_2 –C catalyst by in situ carbonization of glucose. Pt nanoparticles deposited on the boundaries of the mixed support exhibit significantly enhanced stability in fuel cell environments [136]. These works present a new concept of triple junction structure to promote the performance of Pt electrocatalysts however controlling the thickness of TiO_2 on mesoporous carbon and preventing phase segregation continues to be a synthetic challenge [137].

Thus, engineering the interface between the metal and metal oxide should not be overlooked in the use of titania for electrocatalysts composites. This interface could be an important source of the synergy between activity and stability. Quite possibly, there is a way to utilize a stable form of TiO_2 by depositing on carbon framework from a simple sol-gel process to fabricate a high surface area support with sufficient conductivity before depositing the Pt catalyst to form unique interfaces and heterojunctions.

Demonstration of a new approach which could offer the benefits of stability and improved catalytic activity without sacrificing valuable surface area is an important objective of this study. Growing TiO_2 onto a substrate like carbon from a solution deposition process offers an ideal support that can withstand transformation temperatures needed for composite preparation which can be scaled up well due to its simplicity.

1.8 Thesis Objectives

The standard catalyst material support used today, graphitic carbon, is electrically conductive, but in the harsh operating environment of the fuel cell, will degrade over time. This degradation can lead to the agglomeration of the catalyst material and loss of electrochemical surface area, reducing the performance and lifetime of the cell. It is therefore of great interest to develop a catalyst/support structure that is economical, conductive, and stable, while also allowing for a high electrochemical surface area; a TiO_2/C nanostructured materials holds a great deal of potential as a conductive and stable support for catalyst nanoparticles.

The primary objective of this study was to investigate the influence of the support material on the performance of the electrocatalyst in terms of activity and durability. I have investigated different strategies for the deposition of TiO_2 nanoparticles on the surface of carbon black, optimized the deposition of Pt catalyst nanoparticles on these modified substrates, and studied in great details their performance and durability under simulated FC conditions. Specific objectives include:

- i. Modify a commercial carbon substrate to induce surface functional groups.
- ii. Synthesize conductive and stable TiO_2/C composite catalyst supports
- iii. Deposit uniform Pt NPs on composite supports

- iv. Minimize Pt NPs agglomeration and growth during synthesis by optimization the deposition of TiO_2 nanoparticles on carbon.
- v. Evaluate the catalytic activity for ORR and methanol oxidation reaction (MOR) under half cell conditions.
- vi. Evaluate stability of prepared catalysts and performance loss with potential cycling

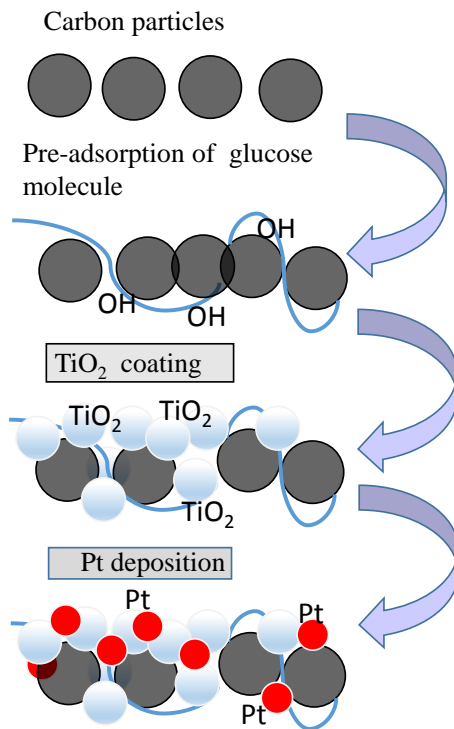


Figure 1.7: Glucose doped composite catalysts synthetic approach

1.9 Thesis organization

This is a manuscript based thesis which contains seven chapters (Introduction, Material and Methods, Composite Support Development, ORR Characterization, Methanol Oxidation Reaction and Conclusions). Overall two papers were published based on this research, and one is currently under revision.

Chapter 1 is an introduction to PEMFCs and the main technological challenges associated to this technology. This is followed by an overview of fuel cell catalyst materials, activity and stability, the use of metal oxide as possible carbon support replacement for Pt based

catalyst, and development of TiO₂/C composite supports. Finally, the research objectives and thesis structure are outlined.

Chapter 2 describes the experimental methods used for the synthesis and characterization of catalyst nanoparticles and substrate materials.

Chapter 3 is a report on the synthesis and characterization of TiO₂/C composite supports. The surface treatment approaches used to modify pristine carbon surface functional group for anchoring TiO₂ NPs. Furthermore, the physical properties of TiO₂/C prepared via glucose doping are compared to those prepared via an acid treatment approach to demonstrate the benefits of the former over the latter.

Chapter 4 is a summary of the studies carried out to evaluate the structural and electrochemical performance of two catalyst materials: Pt/TiO₂/G-ATV (glucose doped acid treated catalyst support) and a standard Pt/ATV catalyst.

Chapter 5 is a study of glucose doped TiO₂/C composites as a possible replacement for acid treatment. Chemical and physical characterization studies are introduced and used to explain the improved catalytic activity of Pt towards the ORR and durability of the composite based catalysts following rigorous potential cycling up to 4000 cycles.

Chapter 6 is oriented to describe the performance of glucose doped composite catalysts material for methanol oxidation reaction in comparison to an in-house Pt/C catalyst. The effects of illumination, electrolyte concentration, and temperature were evaluated using a RDE system. In particular, this chapter aims to highlight the contributions of the individual catalyst component to the photocatalytic and electrocatalytic activity. A robust testing protocol for accelerated stress test for MOR with Pt surface area loss was reported to simulate real fuel cell durability data.

Chapter 7 summarizes the content of this thesis with overall conclusions, tying this work together. The prospect of future research work was briefly outlined.

Chapter 8 contains appendices for copyright licenses

1.10 References

- 1) Outlook, A. E. (2009). Energy information administration. *Department of Energy*, 92010(9).
- 2) Pike, R. and Earis, P. (2010). *Energy and Environmental Science* 3(2), 173.
- 3) Hegerl, G. C., Zwiers, F. W., Braconnot, P., Gillett, N. P., Luo, Y., Marengo Orsini, J. A., Nicholls, N., Penner, J. E., and Stott, P. A. (2007). *In climate change*, Cambridge University Press, Cambridge.
- 4) Ferguson, C. R. and Kirkpatrick, A. T. (2001). *Internal Combustion Engines*. John Wiley & Sons, New York, 2nd edition.
- 5) Jia, J., Seitz, L. C., Benck, J. D., Huo, Y., Chen, Y., Ng, J. W. D., and Jaramillo, T. F. (2016). *Nature Communications*, 7.
- 6) Larminie, J.; Dicks, A. (2003). *Fuel Cell Systems Explained*; John Willey & Sons Ltd.
- 7) James. B.D, and Kalinoski, J.A. (2008). *DOE Hydrogen Program Review*, "Mass Production Cost Estimation for Direct H₂ PEM Fuel Cell Systems for Automotive Applications"
- 8) Hydrogen, F. C. (2011). Infrastructure Technologies Program Multi-Year Research, Development and Demonstration Plan. *US Department of Energy*.
- 9) Papageorgopoulos, D., PEMFC R&D at the DOE Fuel Cell Technologies Program, D.o. Energy, Editor. 2011, United States Government: Arlington, VA.
- 10) Gasteiger, H. A., Panels, J. E., and Yan, S. G. (2004). *Journal of Power Sources*, 127(1), 162-171.
- 11) Marković, N. M., Grgur, B. N., and Ross, P. N. (1997). *The Journal of Physical Chemistry B*, 101(27), 5405-5413.
- 12) U.S. Department of Energy. *Fuel cell hand book*, 7th ed., West Virginia: Office of Fossil fuel, National Energy Technology Laboratory; October 2000.
- 13) Kirubakaran, A., Jain, S., and Nema, R. K. (2009). *Renewable and Sustainable Energy Reviews*, 13(9), 2430-2440.
- 14) Coors, W. G. (2003). *Journal of Power Sources*, 118(1), 150-156.
- 15) Solvay. Solvay has successfully commissioned the largest PEM fuel cell in the world at Solvin's Antwerp plant. 2012 7th April 2012]; Available from:

<http://www.reuters.com/article/2012/02/06/idUS88888+06-Feb-2012+HUG20120206>.

- 16) O'Hayre, R., Barnett, D.M., and Prinz F.B. (2005). *Journal of The Electrochemical Society*, 152(2): p. A439-A444.
- 17) Popov, B. N., Li, X., Liu, G., and Lee, J. W. (2011). *International journal of hydrogen energy*, 36(2), 1794-1802.
- 18) Nørskov, J. K.; Rossmeisl, J.; Logadottir, A.; Lindqvist, L.; Kitchin, J. R.; Bligaard, T.; and Jónsson, H., (2004). *The Journal of Physical Chemistry B*, 108 (46), 17886-17892.
- 19) F. Colmati, E. Antolini, E.R. Gonzalez; (2005). *Electrochim. Acta*. 50: p.5496
- 20) Takasu, Y., Fujiwara, T., Murakami, Y., Sasaki, K., Oguri, M., Asaki, T., and Sugimoto, W. (2000). *Journal of the Electrochemical Society*, 147(12), 4421-4427.
- 21) Sharma, S., and Pollet, B. G. (2012). *Journal of Power Sources*, 208, 96-119.
- 22) Watanabe, M., Uchida, M., and Motoo, S. (1987). *Journal of electroanalytical chemistry and interfacial electrochemistry*, 229(1-2), 395-406.
- 23) Pourbaix, M. (1966). *Atlas of electrochemical equilibria in aqueous solutions*, 1st English ed., Pergamon Press, Oxford, New York.
- 24) Uchimura, M., and Kocha, S. S. (2007). *ECS Transactions*, 11(1), 1215-1226.
- 25) Shao-Horn, Y., Sheng, W. C., Chen, S., Ferreira, P. J., Holby, E. F., and Morgan, D. (2007). *Topics in Catalysis*, 46(3-4), 285-305.
- 26) Chen, Z., Waje, M., Li, W., and Yan, Y. (2007). *Angewandte Chemie International Edition*, 46(22), 4060-4063.
- 27) Wilson, M. S., Garzon, F. H., Sickafus, K. E., & Gottesfeld, S. (1993). *Journal of The Electrochemical Society*, 140(10), 2872-2877.
- 28) Ferreira, P. J., Shao-Horn, Y., Morgan, D., Makharia, R., Kocha, S., and Gasteiger, H. A. (2005). *Journal of The Electrochemical Society*, 152(11), A2256-A2271.
- 29) Zhang, G., Sun, S., Cai, M., Zhang, Y., Li, R., & Sun, X. (2013). *Scientific reports*, 3.

- 30) Mathias, M. F., Makharia, R., Gasteiger, H. A., Conley, J. J., Fuller, T. J., Gittleman, C. J., and Van, S. G. (2005). *Electrochem. Soc. Interface*, 14(3), 24-35.
- 31) Kinoshita, K., Lundquist, J. T., and Stonehart, P. (1973). *Journal of Electroanalytical Chemistry and Interfacial Electrochemistry*, 48(2), 157-166.
- 32) Fuller, B. W., Gray, G. E., and Fuller, T. F. (2007). *Electrochemical and Solid-State Letters*, 10(5), B101-B104.
- 33) Inaba, M. (2009). *ECS Transactions*, 25(1), 573-581.
- 34) "Driving cycle." Available from: http://en.wikipedia.org/wiki/Driving_cycle.
- 35) Borup, R. V.H. "Durability Improvements through Degradation Mechanism Studies." Available from:
http://www.hydrogen.energy.gov/pdfs/review11/fc013_borup_2011_o.pdf
- 36) Borup, R., (2007). *Chemical Reviews*, 107(10): p. 3904-3951.
- 37) Mark Mathias, H.G., Rohit Makharia, T.F. Shyam Kocha, Tao Xie, and Jason Pisco, "Can available membranes and catalysts meet automotive polymer electrolyte fuel cell requirements?" Available
from: http://web.anl.gov/PCS/acsfuel/preprint%20archive/Files/49_2_Philadelphia_10-04_1010.pdf
- 38) Yoshizawa, K, Ikezoe, R.S., Aoyama, T, Arai, T and Iiyama, A. "FCV development at Nissan." Available from: http://isjaee.hydrogen.ru/pdf/pdf/09-10/Yoshizawa_41.pdf
- 39) Wu, J., Yuan, X. Z., Martin, J. J., Wang, H., Zhang, J., Shen, J., and Merida, W. (2008). *Journal of Power Sources*, 184(1), 104-119.
- 40) Yang, Z., Ball, S., Condit, D., and Gummalla, M. (2011). *Journal of The Electrochemical Society*, 158(11), B1439-B1445.
- 41) Arisetty, S., Wang, X., Ahluwalia, R. K., Mukundan, R., Borup, R., Davey, J., and Blanchet, S. (2012). *Journal of The Electrochemical Society*, 159(5), B455-B462.
- 42) Dhanushkodi, S. R., Kundu, S., Fowler, M. W., and Pritzker, M. D. (2014). *Journal of Power Sources*, 245, 1035-1045.

- 43) US DOE, DOE cell component accelerated stress test protocols for PEM fuel cells, http://www1.eere.energy.gov/hydrogenandfuelcells/fuelcells/pdfs/component_durability_profile.pdf (2007).
- 44) Mathias, M.; Makharia, R.; Gasteiger, H.; Conley, J.; Fuller, T.; Gittleman, C.; Kocha, S.; Miller, D.; Mittsteadt, C.; Xie, T.; Yan, S.; and Yu, P. (2005). *Interface* 14, 24-35.
- 45) Kangasniemi, K.; Condit, D.; and Jarvi, T. (2004). *Journal of the Electrochemical Society* 151, E125-E132.
- 46) Kinoshita, K. Carbon: Electrochemical and Physicochemical Properties; John Wiley and Sons, New York, pp 316-334, 1988.
- 47) Roen, L.; Paik, C.; and Jarvi, T. (2004). *Electrochemical and Solid-State Letters* 7, A19-A22.
- 48) Maas, S.; Finsterwalder, F.; Frank, G.; Hartmann, R.; and Merten, C. (2008). *Journal of Power Sources* 176, 444-451.
- 49) Garcia, B.; Fuentes, R.; and Weidner, A. (2007). *Journal of Electrochemical and Solid-State Letters* 10, B108-B110.
- 50) Zhang, S., Yuan, X. Z., Hin, J. N. C., Wang, H., Friedrich, K. A., and Schulze, M. (2009). *Journal of Power Sources*, 194(2), 588-600.
- 51) Wu, J., Yuan, X. Z., Martin, J. J., Wang, H., Zhang, J., Shen, J., and Merida, W. (2008). *Journal of Power Sources*, 184(1), 104-119.
- 52) Baumgartner, W. R., Wallnöfer, E., Schaffer, T., Hacker, V., Peinecke, V., and Prenninger, P. (2006). *ECS Transactions*, 3(1), 811-825.
- 53) Maas, S.; Finsterwalder, F.; Frank, G.; Hartmann, R.; and Merten, C. (2008). *Journal of Power Sources* 176, 444-451.
- 54) Yu, X., and Ye, S. (2007). *Journal of Power Sources*, 172(1), 145-154.
- 55) Coloma, F., Sepulvedaescribano, A., and Rodriguezreinoso, F. (1995). *Journal of Catalysis*, 154(2), 299-305.
- 56) Postole, G., Bennici, S., and Auroux, A. (2009). *Applied Catalysis B: Environmental*, 92(3), 307-317.
- 57) Li, W., Liang, C., Zhou, W., Qiu, J., Zhou, Z., Sun, G., and Xin, Q. (2003). *The Journal of Physical Chemistry B*, 107(26), 6292-6299.

- 58) Serp, P., Corrias, M., and Kalck, P. (2003). *Applied Catalysis A: General*, 253(2), 337-358.
- 59) Wang, C., Waje, M., Wang, X., Tang, J. M., Haddon, R. C., and Yan, Y. (2004). *Nano letters*, 4(2), 345-348.
- 60) Wang, S., Jiang, S. P., White, T. J., Guo, J., and Wang, X. (2009). *The Journal of Physical Chemistry C*, 113(43), 18935-18945.
- 61) Borup, R., Meyers, J., Pivovar, B., Kim, Y. S., Mukundan, R., Garland, N., and Zelenay, P. (2007). *Chemical reviews*, 107(10), 3904-3951.
- 62) Wang, X.; Li, W.; Chen, Z.; Waje, M.; and Yan, Y. (2006). *Journal of Power Sources*, 158 (1), 154-159.
- 63) Shao, Y.; Yin, G.; Gao, Y.; and Shi, P. (2006). *Journal of The Electrochemical Society*, 153 (6), A1093-A1097.
- 64) Kou, R.; Shao, Y.; Wang, D.; Engelhard, M. H.; Kwak, J. H.; Wang, J.; Viswanathan, V. V.; Wang, C.; Lin, Y.; Wang, Y.; Aksay, I. A.; and Liu, J., (2009). *Electrochemistry Communications*, 11 (5), 954-957.
- 65) Shao, Y.; Zhang, S.; Wang, C.; Nie, Z.; Liu, J.; Wang, Y.; and Lin, Y. (2010). *Journal of Power Sources*, 195 (15), 4600-4605.
- 66) Sharma, S.; Ganguly, A.; Papakonstantinou, P.; Miao, X.; Li, M.; Hutchison, J. L.; Delichatsios, M.; and Ukleja, S., (2010). *The Journal of Physical Chemistry C*, 114 (45), 19459-19466.
- 67) Qiu, J.-D.; Wang, G.-C.; Liang, R.-P.; Xia, X.-H.; and Yu, H.-W., (2011). *The Journal of Physical Chemistry C*, 115 (31), 15639-15645.
- 68) Li, Y.; Gao, W.; Ci, L.; Wang, C.; Ajayan, P. M., (2010). *Carbon*, 48 (4), 1124-1130.
- 69) Du, D., Liu, J., Zhang, X., Cui, X., and Lin, Y. (2011). *Journal of Materials Chemistry*, 21(22), 8032-8037.
- 70) Wu, S., Yin, Z., He, Q., Huang, X., Zhou, X., & Zhang, H. (2010). *The Journal of Physical Chemistry C*, 114(27), 11816-11821.
- 71) Maiyalagan, T., Dong, X., Chen, P., and Wang, X. (2012). *Journal of Materials Chemistry*, 22(12), 5286-5290.

- 72) Zhou, Y. G., Chen, J. J., Wang, F. B., Sheng, Z. H., and Xia, X. H. (2010). *Chemical Communications*, 46(32), 5951-5953.
- 73) Yu, X., and Ye, S. (2007). *Journal of Power Sources*, 172(1), 145-154.
- 74) Joo, S. H.; Choi, S. J.; Oh, I.; Kwak, J.; Liu, Z.; Terasaki, O.; and Ryoo, R., (2001). *Nature*, 412 (6843), 169-172.
- 75) Ding, J.; Chan, K.Y.; Ren, J.; and Xiao, F, (2005) *Electrochimica Acta* , 50 (15), 3131-3141.
- 76) Joo, S. H.; Pak, C.; You, D. J.; Lee, S.-A.; Lee, H. I.; Kim, J. M.; Chang, H.; and Seung, D., (2006). *Electrochimica Acta*, 52 (4), 1618-1626.
- 77) Su, F.; Zeng, J.; Bao, X.; Yu, Y.; Lee, J. Y.; and Zhao, X. S., (2005). *Chemistry of Materials* 17 (15), 3960-3967.
- 78) Choi, W. C.; Woo, S. I.; Jeon, M. K.; Sohn, J. M.; Kim, M. R. and Jeon, H. J., (2005). *Advanced Materials*, 17 (4), 446-451.
- 79) Song, S.; Liang, Y.; Li, Z.; Wang, Y.; Fu, R.; Wu, D.; and Tsiakaras, P(2010). *Applied Catalysis B: Environmental*, 98 (3–4), 132-137.
- 80) Shanahan, P. V.; Xu, L.; Liang, C.; Waje, M.; Dai, S.; and Yan, Y. S., (2008). *Journal of Power Sources*, 185 (1), 423-427.
- 81) Tang, J. M., Jensen, K., Waje, M., Li, W., Larsen, P., Pauley, K., and Haddon, R. C. (2007). *The Journal of Physical Chemistry C*, 111(48), 17901-17904.
- 82) Alcaide, F., Álvarez, G., Miguel, O., Lázaro, M. J., Moliner, R., López-Cudero, A., & Aldaz, A. (2009). *Electrochemistry Communications*, 11(5), 1081-1084.
- 83) Wang, L., Ge, L., Rufford, T., and Zhu, Z. (2015). *Functionalization and Applications of Boron Nitride and Other Nanomaterials* (pp. 409-440). CRC Press.
- 84) Oh, H. S., Kim, K., Ko, Y. J., and Kim, H. (2010). *International journal of hydrogen energy*, 35(2), 701-708.
- 85) Andersen, S. M., Borghei, M., Lund, P., Elina, Y. R., Pasanen, A., Kauppinen, E., and Skou, E. M. (2013). *Solid State Ionics*, 231, 94-101.
- 86) Ramesh, P., Itkis, M. E., Tang, J. M., and Haddon, R. C. (2008). *The Journal of Physical Chemistry C*, 112(24), 9089-9094.
- 87) Campbell, C. T. (2012). *Nature chemistry*, 4(8), 597-598.

- 88) Park, K. W., Choi, J. H., Kwon, B. K., Lee, S. A., Sung, Y. E., Ha, H. Y., and Wieckowski, A. (2002). *The Journal of Physical Chemistry B*, 106(8), 1869-1877.
- 89) Adjemian, K. T., Dominey, R., Krishnan, L., Ota, H., Majsztrik, P., Zhang, T. and Leahy, J. (2006). *Chemistry of Materials*, 18(9), 2238-2248.
- 90) Sasaki, K., Takasaki, F., Noda, Z., Hayashi, S., Shiratori, Y., and Ito, K. (2010). *ECS Transactions*, 33(1), 473-482.
- 91) Graves, J. E., Pletcher, D., Clarke, R. L., and Walsh, F. C. (1991). *Journal of applied electrochemistry*, 21(10), 848-857.
- 92) Bauer, A., Song, C., Ignaszak, A., Hui, R., Zhang, J., Chevallier, L and Rozière, J. (2010). *Electrochimica Acta*, 55(28), 8365-8370.
- 93) Murray, J. L., and Wriedt, H. A. (1987). *Journal of Phase Equilibria*, 8(2), 148-165.
- 94) Smith, J. R., Walsh, F. C., & Clarke, R. L. (1998). *Journal of applied electrochemistry*, 28(10), 1021-1033.
- 95) Glassford, K. M., and Chelikowsky, J. R. (1992). *Physical Review B*, 46(3), 1284.
- 96) Mo, S. D., & Ching, W. Y. (1995). *Physical Review B*, 51(19), 13023.
- 97) Ioroi, T., Siroma, Z., Fujiwara, N., Yamazaki, S. I., and Yasuda, K. (2005). *Electrochemistry Communications*, 7(2), 183-188.
- 98) Smith, J. R., Walsh, F. C., and Clarke, R. L. (1998). *Journal of applied electrochemistry*, 28(10), 1021-1033.
- 99) Roller, J. M., Arellano-Jiménez, M. J., Yu, H., Jain, R., Carter, C. B., and Maric, R. (2013). *Electrochimica Acta*, 107, 632-655.
- 100) Chen, G., Bare, S. R., and Mallouk, T. E. (2002). *Journal of the Electrochemical Society*, 149(8), A1092-A1099.
- 101) Schaffer, J. P., Saxena, A., Antolovich, S. D., Sanders, T. H., and Warner, S. B. (1995). *The science and design of engineering materials* (p. 577). Chicago: Irwin.
- 102) Linsebigler, A. L., Lu, G., and Yates Jr, J. T. (1995). *Chemical reviews*, 95(3), 735-758.
- 103) Schierbaum, K. D., Fischer, S., Torquemada, M. C., De Segovia, J. L., Roman, E., and Martin-Gago, J. A. (1996). *Surface science*, 345(3), 261-273.

- 104) Fujishima, A., and Honda, K. (1971). *Bulletin of the chemical society of Japan*, 44(4), 1148-1150.
- 105) Tauster, S. J., Fung, S. C., and Garten, R. L. (1978). *Journal of the American Chemical Society*, 100(1), 170-175.
- 106) Bonanni, S., Ait-Mansour, K., Harbich, W., and Brune, H. (2012). *Journal of the American Chemical Society*, 134(7), 3445-3450.
- 107) Baker, L. R.; Hervier, A.; Seo, H.; Kennedy, G.; Komvopoulos, K.; and Somorjai, G. A. (2011). *The Journal of Physical Chemistry C*, 115, 16006.
- 108) Boffa, A. B.; Bell, A. T.; and Somorjai, G. A. (1993). *Journal of Catalysis*, 139, 602.
- 109) Boffa, A.; Lin, C.; Bell, A. T.; and Somorjai, G. A. (1994). *Journal of Catalysis*, 149, 149.
- 110) Pietron, J. J.; Stroud, R. M.; and Rolison, D. R. (2002). *Nano Letters*, 2, 545.
- 111) Molina, L. M.; Rasmussen, M. D.; and Hammer, B. (2004). *Journal of Chemical Physics*, 120, 7673.
- 112) Akubuiro, E. C.; Verykios, X. E. (1998). *Journal of Catalysis*, 113, 106.
- 113) Liu, L.; Zhou, F.; Wang, L.; Qi, X.; Shi, F.; and Deng, Y. (2010). *Journal of Catalysis*, 274, 1-10
- 114) Robertson, J. (2010). *Physica status solidi (a)*, 207(2), 261-269.
- 115) Hepel, M., Dela, I., Hepel, T., Luo, J., and Zhong, C. J. (2007). *Electrochimica acta*, 52(18), 5529-5547.
- 116) Gustavsson, M., Ekström, H., Hanarp, P., Eurenus, L., Lindbergh, G., Olsson, E., and Kasemo, B. (2007). *Journal of Power Sources*, 163(2), 671-678.
- 117) Rajalakshmi, N., Lakshmi, N., and Dhathathreyan, K. S. (2008). *International journal of hydrogen energy*, 33(24), 7521-7526.
- 118) Huang, S. Y., Ganesan, P., and Popov, B. N. (2010). *Applied Catalysis B: Environmental*, 96(1), 224-231.
- 119) Ho, V. T. T., Pan, C. J., Rick, J., Su, W. N., and Hwang, B. J. (2011). *Journal of the American Chemical Society*, 133(30), 11716-11724.
- 120) Chen, G., Bare, S. R., and Mallouk, T. E. (2002). *Journal of the Electrochemical Society*, 149(8), A1092-A1099.
- 121) Leary, R., & Westwood, A. (2011). *Carbon*, 49(3), 741-772.
- 122) Foo, K. Y., and Hameed, B. H. (2010). *Advances in colloid and interface science*, 159(2), 130-143.

- 123) Matos, J., Chovelon, J. M., Cordero, T., and Ferronato, C. (2009). *Open Environ. Eng. J*, 2, 21-29.
- 124) Huang, Q., Tian, S., Zeng, D., Wang, X., Song, W., Li, Y., and Xie, C. (2013). *ACS Catalysis*, 3(7), 1477-1485.
- 125) Li, Y., Li, L., Li, C., Chen, W., and Zeng, M. (2012). *Applied Catalysis A: General*, 427, 1-7.
- 126) Tao, Y., Wu, C. Y., and Mazyck, D. W. (2006). *Industrial & engineering chemistry research*, 45(14), 5110-5116.
- 127) Zhang, J., Huang, Z. H., Yong, X. U., and Kang, F. Y. (2011). *New Carbon Materials*, 26(1), 63-70.
- 128) Liu, S. X., Chen, X. Y., and Chen, X. (2007). *Journal of hazardous materials*, 143(1), 257-263.
- 129) Haro, M., Velasco, L. F., and Ania, C. O. (2012). *Catalysis Science & Technology*, 2(11), 2264-2272.
- 130) Chhina, H., Campbell, S., and Kesler, O. (2009). *Journal of the Electrochemical Society*, 156(10), B1232-B1237.
- 131) Zhang, S. X., Kundaliya, D. C., Yu, W., Dhar, S., Young, S. Y., Salamanca-Riba, L. G., and Venkatesan, T. (2007). *Journal of Applied Physics*, 102(1), 013701.
- 132) Shim, J., Lee, C. R., Lee, H. K., Lee, J. S., & Cairns, E. J. (2001). *Journal of Power Sources*, 102(1), 172-177.
- 133) Von Kraemer, S., Wikander, K., Lindbergh, G., Lundblad, A., and Palmqvist, A. E. (2008). *Journal of Power Sources*, 180(1), 185-190.
- 134) Camacho, B. R., Morais, C., Valenzuela, M. A., & Alonso-Vante, N. (2013). *Catalysis today*, 202, 36-43.
- 135) Bauer, A., Song, C., Ignaszak, A., Hui, R., Zhang, J., Chevallier, L., and Rozière, J. (2010). *Electrochimica Acta*, 55(28), 8365-8370.
- 136) Jiang, Z. Z., Wang, Z. B., Chu, Y. Y., Gu, D. M., and Yin, G. P. (2011). *Energy & Environmental Science*, 4(3), 728-735.
- 137) Nemeth, Z., Reti, B., Pallai, Z., Berki, P., Major, J., Horvath, E., and Hernadi, K. (2014). *physica status solidi (b)*, 251(12), 2360-2365

CHAPTER TWO

(MATERIALS AND METHODS)

2.1 Chemicals and materials

Distilled water with 18 MΩ/cm resistivity was used to prepare all aqueous solutions. Sulfuric acid (H₂SO₄, 95-98%, Cl⁻ ≤ 2ppm, ACS reagent grade, Sigma-Aldrich) and perchloric acid (double distilled 70 wt. % HClO₄ with <0.1 ppm chloride, Sigma Aldrich) were used to prepare 0.5M H₂SO₄ and 0.1N HClO₄ which functioned as the supporting electrolytes for methanol ((99.6%, Sigma-Aldrich), ethanol (99.6%, Sigma-Aldrich). Isopropanol (97%, Sigma-Aldrich), glucose (99.5%, Sigma-Aldrich), and sodium borohydride (NaBH₄, 98%, Sigma-Aldrich) were used as received.

Commercial Vulcan XC-72R was obtained from Cabot Corporation. Nafion® 5% solution in a mixture of lower aliphatic alcohols and water was purchased from Ion Power. TiO₂/carbon composites were synthesized from titanium (IV) tetraisopropoxide (TTIP, 97%, Sigma-Aldrich) in isopropanol. Hydrated hexa-chloroplatinic acid (H₂PtCl₆·H₂O, ≥37.50% Pt basis, ACS reagent grade, Sigma-Aldrich) was used as platinum source and nanoparticle synthesis. Sodium borohydride (NaBH₄, 98%, Sigma-Aldrich) was used as reducing agent during nanoparticle synthesis. High-purity argon (99.999% AR 5.00-H-T) and nitrogen (99.999% NI5.00H-T) gases obtained from Praxair Canada Inc. bubbled through acid support electrolyte and alcohol solutions to remove dissolved O₂. Oxygen gas (99.99% OX4.0HC-T, Praxair Canada Inc.) was used to purge electrolyte solutions during oxygen reaction activity measurements. Platinum foils were used as substrates for composite materials in spectroscopy and microscopy studies. All chemicals were used as received unless otherwise specified.

2.2 Synthesis of catalyst materials: General procedure

The general procedures for catalyst development is described in this chapter while that more specific procedures are described in detail in the relevant chapters.

2.2.1. Carbon functionalization

Pristine Vulcan carbon (PV) was subjected to acid treatment to modify its surface properties using a procedure similar to that described by Ho et al. [1]. The as received carbon black was treated in 3 M HNO₃ solution to induce hydrophilic functional groups. Vulcan carbon was refluxed in 3 M HNO₃ solution at 120 °C for 3 hours. The mixture was

sonicated for 40 minutes prior to refluxing. The mixture was then allowed to stir for another 2 hours at room temperature with the suspension filtered through a sintered glass funnel. The functionalised material was washed copiously with distilled water until a neutral pH was achieved, after which the residue sample was dried in a vacuum oven at 80 °C for 5 hours. The product is hereafter referred to as acid treated Vulcan (ATV).

2.2.2 Glucose pre-adsorption on carbon substrate

For these syntheses, 500 mg of carbon (ATV or PV) was suspended in 60mL of a 15 wt% glucose in ethanol/water solution with 80 wt% ethanol. The resultant mixture was sonicated for 120 minutes at room temperature in an ultrasonic bath, after that the mixture was centrifuged at 1600 RPM for 20 minutes at room temperature. The carbon/glucose product precipitated out of the solution was washed with the same ethanol/water solution to remove any non-adsorbed glucose. The solids were dried in a vacuum oven at 60 °C overnight. The products are hereafter referred to as glucose doped acid treated Vulcan (G-ATV) and glucose doped pristine Vulcan carbon (G-PV).

2.2.3 TiO₂ Deposition: Synthesis of TiO₂/G-PV, TiO₂/G-ATV and /TiO₂/ATV composite supports

For these synthesis, approximately 500 mg of ATV, G-ATV or G-PV carbon were suspended in 50 mL of isopropanol and sonicated for 2 hours. After this period, 4-10 mL of a 0.2 M TTIP isopropanol solution was slowly added to these carbon supports under vigorous stirring. The mixture was refluxed in a three-neck round bottom flask (~ 82 to 85 °C) under nitrogen for 3 hours while being stirred before the drop-wise addition of 200 µL water/isopropanol solution, refluxing was continued for an additional 5 hours. The solution was maintained under reflux and uniform stirring for four days until a viscous gel was obtained. The resultant gel was filtered and washed with deionized water to eliminate the isopropanol.

The solid products were dried in a vacuum oven at 80 °C for 4 hours. The amount of TiO₂ precursor, TTIP diluted in isopropanol was altered to produce different weight percent ranges of TiO₂ on the modified carbon supports. The characterization tests show the obtained composite materials are highly amorphous thus, the samples were annealed at

500 °C for 2 hours to induce formation of crystalline TiO₂ anatase and induced the pyrolysis of glucose molecules in an inert environment [2]. An alternate post annealing treatment was done at 850 °C for 4 hours to produce rutile form of TiO₂. TiO₂ on G-PV, ATV and G-ATV are here after referenced as TiO₂/G-PV, TiO₂/ATV, and TiO₂/G-PV composite supports respectively. Dried samples were finely ground using a mortar and pestle, and placed in a glass vial for storage.

2.2.4 Pt deposition on TiO₂/C substrates

After heat treatment, Pt was deposited using a chemical impregnation method similar to that described in other studies [3]. Briefly, Pt nanoparticles were deposited on heat pre-treated (500 or 850 °C) TiO₂/ATV, TiO₂/G-PV or TiO₂/G-ATV substrates by reduction of H₂PtCl₆ with NaBH₄ [4], because it provides a straightforward, low-cost method for the reduction of the Pt precursor at room temperature in aqueous solution. Additionally, fast reduction kinetics offered by borohydride are expected to increase the nucleation rate and lower the average particle size of the product compared with some other reducing agents. The support was suspended in deionized water and subjected to sonication for 20 min before Pt precursor was added. The platinum precursor, chloroplatinic acid hexahydrate (H₂PtCl₆.6H₂O) was added to the suspension to give a 20 wt% Pt catalyst. After that, the mixture was stirred for an additional 3 hours. Subsequently, the temperature was lowered to 0°C and the reducing agent, NaBH₄, added to the mixture. After 6 hours, the solid product was filtered, washed with distilled water and dried in a vacuum oven at 80 °C overnight. For comparison, Pt nanoparticles were also deposited on ATV and G-PV as control materials in this thesis.

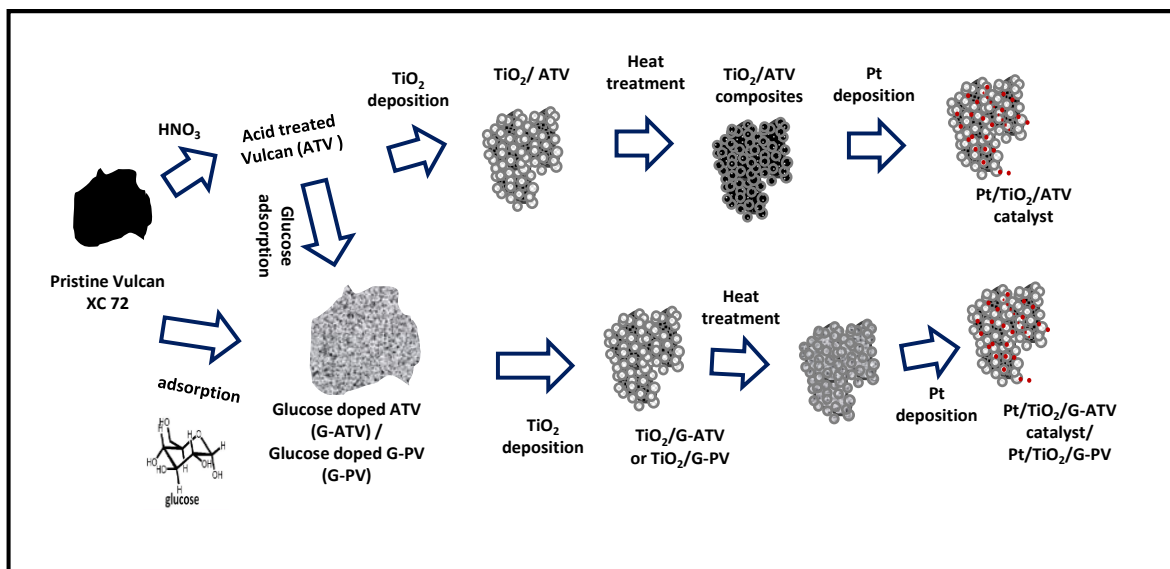


Figure 2.1: Synthesis of Pt based composite catalyst materials

2.3 Electrochemical measurements and sample preparations

2.3.1 Electrochemical cell cleaning

For the electrochemical studies, all glassware was thoroughly cleaned to remove any impurities that could contaminate the electrolyte and hinder catalyst activity. In this thesis, the cell was cleaned according to the following procedure: The cell was filled with concentrated H_2SO_4 and shake gently to ensure the interior surface is wet with the acid and soaked for approximately 6 hours. Following this treatment, the cell is rinsed with distilled water and subsequently with 0.5 M H_2SO_4 electrolyte solution. This is carried out periodically to ensure that the cell is contaminant free.

2.3.2 Glassy carbon electrode cleaning

The glassy carbon (GC) electrode was cleaned and polished according to the following procedure. A clean GC electrode will guarantee meaningful and reproducible substrate for the study of catalyst materials. Electrochemical reactions are highly surface sensitive and a careful electrode preparation is always required [5]. In this thesis, the GC electrode was treated with aqua regia (under ambient conditions to completely get rid of contaminants) followed by immersion in distilled water. The GC electrode was then polished with a series of abrasives of decreasing size alumina slurries which is a common

procedure used in the literature [6]. The polishing operations are detailed as (i) Polishing the GC with 0.05 μm Alumina slurry on micro cloth in a “figure eight” pattern for ten minutes, (ii) Thorough cleansing with distilled water to remove traces of alumina slurry and (iii) GC electrode kept in ultrasonic bath for some time in water to get a contaminant free surface.

2.3.3 Catalyst ink preparation and casting procedure

Catalysts were evaluated electrochemically as thin film catalyst layers immobilized on a GC electrode. For the preparation of the catalyst ink, 5-10 mg of catalyst was added to a solution containing 100 μL of 5% Nafion® solution, 200 μL of isopropyl alcohol, and 200 μL of water. Care should be taken that isopropanol should be added after distilled water to avoid potential ignition on catalyst surface and inadvertent annealing of the catalyst. The catalyst ink was sonicated in an ultrasonic bath for 30 min, and 5 μL of ink was deposited onto the surface of a glassy carbon electrode (0.196 cm^2) and dried for 5 minutes. The average catalyst loading was 0.05 mg/cm^2 with 30 wt% Nafion loading.

2.3.4 Half-cell electrochemical measurements

The electrochemical measurements were performed in electrolyte solution at room temperature using a three-electrode cell as shown in Fig. 2.2. In a three electrode setup the potential is applied between the GC working electrode and the reference electrode, while the current passes between the working and counter electrodes. The three electrodes were rinsed with distilled water before being inserted into the three electrode electrochemical cell. In this work, Ag/AgCl/0.1M KCl was used as a reference electrode and a Pt counter electrode. All the potentials in this and the following chapters have been converted to the normal hydrogen electrode (NHE) scale for comparison with other studies.

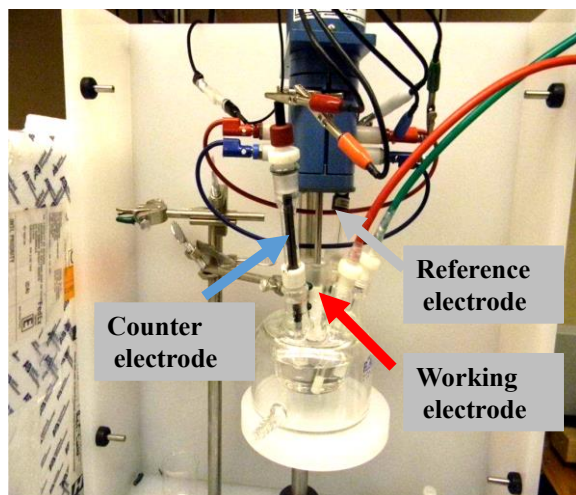


Figure 2.2: A three electrode electrochemical cell set up schematic

Electrochemical measurements were carried out in 0.5 M H_2SO_4 aqueous solutions as the supporting electrolyte. Cyclic voltammogram (CV) measurements for cleaning were performed in a potential range between 0.04 to 1.5 V at a scan rate of 100 mV/s for 20 cycles until a steady state CV was achieved. These measurements were performed at 25 °C using a Solartron 1470 potentiostat in combination with a Solartron 1260 impedance analyser controlled using Multistat 1.1d software (Scribner Associates Inc.) for electrochemical impedance spectroscopy (EIS) experiment.

The electrocatalyst degradation was investigated by repeated potential cycling from 0.04 to 1.5 V at a scan rate of 50 mV/s in a deaerated 0.5 M H_2SO_4 . A similar procedure has been used in other studies to evaluate the stability of home-made catalyst materials [10]. A continuous assessment of the catalysts performance with time was carried out using CV and EIS. The upper potential limit of 1.5V allowed to obtain degradation data in a relatively short period of time. All EIS measurements for platinised supports were made over a frequency range of 100 kHz to 0.1 Hz at a DC bias potential of 0.45 V vs. NHE. The uncompensated resistance was subtracted from all impedance spectra. EIS data was interpreted via the transmission line model for fuel cell catalyst layers [11].

The ORR activity was determined using a Gamry Reference 600 potentiostat and a Pine Instrument rotating disc electrode system. The electrolyte was purged with oxygen for 15 minutes and during all experiments the oxygen gas was used as a blanket to cover the

electrolyte. The potential was swept from 1.0 to 0.3 V at a scan rate of 5 mV/s at various rotation rates from 400 to 2500 rpm. Background currents will be obtained in nitrogen saturated electrolyte and removed in order to eliminate capacitive contributions. The current potential curve at 1600 rpm was then used to examine the Pt mass specific activity, and Pt area specific activity.

The studies on methanol oxidation were performed in N₂ saturated 0.5M H₂SO₄/0.5 M methanol solutions at room temperature otherwise stated. The potential was swept from 0 V to 1.1 V at 50mV/s. Carbon monoxide (CO) stripping experiments were performed in 0.5 M H₂SO₄ by saturating the electrolyte with CO and holding the working electrode at a potential of 0.2 V for 10 minutes at 25 °C (room temp). The cell was then purged with N₂ for 15 minutes while the electrode potential was maintained at 0.2 V. The potential was then scanned in the positive direction to 0.9 V at 50 mV/s.

2.4 Materials characterization techniques

Several physical characterization methods are employed in this thesis to fully evaluate and understand at the molecular level the specific structures, morphology, and size of synthesized catalyst materials. This involves imaging the material structure, identifying elemental and surface compositions. This subsection will provide experimental details with the basic theoretical principles regarding various physical techniques used in this thesis. Herein, a number of the experimental techniques used for this thesis work are described.

2.4.1 Scanning electron microscope (SEM)

SEM is a versatile characterization technique that is used to determine surface morphology and atomic composition of a wide range of materials for energy and non-energy related applications. SEM provides high-resolution image because of the small wavelength (de Broglie) of electrons. A typical SEM consists mainly of an electron gun, a spray aperture, different electromagnetic lenses, scanning coils, and electron detectors. In principle, one can get insight into the material by irradiating its surface in a coherent pattern with a focused beam of electrons. This electron beam will interact with the sample surface

and emit certain signals in the form of secondary electrons, backscattered electrons, characteristic X-rays and photons [12].

Images are formed by processing resultant signals from interactions occurring between the focused electron beam and the surface of the sample under investigation [12]. These images can range in size from several nanometers to the micrometer scale. The energy of secondary electrons is relatively low (0-30 eV) and together with inelastically scattered primary electrons, they are used to analyze the surface topography. On the other hand, the back scattered electrons are highly energetic and elastically scattered below the sample surface. These electrons are used to analyze the bulk properties and compositional aspects of the specimen.

The other signals that are emitted from the sample include x-ray signals, Auger electrons, which intensity strongly depend on incident energy and sample composition. SEM in comparison to other optical microscopy provides relatively large depth of analysis, producing an image that is a good representation of the sample.

In this work, SEM was utilized mainly for investigation of the distinct microstructure and morphology of the catalyst materials being developed. Samples for SEM analysis were prepared by dispersing very small samples in about 1 mL of methanol. The mixture was sonicated for about 15 min to obtain a homogeneous suspension. One drop of the suspension was poured onto carbon coated copper grid, allowed to dry and gold coated before being mounted for analysis.

2.4.2 Transmission electron microscope (TEM)

Transmission electron microscopes (TEMs) on the other hand, provide much better image resolution of nanomaterials with precision approaching the atomic scale compared to SEM device. The mode of operation involves irradiating a sample with an electron beam of constant current density that is produced using field emission or thermionic processes. This electron beam is further passed through several condensers to provide illumination of a very small area of interest [13]. The electrons will interact with the atoms of the sample being investigated by either inelastic or elastic scattering. The resulting signals are then collected and processed using dynamic theories of electron diffraction [13], resulting in an image that is magnified, focused and projected for easy viewing. TEM devices allow

imaging on the nanometer scale, and with high resolutions can be obtained, that facilitate imaging of the crystal defects, atomic rows and crystalline structures of sample materials.

Specimen samples for microscopy analysis were prepared by dispersing very small samples in about 1 mL of methanol. The mixture was sonicated for about 15 min to obtain a homogeneous suspension. One drop of the suspension was poured onto carbon coated copper grid and allowed to dry before being placed in the microscope. The TEM characterization was carried out using either a JEOL JEM-2010 200kV high-resolution TEM LaB6 filament or a Philips CM 10 instrument equipped with an AMT digital camera system. The image diameters of the particles (Pt) obtained from TEM analysis were measured using ImageJ.

2.4.3 Thermogravimetric analysis (TGA) and Differential scanning calorimetry (DSC)

Thermogravimetric analysis (TGA) is a well-known destructive analysis technique that evaluates weight change of a sample in response to a change in temperature. The Q600 TGA system used in this thesis consists of two arms with sample holder which continually measures the mass of the sample, and a combustion chamber, which heats/cool the sample to the desired temperature. TGA has often been employed in several scientific fields to determine the decomposition temperature of materials, thermal stability, adsorbed moisture content, relative organic composition, required reaction temperatures or reaction kinetics. A more thermal stable catalyst begins to decompose or combust at higher temperatures and may combust less rapidly depending on the catalyst structure. The catalyst sample being studied, are mainly composed of carbonaceous matter, with varying levels of graphitization, surface group functionalization, and metal content.

TGA and differential scanning calorimetry (DSC) was performed on samples to identify the elemental mass composition, decomposition temperatures and possibility of phase changes of the material. In this thesis, this was done with a TA Instruments Q600 SDT thermal analyzer in argon or under dry air. Mass and temperature calibrations were done periodically to ensure reproducibility of experimental results.

In a typical run, sample (ca. 10 mg) were heated from room temperature to 1000 °C at a rate of 20 °C/min under flowing air (50 mL/min), which enables the determination of

the weight percent of the individual components. Fig. 2.3 illustrates a simple TGA plot where the sample was heated to 800 °C in air. Both the weight versus temperature and mass normalised heat flow versus temperature curves are shown. The sample demonstrates some characteristic behaviours often seen for carbonaceous materials. From room temperature to 400 °C, there is only slight mass loss and is most likely due to water or surface group removal on the material. Starting at 400 °C, there is an increase in mass loss as the material starts to decompose and burn. This rapid weight loss continues to about 630 °C where the percentage mass versus temperature curve levels off. At this point, the organic carbon material is practically completely burned off and trace residuals of metals, ash and other inorganic materials remain in the sample holder.

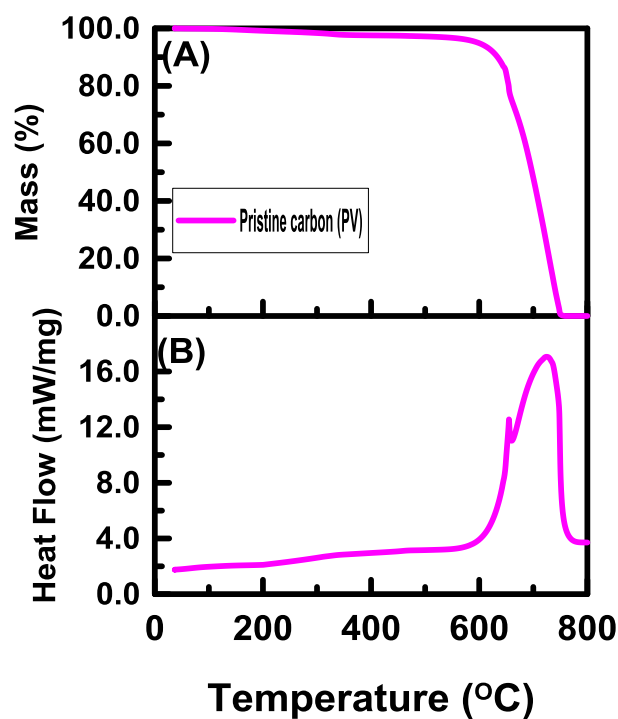


Figure 2.3: TGA and DSC curves of Vulcan carbon in air

2.4.4 Raman spectroscopy analysis

This is an analytical technique relying upon inelastic scattering of monochromatic light (a laser) with molecules as a result of molecular excitation such as vibration, rotation or electronic energy of a molecule. It is much like infrared (IR) spectroscopy. However, whereas IR bands arise from a change in the dipole moment of a molecule due to an interaction of light with the molecule. In a typical experiment, laser light strikes the molecule, which produces distortion in the electronic cloud thus polarising the molecule. The molecular distortion produces dipole moments and begin to oscillate periodically with a characteristic frequency. As the high energy vibrations relax, they emit a photon of lesser energy than the incident photon ($E_{emit} < E_{inc}$), in a process called Stokes scattering [39]. On the other hand, the scattered light may be of higher energy than the incident ($E_{emit} > E_{inc}$), which is called anti-Stokes scattering. In reality, a third mechanism, Raleigh scattering, where the emitted photons are of equal energy to the incident ($E_{emit} = E_{inc}$), is the most prevalent, thus the most intense because the instrument is designed to eliminate this region of Raman spectrum. This is important because it means that only polarizable molecules can be analyzed by Raman spectroscopy [14]. The emitted scattering light from the molecule can have different characteristic frequencies that can be measured and used to identify different species or functional groups in a sample.

In this thesis, a Raman system (Renishaw Raman Imaging Microscope system 2000 with an argon laser 514.5 nm excitation and a nominal power of 25 mW) was used to characterize the PV, ATV, G-ATV, and G-PV carbon samples before and after functionalization with TiO₂. Silicon glass was used for calibration with an intense {100} band, which was centered on the full width at half maximum at $\sim 520.7 \text{ cm}^{-1}$. The silicon slide requires no special preparation, as a visual inspection is sufficient for determining if any cleaning is needed. The peak intensity of this material is very sharp, pronounced and well-studied which allows for optimal use of a sample for calibration.

The Raman spectrometer used in this work has a camera included that allows images to be displayed on the computer monitor. The area of the sample that was located in the focal plane was the area that was subjected to Raman analysis. Using white light to illuminate the sample via an optical fiber, the objective lens was then used to focus on the sample's region of interest. Once the surface of the sample being analyzed is in the focal

plane, the laser beam (visible on the video monitor) will converge to its smallest possible size. The beam spot will be diverged when in both under-focused and over-focused conditions with respect to the surface of the sample being analyzed. At this point, the analysis parameters can be set and the sample is ready to be analyzed.

Raman spectra were collected in the range 4000-100 cm^{-1} . Repeated acquisitions (20 scans) with an acquisition time of 15 s at the highest magnification (50 \times) were accumulated to improve the signal-to-noise ratio. To ensure uniformity, the spectrum was collected in 3 or 4 different sample locations. The average size of carbon-based material can be determined in terms of changes in position, width and intensity ratio of two Raman peaks observed at 1345 cm^{-1} (the disordered, or D peak) and 1575 cm^{-1} (the graphite, or G peak). When the crystallites become larger, the peaks become narrower; their maxima move to higher frequencies and the intensity of the G peak systematically increases in comparison with the D peak [14].

2.4.5 X-ray diffraction (XRD)

X-ray diffraction (XRD) is a technique used to provide structural characterization of a sample material utilizing X-ray beams. XRD is used to identify crystalline materials with known diffraction patterns or to determine the structure of newly developed materials. XRD is based on the interaction of a monochromatic x-ray beam with a crystal lattice. Diffraction occurs when irradiation by electromagnetic waves interact with a regular array of scattering centers that have a spacing similar in size to the wavelength of the radiation [15]. Thus, X-rays with wavelengths similar to the spacing of atoms (the scattering centers) in a crystalline sample will provide diffraction patterns useful for interpretation of the specific atomic arrangement present in the sample. The crystal lattice being a periodic arrangement of atoms in 3-dimensions, can act as a grating element to scatter the x-rays. The scattered waves from the atomic lattice can interfere constructively under special conditions and give rise to sharp interference maxima with the same symmetry as in the distribution of atoms in a given material. The criteria for constructive interference to occur according to Bragg's law is given by,

$$n\lambda = 2d\sin\theta \quad (2.1)$$

where d , θ , n and λ are the distance between the lattice planes, diffracted angle, diffraction order, and the wavelength of the x-ray, respectively. In the present work, a Cu $K\alpha$ X-ray source was utilized with a wavelength of 1.54 Å.

The main purpose for collecting XRD patterns in our samples is to investigate the crystalline structure of carbon, Pt, and TiO₂ NPs. Also, since Pt nanoparticles are dispersed on composite support material in this work, the average diameter of these nanoparticles can be evaluated by using the Scherrer equation [16-17]

$$d = \frac{0.9\lambda K_{\alpha}}{B(2\theta)\cos\theta_{max}} \quad (2.2)$$

K_{α} is a dimensionless shape factor taken as 0.95 in this work, $B(2\theta)$ is the half width peak and θ_{max} is the maximum angle of the peak. For the materials synthesized and analysed in this study, average Pt NPs diameters were estimated using the Pt (220) peak located at ca. 67.75 ° to minimise interference between this peak and the characteristic peaks of the carbon support. XRD experiments were performed with a Rigaku Ultima IV X-ray diffractometer equipped with graphite monochromator, K-β filter and a Cu $K\alpha$ 0.154 nm X-ray source. Samples were scanned from 10 to 85 with a step size of 0.02° using a standard speed with an equivalent counting time of 14.7 seconds per step. The detector radiation was set at 40 kV and 44 mA.

2.4.6 X-ray photoelectron spectroscopy (XPS)

X-ray photoelectron spectroscopy (XPS) is a technique to analyze the chemical state and elemental composition of a material primarily at the top surface region between 0.5 to 5 nm [40] of a sample, with the possibility for higher probing depths. In XPS, an x-ray beam irradiates the material and emits the core-level electrons. The binding energy of the electrons can be determined by detecting the kinetic energy of the emitted electrons from the material. Each electron has its own set of electron binding energies. The measured kinetic energies, therefore, provide elemental identification. XPS sampling is commonly conducted under ultra-high vacuum conditions involving a source of radiation and an electron energy analyzer. The electron energy analyzer determines the kinetic energy of

the emitted electrons from the specimen. For XPS, the radiation source is from Al $K\alpha$ or Mg $K\alpha$ X-rays.

The basic principle of XPS is shown in Fig. 2.4. Ejected electrons that have escaped the surface with elastic collision give characteristic peaks as a function of electron intensity in a spectrum. Other electrons that undergo inelastic scattering suffer energy loss due to the inelastic collisions and contribute to the background on the low kinetic energy side of the spectrum. Standard binding energy values of most elements have been determined and can be used to identify the unknown elements present on the surface and their oxidation states. The loss of valence charge density or oxidation of an element causes an increase in the binding energy or loss in the kinetic energy of the core electrons. The difference in the binding energy then gives information on the chemical environment and the valence state of the atoms. For quantitative analysis, a curve-fitting process is usually used to determine different atomic percentages.

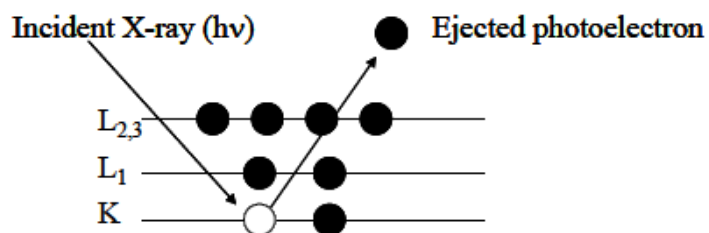


Figure 2.4: Photoionization of an atom by the ejection of a 1s electron by X-ray radiation [40].

XPS spectra are graphed as an intensity vs. binding energy (eV) plot. The unique benefit of XPS as an experimental technique arises from the ability to quantify surface atomic concentrations in addition to the determination of elemental oxidation state. XPS characterization was performed with a ThermoFisher Scientific K-Alpha (1486.65 eV) system. Charge compensation applied with combined e/Ar flood-gun. The energy range was shifted so that place main C1s peak appeared at 284.6 eV. Powdered samples were spread onto double-sided adhesive C tape, using enough powder to cover the tape completely. Data work-up was performed with software provided with the instrument (Advantage 5.926).

2.4.7 Brunauer Emmett Teller (BET) surface area analysis

BET is commonly used to measure the specific surface area of a material by adsorbing gas molecules on a solid surface. This method works by measuring the adsorption of nitrogen molecules onto a sample surface at set pressures. A sample of known weight is brought to a precise temperature and near-vacuum pressure. Then, gaseous N₂ is added to the sample cell in known amounts, and the pressure change is recorded. N₂ molecules physically adsorb to the surface and cover a known area ($\sim 16 \text{ \AA}^2$). An isotherm of the adsorption and then desorption of N₂ (as pressure is reduced to vacuum levels) is recorded at set points throughout the test. By measuring the amount of N₂ adsorbed and the pressure change, the total surface area of the sample can be determined. Knowing the weight of the sample to good precision allows for the calculation of the specific surface area of the sample in m²/g.

Two important assumptions are made when using this method: (i) only one N₂ molecule can occupy a surface site on the sample and (ii) there is no interaction between adjacent molecules of N₂. Unfortunately, these assumptions are not entirely true since multilayer adsorption can take place and nitrogen molecules in adjacent sites can interact. Despite the discrepancies between the model assumptions and the real physical phenomenon, gas sorption remains a highly reproducible method and an excellent tool for determining the material surface area and pore size.

Conducting a gas-sorption analysis involves several steps. The sample weight must be accurately known. To do this, the empty cell is first weighed, then measured again after the material is added. Following this, degassing is done to remove any residual contaminants, mainly water, from the sample surface so that it is dry and clean before analysis. Degassing is done at 200°C under vacuum. At the end of the experiment, the sample in the cell is weighed again after degassing to get the true sample weight. A controlled amount of inert gas such as nitrogen (N₂), argon (Ar), or krypton (Kr) is then introduced, which adsorbs on the surface of the material. The sample is placed under vacuum at a low temperature, usually the boiling point of liquid nitrogen (-195.6°C). The sample is then subjected to a wide range of pressures. A number of gas molecules adsorbed will vary as the pressure of the gas is varied. When the quantity of adsorbate on a surface

is measured over a wide range of relative pressures at constant temperature, the result is an adsorption isotherm. The resulting adsorption isotherm is analyzed according to the BET method. The BET equation can be written as:

$$\frac{P}{n(P_0 - P)} = \frac{1}{Cn_m} + \frac{c-1}{Cn_m} \frac{P}{P_0} \quad (2.3)$$

P, P_0, c, n, n_m are the adsorption pressure, the saturation pressure, a constant, the amount adsorbed (weight of adsorbate) at the relative pressure P/P_0 , and the monolayer capacity (weight of adsorbate constituting a monolayer of surface coverage), respectively [18]. Through the slope and intercept of a plot of $1/[n \left(\frac{P_0}{P-1} \right)]$ against (P_0/P) , n_m can be determined. The average area (a_m) occupied by a molecule of adsorbate in the monolayer for N_2 is 16.2 \AA^2 . The BET surface area can be calculated as:

$$A = a_m n_m N_A / M_{N_2} \quad (2.4)$$

where N_A is the Avogadro's number, and M_{N_2} is the molar mass of N_2 , 28 g mol^{-1} . The specific surface area is then calculated by dividing the area A by the sample weight. In this thesis, about 120 mg of powder samples were degassed in flowing N_2 at $300 \text{ }^\circ\text{C}$ for 4 h (unless otherwise stated) in the sample degas station. The degasser has two heating stations for degassing samples and two cooling stations. The pore size distribution with specific surface areas of the calcined supports were determined via N_2 adsorption/desorption according to the BET method using a Nova 1200e surface area analyzer. This analysis took about 6 h to complete a measurement.

The specific adsorption pore volumes (i.e. pore size distribution) were calculated by the Barrett-Joyner-Halenda (BJH) method [18]. This method relates the amount of adsorbate removed from the pores of the material, as the relative pressure (P/P_0) is decreased from a high to low value, to the size of the pores. The method is based on the Kelvin equation:

$$RT \ln \frac{P}{P_0} = -2\sigma V_m / r_k \quad (2.5)$$

In this equation, P is the pressure at which a cylindrical pore of Kelvin radius r_k is filled, σ is the surface tension, V_m is the molar volume, P_0 is the saturation pressure of the liquid adsorbate at temperature T . The r_k value was corrected with the thickness of the adsorbed multilayer, t to get the true pore radius r_p as follow:

$$r_p = r_k + t \quad (2.6)$$

The t values can be calculated from the Halsey equation:

$$t(\text{\AA}) = j \left[\frac{2.171}{\log\left(\frac{P}{P_0}\right)} \right]^{1/3} \quad (2.7)$$

j (3.54 Å) is the thickness of one molecular layer of nitrogen.

To avoid evaporation of N_2 and the consequent fall of N_2 levels in the containing Dewar an isothermal jacket was employed. This basically is a close-fitting, porous sleeve that surrounds the sample tube stem and maintains, by capillary action, a fixed level of N_2 around the tubes as long as its lower end dips into N_2 . The upper end of the jacket creates a sharp temperature demarcation line below which the temperature is that of liquefied N_2 . The stable temperature boundary environment can be maintained for as long as 20 hours.

2.5 Electrochemical characterization techniques

2.5.1 Cyclic voltammetry (CV) and electrochemical surface area (ECSA) determination

This is a useful technique which allows both qualitative and quantitative information about catalysts and their electrochemical reactions to be acquired. It is performed by cycling the potential between two points and recording the current in the potential cycling region. The observed current indicates the extent at which cathodic or anodic reactions are taking place. The voltage is first swept from low to high and then back to the initial voltage. The point at which the voltage stops increasing and begins decreasing has been termed the “switching” potential. The potential range chosen for CV procedures depends entirely upon the application. A typical CV for Pt supported on carbon black in a H_2SO_4 medium is shown in Fig.2.5. There are clearly five distinct potential regions, namely: (i) hydrogen adsorption region, (ii) hydrogen desorption region, (iii) double-layer region, (iv) Pt oxidation

region where Pt surface is oxidised to PtOH and then to PtOx and (v) PtO reduction to Pt

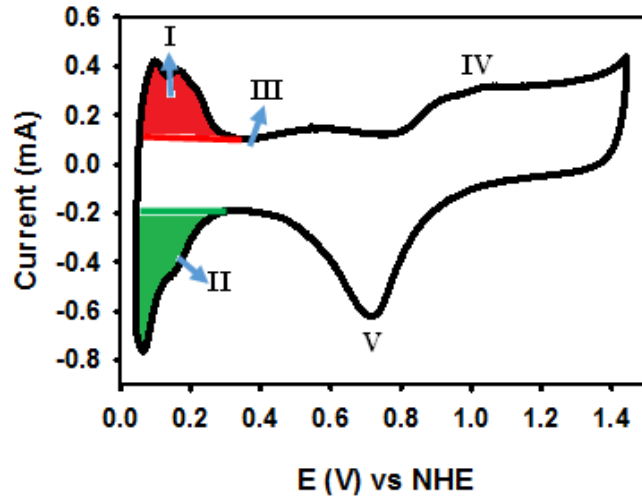


Figure 2.5: Half cell CV of Pt supported on carbon black in 0.5 M H₂SO₄ solution

In sulfuric acid solution, H⁺ is reversibly adsorbed to form a monolayer at potentials between 0.05 and 0.4 V via the reaction:



In this equation, underpotential deposited hydrogen (H_{upd}) refers to the adsorbed hydrogen atom on the catalyst surface. This process is reversible, with adsorption taking place on the cathodic sweep (negative-going), and desorption following when the sweep is reversed.

The electrochemical surface area (ECSA) provides a quantitative measure of the catalyst surface area that is available for electron transfer process. The ECSA is an important proper and need to be evaluated prior to every experiment in order to compare current densities measured for different catalysts and catalysts loadings. It is usually expressed in terms of surface area per unit mass of active catalyst material in the electrode (m²/g). The ECSA of the catalyst was evaluated by measuring the integrated area of the hydrogen adsorption peaks (green and red areas) on the CV in terms of the total charge passed during the H⁺ adsorption. This is the total charge (μC) in the labeled region (I) of Figure 2.4. The ECSA of a metal catalyst is calculated using the equation:

$$ECSA (m^2/g) = \frac{Charge (\mu C)}{Q_r * m(Pt)} \quad (2.9)$$

where Q_r is $210 \mu C/cm^2$ is a well-established value for the charge required to reduce a monolayer of protons on Pt, with the assumption that one metal atom adsorbs only one hydrogen atom [19], $m(Pt)$ is the metal loading of the working electrode in mg. Throughout most of this thesis, the charge under the H_2 desorption curves was used to determine the Pt surface area.

2.5.2 Stripping Voltammetry

ECSA can also be determined through CO-stripping. In this method, a monolayer of CO is adsorbed on the surface of Pt by purging the solution with CO gas at 0.15V vs NHE. The crystalline planes, temperature and deposition potential affect the CO adsorption. It is well known that CO molecule can be adsorbed on the surface of Pt on two different configurations. A linear adsorption configuration means one CO atom occupies one Pt atom and the charge density is $420 \mu C/cm^2$, because two electrons are involved in CO oxidation [20-21]. CV can also be used to assess the CO tolerance of a catalyst via CO-stripping. CO strongly adsorbs onto the surface of many metal catalysts, it blocks the reaction sites for electrochemical reaction, thus affecting the catalyst performance. The onset and peak potentials of the CO oxidation peak are a measure of the CO tolerance of a catalyst; low onset and peak potentials are desirable.

2.5.3 Rotating disc electrode (RDE) and oxygen reduction reaction

In RDE experiments, forced convection is used to control mass transport of electrochemical species in solution to the electrode surface by moving the electrode under well-controlled hydrodynamic conditions. The steady-state laminar flow conditions at the electrode surface can provide valuable information about the kinetics of electrochemical redox systems by changing the electrode potential. The electrode is generally a disc surrounded by a non-conducting sheath of PTFE (polytetrafluoroethylene) that is rotated around an axis perpendicular to the face of the disc and acts as a pump, pulling the solution vertically upwards towards the disc and then throwing it outwards. On the surface of the working electrode, there is a stagnant reaction layer covering the surface. The reactants transport through this layer by diffusion will reach the electrode surface where the

oxidation or reduction will take place. The rate of convective/diffusion to the disc is strongly dependent on the rotation rate of the disc (Fig. 2.6).

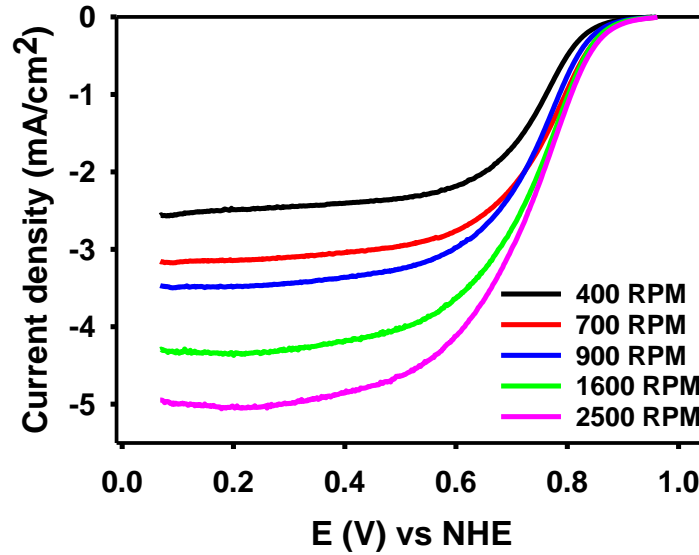


Figure 2.6: ORR polarization curves Pt supported on carbon black in oxygen saturated 0.5 M H₂SO₄ electrolyte solution.

The current density at a specific voltage and rotation speed can be expressed by the Koutecky-Levich (K-L) equation seen in Equation:

$$\frac{1}{i} = \frac{1}{i_d} + \frac{1}{i_k} \quad (2.10)$$

where i is the overall or total current density, i_d is the diffusion controlled current density assuming the effect of the Nafion coating is negligible and i_k is the reaction kinetics controlled current density. The limiting current is achieved when the overall process is controlled by the mass transport rate of reactant to the electrode surface ($1/i_k \rightarrow 0$ and $i = i_d$). Under these conditions, the steady-state diffusion-controlled current can be described by the Levich equation:

$$i_d = 0.62 n F A D^{2/3} C \nu^{-1/6} \omega^{1/2} \quad (2.11)$$

where n is the number of electrons transferred in the reaction, F is the Faraday constant, A is the electrode area (cm^2), D is the diffusion coefficient of reactant in the bulk solution (cm^2/s), ν is the kinematic viscosity (cm^2/s), ω is the angular rate of rotation of the electrode (rad/s), and C is the reactant concentration (mol/L) in the bulk solution. All of these, with the exception of ω are constant values for a given temperature, composition, and applied potential condition and can be combined into a single constant B .

Thus, equation 2.10 can be expressed as:

$$\frac{1}{i} = \frac{1}{i_k} + \frac{1}{(B\omega^{1/2})} \quad (2.12)$$

A plot of i^{-1} versus $\omega^{-1/2}$ is then referred to as a K-L plot and should display linear behavior (assuming a first order reaction with respect to oxygen) with y-intercept of i_k^{-1} and a slope of B^{-1} . This can be applied to determine the kinetically limited current density of catalyst materials at various potentials (eliminating the effects of diffusion) and the number of electrons transferred which will provide indication of the catalyst selectivity towards the more efficient 4 electron reduction process [22]. The rotation rate used in this thesis work varied from 400- 2500 rotation rate per minute (RPM). RDE measurements were done mostly at room temperature; higher temperature studies were limited to 55 °C since manufacturer instructions do not recommend using Teflon as electrode sheath above this limit to avoid gaps between the disk and the Teflon support. The material to be studied were deposited on a GC RDE as thin film, and tests such as cyclic voltammetry and oxidation cycles were applied.

2.5.4 Methanol oxidation reaction (MOR)

CV was also used to evaluate the activity of the catalyst materials for methanol oxidation (Fig.2.7). Like CO tolerance, the method for comparing the catalytic activity of methanol oxidation involves looking at two important features on the voltammetry: the onset and peak potentials of methanol oxidation on the anodic scan. The onset and peak potentials indicate the methanol oxidation overpotential.

From the CV for methanol, it can be seen that there is one peak in the forward (anodic) direction and one peak in the reverse (cathodic) direction. The peak in the forward direction (0.4 V to 0.9 V vs NHE) corresponds to the oxidation of methanol. In principle, the onset potentials vary with the nature of working electrode material and lower onset potentials generally indicate catalytic enhancement. Oxidation processes during CV are diffusion limited; therefore, species at the surface of the static electrode begin to deplete rapidly during potential sweeps but, the slow diffusion of methanol from bulk solution causes the peak to round off near 0.75 V. The current proceeds to drop as the species at the surface of the electrode depletes. The highest point in the forward scan of CV is termed the peak anodic current.

When comparing CVs from different electrodes, the i_{pa} is the single most important feature. At any constant scan rate (50 mV/s) the i_{pa} is expected to be directly proportional to the catalytic ability of the electrode surface [23-27]. When surface area effects are normalized, the current density (j) can be determined and higher peak current density (j_{pa}) is indicative of faster oxidation kinetics. It is; therefore, correct to say that an electrode which produces a higher j_{pa} has greater catalytic ability for the electrooxidation of methanol [28-29]. In the reverse scan there is also a peak between 0.6 V to 0.3 V. It is generally agreed that this peak, (I_R) is associated with the removal of incompletely oxidized carbonaceous species (mostly CO) formed during the forward scan [30]. Studies have shown that comparing the ratio of I_F to I_R can provide information about the tolerance of composite electrodes to carbonaceous poisons [30-33].

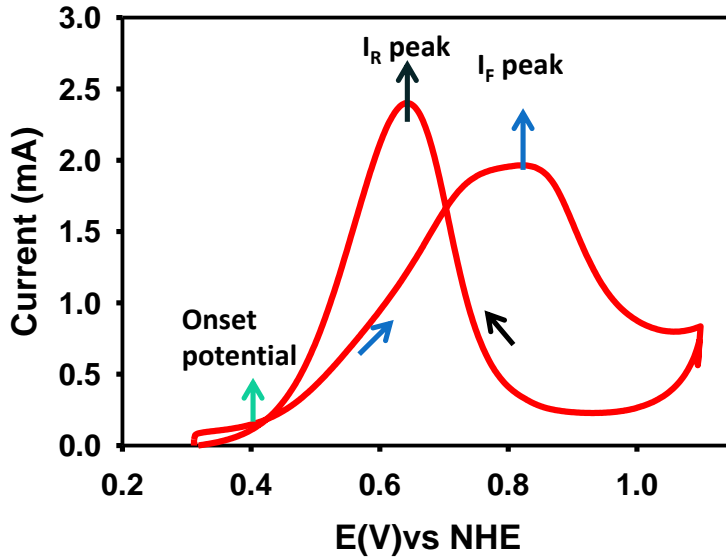


Figure 2.7: CV of methanol oxidation reaction in 0.5 M CH₃OH + 0.5 M H₂SO₄ solution

2.5.5 Electrochemical impedance spectroscopy

Conventionally, the performance of the catalyst is evaluated in an operating fuel cell mode using the DC methods [34–36]. The information gathered from a DC analysis usually provides the sum of various polarizations of the electrode, which is difficult to separate into individual contributions [37]. Electrochemical impedance spectroscopy (EIS), an AC method, can be used to investigate electrode-electrolyte interface and allows the simultaneous resolution of various charge-transfer and mass-transfer processes (kinetic, ohmic, and diffusion).

EIS measures the conductive and dielectric properties of electroactive systems over a wide range of frequencies. This may be due to changes in the physical structure, as well as chemical processes taking place within the catalyst material, or to a combination of both [38]. The EIS experiment involves applying a small sinusoidal voltage or current perturbation around a steady-state value and measuring the resulting current or voltage of the same frequency but shifted in phase. The impedance of a pure resistor, inductor and capacitor is given in equations (2.13 to 2.15) and are used to construct impedance response of a circuits in addition to other distributed circuit element.

$$Z_{resistor} = R \quad (2.13)$$

$$Z_{inductor} = j\omega L \quad (2.14)$$

$$Z_{Cap} = -\frac{j}{\omega C} \quad (2.15)$$

where j is $\sqrt{-1}$ and C is the capacitance in Farads (F)

The resistance to the flow of electrons in AC can be described through the following ohmic like relationship:

$$E = I Z \quad (2.16)$$

Where Z is the impedance of electrons caused by the presence of a capacitor or inductor and E is the resulting AC voltage. The amplitude and frequency signal of E is represented by:

$$E = E_{max} \sin(\omega t) \quad (2.17)$$

where E_{max} is the peak amplitude in volts (V), ω is the angular frequency ($\omega = 2 \pi f$ where f is in Hertz (Hz)), and t is time in seconds (s).

In addition, current response from the applied voltage at the same frequency will vary in phase, and thus separated by a phase angle, ϕ , which can be expressed by

$$I = I_{max} \sin(\omega t + \phi) \quad (2.18)$$

Where I_{max} is the peak current response and ϕ is the negative phase angle separating the current and potential waves. With resistor and capacitor in parallel to each other, the total impedance contribution can be represented by:

$$Z_{tot} = Z_{res} + Z_{cap} \quad (2.19)$$

$$Z = R + j \frac{I}{\omega C} \quad (2.20)$$

$$Z = Z' + j Z'' \quad (2.21)$$

Where Z' is the impedance from the resistive contribution, or real impedance, and Z'' is the capacitive contribution or the imaginary impedance.

The two primary regions of resistance in most fuel cells are at the electrode-electrolyte interfaces and in the electrolyte or compartment-separating material [38]. In addition, accumulation of counter-ions near the electrodes gives rise to an electrochemical capacitance at the solid-liquid interface. The imaginary impedance corresponds to capacitance arising from an electric double layer at the electrode-electrolyte interface and is assumed to be uniformly distributed throughout an entire electrode. The real impedance also consists of several components: the resistance of the connecting wires and contact with the fuel cell electrodes, resistance in the catalyst layers and the ionic resistance of the membrane. Thus, catalyst layer resistance is a combination of both the electronic and ionic resistance.

Measurements can be conducted over a wide range of frequencies, resulting in the construction of an impedance spectrum. Using this data, the real and imaginary impedances are calculated and plotted against each other for different perturbation frequencies in what are called Nyquist impedance spectra. Although other types of plots such as the Bode plots, where the magnitude of the impedance and the phase angle are plotted against frequency. The Nyquist plots are the most common way of analyzing impedance data [11].

With Nyquist, another commonly distributed element circuit can be observed- Warburg element, which represents diffusion processes to the electrode surface in the absence of migration. This is commonly extracted within the high frequency region with a 45° slope is formed. The projection of Warburg slope with the X-axis gives the total resistance associated with the entire electrode ($R_{\Sigma}/3$) [11], mainly the predominant contributions of the support electronic and membrane ionic resistances.

The various transport processes taking place in the actual fuel cell depend on the steady-state value of the overpotential at which the EIS experiment is conducted [39]. At low overpotentials when the mass transport resistance is not significant, the main contributor to the impedance is the charge transport in the catalyst layer. At moderate overpotentials proton, gas, and water transport begin to contribute to the total impedance

of the cell. At high overpotentials gas diffusion in the gas diffusion layer (GDL) and the catalyst layer become dominant, especially when air is used as the oxidant. In the various layers of the fuel cell, one or more of the transport processes described above are important depending on cell design and operating conditions [39].

These transport processes can be modelled using circuit elements and the interpretation of the EIS spectra is often difficult. For instance, simple fitting models based on these equivalent circuit analogues and physical models are used to extract the parameters that represent the underlying cell processes [39–40]. This involves reducing the transport processes into electrical analogues made of networks of resistors and capacitors, and sometimes, inductors. This approach provides a quick visualization tool to understand system behavior and limitations. Resistors and capacitors describe the behaviour of electrochemical reaction kinetics, ohmic conduction processes and even mass transport. The impedance behaviour of the electrochemical reaction interface can be modelled as a parallel combination of a resistor (R_t) and C_{dl} , the double-layer capacitance due to the separation of charge occurring across the reaction interface (Fig. 2.8)

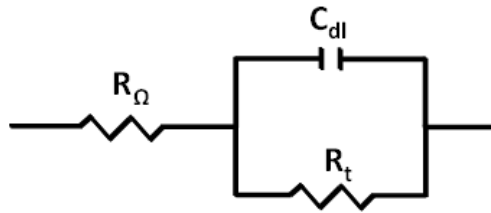


Figure 2.8: Diagram of simple circuit to model electrode/electrolyte interface.

A more complex circuit, the transmission line can be used to model porous fuel cell electrode system (Fig. 2.9) and describe the behavior of this fuel cell electrode material [41-42]. In this model two parallel resistive rails are present, $R_{\text{electronic}}$ and R_{ionic} . $R_{\text{electronic}}$ is used to describe the resistance associated with the transport of electrons through the carbon support, while R_{ionic} describes the resistance associated with the transport of ions through the ionomer membrane. Here, the capacitors represent the catalyst sites, and carbon surface exposed to the electrolyte connecting each rail [42]. In this case, ionic resistance refers to the ease of protons flow from Pt sites in the catalyst layer to the membrane. The electronic resistance is mostly due to the catalyst support component and is generally less compared to the ionic resistance [11].

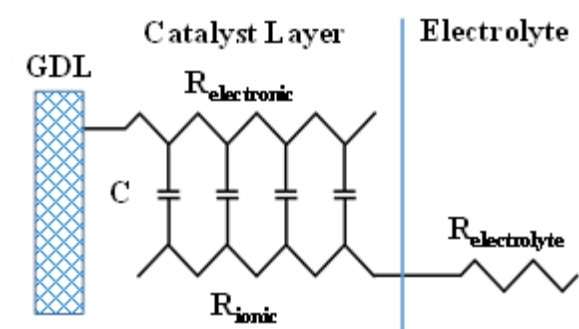


Figure 2.9: A sample transmission line model for fitting impedance data ¹¹

In this thesis, EIS measurements were conducted using a Solartron 1260 frequency response analyzer controlled using Multistat software (Scribner Associates). The primary goal of obtaining impedance measurements was to evaluate the conductivity and resistance of electrode materials in half-cell operating conditions. These measurements were collected over a frequency range of 100 kHz to 0.1 Hz at two different DC bias potential of 0.425 V vs. NHE) respectively.

EIS was also used to investigate the kinetics of methanol electrooxidation at a given potential. We have chosen a specific potential where CO removal is limiting [43]. The qualitative features of the EIS spectra were analyzed using the equivalent circuits of Fig 2.10. The element values for these circuits were converted to parameters relevant in the kinetic theory for mechanisms with a single adsorbed species [44]: When a faradaic process occurs at the electrode, there is the generation of a faradaic impedance that is in parallel with the double layer and if the reaction is irreversible, then the faradaic impedance can be considered as a pure resistance and is called the charge transfer resistance and is reflected in this equivalent circuit used to fit the EIS data. R_s represents the uncompensated solution resistance, R_2 defines a high-frequency relaxation with a resistance which must be accounted for at this potential and Inductance (L_1) is related to methanol dehydrogenation and the intermediates adsorption reactions [45]. In this case, the parallel combination of

the charge transfer resistance (R_{ct}) and the constant phase element (CPE) take into account the methanol adsorption and oxidation. This parallel combination leads to a depressed semi-circle in the corresponding Nyquist impedance plot.

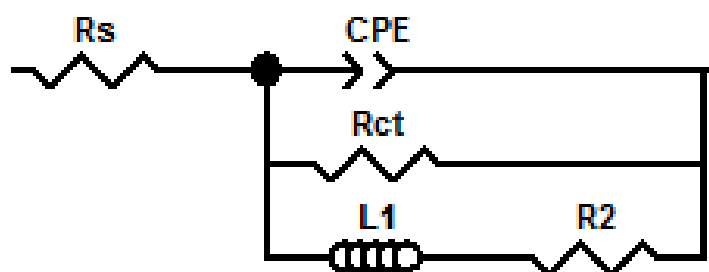


Figure 2.10: Equivalent circuit used in modeling methanol oxidation reaction ⁴⁵.

2.6 References

- 1) Ho, V. T. T., Pan, C. J., Rick, J., Su, W. N., and Hwang, B. J. (2011). *Journal of the American Chemical Society*, 133(30), 11716-11724.
- 2) Hyam, R. S., Lee, J., Cho, E., Khim, J., and Lee, H. (2012). *Journal of nanoscience and nanotechnology*, 12(12), 8908-8912.
- 3) Elezović, N. R., Babić, B. M., Gajić-Krstajić, L., Radmilović, V., Krstajić, N. V., and Vračar, L. J. (2010). *Journal of Power Sources*, 195(13), 3961-3968.
- 4) Mayer, A. B., Mark, J. E., and Hausner, S. H. (1998). *Die Angewandte Makromolekulare Chemie*, 259(1), 45-53.
- 5) Mayrhofer, K. J., Hanzlik, M., and Arenz, M. (2009). *Electrochimica Acta*, 54(22), 5018-5022.
- 6) Kissinger, P., and Heineman, W. R. (1996). *Laboratory Techniques in Electroanalytical Chemistry*, revised and expanded. CRC press.
- 7) Bagotsky, V. S. (Ed.). (2005). *Fundamentals of electrochemistry* (Vol. 44). John Wiley & Sons.
- 8) Mabbott, G. A. (1983). *Journal of Chemical Education*, 60(9), 697-702
- 9) Somorjai, G. A., & Li, Y. (2010). John Wiley & Sons.

- 10) Saleh, F. S., & Easton, E. B. (2012). *Journal of The Electrochemical Society*, 159(5), B546-B553.
- 11) Easton, E. B., & Pickup, P. G. (2005). *Electrochimica Acta*, 50(12), 2469-2474.
- 12) Goldstein, J. I., Newbury, D. E., Echlin, P., Joy, D. C., Lyman, C. E., Lifshin, E., and Michael, J. R. (2003). Special topics in electron beam x-ray microanalysis. In *Scanning Electron Microscopy and X-ray Microanalysis* (pp. 453-536). Springer US.
- 13) Kohl, H., and Reimer, L. (2008). *Transmission Electron Microscopy: Physics of Image Formation*. Springer-Verlag New York.
- 14) Leng, Y. (2009). *Materials characterization: introduction to microscopic and spectroscopic methods*. John Wiley & Sons.
- 15) Askeland, D. R., and Wright, W. J. (2015). *Science and Engineering of Materials*. Nelson Education.
- 16) Li, W., Liang, C., Zhou, W., Qiu, J., Zhou, Z., Sun, G., and Xin, Q. (2003). *The Journal of Physical Chemistry B*, 107(26), 6292-6299.
- 17) Radmilovic, V., Gasteiger, H. A., and Ross, P. N. (1995). *Journal of Catalysis*, 154(1), 98-106.
- 18) http://www.beckmancoulter.com/coultercounter/homepage_tech_bet.jsp. 2008.
- 19) Clavilier, J., Armand, D., and Wu, B. L. (1982). *Journal of Electroanalytical Chemistry and Interfacial Electrochemistry*, 135(1), 159-166.
- 20) Rush, B. M., Reimer, J. A., and Cairns, E. J. (2001). *Journal of The Electrochemical Society*, 148(2), A137-A148.
- 21) Rodes, A., Gómez, R., Feliu, J. M., and Weaver, M. J. (2000). *Langmuir*, 16(2), 811-816.
- 22) Dundar, F., Smirnova, A., Dong, X., Ata, A., and Sammes, N. (2006). *Journal of fuel cell science and technology*, 3(4), 428-433.
- 23) Shao, Z. G., Zhu, F., Lin, W. F., Christensen, P. A., Zhang, H., and Yi, B. (2006). *Journal of the Electrochemical Society*, 153(8), A1575-A1583.
- 24) Du, W., Xie, X., Xu, D., & Huang, C. (2008). *Energy and Fuels*, 22(5), 3346-3350.

- 25) Li, W., Wang, X., Chen, Z., Waje, M., and Yan, Y. (2006). *The Journal of Physical Chemistry B*, 110(31), 15353-15358.
- 26) Wang, Z. B., Zuo, P. J., Liu, B. S., Yin, G. P., and Shi, P. F. (2009). *Electrochemical and Solid-State Letters*, 12(1), A13-A15.
- 27) Wang, J., Xi, J., Bai, Y., Shen, Y., Sun, J., Chen, L and Qiu, X. (2007). *Journal of Power Sources*, 164(2), 555-560.
- 28) Shivhare, M. R., Allen, R. G., Scott, K., Morris, A. J., and Martin, E. B. (2006). *Journal of Electroanalytical Chemistry*, 595(2), 145-151.
- 29) Bergamaski, K., Pinheiro, A. L., Teixeira-Neto, E., and Nart, F. C. (2006). *The Journal of Physical Chemistry B*, 110(39), 19271-19279.
- 30) Gu, Y. J., and Wong, W. T. (2006). *Langmuir*, 22(26), 11447-11452.
- 31) Sun, Z., Wang, X., Liu, Z., Zhang, H., Yu, P., and Mao, L. (2010). *Langmuir*, 26(14), 12383-12389.
- 32) Albiter, M. A., Crooks, R. M., and Zaera, F. (2009). *The Journal of Physical Chemistry Letters*, 1(1), 38-40.
- 33) Lee, S. W., Chen, S., Sheng, W., Yabuuchi, N., Kim, Y. T., Mitani, T., and Shao-Horn, Y. (2009). *Journal of the american chemical society*, 131(43), 15669-15677.
- 34) Springer, T. E., Zawodzinski, T. A., and Gottesfeld, S. (1991). Polymer electrolyte fuel cell model. *Journal of the Electrochemical Society*, 138(8), 2334-2342.
- 35) Springer, T. E., Wilson, M. S., and Gottesfeld, S. (1993). *Journal of the Electrochemical Society*, 140(12), 3513-3526.
- 36) Zawodzinski, T. A., Springer, T. E., Uribe, F., and Gottesfeld, S. (1993). *Solid state ionics*, 60(1-3), 199-211.
- 37) Piela, P., Fields, R., and Zelenay, P. (2006). *Journal of the Electrochemical Society*, 153(10), A1902-A1913.
- 38) Bard, A., Faulkner, L. (2001) *Electrochemical Methods: Fundamentals and applications*, 2nd ed. John Wiley and Sons, New York.
- 39) Kulikovsky, A. A., and Eikerling, M. (2013). *Journal of Electroanalytical Chemistry*, 691, 13-17.

- 40) Springer, T. E., Zawodzinski, T. A., Wilson, M. S., and Gottesfeld, S. (1996). *Journal of the Electrochemical Society*, 143(2), 587-599.
- 41) Yuan, X.-Z. S., C.; Wang, H.; and Zhang, J., *Electrochemical Impedance Spectroscopy in PEM Fuel Cells: Fundamentals and Applications*. Springer-Verlag London: 2010; p 420.
- 42) Lefebvre, M. C.; Martin, R. B.; and Pickup, P. G., (1999). *Electrochem. Solid-State Letter*, 2 (6), 259-261.
- 43) Wu, G., Li, L., and Xu, B. Q. (2004). *Electrochimica Acta*, 50(1), 1-10.
- 44) Li, G., Yao, S., Zhu, J., Liu, C., & Xing, W. (2015). *Journal of Power Sources*, 278, 9-17.
- 45) Seland, F., Tunold, R., & Harrington, D. A. (2006). *Electrochimica Acta*, 51(18), 3827-3840.

CHAPTER THREE

Physicochemical characterization of modified carbon and TiO₂/C composite
catalyst supports for fuel cell application

3.1 Introduction

The use of high surface area nanosized TiO_2 holds promise in catalysis both as active phase and support. The preparation conditions under which the TiO_2 powders are synthesized lead to significant variation in their morphology, particle size, specific surface area, crystallinity, pore structure, and as well as photoactivity [1-4]. In the case of metal oxides, it is important to simultaneously maximize the surface area and improve the inherent poor electrical conductivity [5]. These goals have been partially achieved by the application of new synthetic procedures that can produce TiO_2 materials with high surface area [6] and by combining with carbon materials to improve the electrical conductivity [7-8]. This is due to the unique, controllable structural and electrical properties of the carbon base material that provide adequate support for the growth of metal oxide nanoparticles (i.e. TiO_2) via non-covalent attachment to the carbon core [9]. As a result, there are numerous reports on the dispersion of carbon materials in TiO_2 sols [10] and immobilization of TiO_2 on carbon for catalytic application [11-12].

A common route for the creation of these nanocomposites involves simple mixing in solution with a low level of interaction between the generated TiO_2 nanoparticles and the carbonaceous nanomaterials [13]. Other methods have also been developed to prepare TiO_2/C composites in which the shell thickness is controlled through the concentration of the coating materials [14-15]. The sol-gel method, in particular, has been shown to facilitate chemical interaction between carbon and TiO_2 [16]. The method also allows controlling the texture, the chemical, and the morphological properties of the solid. Moreover, this technique provides molecular scale mixing, high purity of the precursors, and homogeneity of the sol-gel products [17]. The precipitation of TiO_2 precursors onto the core carbon particles where subsequent hydrolysis and condensation processes take place results in the formation of thin films of TiO_2 nanoparticles on the surface of the carbon substrate. However TiO_2 coatings are exceptionally difficult to synthesize on pristine carbon material without segregation by this general method because the titanium precursor is highly

reactive and undergo hydrolysis rapidly to form secondary particles, which can easily aggregate on the core surface [14].

Careful examination of some reports has also shown that a homogeneous coverage of carbonaceous materials by TiO_2 have not been achieved with good carbon- TiO_2 bond since it is often difficult to obtain an interaction between TiO_2 and carbonaceous material. Hence, general and efficient strategies enabling the fabrication of TiO_2 coatings on carbon substrate remain highly challenging [18].

Although different forms of carbon have been used as substrates in those studies, carbon blacks are a primary support for Pt for low-temperature fuel cells [due to their high](#) surface area, electric conductivity, porosity, stability, and low cost [19-20]. For fuel cell applications, Vulcan XC-72R carbon has shown to have a suitable surface and pore volume [21]. Carbon blacks, in general, have a significant number of structural defects that affect their reproducibility as substrates and a surface treatment is usually required [22-23]. The surface treatment also introduces functional groups on the surface of carbon that can serve as nucleation points for the metallic precursors [24-25]. These oxygenated groups help to diminish the carbon hydrophobicity, thereby favoring the accessibility of the aqueous metallic precursors [26]. On the other hand, the less acidic groups increase the interaction between the metal precursor and the carbon support, thus avoiding the agglomeration tendency of the metal on the carbon [19, 27]. As a result, various surface modification schemes have been used to pre-treat carbon surfaces, most common of these is oxidation of the carbon material [28-29].

This chapter contains two different approaches to induce surface functional groups on carbon black: acid treatment and glucose adsorption. The former approach is done by charging the carbon substrate with surface functional groups via covalent bonding upon strong acid treatment, but, this harsh and defect-inducing conditions can adversely affect the electronic properties of the carbon substrate and could lead to a heterogeneous mixture of oxidized surface sites [30-31]. In addition, it provides little control over the nature, location, and quantity of the introduced functional groups and also seems to etch carbon surfaces [32]. The TiO_2 coating on the treated carbon surface tends to be highly non-uniform in thickness with much of oxide being present as particles [32]. An alternative

approach to acid treatment is needed to improve the chemical contact between TiO_2 and carbon during the synthesis and crystallization processes. The second approach developed as part of this thesis is a sol-gel method that involves the pre-adsorption of glucose molecules on the surface of pristine carbon, Vulcan XC-72, to induce a more uniform deposition of TiO_2 nanoparticles on carbon. To the best of our knowledge, there have not been any reports on the synthesis of TiO_2 /Vulcan carbon composites using a sol-gel method without structure directing agents for fuel cell application.

Briefly, TiO_2 /carbon materials have been prepared by: (i) a conventional sol-gel method on acid treated Vulcan carbon to produce TiO_2 /ATV composites and (ii) a new approach that involved the preadsorption of glucose, an $-\text{OH}$ rich molecule, on the surface of carbon to produce TiO_2 /G-PV composites with different TiO_2 content. A successful TiO_2 coating is expected to form a thin film shell around the core carbon support. The objective of the work included in this chapter was to investigate the physicochemical properties of modified carbon and TiO_2 /carbon composite materials, along with their electrochemical stability under half-cell conditions. Structural changes arising from surface chemistry, surface area, particle size, and particle size distribution, and metal-metal oxide electronic interactions will impact the electrochemical performance following deposition of Pt NPs.

3.2 Physical characterization of modified carbon and composite supports

Powder X-ray diffraction (XRD) analysis was used to characterize the TiO_2 and carbon crystal phase. The experiments were performed with a Rigaku X-ray system and PDX2 software. A Cu K-Alpha 0.154 nm X-ray source was used, scanning from 10 to 85 2θ with a step size of 0.02. XPS characterization was performed with a ThermoFisher Scientific K-Alpha (1486.65 eV) system. Charge compensation applied with combined e/Ar flood-gun. The energy range was shifted so that main C1s peak appeared at 284.6 eV. Powdered samples were spread onto double-sided adhesive C tape, using enough powder to completely cover the tape. Data work-up was performed with software provided with the instrument (Advantage 5.926).

Thermal gravimetric analysis (TGA) and differential scanning calorimetry (DSC) provided semi-quantitative information about the samples composition, as well as, for identifying decomposition temperatures and phase changes of the materials. Thermal decomposition studies were performed with an SDT Q600 Thermal Gravimetric Analyzer from TA Instruments controlled by Q Series software. Samples were heated in alumina pans from room temperature to 1000°C at a heating rate of 20°Cmin⁻¹. The atmosphere in the furnace was either extra dry air (Praxair) or argon (99.999%, Praxair) flowing at 50 mLmin⁻¹. A confocal Renishaw Raman Imaging Microscope System 2000 was used as the primary characterization tool for determining the samples' composition and their phase structure. Spectra were collected in the range 4000-100 cm⁻¹ with an argon ion laser at 514 nm at 25 mW output power. Repeated acquisitions (40 scans) with a collection time of 10 s and 50x magnification (50x) were acquired to improve the signal-to-noise ratio. The spectra were an average of spectra obtained from three samples.

The samples were also analysed with a JOEL JSM6610- Scanning Electron Microscope (SEM); with an Oxford/SDD EDS detector. The samples were mounted using carbon tape X-Ray Microanalysis; digital imaging via SE, BSE and X-ray signals. The samples mounted on carbon tape were sputter coated with a gold film and examined at 20 kV at a working distance of 8mm. The Scherrer equation was used to calculate particle size from the spectral line broadening. TEM characterization studies were carried out using either a JEOL JEM-2010 200kV high resolution TEM LaB6 filament or a Philips CM 10 instrument equipped with an AMT digital camera system.

For IR absorption analysis; ~5 mg of sample was carefully mixed with ~95 mg of dried KBr (IR grade, Aldrich) and pressed into a pellet. FTIR spectra (4000-650 cm⁻¹) were measured using a Perkin Elmer spectrum 100. The surface area determination experiments were carried out by nitrogen sorption measurements using the Brunauer-Emmett- Teller (BET) equation. These measurements were carried out using a Micromeritics 2390a instrument from Quantachrome using nitrogen as the adsorbent. The typical sample mass was 100 mg. The samples were degassed under nitrogen flow at 300 °C, for a minimum of 2 h prior the actual measurement.

3.3 Electrochemical measurement and support durability study

Electrochemical measurements were performed on thin films prepared by dropping a catalyst ink on the surface of a GC electrode. Electrode inks were prepared by dispersing ca. 10 mg of support material in 500 μL of solution containing Nafion[®], water, and isopropyl alcohol. This mixture was put in an ultrasonic bath to sonicate for 45 minutes. 5 μL of the ink were deposited onto the glassy carbon disk surface (diameter = 5 mm) of a rotating disk electrode (RDE) using a microsyringe. The deposited ink was allowed to dry in air for 20 minutes before electrochemical measurements were performed. Electrochemical measurements were made in a conventional three electrode cell equipped with a Pt wire counter electrode and silver/silver chloride (Ag/AgCl/ 0.5M KCL) reference electrode at room temperature using 0.5 M H_2SO_4 aqueous solution as the electrolyte. The electrode potential values were converted to NHE using 0.65V.

A Solartron SI 1260 Impedance Analyzer was used in combination with a Solartron 1470 E multichannel potentiostat and Multistat 1.1d software (Scribner Associates Inc.) for electrochemical measurement. For electrochemical impedance spectroscopy analysis, a constant D.C. bias of 0.0 V vs. OCP was applied across a sensor and a small A.C. perturbation was applied with amplitude of 5 mV. The frequency of the A.C. potential is scanned from high to low frequency over the range 0.1 Hz to 100 kHz and the resulting current is measured. The D.C. limit is achieved as the A.C. frequency approaches infinity. A D.C bias potential of 0.60V vs NHE was used in this study for impedance measurement. The support stability was investigated by repeated potential cycling with the appropriate lower and upper potential limits in an acid solution.

3.4 Results and Discussion

As described, modified supports were synthesized under different conditions, this section discusses the results of different composites and compares findings with the work of others.

3.4.1 Materials Characterization

FTIR Analysis

Since carbon blacks are hydrophobic in nature, the addition of hydrophilic functional groups was carried out to modify the wettability of the PV surface. FTIR spectroscopy was used to study the functionalities on the carbon surface. Because carbon is a very strong absorber in the infrared region, special conditions for sample preparation and methods of detection were used in order to improve the signal level. Carbon sample was diluted with a large amount of KBr. The presence of KBr will not interfere with the detection of CO_2 function groups (a doublet at $2300\text{--}2400\text{ cm}^{-1}$) and molecular water (fringes in the $1400\text{--}1700$ and $3350\text{--}3800\text{ cm}^{-1}$) on the carbon surface if it is properly dried.

Figure 3.1 shows the FT-IR results of pristine and modified carbon samples, obtained at different conditions. From this figure, it can be inferred that untreated carbon has a trace of oxygen containing groups. This observation has been reported elsewhere in the literature and is said to be due to chemisorbed oxygen on the carbon surface obtained immediately after synthesis to satisfy valence requirements [33]. Chemical treatments such as wet oxidation in HNO_3 can functionalize the carbon surface with the bands at 3419 , 1626 and 1058 cm^{-1} attributed to the presence of hydroxyl groups ($-\text{OH}$), carboxyl ($-\text{COOH}$), and carbonyl ($-\text{C}=\text{O}$) groups that are necessary to tether metal ions to the surface of carbon [34]. For the oxidised carbon, ATV shows an increment of these functional groups. The peak at 950 cm^{-1} is due to the O–H bend in carboxylic acid is clearly observed in ATV which indicates the presence of carboxylic acids [35]. The absorption band at 1736 cm^{-1} is attributed to carbonyl stretching frequencies for carboxylic acids and quinone which are known to be produced by nitric acid treatment of carbons, the peak at 1376 cm^{-1} can be due to lactone, phenol and/or OH functional groups [36]. ATV in comparison to PV also show a more intense peak at 1376 cm^{-1} that is assignable to the bending vibration of the O-H.

The interaction of the metallic precursor with the support depends on the nature of the surface groups produced as a consequence of the oxidation treatment. Depending on the nature and extent of nitric acid treatment, functionalised carbon will display a high density of strong acidic sites which have a positive effect on the development of active sites that can coordinate interaction with metal precursor during impregnation. This, in

turn, will favour the metal dispersion on the carbon surface and consequently improve catalytic cell performance. However, this treatment often affects the long-term durability of the catalyst material and thus the need to preserve carbon substrate with a less rigorous treatment approach.

In addition, G-PV shows the sp^3 C-H stretching absorptions that arise from the alkyl chain appear at $\sim 2900\text{-}3000\text{ cm}^{-1}$ with a broad peak corresponding to the O-H group of water centered at 3385 cm^{-1} and the carbonyl absorptions observed at $1670\text{-}1700\text{ cm}^{-1}$ [37]. The increase in the relative intensities of the bands at 3385 cm^{-1} suggests that there are more O-H groups on the surface after treatment in acid and with glucose adsorption. All these observations confirm that the surface of the PV has been functionalized and activated with these functional groups.

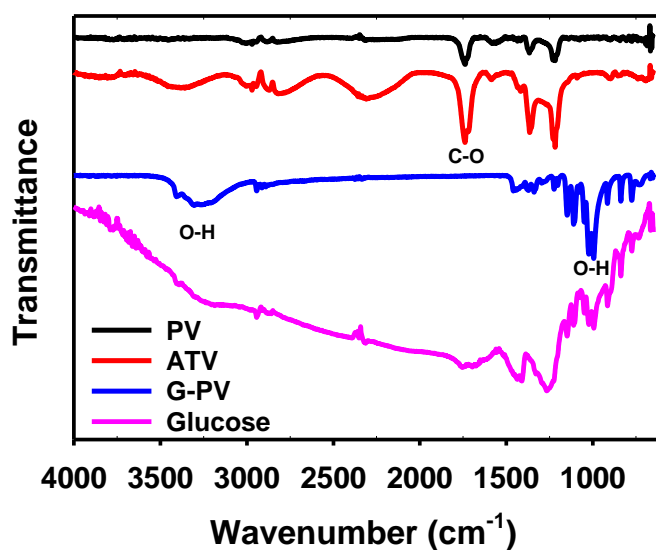


Figure 3.1: FTIR spectra of Glucose, Pristine Vulcan (PV) acid treated Vulcan (ATV) and glucose doped Vulcan (G-PV).

Thermogravimetric Analysis

Thermogravimetric analysis (TGA) is a traditional method for determining the composition and oxidative stability of catalyst materials [38]. A previous study has shown a correlation between oxidative and electrochemical stability [39]. TGA curves are shown in Figure 3.2 for carbon substrates in argon (A and B) and air (C and D), respectively. As expected the mass loss is affected by the pre-treatment and the presence of glucose. The pyrolysis of PV, ATV, and G-PV in an inert atmosphere up to 800 °C leaves the following residual masses, 98%, 87%, and 76%, respectively. The lowest residual mass is observed for G-PV due to the presence of glucose while PV is quite stable up to 800 °C. In air, the heat flow (DSC) profiles are also quite distinct between carbon substrates. Two different peaks can be observed for the modified samples, which can be associated with the thermal combustion of attached functional groups and oxidation of the parent Vulcan carbon at the higher temperature [40]. These functional groups yielding CO₂ can decompose at different temperatures: carboxylic acids at about 375°C and carboxylic anhydrides and lactones at much higher temperature [40]. Other CO-yielding groups such as phenols, ethers, and carbonyls functional groups of the base carbon material will also decompose at much higher temperature; 575–825 °C [40].

In air, the more aggressive treatment involving HNO₃ introduces defects on carbon that can contribute to the higher thermal instability of ATV. The small peak at 220°C in the case of G-PV is surely linked to thermal oxidation of glucose carbon in air, but the carbon substrate is significantly more stable than ATV. Overall, this comparative analysis shows that ATV becomes thermally unstable at temperature above 500°C in comparison to PV and G-PV samples.

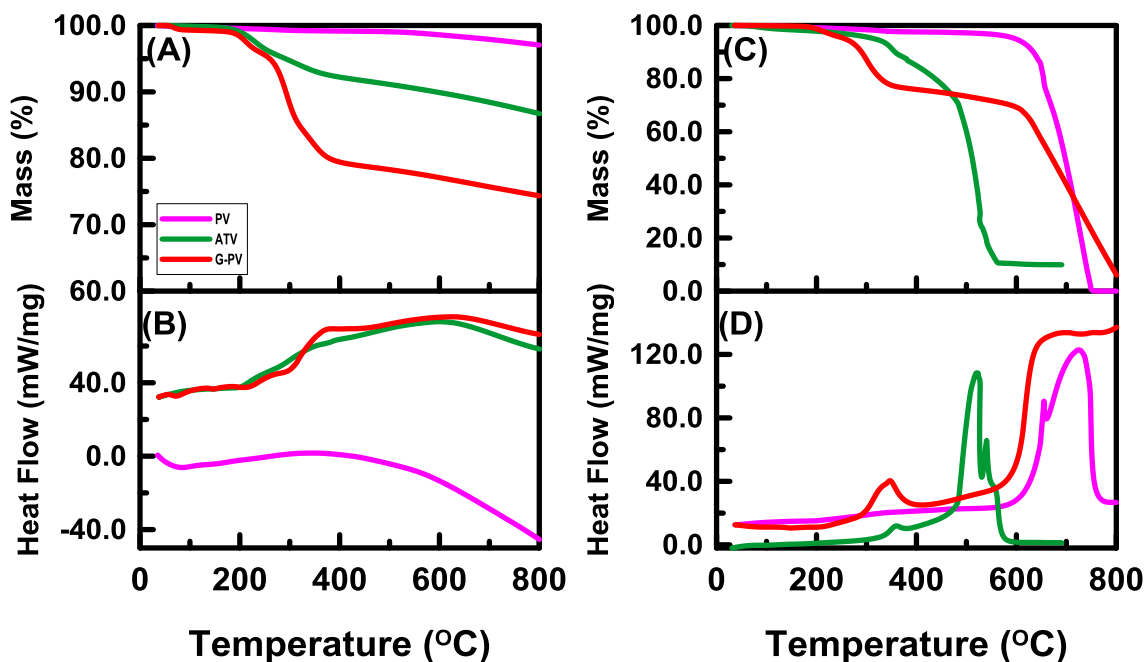


Figure 3.2: The (A) TGA and (B) DSC curves obtained under argon and (C) and (D) in air for Pristine Vulcan (PV) and Acid treated Vulcan (ATV). Experimental conditions: sample mass ~ 10 mg, gas flow rate: 50 mL/min and heating rate of 20 °C/min.

Figure 3.3A and B shows the TGA-DSC profiles of the two composites: TiO_2 /ATV and TiO_2 /G-PV samples. These measurements were performed under air. Between room temperature and 800 °C, the weight loss stages were due to the removal of H_2O , adsorbed nitrate ions and glucose carbon. At higher temperatures, the oxidation of carbon black can be observed. The peak occurring at 585 °C is at a position which correlates with the oxidation of Vulcan carbon. This major peak is occurring at lower temperature in comparison to the untreated Vulcan carbon (Figure. 3.2C). This shift may be ascribed to the presence of TiO_2 grafted on modified carbon substrates. Thus, it is possible that the interaction of TiO_2 nanoparticles with carbon in air is facilitating thermal oxidation of carbon substrate [41]. There is no much difference in the TGA profiles of the two composite catalysts except for the carbon and TiO_2 mass content. The heat flow plots of the composites depict that the oxidation of carbon particles occurred at two different temperatures (360 and 600 °C). Figure 3.3 (C-D) shows the TGA profiles of calcined

TiO₂/G-PV composites with different TiO₂ loadings on the G-PV support. Increased TiO₂ loading has minimal impact on the thermal stability of the composite material. Table 3.1 lists the compositions of composite supports prepared with ATV and G-PV carbon substrates.

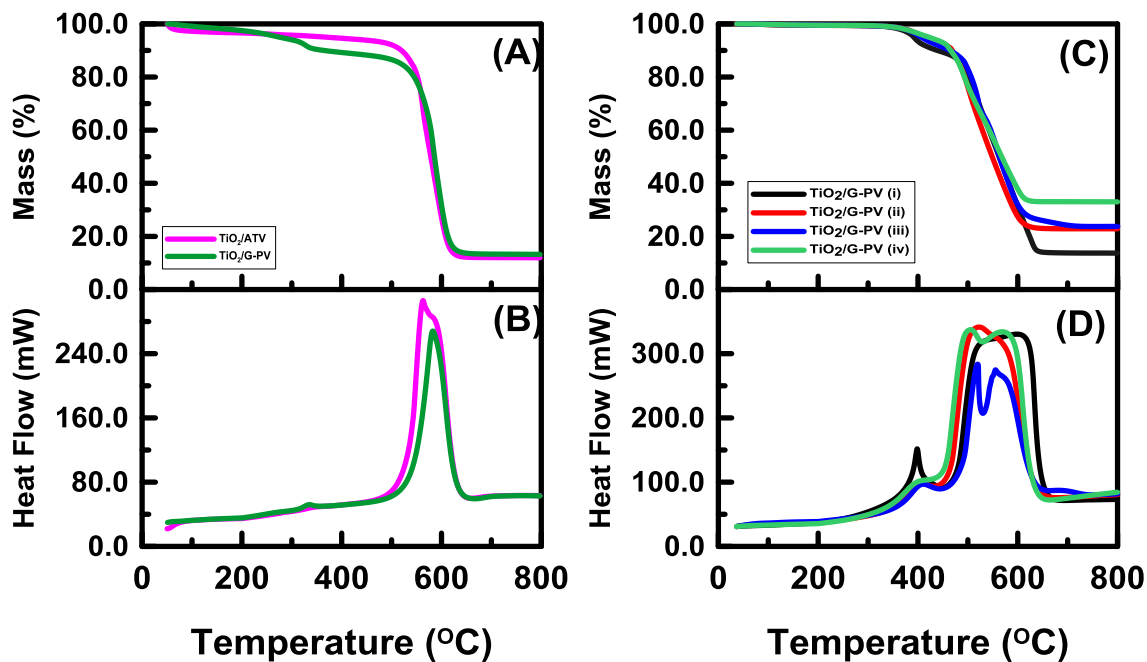


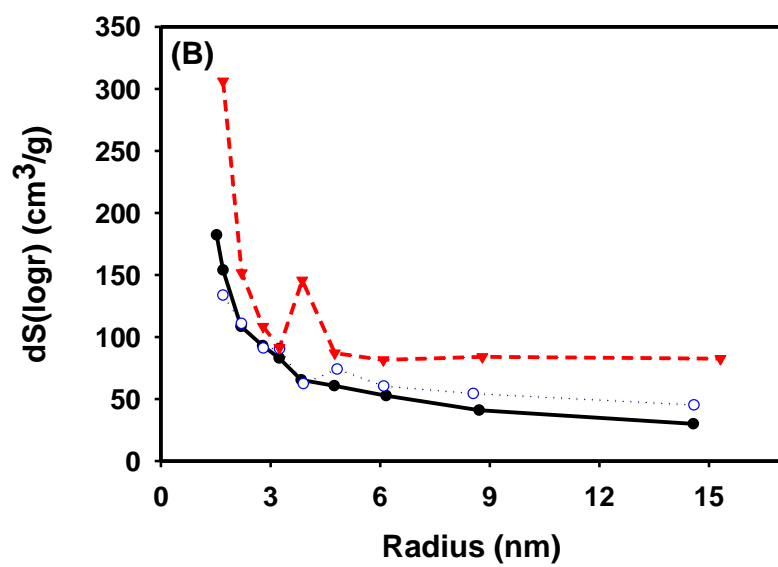
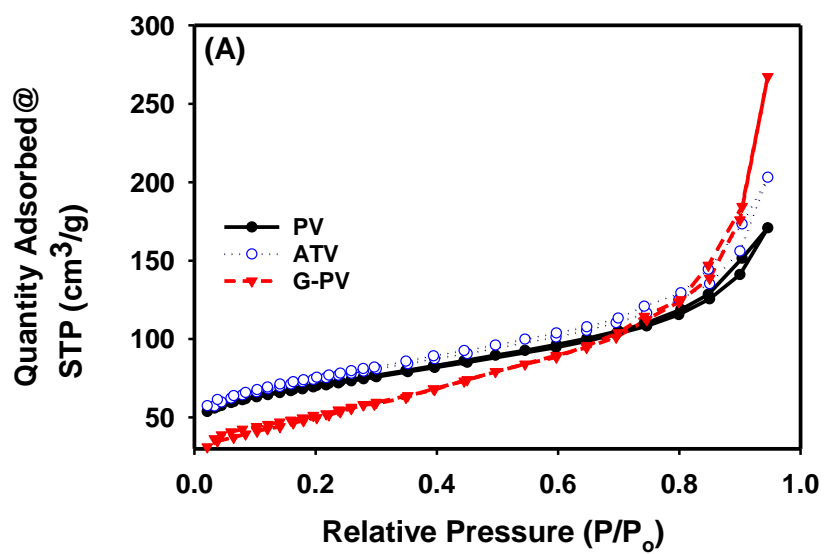
Figure 3.3: (A) TGA and (B) DSC curves of TiO₂/ATV and TiO₂/G-PV supports in air (C) TGA and (D) DSC curves of TiO₂/G-PV supports with different compositions of TiO₂ obtained under air. Experimental conditions: sample mass ~ 10 mg, gas flow rate: 50 mL/min, and heating rate 20 °C/min.

Table 3.1: Summary of TiO₂ contents on the modified carbon supports.

Samples	Carbon (wt %)	TiO ₂ (wt %)
TiO ₂ / ATV	97.2	2.8
TiO ₂ /ATV	92.5	7.5
TiO ₂ / ATV	90.0	10
TiO ₂ / ATV	86.0	14
TiO ₂ / G-PV	92.0	8.0
TiO ₂ / G-PV	86.0	14
TiO ₂ / G-PV	78.0	22
TiO ₂ / G-PV	76.0	24
TiO ₂ / G-PV	68.0	32

BET Analysis

Nitrogen adsorption-desorption isotherms and the pore size distribution derived from desorption branch for PV, ATV and G-PV are shown in Figure 3.4. All isotherms are multi-layer adsorption with minimal adsorption-desorption hysteresis and similar to those reported in the literature for Vulcan XC-72 [42]. This kind of isotherm denotes a structure with large pores with small microporosity. BJH method was used to analyze the desorption branch of the isotherms at relatively high pressure to obtain the pore size distribution of these carbon support materials. A porous support is needed to enhance deposition of the base metal material with faster diffusion rates comparable to microporous material [43]. The pore diameter distribution of the treated carbon confirms a pore diameter of the carbon particles in the range of 2 - 15 nm, similar to the literature value of 10.9 nm reported for Vulcan XC-72 through BJH pore size analysis [42].



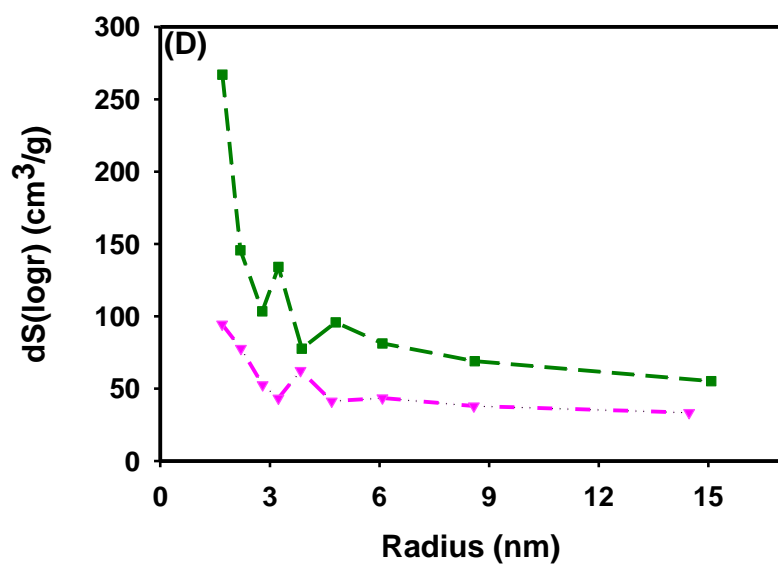
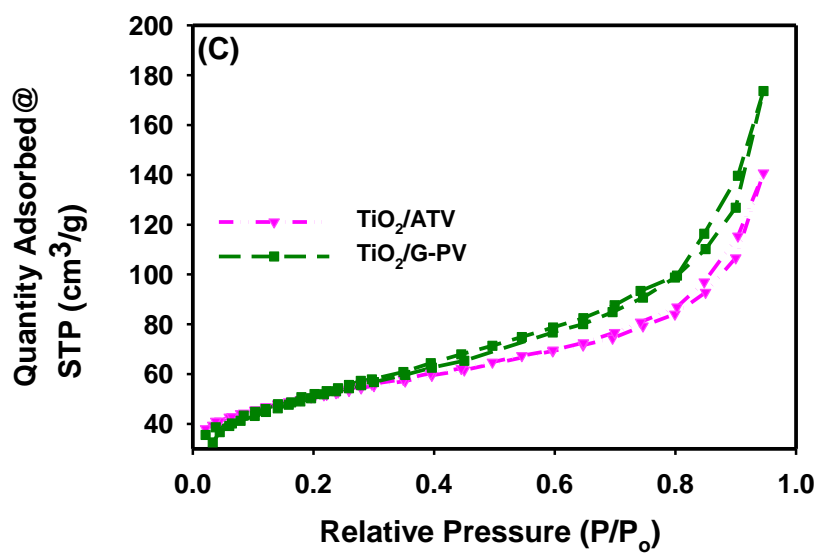


Figure 3.4: Nitrogen adsorption–desorption isotherms (A) at 77 K for pristine and modified Vulcan carbon with respective pore size distribution (B) and for composite supports after calcination (C) as well as pore size distribution curves (D).

The textural parameters such as specific surface area are given in Table 3.2. It can be observed from the table that the ATV carbon showed higher specific surface area (238 m²/g). This high surface area exhibited by the acid treated carbon is mainly due to opening of the pores of carbon in boiling HNO₃ solution. The high specific surface area will contribute significantly in achieving excellent dispersion of the base metal during the catalysts synthesis.

The isotherms of the TiO₂/ATV and TiO₂/G-PV composites show a steep uptake at high relative pressures with no sign of levelling off due to capillary condensation mainly in the pores. The calcined TiO₂/C composite materials that were prepared by acid treatment of PV carbon followed by a sol-gel coating shows a decrease in total surface area from 251 for ATV to 128 m²/g as TiO₂ loading was increased from 3 to 14 wt%. This observed decrease in total surface area may be due to an increase in the amount of TiO₂ dominating that of carbon particles. A similar observation was noticed for glucose doped composite supports (TiO₂/G-PV). Here the total surface areas observed decreased from 234 for PV carbon to 121 m²/g, respectively, with increasing coating loading up to 32 wt%. The decrease in the surface area results from the densification of amorphous TiO₂ networks and the grain growth of TiO₂ nanoparticles [44].

The observed total surface areas for composite samples TiO₂/G-PV are higher than their TiO₂/ATV counterpart. The behaviour can be assigned to a better distribution of TiO₂ nanoparticles on the surface of carbon in the case of TiO₂/G-PV while phase segregation could explain the rapid decrease in surface area in the case of TiO₂/ATV. A similar trend was observed by Li *et al.* in the case of TiO₂/carbon multiwall nanotube materials [45]. In comparison, pure TiO₂ synthesized in the same conditions present very low surface area and porosity with respect to carbon based composite supports. The surface areas of the composites depends on the TiO₂ content and thermal treatment condition.

Table 3.2: BET surface area data for reference and composite materials.

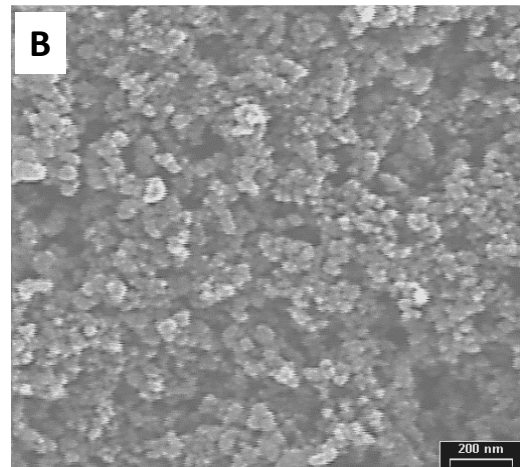
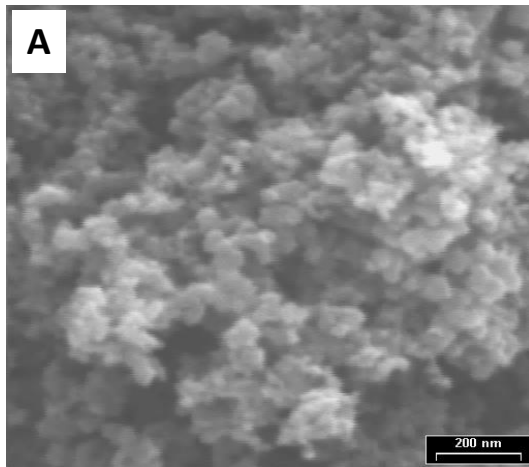
Samples	TiO ₂ (wt %)	BET surface area (m ² /g)
PV	---	234 ± 5.6
ATV	---	251±2.3
G-PV [#]	---	182±1.3
TiO ₂ [#]	100	79.2±4.1
TiO ₂ /ATV	2.8	240±2.9
TiO ₂ /ATV	5.0	236±3.7
TiO ₂ /ATV	7.6	188±1.8
TiO ₂ /ATV	10.3	171±1.4
TiO ₂ /ATV	13.5	128±0.8
TiO ₂ / G-PV	8.0	208±2.2
TiO ₂ / G-PV	13.5	177±3.7
TiO ₂ / G-PV	22.0	138±1.9
TiO ₂ / G-PV	24.0	141±3.3
TiO ₂ / G-PV	32.0	121±2.1

[#]after annealing under nitrogen for 2 hours at 500 °C.

Morphological characterization by electron microscopy

The scanning electron microscope images of PV, ATV and G-PV carbon samples are shown in Figures 3.5 (A), (B) and (C), respectively, from where it can be seen that there is not much morphological change in the carbon sample with respect to the various treatments except for a very small change in particle size. The carbon materials exhibit spherical morphology with some agglomerations between the particles. Also there are spherical aggregates about 150-200 nm in size. An average particle size of ca.40-50 nm is visible from these images. G-PV is characterized by the presence of large and clearly defined carbon spheres with smooth surface that form cluster-like structure. There are basically three types of carbon particle structures:

1. Dense carbon particles.
2. Severely aggregated particles.
3. Uniformly distributed and porous particles.



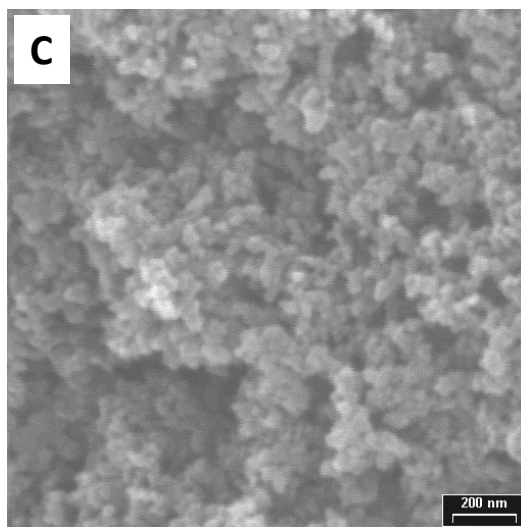


Figure 3.5: Scanning electron micrographs of PV, (A) ATV (B) and G-PV (C) carbon supports.

TEM images of the modified treated carbon supports reveal that each aggregate being made of particles of about 40-50 nm with little difference between materials (Figure 3.6). High resolution TEM micrographs for TiO_2/ATV and $\text{TiO}_2/\text{G-PV}$ are also shown in Figure 3.7. TiO_2 nanoparticles and carbon particles can be seen clearly in these figures. Glucose doped composite shows network of TiO_2 particles deposited on porous carbon network, resulting in the formation of the TiO_2/C hetero-interfaces. Significant dark blotches are visible traceable to agglomerates of TiO_2 on carbon support and are more pronounced on TiO_2/ATV composite support. The carbon particles appear uncovered by TiO_2 while the TiO_2 agglomerates are far removed from the carbon particles on TiO_2/ATV support. In some instance some of the TiO_2 appear to have covered the carbon particles while most of the TiO_2 particles appear to agglomerate away from these particles. These images reveal that TiO_2 is made of aggregated clusters of particles with an average size of about 5-8.4 nm. The average particle size obtained for the synthesized TiO_2 is smaller than the one reported by Guo *et al.* (15 nm) [46], yet comparable to the size previously reported in the literature [47-48]

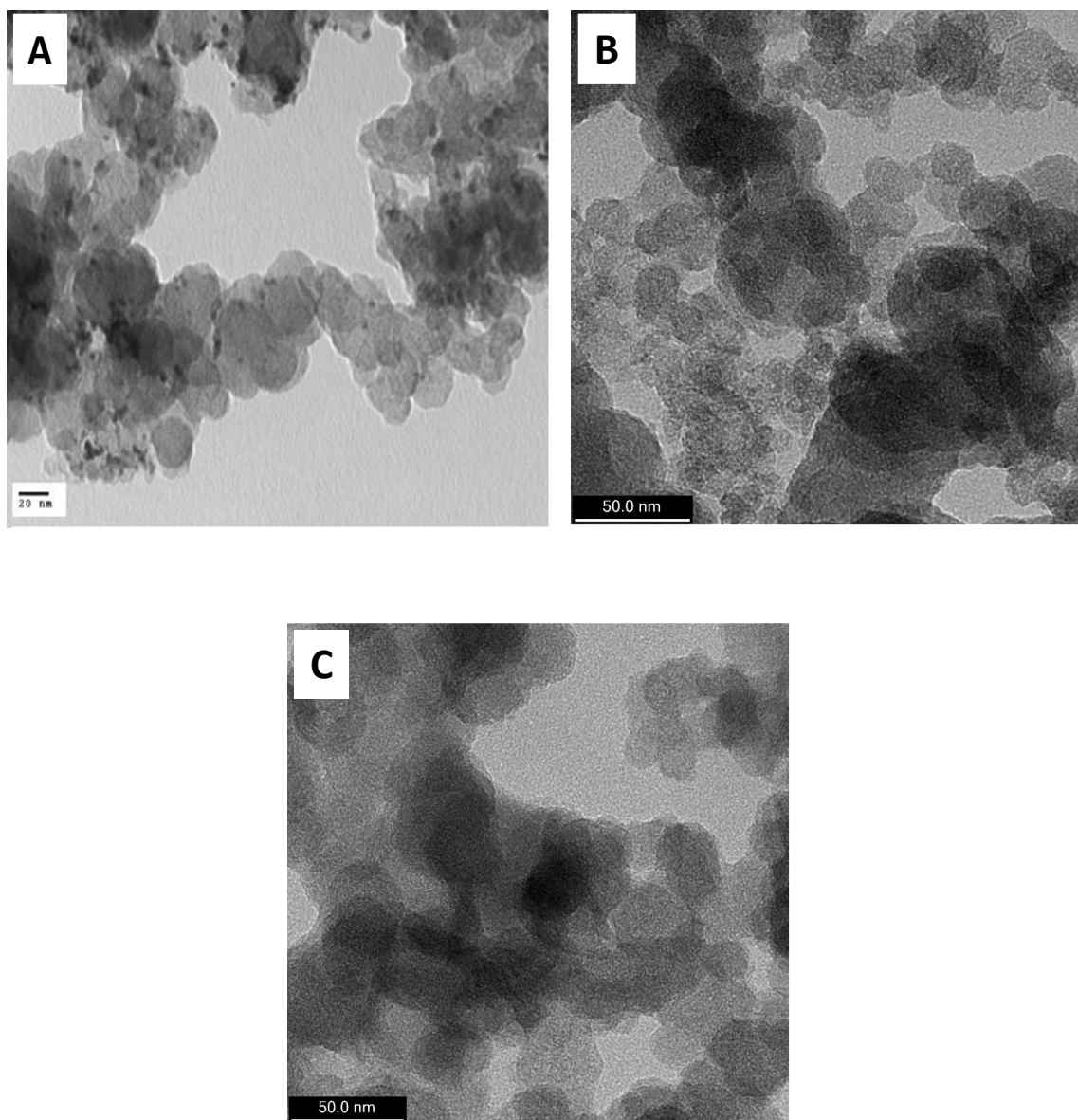


Figure 3.6: Transmission electron micrographs of PV, (A) ATV (B) and G-PV (C) carbon supports

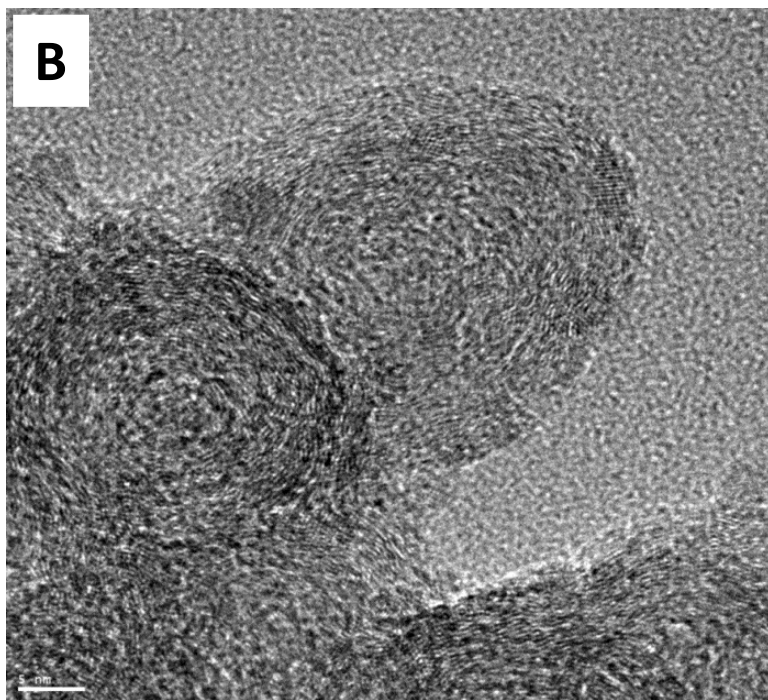
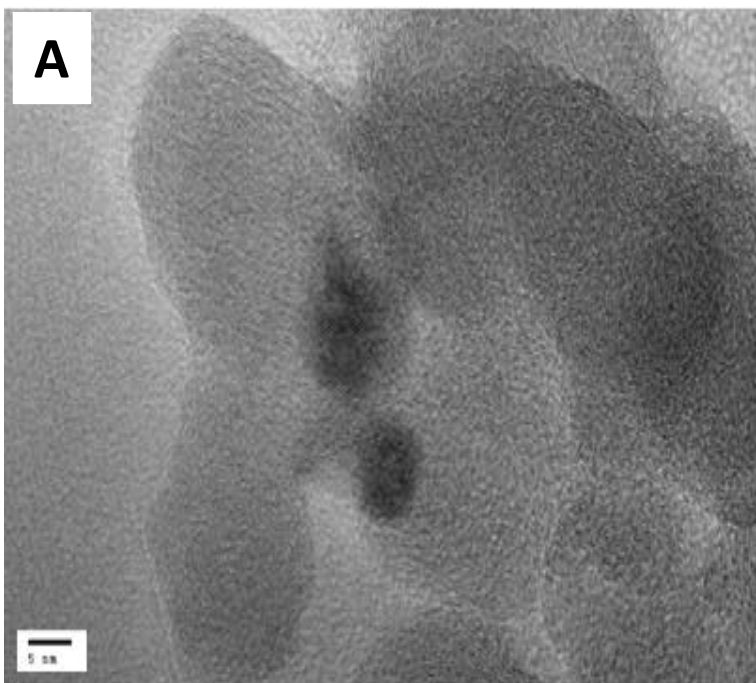


Figure 3.7: Transmission electron micrographs of TiO₂/ATV, (A) and TiO₂/G-PV (B) composite supports (Scale bar: 5 nm).

XRD Analysis

XRD patterns of a plain Vulcan carbon substrate and the modified carbon samples are shown in Figure 3.8A. The three samples show a broad carbon peak at $2\theta = 25^\circ$ assigned to the (002) crystalline plane. However, the G-PV support also show peak reflections between 19° and 20° . This result is similar to the literature data of Bragg reflection of cellulose (a glucose based sample) with broad peaks at ca. 20.2° and 22.1° that were assigned to the (110) and (200) crystalline plane [49]. The X-ray diffraction pattern of commercial TiO_2 anatase nanoparticles (Sigma-Aldrich) is shown in Figure 3.8B. The anatase TiO_2 sample was subjected to heat treatment for 6 hours at 850°C to produce the rutile form since it is well known that the phase transformation from metastable anatase to stable rutile occurs at around 600°C [50]. There were no broad diffraction peaks observed for these samples. The absence of spurious diffraction peaks in this figure also indicates the extent of crystallographic purity [51]. The experimental XRD pattern agrees with the JCPDS card no. anatase TiO_2 (JCPDS No. 21-1272) and rutile (JCPDS No. 21-1276) as well as the XRD pattern of TiO_2 nanoparticles in the literature [52]. In addition dominant anatase and rutile phases with an intensity ratio of the (101) plane of the anatase phase to the (110) plane of the rutile phase of 1 can be observed.

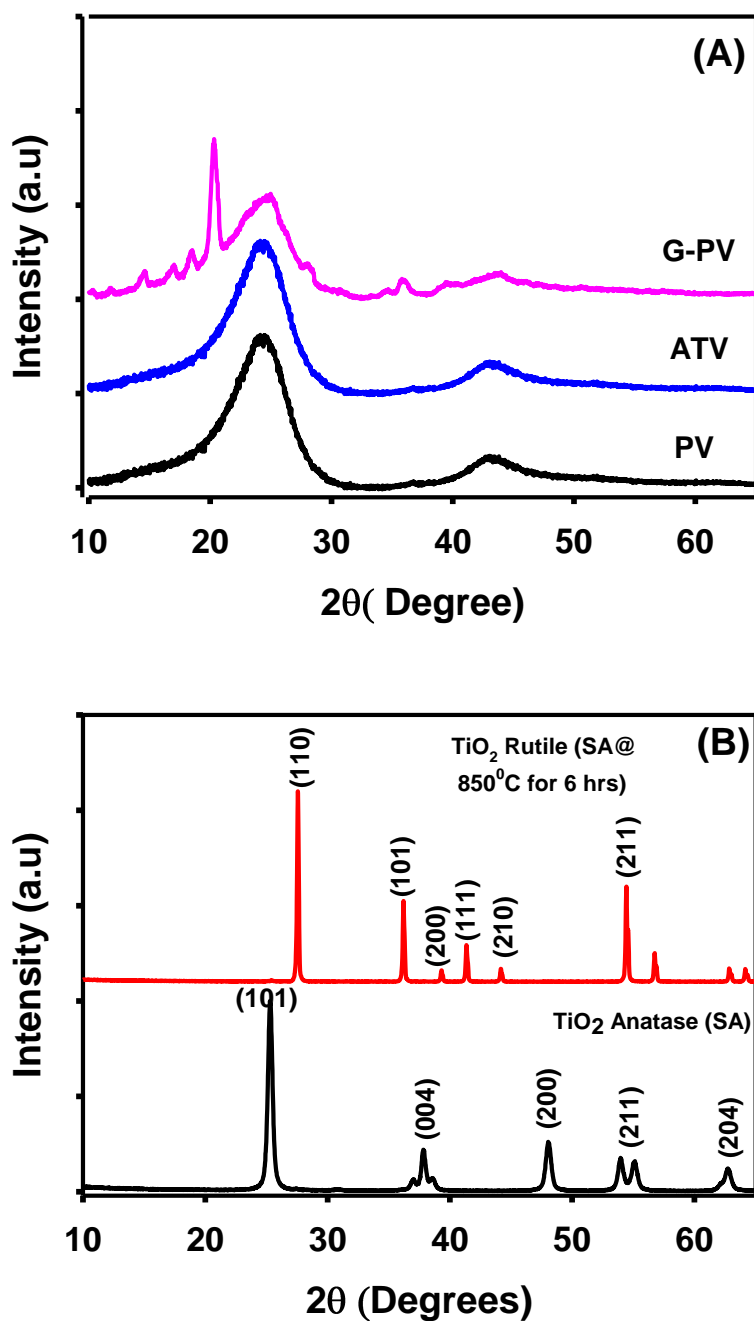


Figure 3.8: XRD patterns for PV, ATV and G-PV (A) as well as the commercial anataseTiO₂ (SA) and rutile phase of SA following heat treatment (B).

The broad diffraction peaks observed in XRD of the composite samples (Figure 3.9) indicates the formed TiO₂ nanoparticles are crystalline and small in particle size. The

diffraction peaks of these composites at these two annealing temperatures contain a mixture of anatase and rutile phases with amorphous carbon. Although, the rutile content becomes dominant following heat treatment at 850°C for 2 hours, which means that the phase transformation of anatase into rutile phase takes place during this process.

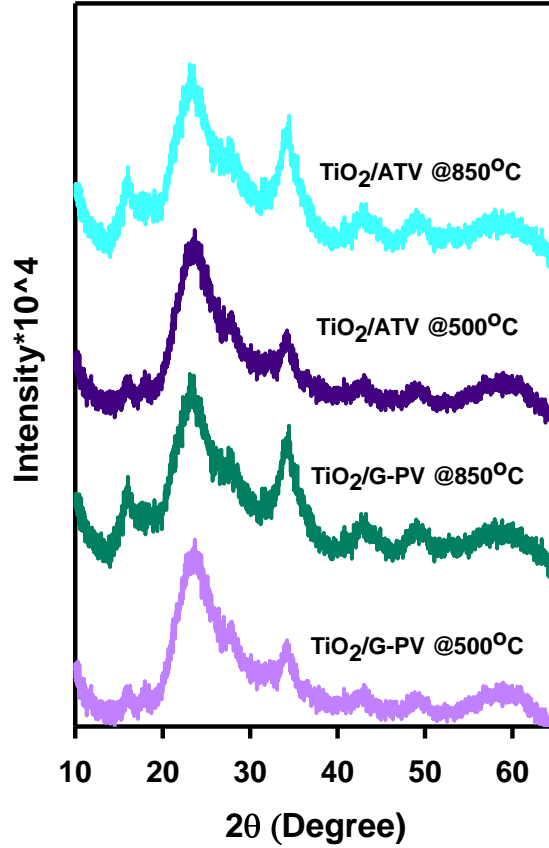


Figure 3.9: XRD patterns for TiO_2/ATV and $\text{TiO}_2/\text{G-PV}$ composites after calcination at two different temperature in nitrogen.

The 2θ peaks at 25.27° and 48.01° confirm its anatase structure [51]. There is an overlap of the dominant carbon peak and TiO_2 peaks in the composite samples. As a result, the TiO_2 phase content and the average crystallite sizes of anatase and rutile in these composite samples could not be estimated from the integrated intensities and the full width at half maximum (FWHM) of the anatase (101) peak and rutile (110) peak according to the Scherrer equation [53]. Composite materials are heat-treated at 500°C for 2 hours to produce dominant crystalline anatase phase in this thesis.

Raman Spectroscopy Analysis

Raman spectroscopy was employed to confirm the crystalline phase of TiO_2 and the existence of carbon in the composite (Figure 3.10). Raman signals were collected and recorded from 100 to 2000 cm^{-1} to identify the presence and nature of the carbon in the composite samples (Figure 3.10A). The Raman spectra show the characteristic G-band and D-band at 1591 cm^{-1} and 1337 cm^{-1} , respectively, due to presence of both graphitic and non-graphitic carbon [54]. The G-band centering at around 1600 cm^{-1} is a Raman active mode of graphite composed of local sp^2 bonded structure while the D-band centering near 1350 cm^{-1} is often associated with bond-angle disorders and graphitic carbon structure [54].

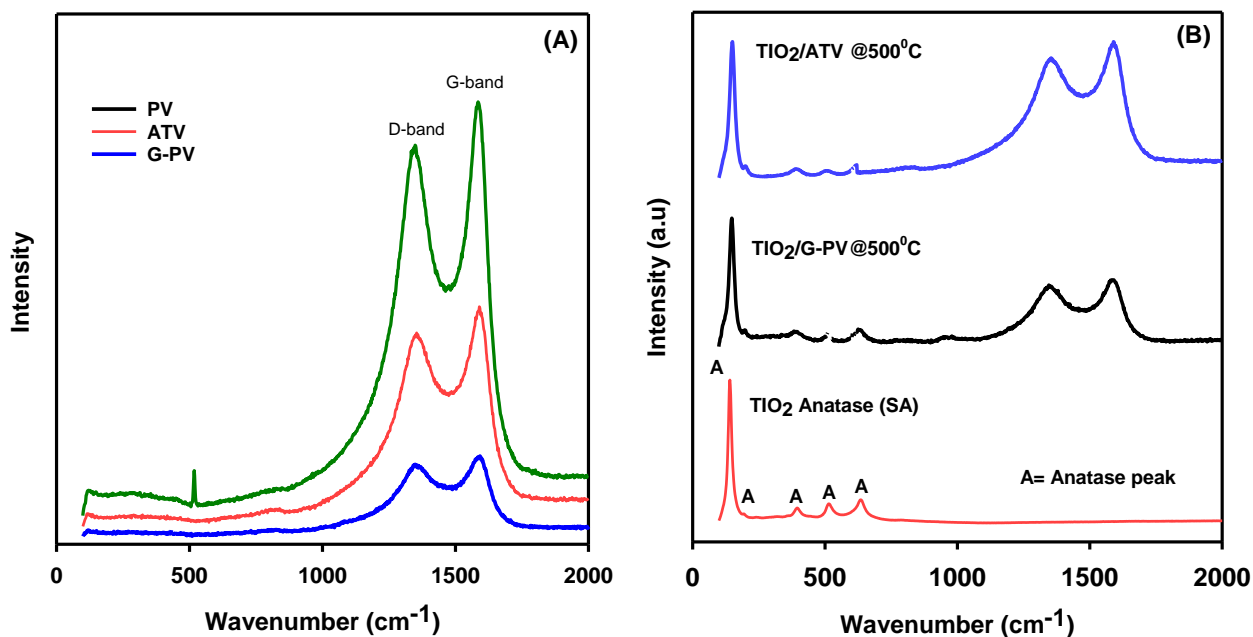


Figure 3.10: Raman spectra carbon supports (A), commercial TiO_2 (SA) with composite support materials, TiO_2/ATV and $\text{TiO}_2/\text{G-PV}$ (B).

The Raman spectra for the composite samples after heat treatment in a nitrogen atmosphere for 2 hours at 500 °C were also collected. The observed peak at around 638 cm^{-1} , 516 cm^{-1} , 396 cm^{-1} , 200 cm^{-1} , and 146 cm^{-1} can be attributed to the characteristic

peaks of the predominant anatase phase [55]. The four fundamental Raman bands due to rutile phase at 826 cm^{-1} , 612 cm^{-1} , 447 cm^{-1} and 143 cm^{-1} were detected but they were very small and not distinct, suggesting anatase TiO_2 as the dominant phase, which is consistent with the XRD analysis. In summary, Raman confirmed the formation of anatase as the predominant TiO_2 phase in the composite $\text{TiO}_2/\text{G-PV}$ and $\text{TiO}_2\text{-ATV}$ samples.

XPS Analysis

The high-resolution XPS spectra for elements detected on the surface of the samples are shown individually in Figures 3.11–3.14. These survey scan spectra show C1s and O1s peaks at 284 and 532 eV in the both as-received Vulcan (PV) and treated carbon support. The observed C1s peak mainly represents amorphous carbon. The increase in the intensity of O1s peak from PV to G-PV indicates the presence of greater oxygen functionalities in the treated samples. The concentration of elements detected on the surface of carbon black powders analyzed (PV, ATV, and G-PV) is shown in Table 3.3. The assignment of C1s spectra into distinct peaks at 283.87, 284.4, 286.5, 289 and 291.5 eV are shown in Table 3.4 which is in agreement with the literature reports [57-58]. From Table 3.4, the predominant C1s peak appears at $284.4 \pm 0.1\text{ eV}$ for pristine and treated carbon samples. Thus the extent of amorphous nature of these materials can be seen.

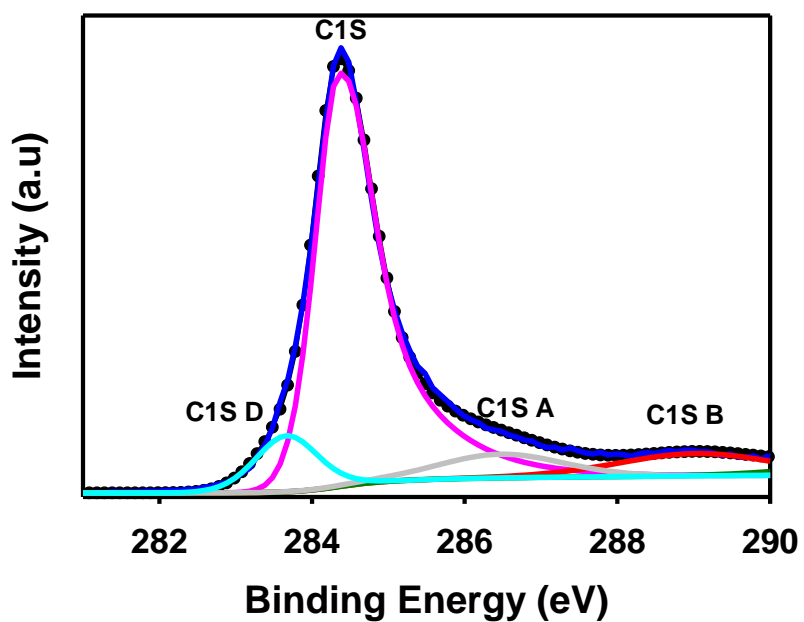


Figure 3.11: XPS analysis C1s spectra pristine Vulcan carbon (PV)

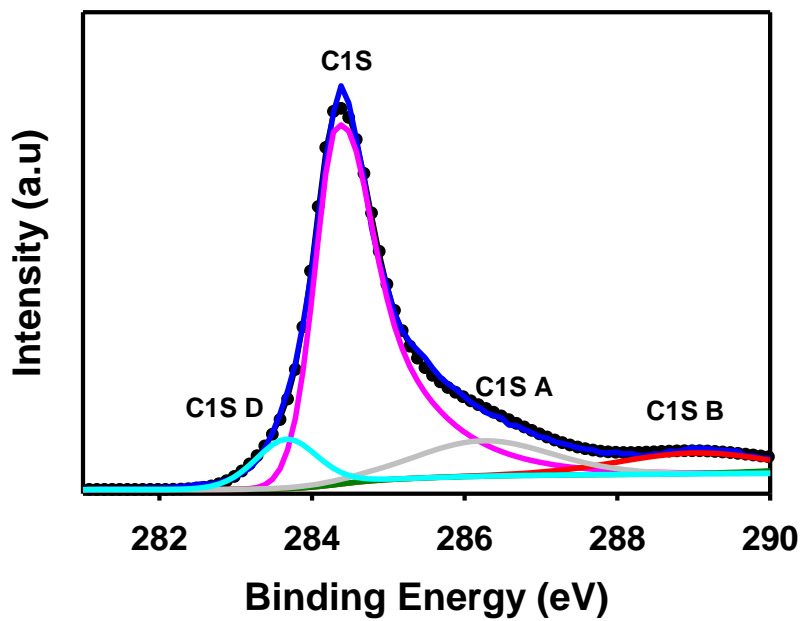


Figure 3.12: XPS analysis C1s spectra glucose doped pristine Vulcan carbon (G-PV)

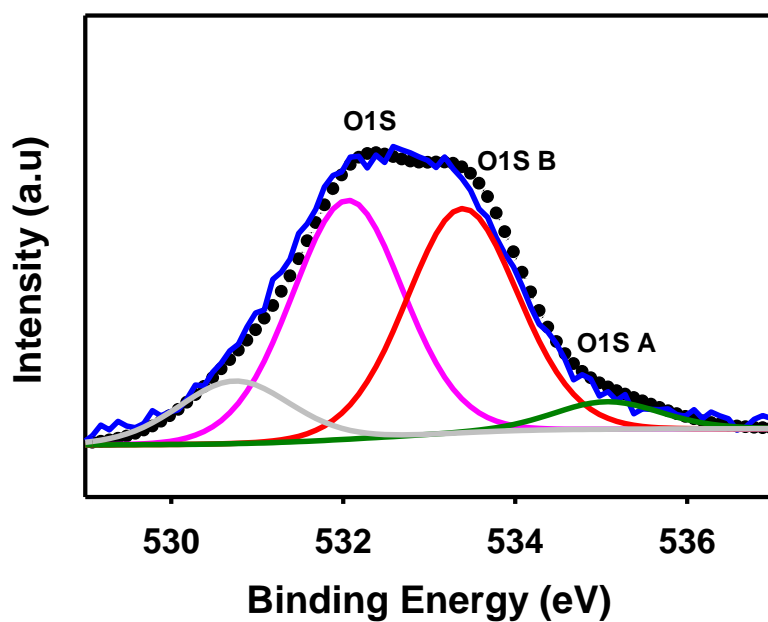


Figure 3.13: XPS analysis O1s spectra pristine Vulcan carbon (PV)

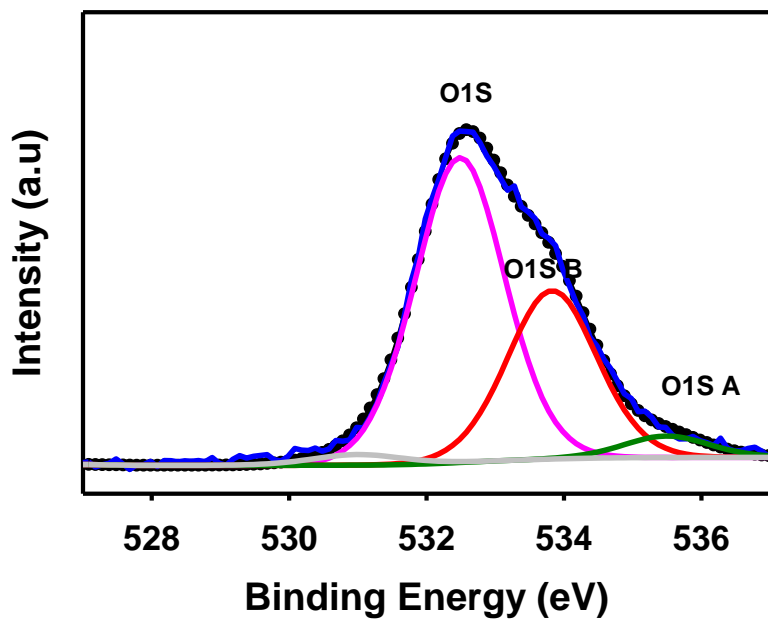


Figure 3.14: XPS analysis O1s spectra glucose doped pristine Vulcan carbon (G-PV)

The peaks that appeared at binding energies 284.3 ± 0.1 and 285.0 ± 0.1 eV are attributed to the sp^2 C and sp^3 C, respectively. Slight shifts can be observed between sp^2 and sp^3 peak positions of these materials. The peaks that appeared at binding energies 289.1, and 291.7 eV can be assigned to the -C=O, and -O-C-O-, functional groups respectively [57]. These functional groups representing 10.4% and 3.3% of the ATV and are much higher than those of the untreated carbon sample, PV (8.4 and 1.9% respectively). However, in comparison to PV, G-PV shows a decrease in the relative intensities of these -C=O, and -O-C-O-, functional groups. This suggests the conversion of these groups into the alcohol groups as shown with the FTIR data. This conversion process can be useful in anchoring the carbon molecules with TiO_2 through the reaction of these hydroxyl groups.

The two peaks of the O1s signal of the carbon samples indicate two chemical states of O. These peaks at binding energies 531.6 ± 0.1 and 533.2 ± 0.1 eV are attributed to the oxygen doubly bonded to carbon in quinones, ketones, and aldehydes and oxygen singly bonded to carbon in ethers and phenols respectively as reported in the studies by Zielke et al.[59-60]. The intensities of both the C-O and C=O peaks increase after treatment. The curve fitting results for the elements detected, based on deconvolution with component peaks at fixed energy, are shown in Table 3.4. The atomic percentage of the oxygen in the sample also increased from 43% (untreated) to 61% (Table 3.4), indicating that the two treatment approaches effectively generated more functional groups on the carbon surface.

Table 3.3: Atomic surface compositions of different elements through XPS analysis

	C1s	O1s	Si2s	Ti2p
Samples	Atomic Concentration (%)			
PV	97.75	2.25	-	-
ATV	82.47	17.53	-	-
G-PV	78.85	21.15	-	-

Table 3.4: States of elements detected by surface analysis through XPS

C 1s peaks	PV	ATV	G-PV
	Binding energy (eV) and amount (%) respectively		
C1s	284.36 74.11%	284.51 75.91%	284.24 68.85%
C1s A (COOH)	286.47 7.12%	286.12 2.45%	286.24 12.28%
C1s B(C-O)	289.03 8.43%	289.03 10.43%	289.03 8.26%
C1s C (C=O)	291.47 1.94%	291.47 3.34	291.47 2.82%
C1s D	283.67 8.40	283.67 7.87%	283.67 7.78%
O 1s peak	532.15 43.28%	532.40 53.67%	532.49 60.45%

Examining the C1s peak of composite supports (Figure 3.15) shows that there are two distinct peaks at 284.6 eV and 285.9 eV. The 284.6 eV is the peak that is being attributed primarily to the elemental carbon secondarily to the graphite structure. The 285.9 eV peak is attributed to the C=O, –COOH and –OH bonds [61-63]. The C 1s spectra of the TiO₂/G-PV composite (Figure 3.15B) shows that a new carbon peak appeared at 288.7 eV. This peak is slightly away from the elemental carbon region and can be assumed to the bond of carbon to another element. This peak may be ascribed to an oxygen bond but there is no satisfactory explanation based on the existing literature data and thus, the need for a more detailed explanation [64]. The pre-adsorption of glucose hydroxyl functional group on PV substrate during non-acid treatment is set-up to generate bonds between the carbon and the nucleating TiO₂ particles following sol-gel synthesis. It is assumed that this peak

is originated from this bond. Carbon can be bonded to titanium through an O (C–O–Ti), or it can be directly bonded to titanium (C–Ti), which, commonly appears at 281.3 eV.

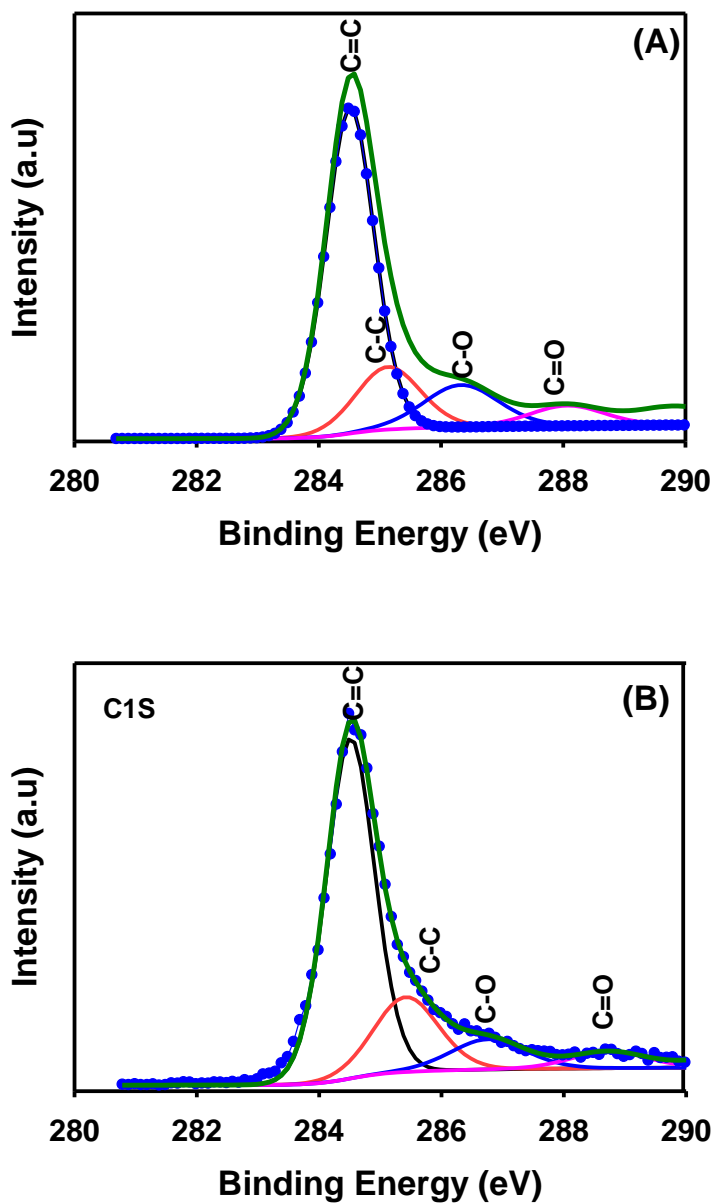


Figure 3.15: XPS analysis C1s spectra of TiO₂/ATV (A) and TiO₂/G-PV (B) composite supports.

XPS of the reference material anatase TiO_2 is shown in Figure 3.16. The titanium atom shows two distinct peaks at 458.4 eV for the $\text{Ti}2p_{1/2}$ and at 464.2 eV for the $\text{Ti}2p_{3/2}$, both in good agreement with the literature data [65]. The $\text{O}1s$ peak for this powder appears with a split. The peak is at 529.6 eV, represents the lattice oxygen. Another $\text{O}1s$ peak appears at 531.5 eV and is attributed to the surface oxygen.

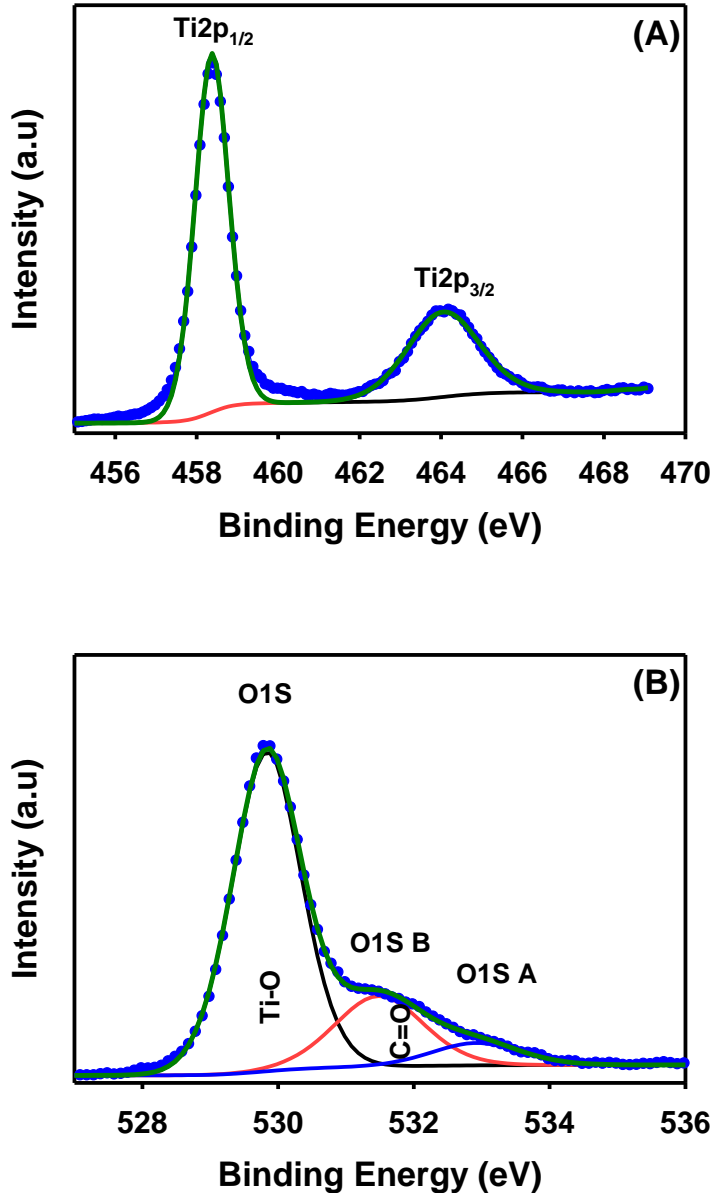
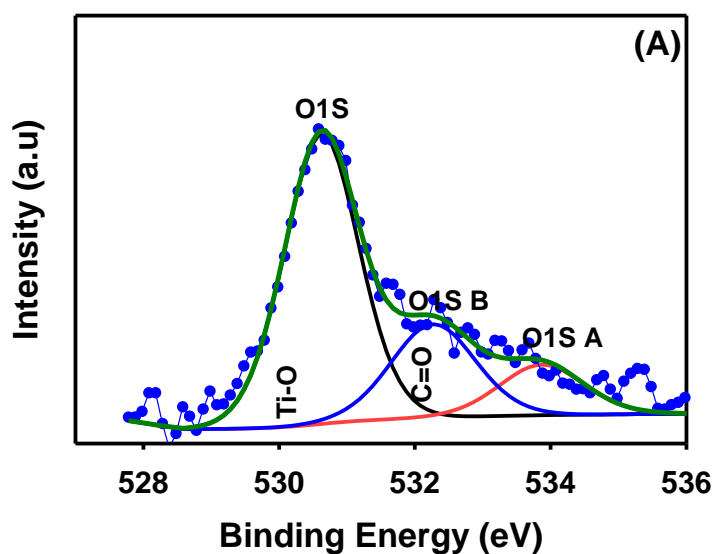


Figure 3.16: XPS analysis Ti (A) and $\text{O}1s$ (B) spectra of commercial TiO_2 (SA)

From the O1s results (Figure 3.17), the most important result is the shift (compared to the reference material values, TiO_2) that has occurred in both peaks. The first peak at 530.6 eV, regarding the lattice oxygen, is shifted by +1.0 eV (original value 529.6 eV) and the second peak that is at 532.7 eV, surface oxygen, has been shifted by +1.1 eV (original value at 531.5 eV). This shift again points to bonding oxygen to a non anatase element which in this case may be carbon. In addition, there are two titanium peaks in $\text{TiO}_2/\text{G-PV}$ at energies 459.4 eV and 465.1 eV for $\text{Ti}2\text{p}_{1/2}$ and $\text{Ti}2\text{p}_{3/2}$ respectively (Figure 3.18). When comparing those peaks with the peaks of the reference material, both appear to be shifted. The $\text{Ti}2\text{p}_{1/2}$ is shifted by 1.0 eV and the $\text{Ti}2\text{p}_{3/2}$ is shifted by 1.1 eV. This means that the analysis of the XPS spectra for composite supports gives strong evidence for a bond between titania and carbon. Due to the absence of a characteristic peak for C–Ti the bond is interpreted as C–O–Ti.



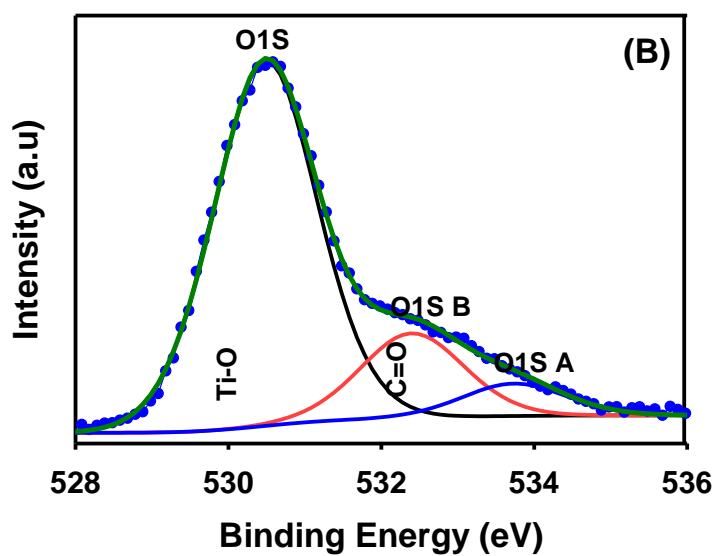
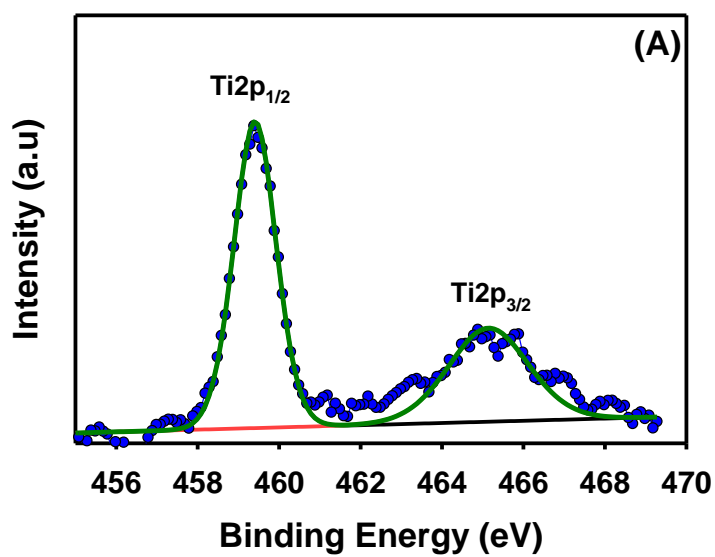


Figure 3.17: XPS analysis O1s spectra of TiO₂/ATV (A) and TiO₂/G-PV (B) composite supports.



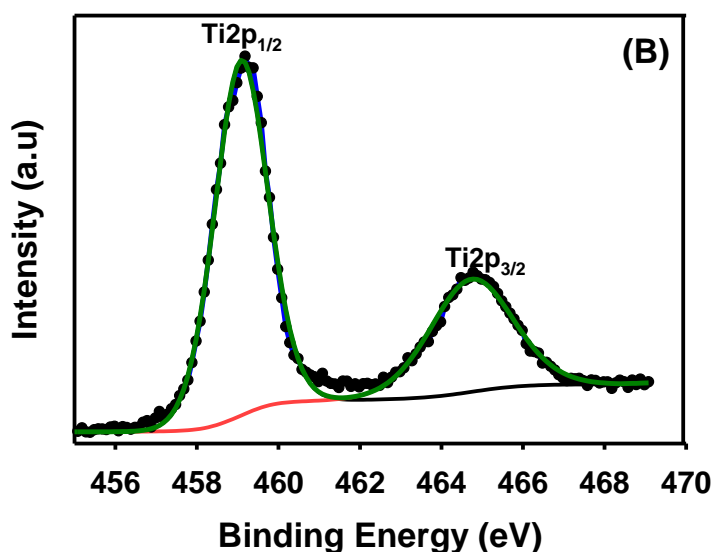


Figure 3.18: XPS analysis Ti spectra of TiO₂/ATV (A) and TiO₂/G-PV (B) composite supports

Table 3.5 summarises XPS data of C1s, O1s and Ti peaks of the reference material and composite supports. The Ti 2p peaks of TiO₂/G-PV support appear to be shifted slightly toward higher binding energy in comparison with TiO₂/ATV nanostructure; this may suggest a potential interaction between TiO₂ and carbon substrate [66]. Further analysis of the O1s spectra shows a main peak with a binding energy of 530.2 eV is attributed to the Ti-O bond of the TiO₂ crystal structure, and the positive peak at 531.6 eV is attributed to the C-O bond, which acts as the binding bond between the TiO₂ and carbon material. Furthermore, the XPS spectra and fitting curves of Ti 2p, C 1s, and O 1s suggest that the Ti-O-C bond is present, which might have formed from the perfect contact between the TiO₂ and carbon backbone [67].

Table 3.5: Summary of XPS analysis of C1s, O1s and Ti peaks of the reference material and composite supports

Peak	TiO ₂ Anatase Reference Peak (eV)	TiO ₂ /ATV Peak (eV)	Peak shift (eV)	TiO ₂ /G-PV Peak (eV)	Peak shift (eV)
C1s Graphite	-	284.5	0.0	284.5	0.0
C1s C-O,C=O	-	286.3	0.4	286.9	1.0
C1s C-O-Ti	-	-	-	288.8	-
O1s A	531.5	532.2	0.7	532.5	1.0
O1s B	529.8	530.5	0.7	530.5	0.7
Ti2p _{1/2}	458.4	459.3	0.9	459.1	0.7
Ti2p _{3/2}	464.1	465.2	1.1	464.8	0.6

3.5 Electrochemical activity

The CVs in 0.5 M H₂SO₄ solution of PV and modified carbon are shown in Figure 3.19. ATV and G-PV supports display the typical set of redox peaks at ~0.55 – 0.60 V, attributed to the quinone/hydroquinone (Q/HQ) surface redox reaction [68-69] while these peaks are essentially non-existent at PV (Figure 3.19A), consistent with the literature [69-70]. These reversible redox peaks are more pronounced on the ATV sample indicating the extent of oxidative treatment. The hydrogen reduction peak cannot be observed in this CV.

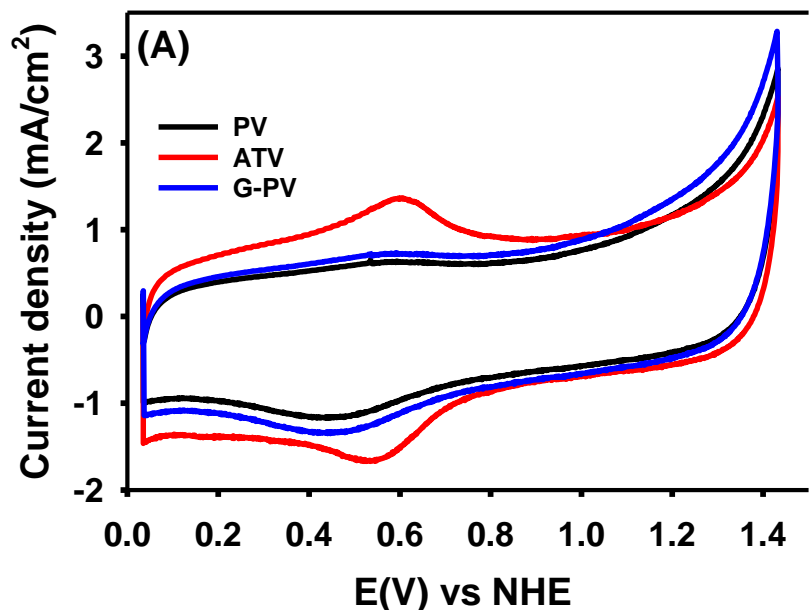


Figure 3.19: Cyclic voltammetry of carbon supports carried out in N₂-saturated 0.5M H₂SO₄ at 25 °C a scan rate of 50mV/s.

TiO₂ NPs were added to the modified carbon supports, to produce TiO₂/ATV and TiO₂/G-PV composite inks. Pure TiO₂ based electrode material shows extremely low current with respect to the composite supports due to the high resistivity of this metal oxide. In the case of the composite supports, TiO₂/GPV and TiO₂/ATV, reduction and oxidation currents were observed in the potential windows of 0.3 V to 1.2 V (Figure 3.20), similar to the behaviour seen in the case of Vulcan XC-72R (PV). Moreover, there is a significant reduction in the pseudo capacitance contribution in the TiO₂/ATV in comparison to the base support, ATV.

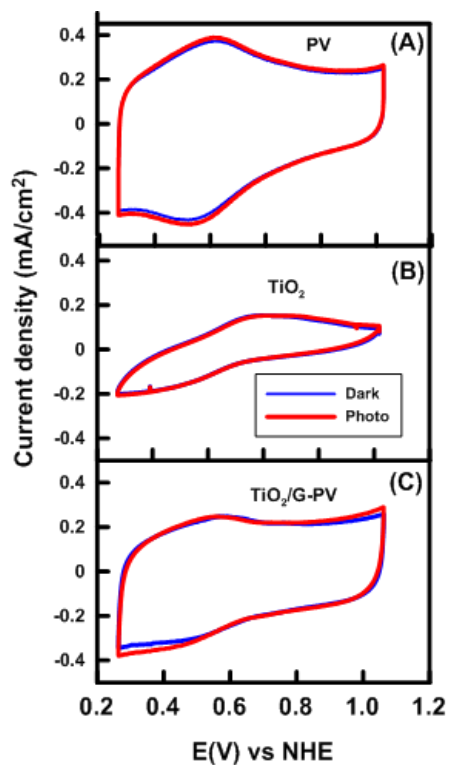


Figure 3.20: Cyclic voltammetry of unplatized supports: (A) PV, (B) TiO_2 and (C) $\text{TiO}_2/\text{G-PV}$ carried out in nitrogen saturated 0.5 M H_2SO_4 at 25 °C and 50 mV/s scan rate. Currents normalized by the GC electrode geometrical area = 0.196 cm^2 .

Figure 3.21 shows a gradual decrease in the CV current as the TiO_2 content is increased from 8wt% to 32wt% on G-PV substrate. This is reasonable as more TiO_2 will increase the resistance of the electrode material.

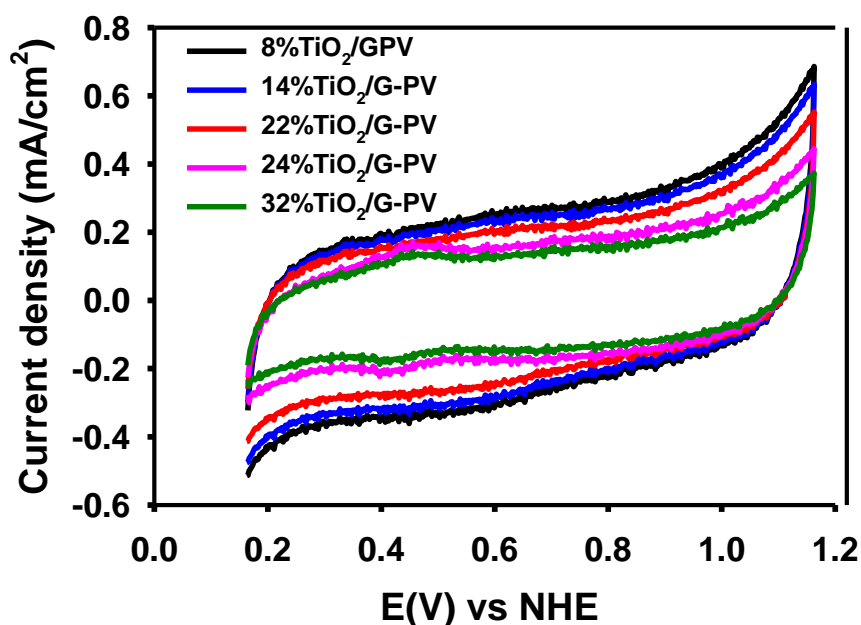


Figure 3.21: Cyclic voltammetry of carbon $\text{TiO}_2/\text{G-PV}$ supports with varied TiO_2 content carried out in N_2 -saturated 0.5M H_2SO_4 at 25 °C a scan rate of 50mV/s

The electrochemical stability of PV and $\text{TiO}_2/\text{G-PV}$ electrodes was investigated by repeated potential cycling up to upper potential limit of 1.4 V in 0.5M H_2SO_4 electrolyte solution as shown in Figure 3.22. The peak current comes from the surface oxide formation due to the hydroquinone–quinone redox couple on the support surface. This peak is expected to become stronger under the aging condition with a general increase in capacitive current for less stable support material. Increasing oxidation and capacitive currents on PV suggest a higher degree of surface carbon oxidation with time. The contribution to oxidative current involves various oxidising groups on the surface of carbon as earlier identified through XPS analysis and confirmed in separate studies by Jarvi and co-workers through thermal gravimetric analysis with a mass spectrometry [71]. In contrast, the peak current is barely visible in the case of $\text{TiO}_2/\text{G-PV}$ electrode with negligible change over the 4000 potential cycles. The capacitive current does not much change with time either. Both facts suggest that $\text{TiO}_2/\text{G-PV}$ surface is more difficult to oxidize than PV. This

suggests that a relatively conductive $\text{TiO}_2/\text{G-PV}$ support can potentially be more corrosion resistant and durable when used in a fuel cell.

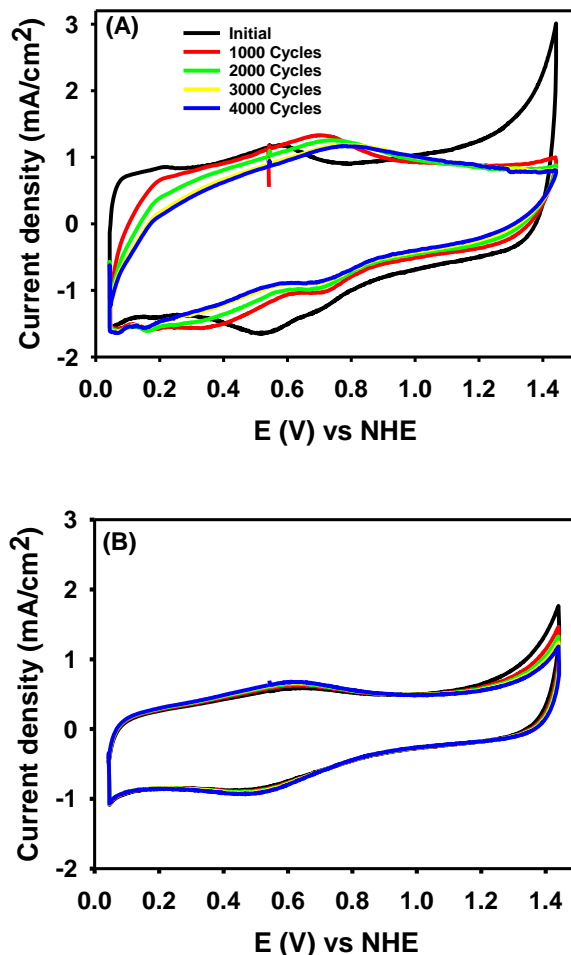


Figure 3.22: CVs of pristine Vulcan (PV) and $\text{TiO}_2/\text{G-PV}$ (B) supports under aging conditions in N_2 -saturated acidic solution at a scan rate of 50 mV/s., temperature: 25 °C

Electrochemical impedance spectroscopy (EIS) measurement at 0.60V vs. NHE was taking at interval under the potential cycling conditions as shown in Figures (3.23-3.25). The high resistivity of the TiO_2 electrode is clearly seen from the Nyquist plots (Figure 3.23a). The Nyquist plot also shows that the electrode becomes more resistive with TiO_2 inclusion however with a gain in stability. The capacitance plots confirm CV results under the potential cycling with higher limiting capacitance for the PV support. There is

negligible change in the TiO_2 and $\text{TiO}_2/\text{G-PV}$ electrodes with time compares with the subtle change on the PV electrode support.

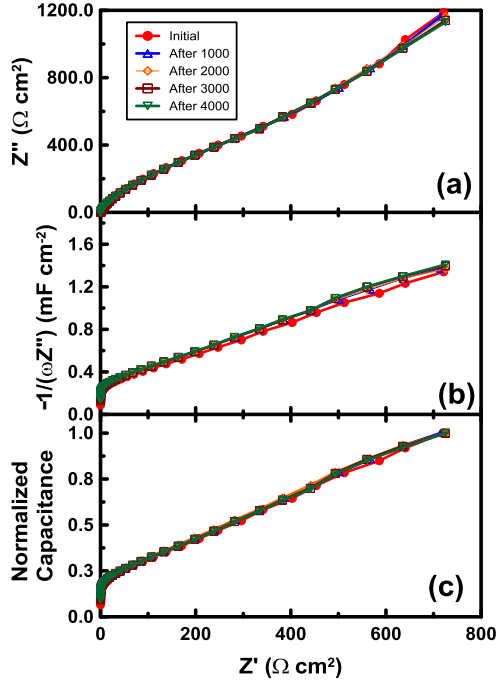


Figure 3.23: Electrochemical impedance spectroscopy (EIS) plots of TiO_2 electrode at 0.60V showing Nyquist plot (a), capacitance plot(b) and normalised capacitance plot (c) in nitrogen saturated 0.5M H_2SO_4 solution scan rate of 50 mV/s, test temperature: 25 °C

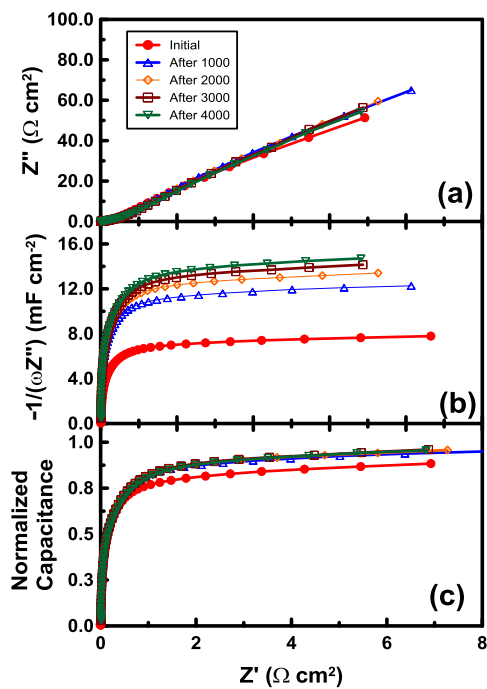


Figure 3.24: Electrochemical impedance spectroscopy (EIS) plots of PV support at 0.60V showing Nyquist plot (a), capacitance plot (b) and normalised capacitance plot (c) in nitrogen saturated 0.5M H_2SO_4 solution scan rate of 50 mV/s, test temperature: 25 °C

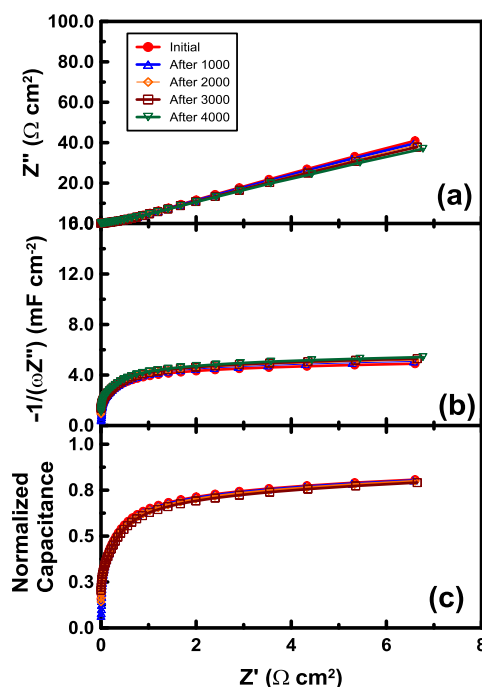


Figure 3.25: Electrochemical impedance spectroscopy (EIS) plots of $\text{TiO}_2/\text{G-PV}$ electrode at 0.60V showing Nyquist plot (a), capacitance plot(b) and normalised capacitance plot (c) in nitrogen saturated 0.5M H_2SO_4 solution scan rate of 50 mV/s, test temperature: 25 °C

3.6 Sol-gel derived TiO_2/C composite supports

TiO_2/C composites have been produced using a new experimental approach that brings more control on the deposition process and maximise the interaction between the metal oxide precursor and the carbon substrate. The sol-gel method was utilized in this work because it allows for the most flexibility with respect to many of the reaction parameters. The mechanism of reaction involves the reaction of titanium isopropoxide with water and hydroxyl groups at the surface of the glucose/carbon interface in isopropanol. Concurrent and competing polymerization reaction takes place following this hydrolysis process [72-73]. The solid inorganic network of titanium formed during the polymerization reaction proceeds as far as the hydrolysis conditions allow or the precursor is consumed. The hydrolysis reaction conditions dictate the relative concentrations of the terminating bonds (OH) of the polymerization reaction by altering the reaction kinetics, thus ultimately controlling particle size and morphology. In the case of ATV, the nucleation and growth

of amorphous TiO_2 nanoparticles take place at the oxygen functional group sites, resulting in a poor control of the overall deposition process.

In summary, this thesis [shows](#) that the heterogeneous nucleation and growth of TiO_2 on carbon black can be preferentially achieved without the need for strong acid treatment. During thermal annealing treatment of the amorphous composites in inert medium, the glucose pyrolysis products can also contribute to the strong coupling effects between components when the amorphous TiO_2 nanoparticles undergo a localized crystallization on G-PV substrate with minimal aggregation and migration. Based on TEM and electrochemical results, the $\text{TiO}_2/\text{G-PV}$ composite obtained using glucose as carbon modifier is close to the desired core-shell material where small TiO_2 nanoparticles are uniformly distributed on the surface of carbon aggregates.

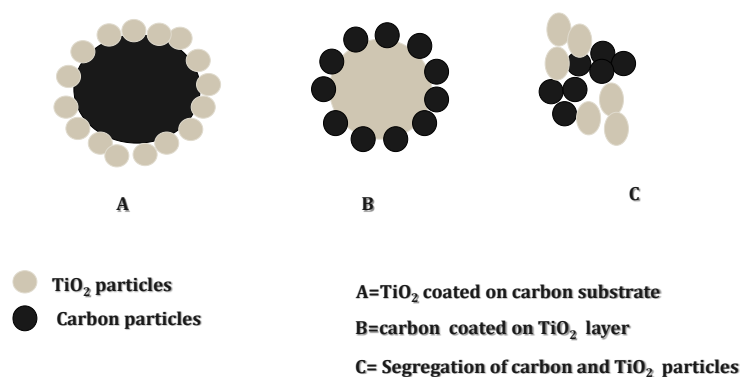


Figure 3.26: Possible configurations of carbon and TiO_2 particles in the synthesized TiO_2/C composite supports

3.7 Conclusions

In the present work two different composites based on Vulcan carbon substrate were synthesized, characterized and electrochemical activity reported. FTIR spectroscopy show that surface functional groups were successfully used as anchoring points during the sol-gel process. TGA was used for semi quantitative analysis and thermal stability of the

modified support materials. The composite supports become thermal unstable in air as a result of the enhanced catalytic activity of the TiO_2 NPs under this thermal oxidative condition.

The materials prepared through glucose pre-adsorption on carbon present higher BET surface areas compared with TiO_2/ATV composites counterpart for the same TiO_2 loading. This higher surface area is an important contribution to catalytic application. Lower surface areas are observed on the composite supports as a result of highly dense TiO_2 particles on the carbon surface as well as the heat treatment effect on the support material.

Microscopy analysis shows little effect on Vulcan carbon following surface treatment, however, $\text{TiO}_2/\text{G-PV}$ composite shows a more relative uniform distribution of $\sim 5\text{-}10$ nm TiO_2 NPs on carbon compared to the more aggregate particles observed on TiO_2/ATV composite support. Thus we conclude the superior of surface glucose hydroxyl functional groups in controlling nucleation growth of TiO_2 NPs during sol-gel synthesis.

Raman spectroscopy and XPS were used to analyze molecular differences in the nanocomposites. Raman spectra show distinct carbon and TiO_2 peaks thus, the sol-gel synthesis method was successful in this study. The XPS analysis of the TiO_2/ATV and $\text{TiO}_2/\text{G-PV}$ confirms both are nanocomposites and consist of carbon material with TiO_2 particles. The shifts in XPS can be assigned to the bond of titanium via an oxygen bridge with a carbon on the modified substrate. In addition to the shift, a new peak that is not explained reasonably from the databases appears at approximately 288.7 eV. It is feasible to attribute this peak to the C–O–Ti bond. Therefore, we conclude that the TiO_2 coating is chemically bonded to the carbon material. The titanium peaks of these composites show displacement compared to the reference material.

These composites prepared through different routes displayed drastically different electrochemical performance. These composites outperformed the benchmark Vulcan carbon following long term durability study. These results look promising as these materials can be used to deposit metal nanoparticles for catalytic applications.

3.8 References

- 1) Sellappan, R., Zhu, J., Fredriksson, H., Martins, R. S., Zäch, M., and Chakarov, D. (2011). *Journal of Molecular Catalysis A: Chemical*, 335(1), 136-144.
- 2) Yuan, J., Zhou, S., Wu, L., and You, B. (2006) *The Journal of Physical Chemistry B*, 110(1), 388-394.
- 3) Song, X., and Gao, L. (2007). *Journal of the American Ceramic Society*, 90(12), 4015-4019.
- 4) Almquist, C. B., and Biswas, P. (2002). *Journal of Catalysis*, 212(2), 145-156.
- 5) Reddy, B. M., Ganesh, I., & Khan, A. (2004). *Journal of Molecular Catalysis A: Chemical*, 223(1), 295-304.
- 6) Retuert, J., Quijada, R., and Arias, V. (1998). *Chemistry of materials*, 10(12), 3923-3927.
- 7) Tan, T., Wang, S., Bian, S., Li, X. and Liu, Z. (2010). *Applied Surface Science*, 256(22), 6932-6935.
- 8) Tian, L., Ye, L., Deng, K., and Zan, L. (2011). *Journal of Solid State Chemistry*, 184(6), 1465-1471.
- 9) Sun, J., Gao, L., and Iwasa, M. (2004). *Chemical communications*, (7), 832-833.
- 10) Yan, X. B., Tay, B. K., and Yang, Y. (2006). *The Journal of Physical Chemistry B*, 110(51), 25844-25849.
- 11) Huang, Q., and Gao, L. (2003). *Journal of Materials Chemistry*, 13(7), 1517-1519.
- 12) Huang, H. C., Huang, G. L., Chen, H. L., and Lee, Y. D. (2006). *Thin Solid Films*, 511, 203-207.
- 13) Sun, J., Gao, L., and Iwasa, M. (2004). *Chemical communications*, (7), 832-833.
- 14) Sakai, H., Kanda, T., Shibata, H., Ohkubo, T., and Abe, M. (2006). *Journal of the American Chemical Society*, 128(15), 4944-4945.
- 15) Wang, P., Chen, D., and Tang, F. Q. (2006). *Langmuir*, 22(10), 4832-4835.
- 16) Woan, K., Pyrgiotakis, G., and Sigmund, W. (2009). *Advanced Materials*, 21(21), 2233-2239.

- 17) Kolen'ko, Y. V., Kovnir, K. A., Gavrilov, A. I., Garshev, A. V., Meskin, P. E., Churagulov, B. R., and Yoshimura, M. (2005). *The Journal of Physical Chemistry B*, 109(43), 20303-20309.
- 18) El-Sheikh, A. H., Newman, A. P., Al-Daffae, H., Phull, S., Cresswell, N., and York, S. (2004). *Surface and Coatings Technology*, 187(2), 284-292.
- 19) Antolini, E. (2009). *Applied Catalysis B: Environmental*, 88(1), 1-24.
- 20) Carmo, M.; dos Santos, A.R.; Rocha, J.G.; and Linardi, M. (2007). *Journal of Power Sources*, 173, 860–866.
- 21) Kumar, S. S., Herrero, J. S., Irusta, S., and Scott, K. (2010). *Journal of Electroanalytical Chemistry*, 647(2), 211-221.
- 22) Alcaide, F., Álvarez, G., Cabot, P. L., Grande, H. J., Miguel, O., and Querejeta, A. (2011). *International Journal of Hydrogen Energy*, 36(7), 4432-4439.
- 23) Zhou, Y., Pasquarelli, R., Holme, T., Berry, J., Ginley, D., & O'Hayre, R. (2009). *Journal of Materials Chemistry*, 19(42), 7830-7838.
- 24) Lee, K., Zhang, J., Wang, H., and Wilkinson, D. P. (2006). *Journal of Applied Electrochemistry*, 36(5), 507-522.
- 25) Li, W., Liang, C., Zhou, W., Qiu, J., Zhou, Z., Sun, G., and Xin, Q. (2003). *The Journal of Physical Chemistry B*, 107(26), 6292-6299.
- 26) Plomp, A. J., Su, D. S., Jong, K. D., and Bitter, J. H. (2009). *The Journal of Physical Chemistry C*, 113(22), 9865-9869.
- 27) Kumar, S. S., Hidyatai, N., Herrero, J. S., Irusta, S., and Scott, K. (2011). *International Journal of Hydrogen Energy*, 36(9), 5453-5465.
- 28) Klein, K. L., Melechko, A. V., McKnight, T. E., Retterer, S. T., Rack, P. D., Fowlkes, J. D., and Simpson, M. L. (2008). *Journal of Applied Physics*, 103(6), 3.
- 29) Banerjee, S., Hemraj-Benny, T., and Wong, S. S. (2005). *Advanced Materials*, 17(1), 17-29.
- 30) Han, K. I., Lee, J. S., Park, S. O., Lee, S. W., Park, Y. W., and Kim, H. (2004). *Electrochimica acta*, 50(2), 791-794.
- 31) Sebastián, D., Suelves, I., Moliner, R., and Lázaro, M. J. (2010). *Carbon*, 48(15), 4421-4431.

- 32) Salzmann, C. G., Llewellyn, S. A., Tobias, G., Ward, M. A., Huh, Y., and Green, M. L. (2007). *Advanced Materials*, 19(6), 883-887.
- 33) Boehm, H. P. (1994). *Carbon*, 32(5), 759-769.
- 34) Parthasarathy, R., Lin, X. M., and Jaeger, H. M. (2001). *Physical Review Letters*, 87(18), 186807.
- 35) Kinoshita K (1988) *Carbon: Electrochemical and Physicochemical Properties* (New York: Wiley)
- 36) Kovtyukhova, N. I., Mallouk, T. E., Pan, L., and Dickey, E. C. (2003). *Journal of the American Chemical Society*, 125(32), 9761-9769.
- 37) Li, Y. H., Xu, C., Wei, B., Zhang, X., Zheng, M., Wu, D., and Ajayan, P. M. (2002). *Chemistry of materials*, 14(2), 483-485.
- 38) Serp, P., Corrias, M., and Kalck, P. (2003). *Applied Catalysis A: General*, 253(2), 337-358.
- 39) Chhina, H., Campbell, S., and Kesler, O. (2006). *Journal of Power Sources*, 161(2), 893-900.
- 40) Haydar, S., Moreno-Castilla, C., Ferro-Garcia, M. A., Carrasco-Marin, F., Rivera-Utrilla, J., Perrard, A., and Joly, J. P. (2000). *Carbon*, 38(9), 1297-1308.
- 41) Huang, S. Y., Ganesan, P., and Popov, B. N. (2011). *Applied Catalysis B: Environmental*, 102(1), 71-77.
- 42) Gao, Y., Wang, C., Pu, W., Liu, Z., Deng, C., Zhang, P., and Mao, Z. (2012). *International Journal of Hydrogen Energy*, 37(17), 12725-12730.
- 43) Chen, C. C., Chen, C. F., Chen, C. M., and Chuang, F. T. (2007). *Electrochemistry communications*, 9(1), 159-163.
- 44) Li, W., Deng, Y., Wu, Z., Qian, X., Yang, J., Wang, Y., and Zhao, D. (2011). *Journal of the American Chemical Society*, 133(40), 15830-15833.
- 45) Li, X., Niu, J., Zhang, J., Li, H., and Liu, Z. (2003). *The Journal of Physical Chemistry B*, 107(11), 2453-2458.
- 46) Guo, X., Guo, D. J., Qiu, X. P., Chen, L. Q., and Zhu, W. T. (2009). *Journal of Power Sources*, 194(1), 281-285.
- 47) Lee, S. W., and Sigmund, W. M. (2003). *Chemical Communications*, (6), 780-781.

- 48) Wang, W., Serp, P., Kalck, P., Silva, C. G., and Faria, J. L. (2008). *Materials Research Bulletin*, 43(4), 958-967.
- 49) Wan, C., and Li, J. (2015). *Materials and Design*, 83, 620-625.
- 50) Hanaor, D. A., and Sorrell, C. C. (2011). *Journal of Materials science*, 46(4), 855-874.
- 51) Shirke, B. S., Korake, P. V., Hankare, P. P., Bamane, S. R., and Garadkar, K. M. (2011). *Journal of Materials Science: Materials in Electronics*, 22(7), 821-824.
- 52) Antić, Ž., Krsmanović, R. M., Nikolić, M. G., Marinović-Cincović, M., Mitrić, M., Polizzi, S., and Dramićanin, M. D. (2012). *Materials Chemistry and Physics*, 135(2), 1064-1069.
- 53) Klug H, Alexander L, X-ray Diffraction Procedures, second ed., John Wiley & Sons, New York, 1962.
- 54) Zhang, L., and Koka, R. V. (1998). *Materials chemistry and physics*, 57(1), 23-32.
- 55) Ohsaka, T., Izumi, F., and Fujiki, Y. (1978). *Journal of Raman spectroscopy*, 7(6), 321-324.
- 56) Chen, C., Long, M., Zeng, H., Cai, W., Zhou, B., Zhang, J., and Wu, D. (2009). *Journal of Molecular Catalysis A: Chemical*, 314(1), 35-41.
- 57) Rosario-Castro, B. I., Contés, E. J., Lebrón-Colón, M., Meador, M. A., Sánchez-Pomales, G., and Cabrera, C. R. (2009). *Materials Characterization*, 60(12), 1442-1453.
- 58) Kundu, S., Wang, Y., Xia, W., and Muhler, M. (2008). *The Journal of Physical Chemistry C*, 112(43), 16869-16878.
- 59) Stankovich, S., Dikin, D. A., Piner, R. D., Kohlhaas, K. A., Kleinhammes, A., Jia, Y., and Ruoff, R. S. (2007). *Carbon*, 45(7), 1558-1565.
- 60) Yang, D., Velamakanni, A., Bozoklu, G., Park, S., Stoller, M., Piner, R. D., and Ruoff, R. S. (2009). *Carbon*, 47(1), 145-152.
- 61) Kónya, Z., Vesselenyi, I., Kiss, J., Farkas, A., Oszkó, A., and Kiricsi, I. (2004). *Applied Catalysis A: General*, 260(1), 55-61.
- 62) Point, S., Minea, T., Bouchet-Fabre, B., Granier, A., and Turban, G. (2005). *Diamond and related materials*, 14(3), 891-895.

- 63) Okpalugo, T. I. T., Papakonstantinou, P., Murphy, H., McLaughlin, J., and Brown, N. M. D. (2005). *Carbon*, 43(1), 153-161.
- 64) Roy, S. S., McCann, R., Papakonstantinou, P., Maguire, P., and McLaughlin, J. A. (2005). *Thin Solid Films*, 482(1), 145-150.
- 65) Wagner, C. D., Naumkin, A. V., Kraut-Vass, A., Allison, J. W., Powell, C. J., and Rumble Jr, J. R. (2003). NIST X-ray Photoelectron Spectroscopy Database, NIST Standard Reference Database 20, Version 3.4 (Web Version). *U. S. Department of Commerce*.
- 66) Zhang, L. W., Fu, H. B., and Zhu, Y. F. (2008). *Advanced Functional Materials*, 18(15), 2180-2189.
- 67) Cong, Y., Li, X., Qin, Y., Dong, Z., Yuan, G., Cui, Z., and Lai, X. (2011). *Applied Catalysis B: Environmental*, 107(1), 128-134.
- 68) Shao, Y., Yin, G., Zhang, J., and Gao, Y. (2006). *Electrochimica Acta*, 51(26), 5853-5857.
- 69) Shao, Y., Wang, J., Kou, R., Engelhard, M., Liu, J., Wang, Y., and Lin, Y. (2009). *Electrochimica Acta*, 54(11), 3109-3114.
- 70) Li, L., and Xing, Y. (2006). *Journal of the Electrochemical Society*, 153(10), A1823-A1828.
- 71) Kangasniemi, K. H., Condit, D. A., and Jarvi, T. D. (2004). *Journal of The Electrochemical Society*, 151(4), E125-E132.
- 72) Yoldas, B. E. (1986). *Journal of Materials Science*, 21(3), 1087-1092.
- 73) Li, W., and Zhao, D. (2013). *Advanced Materials*, 25(1), 142-149.

CHAPTER FOUR

Study of glucose doped acid treated composite catalyst and comparative analysis.

Part of the work described in this chapter has been published as:

Odetola, C., Trevani, L., and Easton, E. B. (2015). Enhanced activity and stability of Pt/TiO₂/carbon fuel cell electrocatalyst prepared using a glucose modifier. *Journal of Power Sources*, 294, 254-263.

<http://dx.doi.org/10.1016/j.jpowsour.2015.06.066>

In last chapter, I have synthesized glucose-doped pristine Vulcan[®] TiO₂/G-PV composite supports for electrochemical application. However, it is not clear how acid treatment influences the adsorption of glucose on carbon, and more importantly, its impact on the long-term stability of the carbon support. Therefore, in this study the deposition of TiO₂ was carried out on glucose-doped acid treated Vulcan[®] XC-72R carbon (G-ATV), followed by post-deposition heat treatment at 500 °C under nitrogen to induce the pyrolysis of glucose and promote TiO₂ crystallization and the deposition of Pt NPs.

4.1 Introduction

Polymer electrolyte fuel cells (PEMFCs) offer efficient and emission-free energy conversion for alternative and sustainable energy systems. The technology looks promising in terms of meeting the increasing energy demand due to its high theoretical energy conversion efficiency, and as a result of that, the last decade has witnessed significant activity in fuel cell electrocatalyst research [1]. However for automotive application, this technology is not currently cost competitive with the internal combustion engine due to the use of high loadings of noble metal catalysts (i.e. Pt), as well as material degradation/durability issues. The kinetically sluggish oxygen reduction reaction (ORR) at the cathode, instability of the Pt catalyst, and the vulnerability of carbon supports to corrosion are obstacles for widespread fuel cell commercialization [2-5].

Carbon black is a popular catalyst support due to its good electronic conductivity, high surface area and chemical stability. However it is susceptible to electrochemical oxidation, particularly under highly acidic and highly high humid conditions [6-9]. Under these corrosive conditions, surface oxides are formed on carbon with subsequent oxidation to CO₂ [10-11]. Attempts to minimise degradation often involve modification of the existing catalyst support or replacement with an alternative support material. However, this poses a significant challenge since very few materials exhibit the combination of high electronic conductivity and high surface area with comparable chemical inertness [12].

Carbon materials with a higher graphitic character, such as carbon nanofibers, carbon nanotubes, carbon nanocages, and graphene present a greater corrosion resistance, with a several fold lower intrinsic corrosion rate [13-15]. However, these are expensive and their inert surfaces present a challenge for catalyst dispersion unless oxidative treatments are performed to introduce defects, which can compromise corrosion resistance [16-18]. As a result, new materials that are less susceptible to carbon corrosion and electrochemical oxidation are still required.

The dispersion of noble metal nanoparticles on metal oxide supports has been shown to enhance their catalytic behaviour and corrosion stability in acidic environments [19-20]. This is widely associated with intrinsic attraction between the metal particles and metal oxide support often refer to as strong metal support interaction (SMSI) effect. This mutual interaction between metal nanoparticles and metal oxide support can change the

chemical environment of the metal particles, thus altering the electronic property and improving stability [21].

While there has been a plethora of studies on metal oxides catalyst supports, titanium oxide is perhaps the most attractive due to their corrosion stability, low cost, commercial availability, and the ease to control size and structure [22-23]. The choice of TiO_2 as a catalyst support is shown to enhance base catalytic activity through structural arrangement at the molecular level [24], facilitates the dispersion of platinum nanoparticles [25], and as well as photo-enhancement of anodic fuel cell reactions [26-27]. Dispersion of Pt nanoparticles on TiO_2 support is easier due to its hydrophilic nature. Moreover, the electrochemically active surface area (ECSA) of Pt catalyst has also been reported to show a significant increase with the addition of TiO_2 due to mutual interaction between Pt and TiO_2 [28].

However, despite the higher durability of TiO_2 based catalysts in relation to conventional carbon supports, its low electronic conductivity limits performance in fuel cell [29]. This is partially solved by reduction of TiO_2 to sub-stoichiometric forms at high temperatures and doping with appropriate metal cations [30-31], but such treatments often lead to decreasing support surface area for catalyst dispersion and a systematic screening of potential semiconductor materials for electrochemical catalysis is still lacking [32].

Ideally the deposition of TiO_2 on carbon would result in a new class of hybrid support material that blends the excellent electrical conductivity and mesoporous structure of carbon black with the corrosion resistance of TiO_2 . However, most of the studies in the literature where this kind of structure have been obtained involved single and multiwall carbon nanotubes, graphene and carbon fibers [33-35]. In addition, controlling the thickness of TiO_2 on mesoporous carbon and preventing phase segregation continues to be a synthetic challenge [36-37].

To overcome the aforementioned issues, we have used glucose, a hydrophilic molecule with multiple hydroxyl groups as a structure-directing agent to control the growth of small and uniform TiO_2 nanoparticles on the surface of acid treated Vulcan carbon. It is worth noting the method has been used to produce hollow TiO_2 nanoparticles for photovoltaics applications and TiO_2 -carbon nanotubes without acid treatment functionalization for lithium-ion battery anodes [38]. However, to the best of our

knowledge, this is the first time that this kind of material has been studied as Pt support for fuel cell application.

As a result, the deposition of TiO_2 was carried out on glucose-doped acid treated Vulcan[®] XC-72R carbon (G-ATV), followed by the deposition of TiO_2 and a post-deposition heat treatment at 500 °C under nitrogen to induce the pyrolysis of glucose and promote TiO_2 crystallization. For comparison, three different groups of catalyst materials were prepared and characterized : (i) Platinum was deposited on various support materials (i) Acid treated Vulcan[®] XC-72R (Pt/ATV), (ii) TiO_2 /acid treated Vulcan[®] XC-72R composite (Pt/5wt% TiO_2 /ATV), (iii) TiO_2 / acid treated Vulcan[®] XC-72R glucose doped composite (Pt/14% TiO_2 /G-ATV). The catalytic activity of Pt on these systems was studied using standard electrochemical methods in 0.5 M H_2SO_4 at room temperature using a three-electrode cell.

4.2 Experimental

4.2.1 Synthesis of Composite Catalysts

To dope glucose on carbon surface, ATV was mixed with 15 wt% glucose in an ethanol/water solution (80 wt% ethanol) and placed in an ultrasonic bath for 120 minutes at room temperature. The carbon/glucose product was filtered and washed with the same ethanol/water solution to remove any excess glucose. The solids were dried in a vacuum oven overnight at 60 °C. This is here- after referred to as glucose doped ATV (G-ATV). This was followed by the deposition of TiO_2 by sol gel synthesis. The as prepared TiO_2 /C composites were heat treated in inert medium prior to deposition of Pt NPs. Figure 4.1 outlines the synthetic routes for the two composite catalysts tested in this work and the details were described in chapter 2 of this thesis.

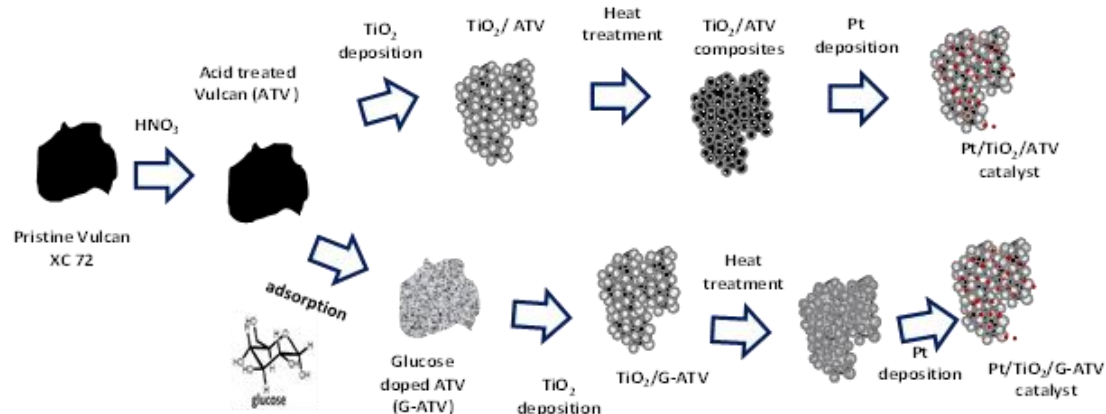


Figure 4.1: Synthesis of Pt/TiO₂/G-ATV catalyst

4.2.2 Materials Characterization

Thermogravimetric analysis was used for compositional analysis of the composite catalysts. These studies were performed with an SDT Q600 Thermal Gravimetric Analyzer from TA Instruments. Samples were heated in alumina pans from room temperature to 1000 °C at a heating rate of 20 °C min⁻¹ under an atmosphere of either flowing air or Argon (50 mL min⁻¹). Mass and temperature calibrations were conducted periodically, to ensure a reliable comparison between samples.

A confocal Renishaw Raman Imaging Microscope System 2000 was used as the primary characterization screening tool during the optimization of the synthesis procedures. Spectra were collected in the range 2000-100 cm⁻¹ with a 514 nm argon ion laser with a 25 mW output power. Repeated acquisitions (40 scans) with an acquisition time of 10 s at a 50x magnification, were accumulated to improve the signal-to-noise ratio. The spectrum was collected for no less than 3 sample locations to ensure uniformity.

XRD experiments were performed with a Rigaku Ultima IV X-ray diffractometer equipped with graphite monochromator, k-β filter and a Cu Kα 0.154 nm X-ray source. Samples were scanned from 10 to 85 with a step size of 0.02°.

X-ray photoelectron spectroscopy measurements to determine the surface properties of the catalysts were performed with a ThermoFisher Scientific K-Alpha (1486.65 eV) system. Charge compensation applied with combined e/Ar flood-gun. The energy range was shifted so that the main C1s peak appeared at 284.6 eV. Powdered samples were spread onto double-sided adhesive C tape, using enough powder to

completely cover the tape. Data work-up was performed with software provided with the instrument (Advantage 5.926).

Brunauer, Emmett and Teller (BET) surface area of modified supports was examined via nitrogen adsorption measurements using a Quantachrome NOVA 1200e BET analyzer. For this determination, ~ 100 mg of sample was degassed under nitrogen flow at 300 °C for a minimum of 2 h prior to adsorption measurements.

The transmission electron microscope (TEM) characterization was carried out using either a JEOL JEM-2010 200kV high resolution TEM LaB6 filament or a Philips CM 10 instrument equipped with an AMT digital camera system. Particle size distribution was performed using Image J software.

4.2.3 Electrochemical Characterization

Electrochemical measurements were performed on thin film catalyst layers deposited from an ink onto glassy carbon electrode (0.196cm²). The inks were prepared by dispersing ca. 10 mg of catalyst in 500 µL of a solution containing Nafion[®], water and isopropyl alcohol. 5 µL of the ink was deposited onto the glassy carbon disk electrode using a microsyringe. The deposited ink was allowed to dry in air for 20 minutes before electrochemical measurements were performed. A Pt loading of 0.1 ± 0.01 mg cm⁻². This loading was chosen as optimal since it closely mimics the ionic and electronic resistances seen in real-world fuel cell catalyst layers [40], yet is sufficiently thin so that mass transport of reactants is not hindered. Cyclic voltammetry (CV) measurements for cleaning were performed in a potential range between 0.04 to 1.5 V at a scan rate of 100 mV/s for 20 cycles until a steady state CV was achieved.

All electrochemical measurements were performed at 25 °C using a Solartron 1470 potentiostat in combination with a Solartron 1260 impedance analyser controlled using Multistat 1.1d software (Scribner Associates Inc.) for electrochemical impedance spectroscopy (EIS) experiment. The electrocatalyst degradation was investigated by repeated potential cycling from 0.04 to 1.4 V at a scan rate of 50 mV s⁻¹ in a deaerated 0.5M H₂SO₄. This procedure was developed by one of the authors and it is described elsewhere [41], to evaluate the stability of the synthesized catalysts. This involves accelerated aging by potential cycling from 0.04 - 1.5 V in an argon saturated electrolyte

solution and continuous assessment of the catalysts performance with time using CV and EIS. All EIS measurements were made over a frequency range of 100 kHz to 0.1 Hz at a DC bias potential of 0.45 V vs. NHE. The uncompensated resistance was subtracted from all impedance spectra. EIS data was interpreted via the transmission line model for fuel cell catalyst layers [40].

4.3 Results and Discussion

4.3.1 Materials Characterization

The TiO₂ and Pt contents in each catalyst were determined using TGA in air. This method has been previously employed for Pt-carbon-SiO₂ composite layers [42] and results in the combustion of all carbon. Figure 4.2 shows mass losses for ATV, G-ATV, TiO₂/G-ATV and Pt/TiO₂/ G-ATV under air. Glucose doped carbon shows two major two mass losses: a small one starting at 200 °C and the major one at around 470 °C. These TGA thermal analyses data on glucose doped carbon substrate is rationalised by the assumption that at least two residual materials are present and thermally decompose in air within these temperature range. This first mass loss is mostly due to the oxidation of glucose OH functional groups on modified carbon support

TiO₂/G-ATV composite support after heat treatment at 500 °C in nitrogen for 2 hours also show two major mass losses. The mass loss at ca. 200 °C is attributed to the presence of carbon derived from glucose, formed during the 500 °C annealing step and subsequent thermal oxidation of ATV. The residual mass at temperatures over 600 °C is attributed solely to TiO₂ and corresponds to the wt% TiO₂ in the sample. Knowing the ratio of TiO₂ to carbon for each support enables the determination of the wt% Pt in each sample from TGA under air. Table 4.1 summarizes the composition of the samples used in the electrochemical studies.

Table 4.1: Physical Properties of TiO₂/ C and Pt Catalysts.

Samples	TiO ₂ (wt %)	Pt (TGA) (wt %)	BET surface area (m ² g ⁻¹)	Pt particle size (nm) TEM	Pt particle size (nm) (XRD)
ATV	–	–	251	–	–
Pt/ ATV	0.0	24.5	–	4.4	4.1
Pt/TiO ₂ /G- ATV	14	13.8	185	4.0	3.7
Pt/TiO ₂ /	5.0	21.2	236	4.4	3.9
ATV					

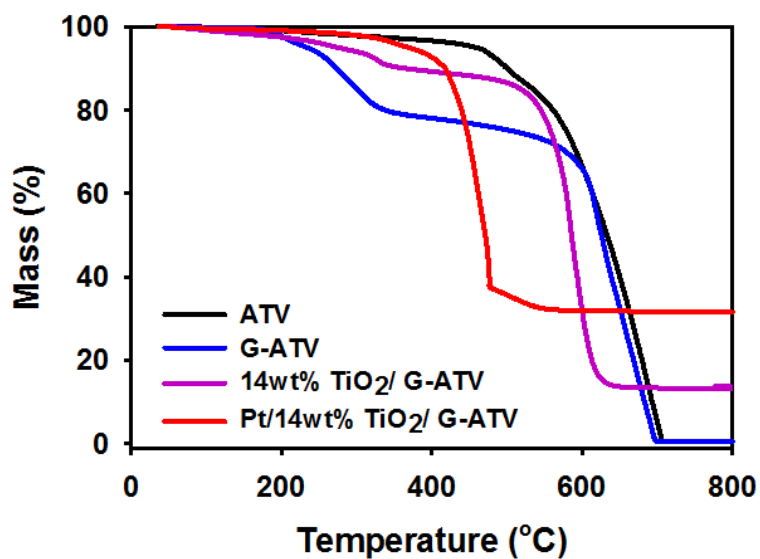


Figure 4.2: Thermogravimetric analysis under air for compositional analysis: ATV, G-ATV, Pt/ 14 wt% TiO₂/ G-ATV and Pt/ 14 wt% TiO₂/ G-ATV catalyst. Experimental conditions: average sample mass: 10 mg, gas flow rate: 50 ml/min, and heating rate 20 °C/min.

Figure 4.3 shows the TEM analysis of two composite supports in this study, 14 TiO₂/G-ATV (a-b) and 5 % TiO₂/ATV. One can see overlapping particles in the images for glucose doped sample with only a minimal number of particles that are aggregated. The relatively uniform distribution and well defined spherical shapes of TiO₂ particles can be inferred on the glucose modified porous carbon substrate. Based on Fig 4.3(b), the TiO₂ NPa on this glucose modified carbon were less than 10 nm which are significantly small and form appreciable uniform growth. In contrast, it is difficult to see TiO₂ particles on ATV and those observed appear not distinct with non-uniform dispersion.

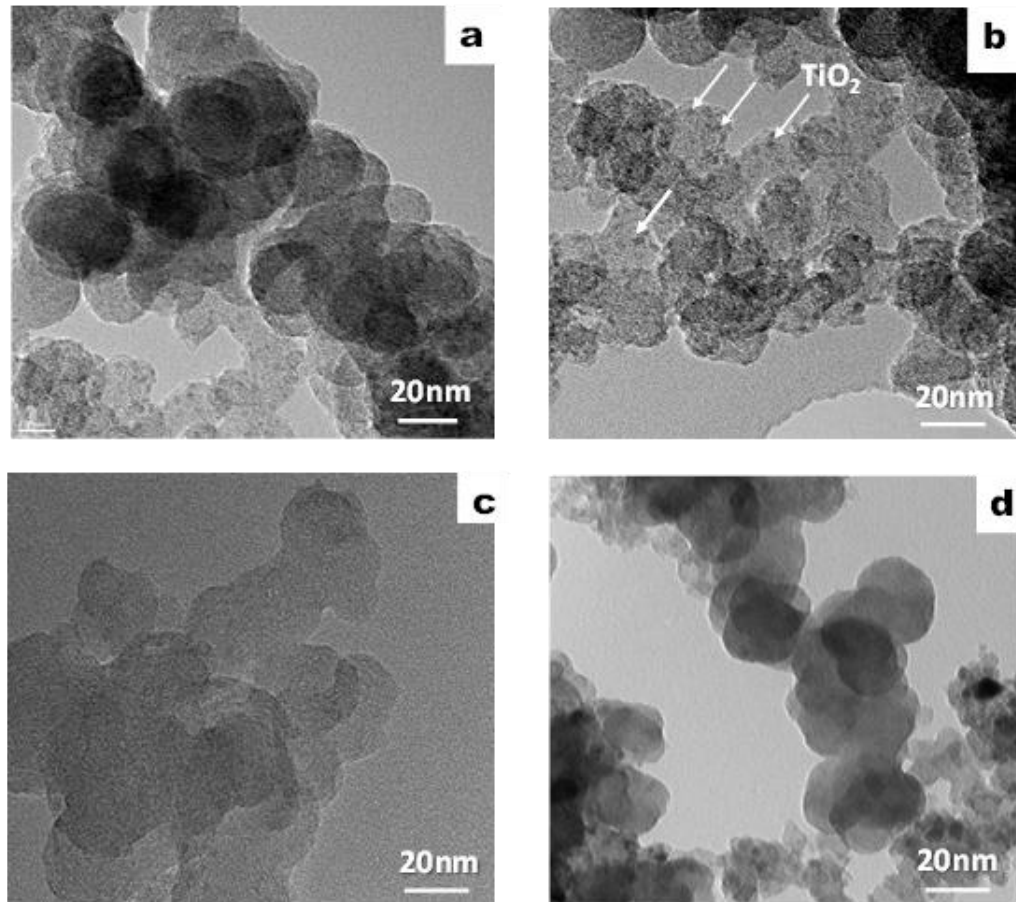


Figure 4.3: TEM characterization: (a-b) 14wt% TiO₂/G-ATV and (c-d) 5wt%TiO₂/ ATV composite supports.

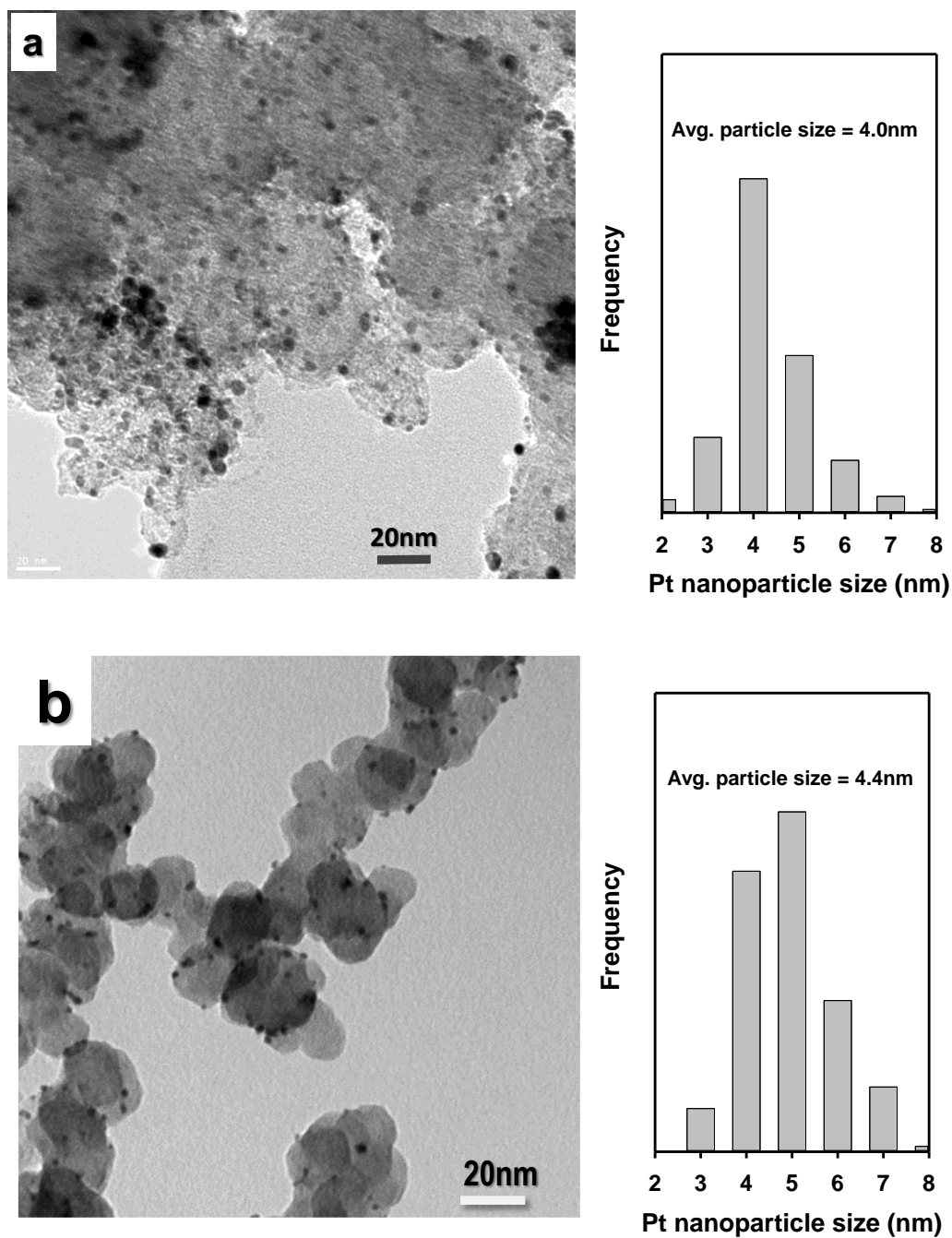


Figure 4.4: TEM characterization: (a) Pt/14 wt% TiO₂/ G-ATV and particle size distribution (b) 5wt% TiO₂/ ATV and particle size distribution.

TEM images of platinised composites are shown in Figure. 5.4. In the case of the glucose doped carbon sample, the morphology is significantly different to the one observed for TiO₂/ATV sample without glucose doping, Figure 4.4b. A more detailed examination reveals that Pt nanoparticles are uniformly dispersed on the surface of the support with a relatively narrow particle size distribution proving the introduction of TiO₂ inhibits the aggregation of Pt particles, even at high TiO₂ loading ratio (14 wt%).

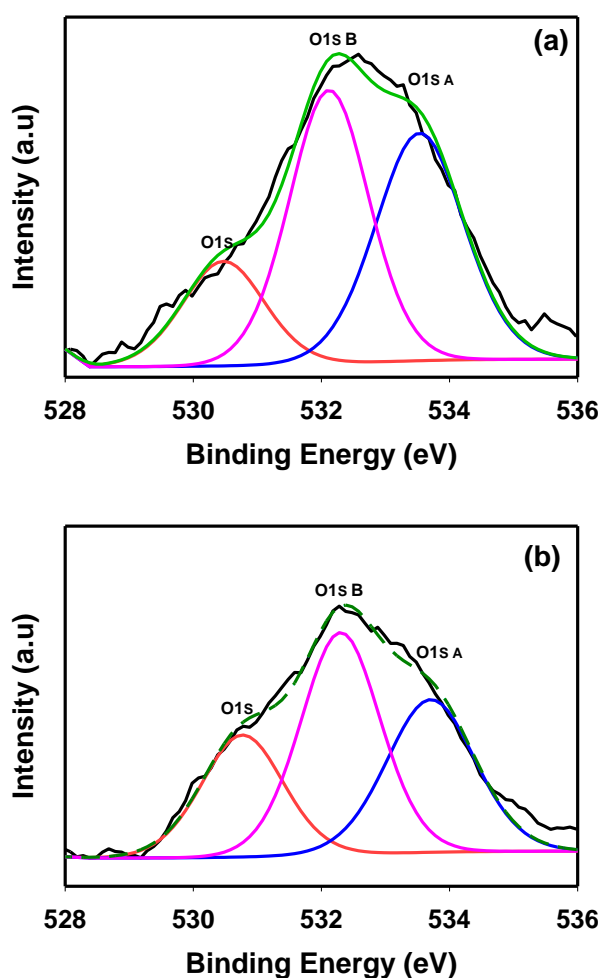


Figure 4.5: XPS characterization: O1s Scan: (a) Pt/14 wt% TiO₂/ G-ATV (b) Pt/5 wt% TiO₂/ ATV

XPS analysis was carried out on Pt/TiO₂/G-ATV and Pt/TiO₂/ATV catalysts. The O1s spectra are shown in Figure 4.5, which were fit to 3 main components. Two main peaks were observed at binding energies of 530.73 eV and 532.31 eV were attributed to TiO₂ and OH functionalities, respectively. The other high BE peak at 533.92 eV possibly originates from alcohol or adsorbed H₂O [43]. In both Pt/TiO₂/ATV and Pt/TiO₂/GATV, TiO₂ particles are in contact with Pt nanoparticles. As a result, one can suspect changes in the electronic structure of the oxide substrate. From Table 4.2, the Pt-TiO₂ mutual interactions can be attributed to a decrease in binding energy (BE) of Pt 4f electrons in the presence of the oxide substrate. The [shift to lower BE](#) suggests an increased electron density on Pt, which can enhance electrochemical activity. Pt 4f signal for Pt/C has been observed at BE 72-71.5 eV [44-45], which is different as compared to 71.3eV for Pt deposited on TiO₂/C composites. The 400-700meV difference in Pt 4f BE suggests a local increase of the electron density on Pt, when Pt is deposited on any of the two oxides investigated. Such slight decrease in Pt 4f BE has already been reported for Pt deposited on oxides of titanium, which confirms our findings, and the increased electron density has been attributed to single metal support interaction (SMSI) in these studies [46-47]. Moreover, the reduction of Pt is more favorable on the glucose doped ATV with 49% metallic Pt formed as compared with 44% on TiO₂/ATV as shown in below.

Table 4.2: XPS Analysis of Pt/TiO₂/ G-ATV and Pt/TiO₂/ ATV Catalysts.

Samples	Pt (0) #71.5eV	Pt (II) #72.6eV	Pt (IV) #74.2eV	% Pt (0)
Pt/14%TiO ₂ /G- ATV	71.3	72.16	73.5	49.0
Pt/5%TiO ₂ / ATV	71.3	72.12	73.6	44.0

- values for Pt states taken from [44-45]

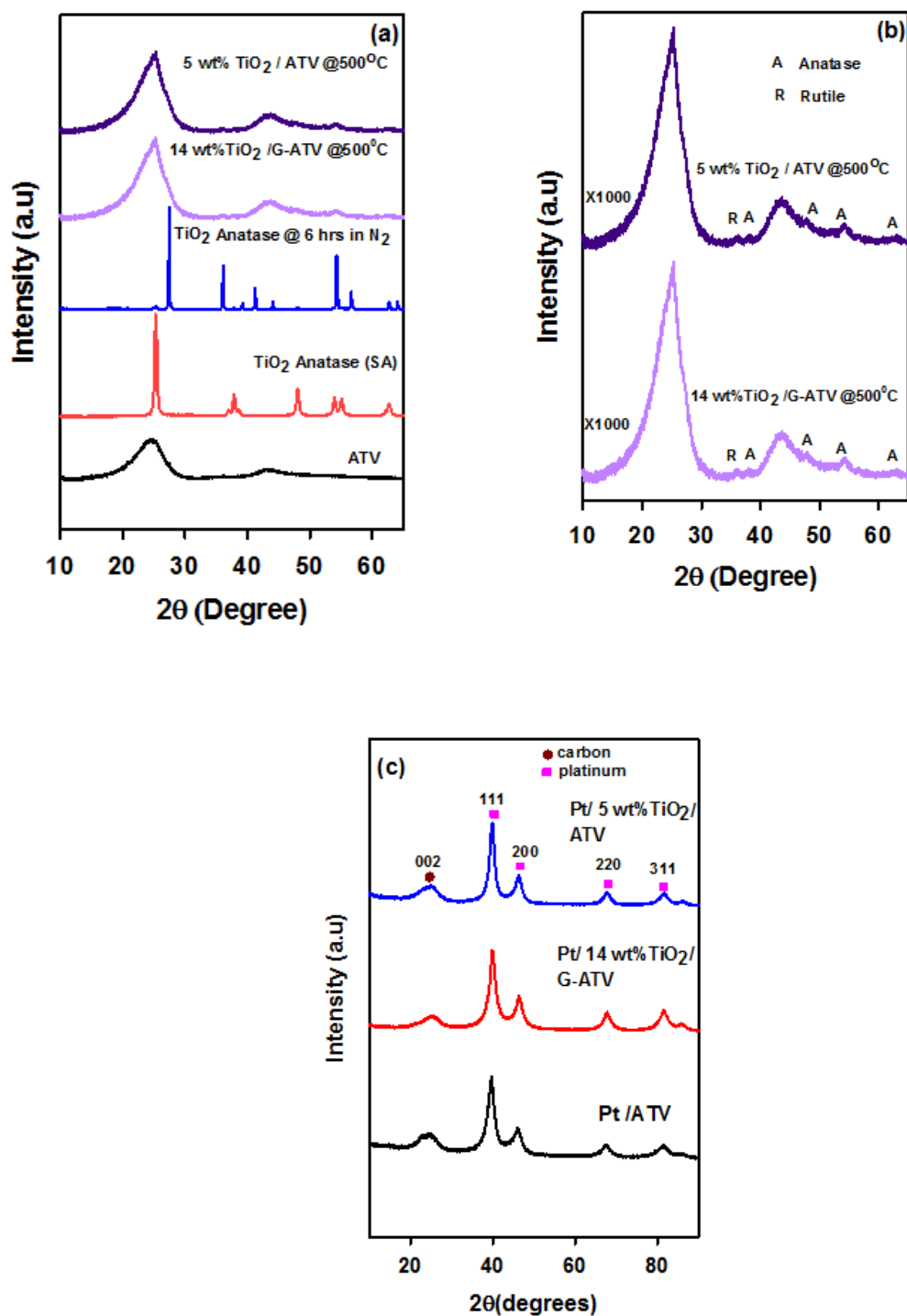


Figure 4.6: XRD patterns of: (a) acid treated Vulcan (ATV), Anatase (SA) and SA annealed at 500°C for 6 hours in N₂, 14 wt% TiO₂/G-ATV and 5wt%TiO₂/ATV (b) 14 wt% TiO₂/G-ATV and 5wt%TiO₂/ATV (c) Pt/ ATV, Pt/14 wt% TiO₂/G-ATV and Pt/ 5wt%TiO₂/ATV

Figure 4.6 compares the XRD patterns of the catalysts and components at different stages of preparation. ATV displays an intense peak at 26.2° as well as a smaller peak around 42.5° , which correspond to the (002) and (100) Bragg peaks expected for the graphitic content in carbon blacks [48-49]. Also shown in this figure are the diffraction patterns obtained for commercially available anatase TiO_2 and a rutile sample obtained by heating anatase at 600°C for 6 hours in nitrogen which displayed their expected reflections [29]. The XRD patterns obtained for both carbon/ TiO_2 composites are dominated by the broad (002) reflection of carbon. However, closer examination of the overlapping peaks (Figure 4.6 (b)) reveal reflections that can be ascribed to both anatase and rutile, despite the fact that annealing temperature is relatively low, temperatures as low as 400°C has been reported for the anatase-to-rutile transition [49]. The inert medium during annealing induced formation of a trace amount of rutile phase of TiO_2 in the composite supports. Figure 4.6(c) compares the diffraction patterns obtained for Pt/14wt% TiO_2 /G-ATV, 5wt% TiO_2 /ATV, and Pt/ATV. All 3 catalysts displayed the characteristic peaks for fcc platinum. The average Pt particle size was determined from the broadening of the Pt (111) peak using the Scherrer equation, and found to be similar for all samples and in good agreement with those determined by TEM. This indicates that the Pt particles deposited are very similar in both terms of both size and crystallinity.

Raman spectra of ATV, commercial anatase TiO_2 and composites annealed at 500°C are shown in Figure 4.7. The spectra exhibit two peaks: the G band at approximately 1582 and 1350 wavenumber for both G and D bands respectively. The spectra of the samples at 500°C reveal peaks at 148, 409, 515 and 633 cm^{-1} that correspond to anatase phase of TiO_2 .

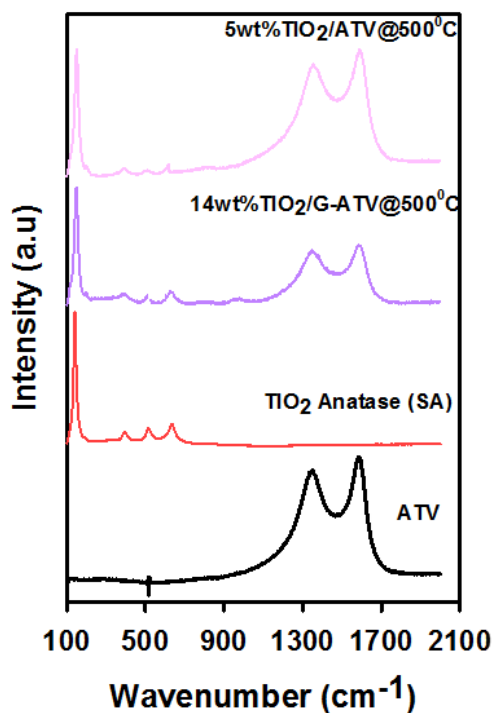


Figure 4.7: Raman spectra of: (a) acid treated Vulcan (ATV), Anatase TiO₂ (SA), 14 wt% TiO₂/G-ATV and 5wt% TiO₂/ATV

The strongest peak at 148 cm⁻¹ is distinct, which indicates that an anatase phase was formed in the as-prepared composite material. These results are in good agreement with the powder XRD data. The successive characterization techniques, TEM, XPS, XRD, TGA and Raman spectroscopy all indicate successful synthesis of TiO₂/carbon composite supports however with the absence of titanium carbide.

Table 4.1 lists the BET surface area data obtained for catalyst support materials. The BET surface area of ATV was determined to be 251 m² g⁻¹, which falls within the 230 – 254 m² g⁻¹ range of BET surface areas reported in the literature for Vulcan XC72. The addition of 5 wt% TiO₂ to ATV leads to a relatively modest reduction in BET surface area (~ 5%) suggesting the material structure is not significantly changed with such small amount of metal oxide. On the other hand, the BET surface area for 14 w% TiO₂/G-ATV was significantly lower than ATV. In this sample, a larger fraction the carbon surface is covered with the denser TiO₂, which also decreases the pore volume, thus the decrease in specific surface area.

4.3.2 Electrochemical Characterization

Typical CVs obtained for each catalyst in N₂-purged 0.5M H₂SO₄ solution are shown in Figure 4.8. The beginning of life (BOL) ECSA of Pt/ ATV, Pt/ 14wt% TiO₂/G-ATV and Pt/ 5wt% TiO₂/ATV are shown in Table 5.3. Pt 14wt% TiO₂/G-ATV has the highest ECSA at 40.4 m² g⁻¹ despite having the highest TiO₂ loading. This may a result of a greater dispersion of Pt nanoparticles on the more uniform composite support. This is in agreement with other findings where dispersion of Pt-catalyst particles was enhanced with minimum aggregation in the presence of TiO₂ and higher electrochemical activity [50-51].

Table 4.3: Summary of electrochemical properties of prepared catalysts

Samples	BOL ECSA (m ² g ⁻¹)	EOL ECSA (m ² g ⁻¹)	Onset Potential for ORR (V)	i _k (mAcm ⁻²)
Pt/ ATV	35.9 ± 3.6 (3)	0.6 ± 1.8(2)	0.89 ± 0.04 (2)	10.6 ± 1.7(2)
Pt/14%TiO ₂ /G- ATV	40.4 ± 2.9 (3)	9.3 ± 2.7 (2)	0.95 ± 0.01(2)	18.3 ± 0.3 (2)
Pt/5%TiO ₂ / ATV	37.1 ± 3.6 (3)	6.2 ± 0.8 (2)	0.88 ± 0.03(2)	11.1 ± 1.9 (2)
E-20 [‡]	55.7 ± 3.5	6.3 ± 2.3	-	-
JM-20 [‡]	52.3 ± 0.3	9.3 ± 0.2	-	-

[‡]:- values recorded for two commercial catalysts, 20wt% Pt/C ETEK and Johnson Matthey following 4000 potential cycles in sulphuric acid medium. (52)

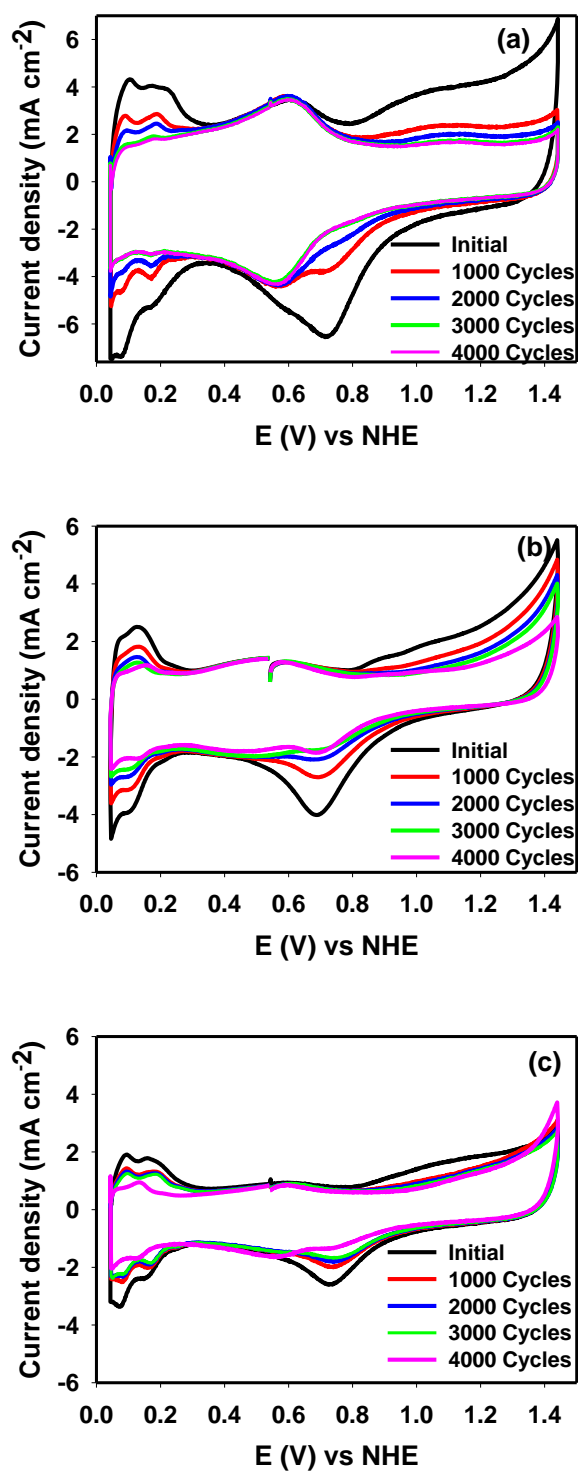
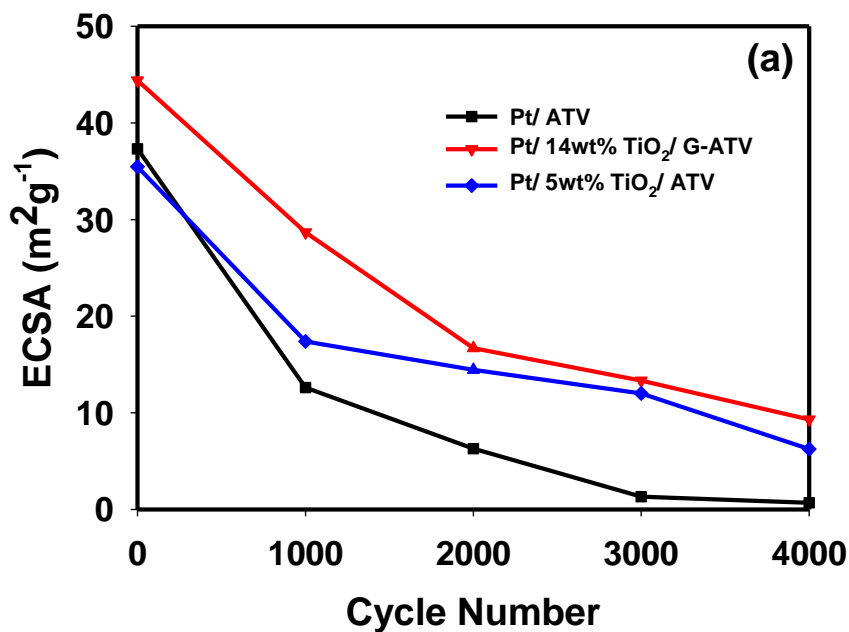


Figure 4.8: Half-cell CVs of : (a) Pt/ ATV (b) Pt/ 14 wt% TiO₂/ G-ATV (c) Pt/ 5 wt% TiO₂/ ATV catalysts under aging conditions in argon-saturated 0.5M H₂SO₄ solution.

Accelerated stress tests were performed on each catalyst using a potential cycling protocol with periodic assessment of catalyst layer health by CV. An upper potential limit of 1.5 V was chosen to mimic fuel cell conditions where the reverse currents [53] and local fuel starvation [54] are present, which exacerbate carbon corrosion. Figure 4.8 shows the changes in the CVs obtained for each catalyst after aging for 1000, 2000, 3000, and 4000 potential cycles. The intensities of the low potential peaks associated with hydrogen adsorption/desorption, as well as the high potential Pt-oxide growth/stripping peaks, decreases with increasing cycle number.

Figure 4.9 shows that the ECSA of each catalyst decreases with increased potential cycling. From the plot, it can be deduced that both composite catalysts show a significantly lower rate of ECSA loss compared to Pt/ ATV.



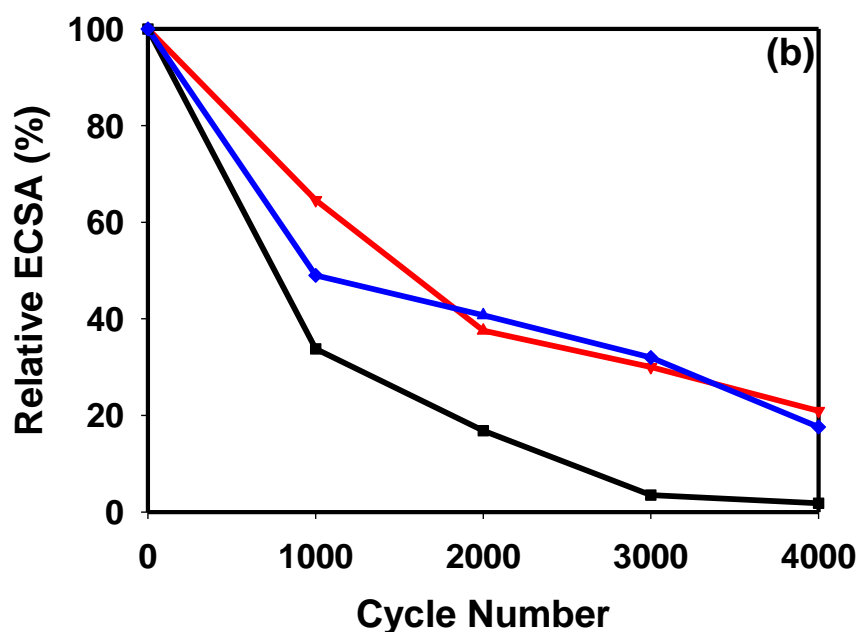


Figure 4.9: Relationship of different catalysts under aging conditions: (a) ECSA vs potential cycle number (b) Normalized ECSA under the catalyst stability assessment period

Moreover a two fold increase in the Pt surface area retention was obtained on the composite catalysts compared with two commercial catalysts E-TEK 20% Pt on Vulcan XC72 carbon black (BASF) and Johnson Matthey HiSpec 3000 20% Pt on carbon black (Alfa Aesar) following 4000 potential cycles as shown in Table 4.3 [52]. There are two plausible explanations for this enhanced stability. The first is an electronic interaction between Pt nanoparticles on TiO_2/C composite support [55-56] that slows the rate of Pt dissolution and agglomeration. The second is a decreased rate of carbon corrosion. Both degradation mechanisms could also be present at the same time. The enhanced ORR activity achieved with Pt/14 wt% $\text{TiO}_2/\text{G-ATV}$ could indicate a more favourably electronic pathway. On the other hand, the CVs for Pt/ ATV show the growth of a peak at ca. 0.5V which is related to the growth of the quinone/hydroquinone groups on the carbon surface. This is indicative of partial oxidation of the carbon surface upon cycling, though not necessarily its corrosion.

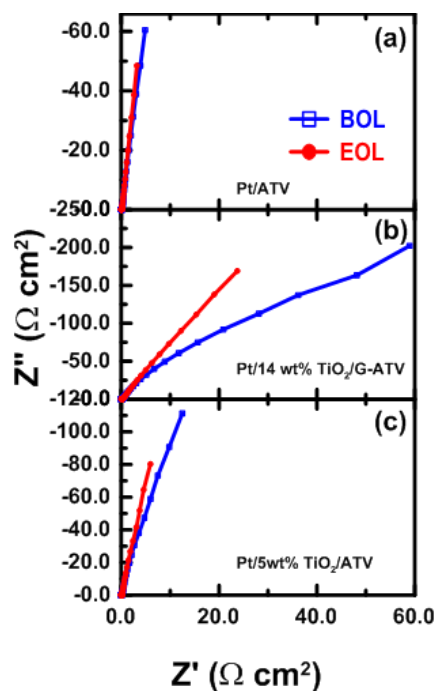


Figure 4.10 : Nyquist plots for : (a)Pt/ ATV , (b) Pt/ 14 wt% TiO₂/ G-ATV and (c) Pt/ 5 wt% TiO₂/ ATV at beginning of life (BOL) and after 4000 potential cycles (EOL).

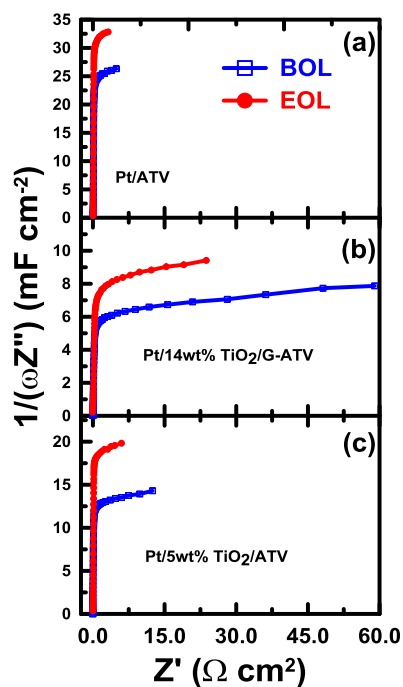


Figure 4.11 : Capacitance plots for : (a)Pt/ ATV , (b) Pt/ 14 wt% TiO₂/ G-ATV and (c) Pt/ 5 wt% TiO₂/ ATV at beginning of life (BOL) and after 4000 potential cycles (EOL).

Saleh and Easton have reported when carbon corrosion occurs in fuel cell catalyst layers, a characteristic change in the EIS profile is observed [41]. Specifically, an increase in the total catalyst layer resistance, R_{Σ} , accompanied by an initial increase and subsequent decrease in capacitance is indicative of carbon corrosion [57]. The EIS responses obtained at BOL and EOL for each catalyst layer are shown as both Nyquist and capacitance plots in Figure 4.10 and Figure 4.11 respectively. Pt/ATV showed the highest limiting (low frequency) capacitance at BOL, which arises due to the higher exposed carbon surface area. As TiO_2 is introduced into the structure, capacitance decreases. This is expected as TiO_2 covers a significant portion of the carbon surface. By projecting the length of the 45° Warburg-type region onto the real axis, we can extract the total catalyst layer resistance, R_{Σ} , which is the sum of the electronic and ionic resistances in the catalyst layer [58]. The addition of TiO_2 into the catalyst layer does lead to a small increase in R_{Σ} which is attributed to an increase in electronic resistance. Such an increase is expected when a metal oxide is added. However, the increased resistance is relatively small, owing to our method of fabrication and as such has minimal influence on electrode performance.

At EOL, both Pt/ATV and Pt/ 5 wt% TiO_2 /ATV based catalyst layer shows a small increase in capacitance and small decrease in R_{\square} , which we attribute to improved hydration of the catalyst layer during testing [59]. Pt/ 14 wt% TiO_2 /G-ATV also shows a small increase in capacitance at EOL; R_{Σ} , was essentially unchanged.

Together, this EIS data indicates that carbon corrosion is not a substantial contributor to the degradation of the three catalysts and that Pt dissolution/agglomeration is the dominant degradation pathway. While one would expect the presence of TiO_2 to enhance carbon corrosion stability, Vulcan XC72 has been shown to not corrode significantly under the testing conditions [57]. Therefore, the enhanced durability of the composite catalysts must be attributed to the electronic interaction of Pt nanoparticles with the TiO_2 /C support that minimised Pt dissolution and aggregation.

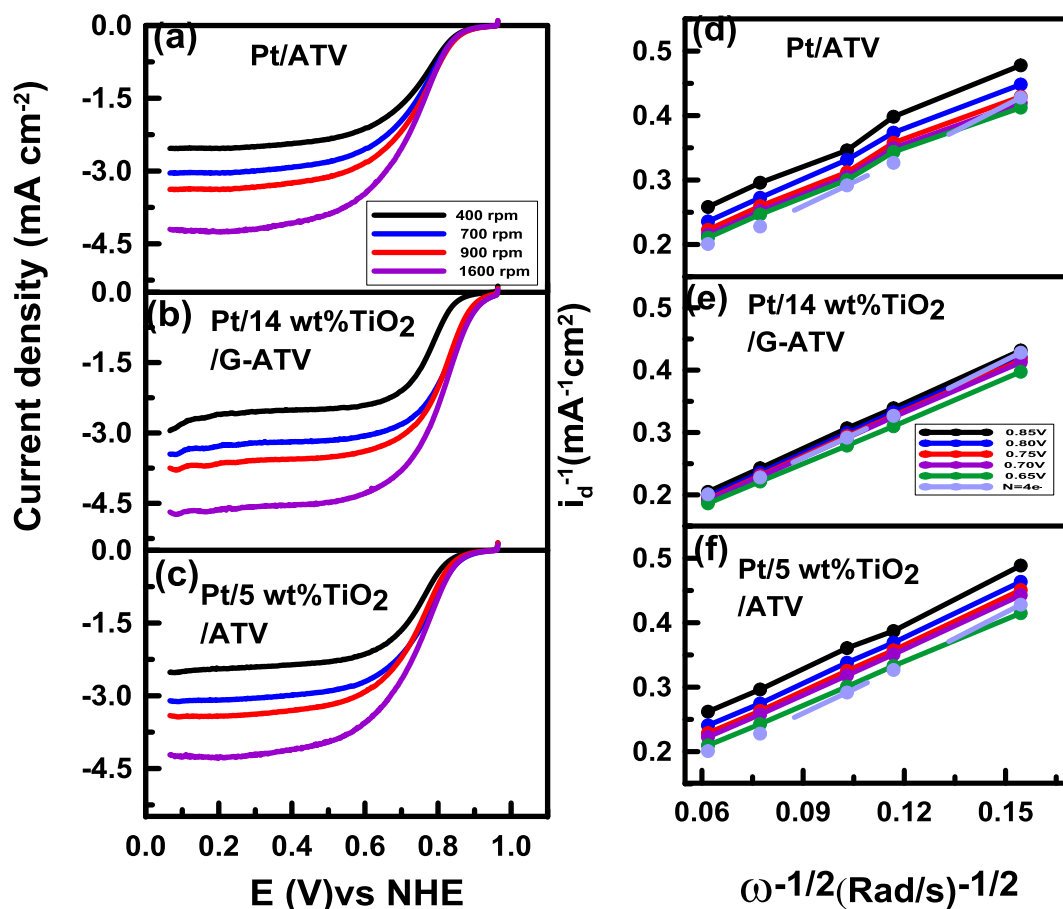


Figure 4.12: ORR activities of each catalyst at beginning of life (a, b, c) corresponding Koutecky-Levich plots are shown in (d, e, and f). Measurements were carried out in O₂-saturated 0.5M H₂SO₄ at 25 °C a scan rate of 5 mV s⁻¹, Pt loading 0.1 ± 0.01 mg cm⁻² 30wt% Nafion loading.

The activity of the synthesized catalysts toward the reduction of oxygen was determined using rotating disc electrode system. Typical ORR curves obtained at different rotation rates are shown in Figure 4.12. The diffusion limiting current increased with increased rotation rates for each catalyst. It can be inferred from these plots that an increase in limiting currents on high performance electrocatalysts is associated with the increase of molecular oxygen diffusion in the boundary layer through the electrode surface. At high cathodic overpotentials, the oxygen reduction rate reaches its maximum as seen by the flat limiting current plateau. Kinetic current densities (i_k) for each catalyst were determined using the Koutecky-Levich equation at differential potentials, in region with kinetic and

mass transfer contribution on the electrode surface. These plots indicate first order ORR kinetics and that the four-electron transfer process takes place on all catalysts.

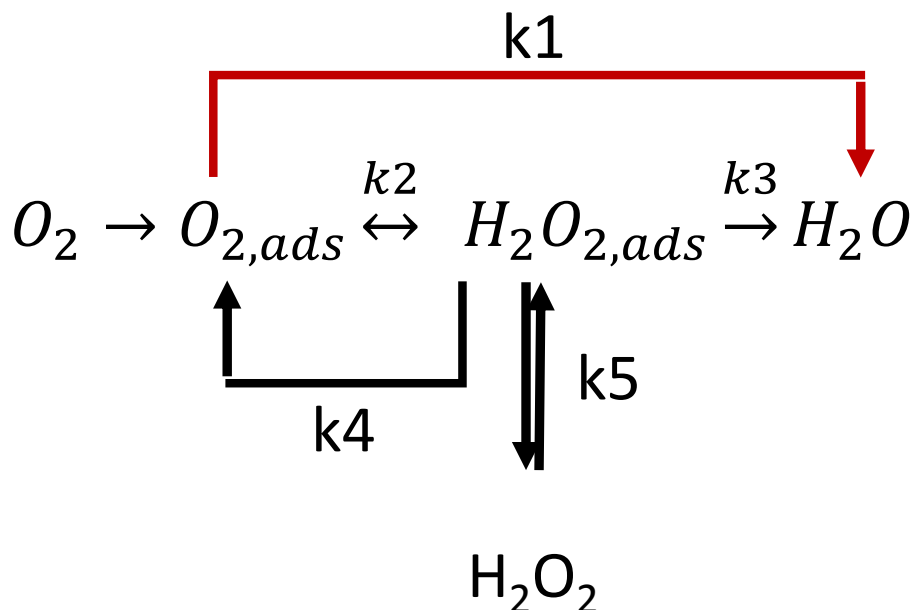


Figure 4.13: Mechanisms of Oxygen reduction reaction on platinum based electrode surface ⁶¹.

These results are consistent with the direct 4-electron path way mechanism of oxygen reduction presented in Figure 4.13. In this cathodic reaction, a multi-electron reaction takes place that involves a number of elementary steps involving different reaction intermediates to produce water and/or hydrogen peroxide [60]. The mechanism shown indicates that O_2 can be reduced either directly to water (direct 4-electron reduction) electrochemically with the rate constant k_1 , or to adsorbed hydrogen peroxide with the rate constant k_2 (2-electron reduction). H_2O_2 can be further reduced to water with the rate constant k_3 , chemically decomposed on the electrode surface k_4 , and/or desorbed into the electrolyte solution k_5 [60].

Figure 4.14 overlays the ORR curves obtained at a fixed rotation rate of 1600 RPM for each catalyst at their beginning of life (BOL). The activities of these catalysts are compared with respect to their onset potentials, the potential at which 5 % of the limiting current is reached [62]. The glucose doped catalyst has the highest onset potential for ORR

activity at 0.97V compared with 0.88V for both Pt/ 5wt% TiO₂/ATV and Pt/ ATV, respectively. After the aging protocol, the onset potentials for oxygen reduction at Pt/ ATV, Pt/ 5wt% TiO₂/ATV, Pt/14 wt% TiO₂/G-ATV electrodes were observed at 0.74, 0.73 and 0.87 V respectively Figure 4.14b. This is in agreement with previous studies in which improvement in oxygen reduction activity on TiO₂ catalyst support was observed due to increased affinity of O₂ on the oxide support [20, 52].

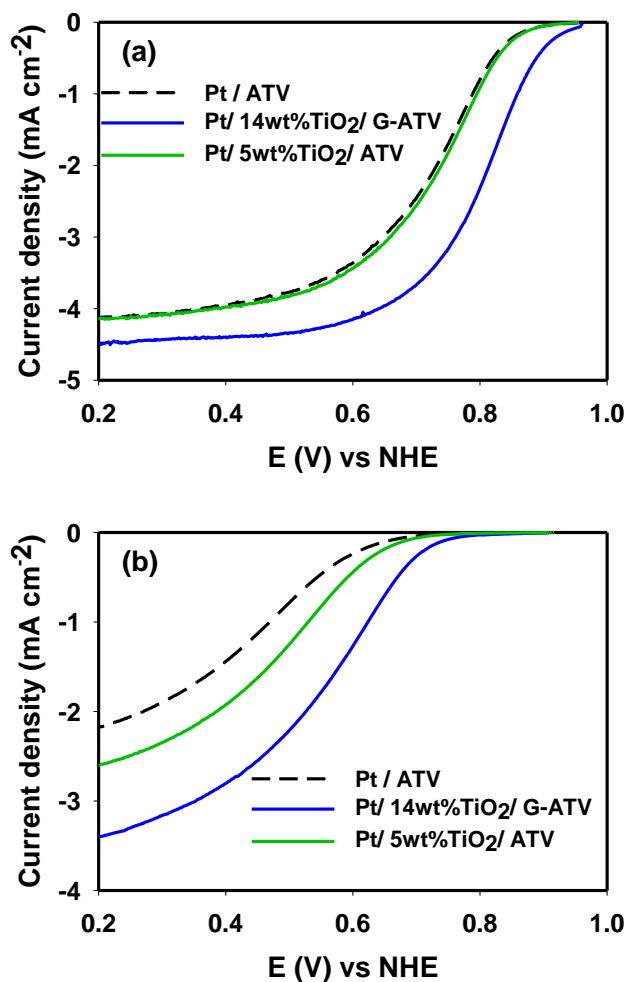


Figure 4.14: Comparison of the ORR activities of each catalyst at (a) beginning of life (BOL) and (b) end of life (EOL, 4000 potential cycles). Measurements were carried out in

O₂-saturated 0.5M H₂SO₄ at 25 °C a scan rate of 5 mV /s using an electrode rotation rate of 1600 RPM.

4.4 Impact of catalyst loading and electrolyte effect on rotating disc electrode measurements

The study was extended in order to follow a well-established by US [Department of Energy](#) (DOE) new protocol that can be used to evaluate electrocatalytic activities originally proposed by Kocha and Garsany [63], more specifically with respect to the loadings of catalyst and choice of electrolyte used in our study. With respect to the catalyst loading used in this thesis, our results are consistent with previous findings and within the limit where kinetic analysis have been performed using a rotating disk electrode without transport limitations [64].

The choice of electrolyte during RDE measurement is very important since anion adsorption on the Pt electrode surface has been reported to be stronger in sulphate medium than in perchloric acid medium. Such adsorption can affect diffusion limiting currents at different rotation speeds on a rotating disc electrode. To show that the impact of sulphate adsorption is minimal in these experiments, we have performed cyclic voltammetry using aforementioned stability protocol and RDE measurements in double distilled 0.1M HClO₄ electrolyte. For possible comparison, the same measurements were done in 0.5M H₂SO₄ electrolyte solution for the 3 catalysts under same ultra-low catalyst loadings of 20 µg cm⁻². At this ultra-low catalyst loading, the catalyst layers are still sufficiently thin enough so that the RDE results show still provide very good information about catalyst activity in terms of onset potential and half wave potential for ORR. ORR curves at different rotation rates are shown below in Figure 4.15 for all catalysts.

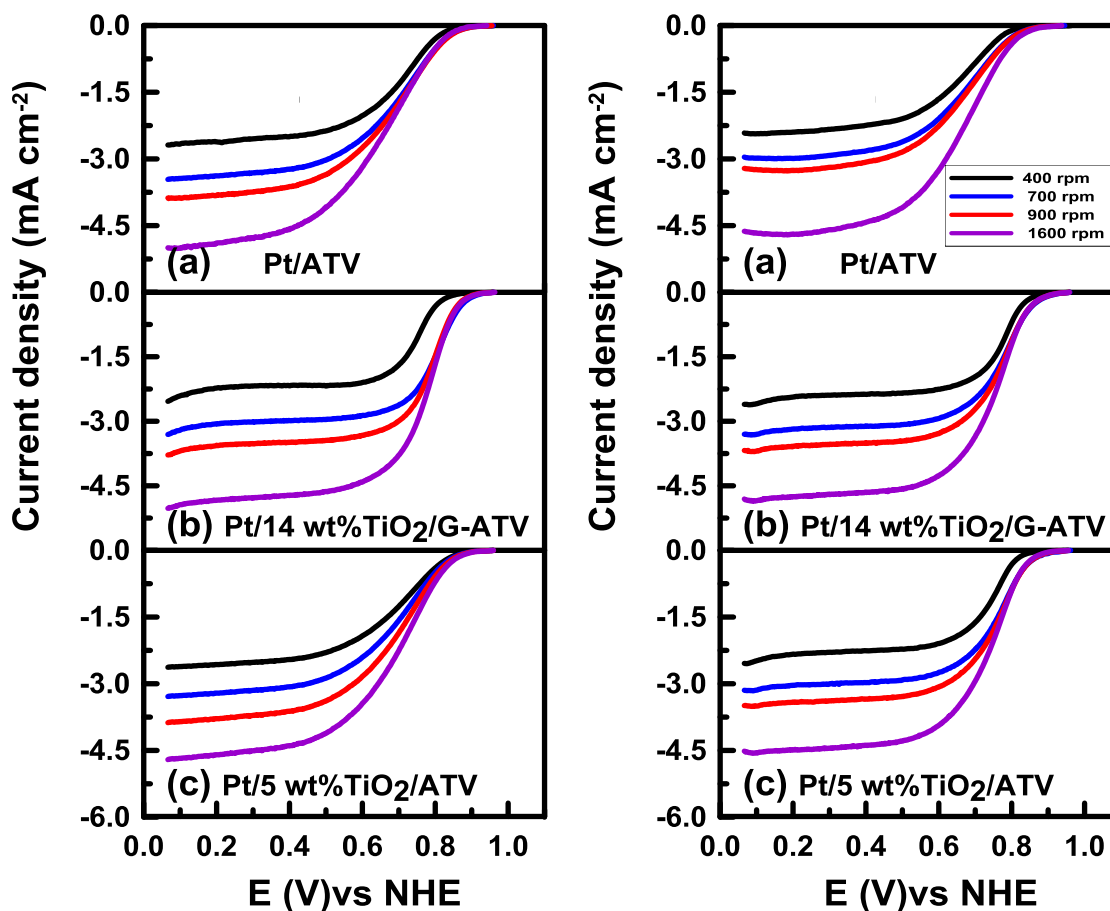


Figure 4.15: Comparison of the ORR activities of each catalyst $20\mu\text{gcm}^{-2}$ Pt loading on all catalysts. Measurements were carried out in O_2 -saturated in 0.1M HClO_4 (left) and $0.5\text{M H}_2\text{SO}_4$ (right) at 25°C a scan rate of 5 mV s^{-1} using electrode rotation rates 400-1600 RPM.

Figure 4.16 compares the ORR activities of these catalysts at 1600RPM in the two electrolyte solutions. The diffusion limiting currents appear similar in these acidic media. The onset potential for oxygen reduction at 1600 RPM and the half wave potential were highest for Pt/14 $\text{TiO}_2/\text{G-ATV}$ catalyst compared with other tested catalysts. This is in agreement with similar trend observed in sulfuric acid medium at the catalyst loadings used in previous results. This further confirms that the electrodes tested in this work are not mass transport limited. The linear dependence of the diffusion limiting currents at a given potential, 0.2V with square root of rotation rates is shown in Figure 4.17. It is expected that the slopes of the lines be proportional to number of electrons exchanged per O_2

molecule for ORR. The slopes of the experimental lines were obtained as $\sim 0.39 \text{ mA cm}^{-2} (\text{rad s}^{-1})^{1/2}$ and $0.38 \text{ mA cm}^{-2} (\text{rad s}^{-1})^{1/2}$ in 0.1M HClO_4 and $0.5 \text{ M H}_2\text{SO}_4$ electrolyte solutions respectively, which are $\sim 12\%$ within the values reported in similar study [65]. All the catalysts show ~ 4 electron transfer process as before with enhanced diffusion limiting currents. Thus these results confirm that the trends in activity are the same in both electrolytes and confirm the validity of our measurements in H_2SO_4 .

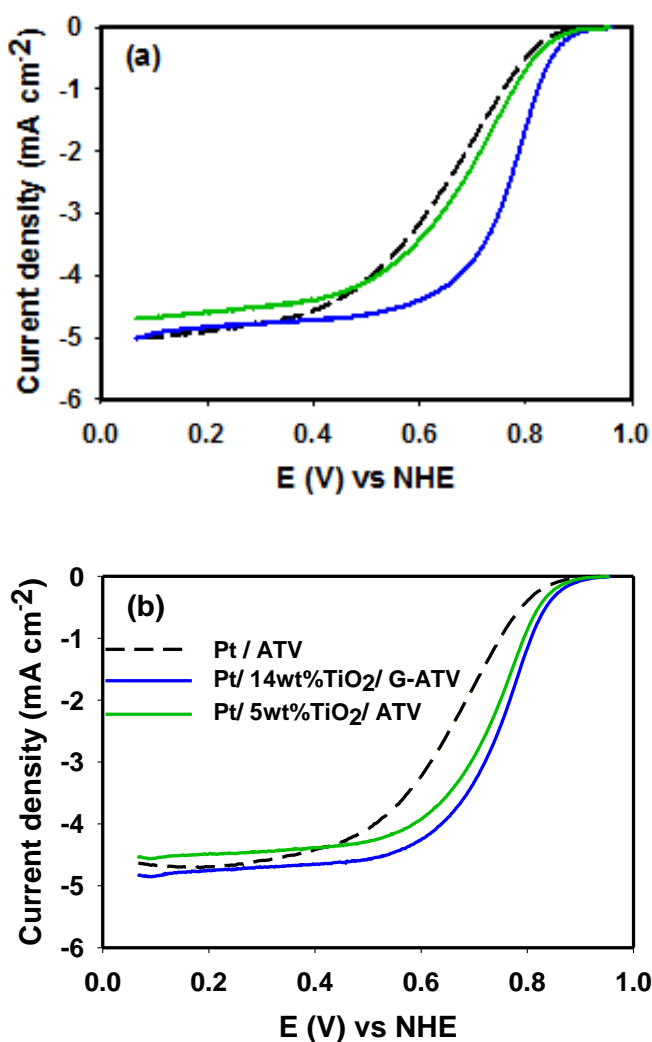


Figure 4.16: Comparison of the ORR activities of each catalyst at 1600RPM in O_2 -saturated (a) 0.1M HClO_4 and (b) $0.5\text{M H}_2\text{SO}_4$. Measurements were carried out at 25°C a scan rate of 5 mV s^{-1} with $20\mu\text{gcm}^{-2}$ Pt loading on all catalysts.

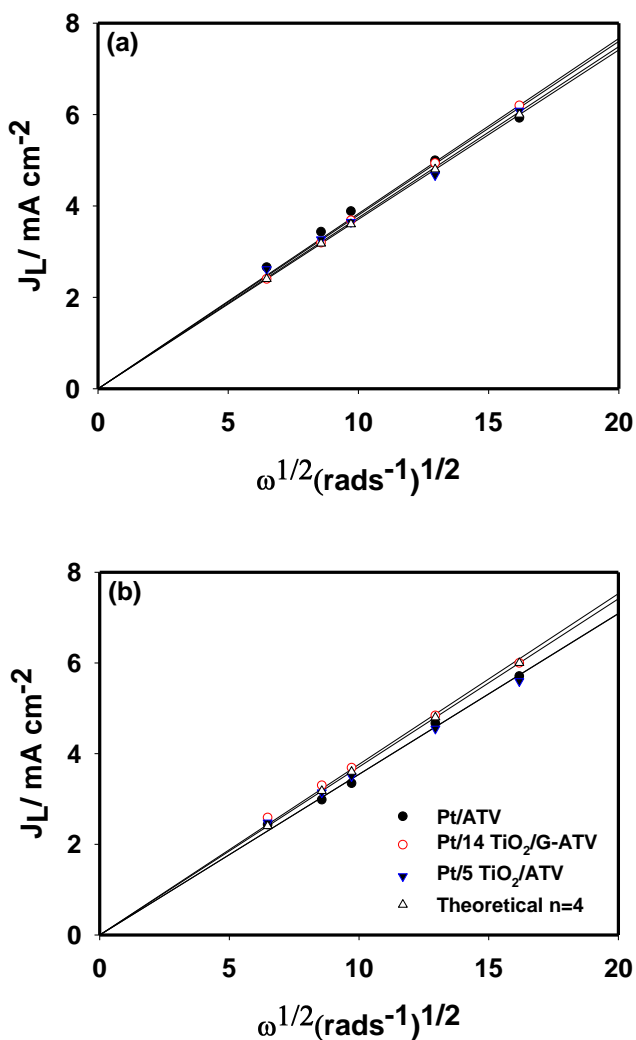


Figure 4.17: Comparison of [Levich](#) plots for kinetic analysis of each catalyst at 0.2V under different rotation rates in O_2 -saturated (a) 0.1M HClO_4 and (b) 0.5M H_2SO_4 . Measurements were carried out at 25 °C a scan rate of 5 mV s^{-1} with $20 \mu\text{g cm}^{-2}$ Pt loading on all catalysts.

The catalyst materials were also evaluated for durability study in the two acidic media for 4000 potential cycles (Figure 4.18). A general decay pattern of the Pt active surface area under was observed under this cycling condition. The normalised surface area

shows similar results of more stable composite catalysts materials over in house fabricated Pt/C catalyst. Given all this, we feel that our measurements are both valid and highly relevant. At this point, we will state that evaluation of electrocatalytic activity in sulfuric acid medium is still a bench mark procedure in the literature up to date with respect to stability study and ORR.

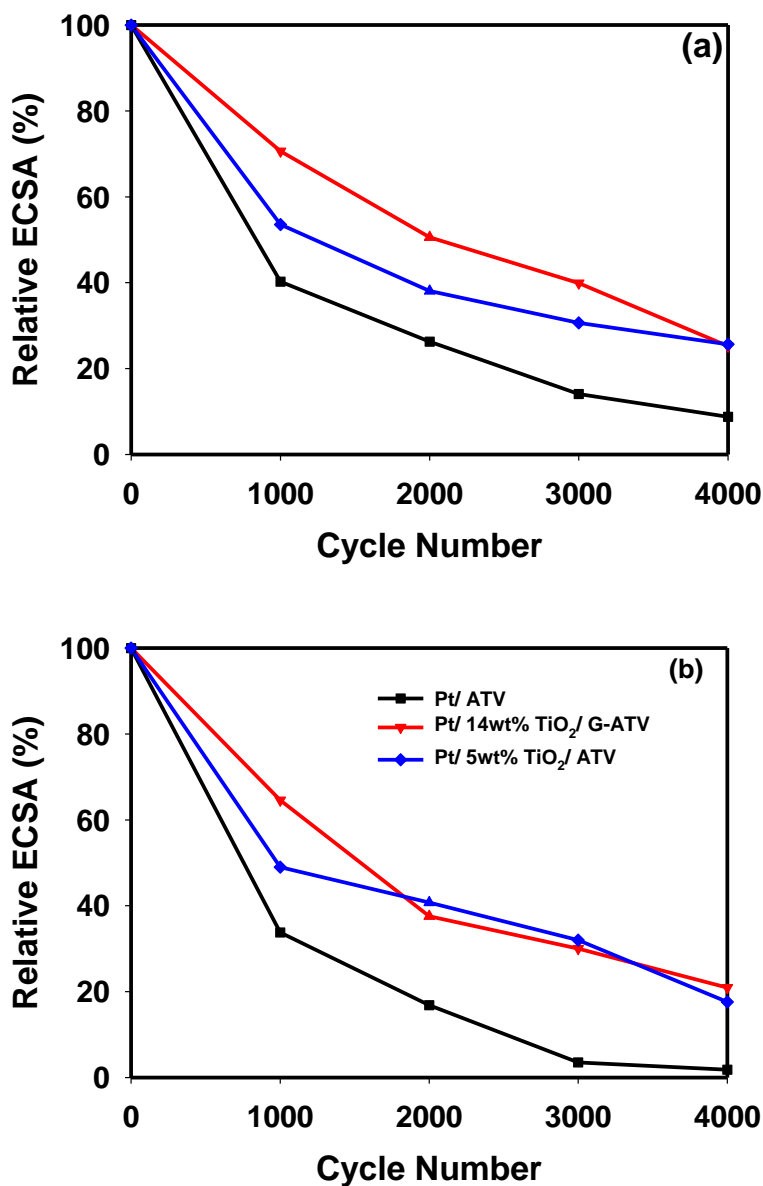


Figure 4.18: Normalized ECSA of catalysts under stability assessment in (a) 0.1M HClO₄ and (b) 0.5M H₂SO₄.

4.5 Conclusion and summary

Glucose doping on acid treated carbon has been evaluated to further activate carbon surface prior to *in situ* TiO₂ deposition to form a composite catalyst support. The addition of glucose leads to a larger amount of TiO₂ deposited onto carbon compared to samples prepared from the base carbon that was not glucose doped. Uniform dispersion of Pt nanoparticles was achieved on both composite support surfaces. Pt/14wt%TiO₂/G-ATV showed a higher ECSA compared with Pt/ATV and Pt/ 5wt%TiO₂/ ATV catalysts. This enhancement in ECSA of Pt/14wt%TiO₂/ATV can be ascribed to thinner films of TiO₂ that subsequently increased dispersion of Pt nanoparticles with minimal increase in catalyst layer resistance. Catalyst prepared on these composite supports displayed high ORR activity and greater durability during accelerated stress tests, which we have attributed to an electronic interaction between Pt and TiO₂.

4.6 References

- 1) He, X., & Hu, C. (2011). *Journal of Power Sources*, 196(6), 3119-3123.
- 2) Shao-Horn, Y., Sheng, W. C., Chen, S., Ferreira, P. J., Holby, E. F., and Morgan, D. (2007). *Topics in Catalysis*, 46(3-4), 285-305.
- 3) Ralph, T. R., Hudson, S., and Wilkinson, D. P. (2006). *ECS Transactions*, 1(8), 67-84.
- 4) Chen, G., Bare, S. R., and Mallouk, T. E. (2002). *Journal of the Electrochemical Society*, 149(8), A1092-A1099.
- 5) Xie, J., Wood, D. L., Wayne, D. M., Zawodzinski, T. A., Atanassov, P., and Borup, R. L. (2005). *Journal of the Electrochemical Society*, 152(1), A104-A113.
- 6) Shao, Y., Yin, G., Gao, Y., and Shi, P. (2006). *Journal of the Electrochemical Society*, 153(6), A1093-A1097.
- 7) Shao, Y., Yin, G., Zhang, J., and Gao, Y. (2006). *Electrochimica Acta*, 51(26), 5853-5857.

- 8) Reiser, C. A., Bregoli, L., Patterson, T. W., Jung, S. Y., Yang, J. D., Perry, M. L., and Jarvi, T. D. (2005). *Electrochemical and Solid-State Letters*, 8(6), A273-A276.
- 9) Stevens, D. A., Hicks, M. T., Haugen, G. M., and Dahn, J. R. (2005). *Journal of the Electrochemical Society*, 152(12), A2309-A2315.
- 10) Maass, S., Finsterwalder, F., Frank, G., Hartmann, R., and Merten, C. (2008). *Journal of Power Sources*, 176(2), 444-451.
- 11) Meyers, J. P., and Darling, R. M. (2006). *Journal of the Electrochemical Society*, 153(8), A1432-A1442.
- 12) Kinoshita, K. (1988). Carbon: electrochemical and physicochemical properties.
- 13) Maiyalagan, T., Viswanathan, B., and Varadaraju, U. V. (2005). *Electrochemistry Communications*, 7(9), 905-912.
- 14) Kongkanand, A., Kuwabata, S., Girishkumar, G., and Kamat, P. (2006). *Langmuir*, 22(5), 2392-2396.
- 15) Antolini, E. (2012). *Applied Catalysis B: Environmental*, 123, 52-68.
- 16) Ko, Y. J., Oh, H. S., and Kim, H. (2010). *Journal of Power Sources*, 195(9), 2623-2627.
- 17) Shao, Y., Yin, G., Gao, Y., and Shi, P. (2006). *Journal of the Electrochemical Society*, 153(6), A1093-A1097.
- 18) Oh, H. S., Lim, K. H., Roh, B., Hwang, I., and Kim, H. (2009). *Electrochimica Acta*, 54(26), 6515-6521.
- 19) Kowal, A., Li, M., Shao, M., Sasaki, K., Vukmirovic, M. B., Zhang, J. H. and Adzic, R. R. (2009). *Nature materials*, 8(4), 325-330.
- 20) Masa, J., Bordoloi, A., Muhler, M., Schuhmann, W., and Xia, W. (2012). *ChemSusChem*, 5(3), 523-525.

- 21) Suzuki, S., Onodera, T., Kawaji, J., Mizukami, T., and Yamaga, K. (2012). *Applied Catalysis A: General*, 427, 92-97.
- 22) Hepel, M., Kumarihamy, I., and Zhong, C. J. (2006). *Electrochemistry communications*, 8(9), 1439-1444.
- 23) Tian, J., Sun, G., Jiang, L., Yan, S., Mao, Q., and Xin, Q. (2007). *Electrochemistry communications*, 9(4), 563-568.
- 24) Jaksic, M. M. (2001). *International journal of hydrogen energy*, 26(6), 559-578.
- 25) Hsieh, C. T., Chang, C. C., Chen, W. Y., and Hung, W. M. (2009). *Journal of Physics and Chemistry of Solids*, 70(6), 916-921.
- 26) Arulmani, D. V., Eastcott, J. I., Mavilla, S. G., and Easton, E. B. (2014). *Journal of Power Sources*, 247, 890-895.
- 27) Li, W., Bai, Y., Li, F., Liu, C., Chan, K. Y., Feng, X., and Lu, X. (2012). *Journal of Materials Chemistry*, 22(9), 4025-4031.
- 28) Lee, W. J., Alhosan, M., Yohe, S. L., Macy, N. L., and Smyrl, W. H. (2008). *Journal of the electrochemical society*, 155(9), B915-B920.
- 29) Ioroi, T., Siroma, Z., Fujiwara, N., Yamazaki, S. I., and Yasuda, K. (2005) *Electrochemistry Communications*, 7(2), 183-188.
- 30) Ho, V. T. T., Pan, C. J., Rick, J., Su, W. N., and Hwang, B. J. (2011). *Journal of the American Chemical Society*, 133(30), 11716-11724.
- 31) Chen, G., Bare, S. R., and Mallouk, T. E. (2002). *Journal of the Electrochemical Society*, 149(8), A1092-A1099.
- 32) Dogan, D. C., Hwang, S. M., Yim, S. D., Sohn, Y. J., Yang, T. H., and Park, G. G. (2013). *ECS Transactions*, 58(1), 1843-1847.
- 33) Rigdon, W. A., Larrabee, D., and Huang, X. (2013). *ECS Transactions*, 58(1), 1809-1821.

- 34) Alexeyeva, N., Bock, C., MacDougall, B. R., and Tammeveski, K. (2013). In *223rd ECS Meeting (May 12-17, 2013)*.
- 35) Chen, H. C., Chen, K. J., Wang, C. H., Lin, C. C., Yeh, C. C., Tsai, H. H., and Lu, T. C. (2012). *Nanoscale Research Letters*, 7(1), 1-5.
- 36) Nemeth, Z., Reti, B., Pallai, Z., Berki, P., Major, J., Horvath, E., and Hernadi, K. (2014). *physica status solidi (b)*, 251(12), 2360-2365.
- 37) Zhang, Y., Utke, I., Michler, J., Ilari, G., Rossell, M. D., and Erni, R. (2014). *Beilstein journal of nanotechnology*, 5(1), 946-955.
- 38) Cong, Y., Li, X., Dong, Z., Yuan, G., Cui, Z., and Zhang, J. (2015). *Materials Letters*, 138, 200-203.
- 39) Odetola, C., Easton, E. B., and Trevani, L. (2016). *International Journal of Hydrogen Energy*, 41(19), 8199-8208
- 40) Easton, E. B., and Pickup, P. G. (2005). *Electrochimica Acta*, 50(12), 2469-2474.
- 41) Saleh, F. S., and Easton, E. B. (2012). *Journal of The Electrochemical Society*, 159(5), B546-B553.
- 42) Eastcott, J. I., Yarrow, K. M., Pedersen, A. W., and Easton, E. B. (2012). *Journal of Power Sources*, 197, 102-106.
- 43) Ohno, T., Tsubota, T., Nishijima, K., and Miyamoto, Z. (2004). *Chemistry Letters*, 33(6), 750-751.
- 44) Zhang, N., Zhang, S., Du, C., Wang, Z., Shao, Y., Kong, F., and Yin, G. (2014). *Electrochimica Acta*, 117, 413-419.
- 45) Huang, D., Zhang, B., Bai, J., Zhang, Y., Wittstock, G., Wang, M., and Shen, Y. (2014). *Electrochimica Acta*, 130, 97-103.
- 46) Chen, B. H., and White, J. M. (1982). *The Journal of Physical Chemistry*, 86(18), 3534-3541.

- 47) Lewera, A., Timperman, L., Roguska, A., and Alonso-Vante, N. (2011). *The Journal of Physical Chemistry C*, 115(41), 20153-20159.
- 48) Easton, E. B., Bonakdarpour, A., and Dahn, J. R. (2006). *Electrochemical and solid-state letters*, 9(10), A463-A467.
- 49) Hirano, M., Nakahara, C., Ota, K., Tanaike, O., and Inagaki, M. (2003). *Journal of Solid State Chemistry*, 170(1), 39-47.
- 50) Akalework, N. G., Pan, C. J., Su, W. N., Rick, J., Tsai, M. C., Lee, J. F., and Hwang, B. J. (2012). *Journal of Materials Chemistry*, 22(39), 20977-20985.
- 51) Shanmugam, S., and Gedanken, A. (2007). *Small*, 3(7), 1189-1193.
- 52) Saleh, F. S., and Easton, E. B. (2013). *Electrochimica Acta*, 114, 278-284.
- 53) Knights, S. D., Colbow, K. M., St-Pierre, J., and Wilkinson, D. P. (2004). *Journal of power sources*, 127(1), 127-134.
- 54) Patterson, T. W., and Darling, R. M. (2006). *Electrochemical and Solid-State Letters*, 9(4), A183-A185.
- 55) Kumar, A., and Ramani, V. (2013). *Journal of The Electrochemical Society*, 160(11), F1207-F1215.
- 56) Jiang, Z. Z., Wang, Z. B., Chu, Y. Y., Gu, D. M., and Yin, G. P. (2011). *Energy & Environmental Science*, 4(7), 2558-2566.
- 57) O'Rian, O. R., Saleh, F. S., and Easton, E. B. (2014). *ECS Transactions*, 61(23), 25-32.
- 58) Lefebvre, M. C., Martin, R. B., and Pickup, P. G. (1999). *Electrochemical and Solid-State Letters*, 2(6), 259-261.
- 59) Saleh, F. S., and Easton, E. B. (2014). *Journal of Power Sources*, 246, 392-401.
- 60) Colmati, F., Antolini, E., & Gonzalez, E. R. (2005). *Electrochimica Acta*, 50(28), 5496-5503.

- 61) Liu, Z., Lee, J. Y., Han, M., Chen, W., & Gan, L. M. (2002). *Journal of Materials Chemistry*, 12(8), 2453-2458.
- 62) Mavilla, S. G., MacLean, B. J., and Easton, E. B. (2013). *ECS Transactions*, 53(12), 31-41.
- 63) Takahashi, I., and Kocha, S. S. (2010). *Journal of Power Sources*, 195(19), 6312-6322.
- 64) Taleb, M., Nerut, J., Tooming, T., Thomberg, T., Jänes, A., and Lust, E. (2015). *Journal of The Electrochemical Society*, 162(7), F651-F660.
- 65) Rahman, M. R., Awad, M. I., Kitamura, F., Okajima, T., and Ohsaka, T. (2012). *Journal of Power Sources*, 220, 65-73.

CHAPTER FIVE

Oxygen reduction reaction and electrochemical stability of Pt/TiO₂/Carbon fuel cell electrocatalysts prepared using a glucose modifier.

Part of the work described in this chapter has been published as:

Odetola, C., Easton, E. B., and Trevani, L. (2016). Investigation of TiO₂/carbon electrocatalyst supports prepared using glucose as a modifier. *International Journal of Hydrogen Energy*, 41(19), 8199-8208.

<http://dx.doi.org/10.1016/j.ijhydene.2015.10.035>

In last chapter, I have employed glucose-doped acid treated Vulcan[®] XC-72R carbon (G-ATV) for the preparation of Pt/TiO₂/G-ATV catalyst. This catalyst showed an improvement in terms of electrochemical performance toward the oxygen reduction reaction (ORR) when compared with undoped Pt/C. However, it will even be more interesting if glucose doping can be applied on the surface of pristine Vulcan without the need for acid treatment, and more importantly, its impact on the long-term stability of the prepared catalysts. Therefore, in this study different TiO₂ contents were deposited on glucose-doped pristine Vulcan[®] XC-72R carbon (G-PV), followed by post-deposition heat treatment at 500 °C under nitrogen to induce the pyrolysis of glucose and promote TiO₂ crystallization and the deposition of Pt NPs. The development of this dual phase composite catalysts for oxygen reduction reaction (ORR) was evaluated under half cell conditions for performance durability. The combination used for this catalyst support has been shown to offer some improvements in performance stability in comparison to a control without TiO₂ addition (Pt/C vs. Pt/ TiO₂/G-PV).

5.1 Introduction

Proton exchange membrane fuel cells (PEMFCs) have shown to be an attractive alternative power source for mobile and stationary applications; however, corrosion of the carbon support and platinum aggregation during long-term operation and start-up-shut-down cycles in automotive applications result in an important reduction of the catalyst electrochemical surface area (ECSA). A problem that it is more severe on the cathode due to the combination of oxidizing and acidic conditions [1-4].

One approach for extending the catalyst lifetime is through surface modification of the carbon support. With proper functionals and chemical links at their interface, metal support interaction has been shown to enhance activity [4-6]. One of the strategies is the functionalization of the support with relatively stable oxygenated groups that can anchor the metal nanoparticles avoiding their agglomeration. However, such treatment often makes the support susceptible to electrochemical corrosion in acid media, and could affect the Pt and the ionomer distribution, thereby altering the electron and proton conductivities in the electrodes [7].

Other materials that are chemically stable under these conditions such as TiO_2 do not have sufficient electrical conductivity for this application. Thus, the synthesis and characterization of metal oxides/carbon composite materials have become a very active area of research [8]. Numerous metal oxides have been studied, with TiO_2 leading the group, either alone or in combination with other transition metals and/or carbon [8-14]. TiO_2 /carbon nanotubes [12, 14] and TiO_2 /graphene [15] are perhaps the most successful materials in terms of electronic conductivity, chemical inertness, and long-term stability under accelerated test conditions. However, carbon nanotubes and graphene are still expensive, and other materials are required to make PEMFCs competitive devices.

In chapter 4, we have employed glucose-doped pristine Vulcan[®] XC-72R carbon (G-PV) for the preparation of Pt/ TiO_2 /G-ATV catalyst. This catalyst showed an improvement in terms of electrochemical performance toward the oxygen reduction reaction (ORR) and electrochemical stability when compared with undoped Pt/C catalysts. However, it is not clear how acid treatment influences the adsorption of glucose on carbon, and more importantly, its impact on the long-term stability of the carbon support.

In this chapter, we examine how PV surface can be functionalised with glucose molecules without the need for the harsh acid treatment prior to TiO_2 deposition. It is worth noting the method has been used to produce hollow TiO_2 nanoparticles for photovoltaics applications and TiO_2 -carbon nanotubes without acid treatment functionalization for lithium-ion battery anodes [16]. However, to the best of our knowledge, this is the first time that this kind of approach has been studied as fuel cell catalysts.

This composite material made from both Vulcan and TiO_2 may be an excellent alternative to pure carbon and could be a platform to demonstrate a proof of concept for further understanding and development. If the crystalline titania nanostructures were well connected and bonded to carbon surface, they should offer composite support that limits carbon oxidation effects from exposure to a corrosive environment. Pt NPs would then be anchored to the titania where a stronger bond with the TiO_2 would be more likely to prevent dissolution of the catalyst while electronic contact with carbon can still percolate an interconnected network. One important objective was to demonstrate that TiO_2 material used in conjunction with graphitic carbon has potential for use in low temperature polymer electrolyte fuel cell electrodes as others have also suggested from RDE and first principle simulations [17-19].

A post-deposition heat treatment at 500 °C under nitrogen was carried out to induce the pyrolysis of glucose and promote TiO_2 crystallization. Pt nanoparticles were deposited on the support systems to form electrocatalyst and their electrochemical properties were evaluated in order to understand the influence of glucose doping on catalyst performance and durability. The ORR activity for each sample was investigated using a rotating disk electrode (RDE) system. The electrocatalysts were tested using an accelerated durability test (ADT) designed to rapidly degrade performance by potential cycling. Cycling tests can be very aggressive towards carbon supported platinum catalysts [20]. The test results were compared for electrocatalysts with and without TiO_2 addition to the carbon substrate. Some of catalyst materials characterized include:

- (i) Pt/C catalysts
- (ii) Pt/glucose doped Vulcan[®] XC-72R (Pt/G-PV)
- (iii) Pt/ TiO_2 /acid-treated Vulcan[®] XC-72R (Pt/wt% TiO_2 /ATV)
- (iv) Pt/ TiO_2 / glucose doped pristine Vulcan[®] XC-72R (Pt/% TiO_2 /G-PV).

5.2 Experimental

Carbon substrate modification routes has been discussed in detail in Chapter 2. Physical characterization of the supported Pt electrocatalyst was done using TGA, XRD, BET, TGA, TEM, HRTEM and XPS, which is detailed in Chapter 3. All cyclic voltammetry (CV) and electrochemical impedance spectroscopy (EIS) measurements were performed at room temperature (25 °C) in N₂ saturated 0.5M H₂SO₄ electrolyte solution. Impedance spectra were collected over a frequency range of 100 kHz to 0.1Hz at a DC bias potential of 0.425 V. The ORR activity for each sample was investigated using a rotating disk electrode (RDE) system from Pine Research Instrumentation in combination with a Gamry Reference 600 potentiostat. For these studies, the electrolyte was saturated with oxygen for 15 minutes, and the potential was swept from 1.0 to 0.3 V at a scan rate of 5 mV/s at rotation rates between 400 and 1600 revolution per minute (rpm). The results start off with materials characterization which is followed directly by electrochemical characterization.

5.3 Physical characterization results and discussion

5.3.1 Thermal analysis and samples composition determination

Samples were exposed to an annealing step under nitrogen at 500 °C for 2 hours. In the case of the glucose-doped samples, this step is a requirement to induce the pyrolysis of glucose. The effect of heat treatment on glucose, ATV, PV, and TiO₂ in argon is illustrated in Fig. 5.1 The only major changes at temperature up to 500 °C was the pyrolysis of glucose with mass losses observed at approximately 340 and 495 °C which are related to the elimination of water and volatile decomposition products [21]. The glucose loading, TiO₂-to-carbon ratio, as well as the Pt content in the catalyst samples, were obtained using thermogravimetric analysis in air instead of argon. Typical TGA and DSC runs for a representative sample, before and after Pt deposition, 14%TiO₂/G-PV and Pt/14%TiO₂/G-PV, are shown in Fig.5.2. The presence of TiO₂ and Pt catalyze the decomposition of carbon with onset temperatures at 280°C and 375 °C vs. 510 °C for PV, but it does not have any impact on the residual masses of TiO₂ and Pt summarized in Table 5.1. There is a significant difference in Pt content between samples prepared with and without glucose despite a 20 wt% Pt loading was targeted for all the samples. The difference is likely due

to changes in the surface properties of the support due to the presence of glucose or glucose pyrolysis products.

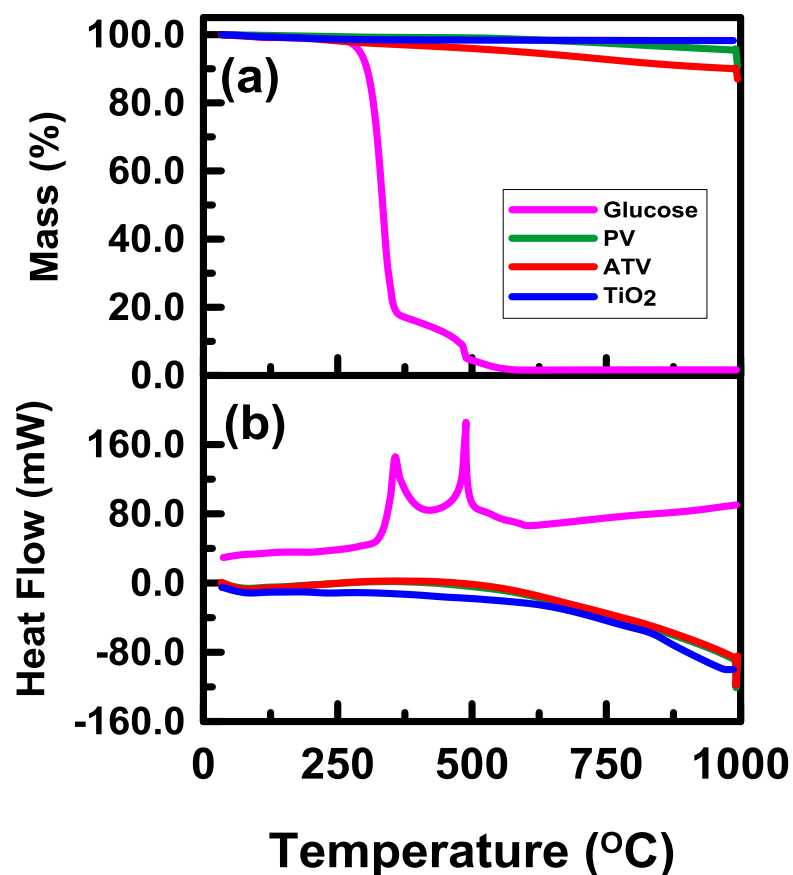


Figure 5.1: The (a) TGA and (b) DSC curves obtained under argon for Glucose (G), Pristine Vulcan (PV), Acid treated Vulcan (ATV) and synthesized TiO₂. Experimental conditions: sample mass ~ 10 mg, gas flow rate: 50 mL/min, and heating rate of 20 °C/min.

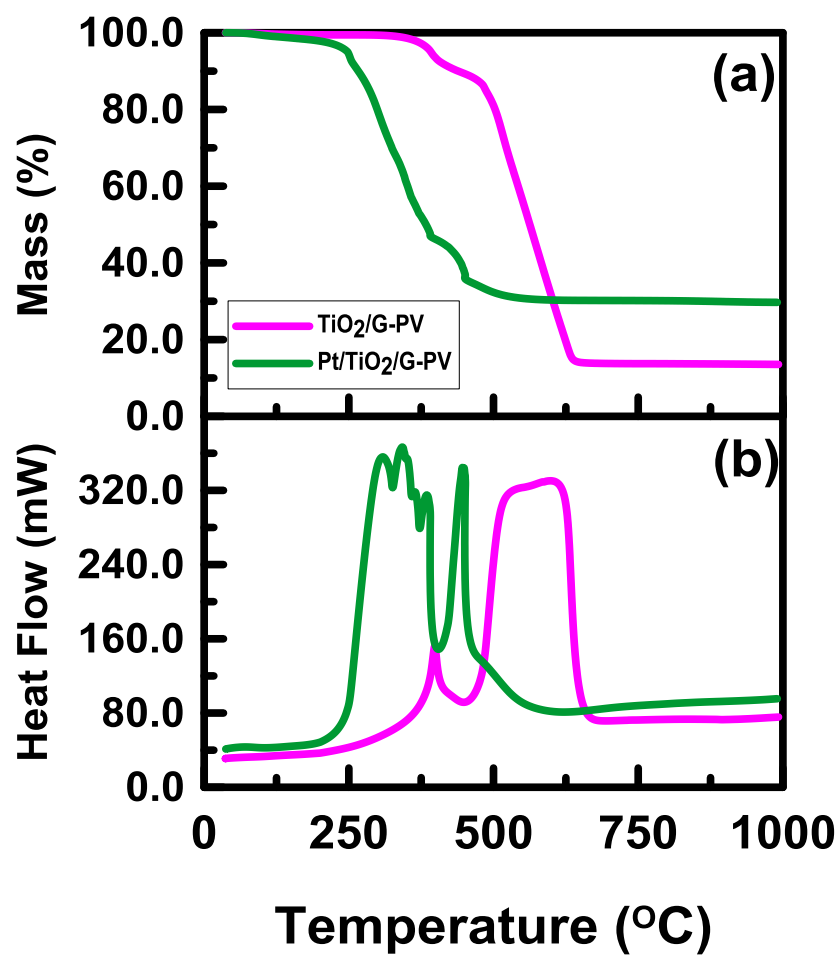


Figure 5.2: (a) TGA and (b) DSC curves obtained under air for 14% TiO₂/ G-PV, and Pt/14% TiO₂/ G-PV. Experimental conditions: sample mass ~ 10 mg, gas flow rate: 50 mL/min, and heating rate 20 °C/min.

Table 5.1: TGA showing weight % of TiO₂ and Pt in the synthesized catalyst materials

Samples	Weight % of TiO ₂	Weight % of Pt
Pt/PV	---	21.6
Pt/ ATV	---	24.5
Pt/ G-PV	---	26.0
Pt/TiO ₂ /ATV	5	23.9
Pt/TiO ₂ /ATV	7.5	21.6
Pt/TiO ₂ /ATV	10.3	20.0
Pt/TiO ₂ /ATV	14	13.8
Pt/TiO ₂ / G-PV	8.0	24.0
Pt/TiO ₂ / G-PV	13.5	16.5
Pt/TiO ₂ / G-PV	22.0	11.9
Pt/TiO ₂ / G-PV	24.0	13.0
Pt/TiO ₂ / G-PV	32.0	10.0

5.3.2 The impact of carbon pre-treatment on the properties of TiO₂/ATV and TiO₂/G-PV substrates.

The second noticeable difference between treatments was the BET surface area of the final materials. The surface area values obtained for TiO₂, the three carbon supports (ATV, PV, and G-PV after annealing at 500 °C in N₂) and the composite materials (TiO₂/ATV and TiO₂/G-PV) with TiO₂ loadings between 3 and 32% are compared in Fig. 5.3. There was an increase in surface area after acid treatment activation from 234 m²/g (PV) to 251 m²/g (ATV). However, the reduction in area after annealing at 500 °C is more pronounced in the case of ATV (192 m²/g) than in G-PV (211 m²/g) that we assign to the

presence of glucose pyrolysis product on the surface of Vulcan carbon. The reduction of the BET surface area on both carbon substrates (ATV and G-PV) after the deposition of TiO_2 is also significant, but again, the effect is more pronounced in the case of the acid treated carbon samples with comparable TiO_2 loadings. A 49 % reduction was observed for ATV with 14 wt% TiO_2 vs. 16% for a 14% TiO_2 /G-PV sample. Similar result was observed on CNT/ TiO_2 [21] with an increased surface area (252.9 m^2/g) when compared with the surface area of the CNTs (158.9 m^2/g) and TiO_2 (98.6 m^2/g) nanoparticles.

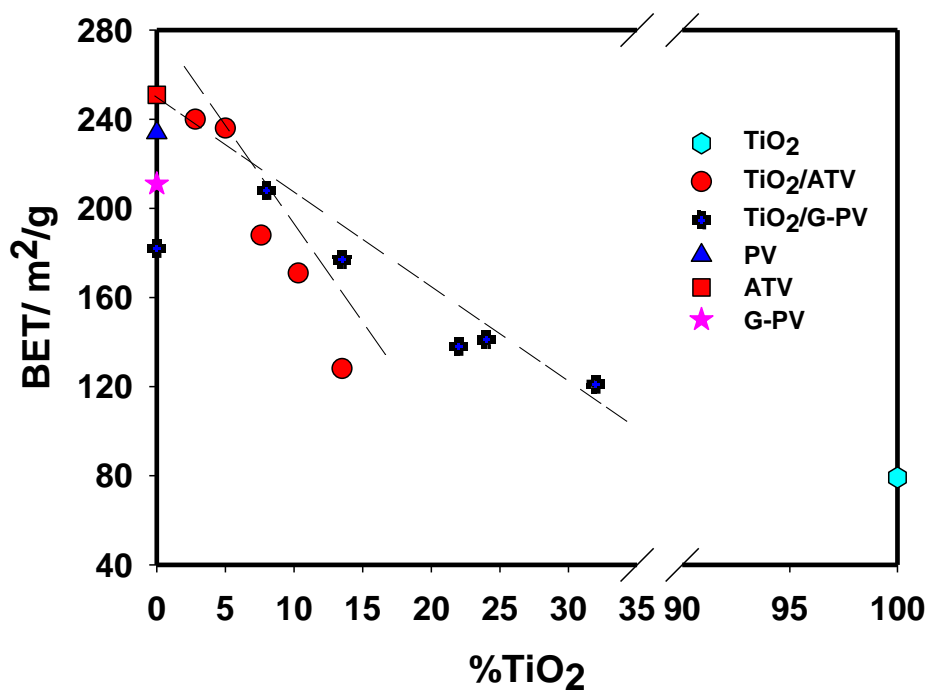


Figure 5.3: BET surface areas of glucose (G), pristine vulcan (PV), acid treated Vulcan (ATV), glucose doped Vulcan (G-PV) and composite supports (TiO_2 /ATV and TiO_2 /G-PV) following heat treated at 500 °C for 2 hours.

5.3.3 Physical Properties of Pt on TiO₂/ATV and TiO₂/G-PV

Figure 5.4 shows the TEM image acquired for Pt/PV. The grey area in these micrographs represents dispersion of Vulcan carbon while the dark tiny spots are Pt NPs. Numerous dark spots which formed agglomerates are seen on this unmodified carbon substrate. The agglomerated Pt particles are of uneven size. The equivalent particle size distributions based on 200 sample collection data are also shown in Figure 5.4 (b). The average particle size of Pt nanoparticles in Pt/PV is 4.4 ± 1.6 nm.

Figure 5.5 shows TEM images of composite catalysts Pt/TiO₂/ATV and Pt/TiO₂/G-PV composite catalysts with their respective particle size distribution data. A more detailed examination reveals that Pt nanoparticles are uniformly dispersed on the surface of the TiO₂/G-PV support with a relatively uniform distribution proving the introduction of TiO₂ inhibits the aggregation of Pt particles, even at high TiO₂ loading ratio. Pt particles appear more dispersed on metal oxide based support than on carbon than however, it is hard to distinguish between the TiO₂ and Pt particles on this TEM image. The original form of the support plays a great role in their TEM images thus the Pt/TiO₂/G-PV material was less likely to agglomerate since TiO₂ particles have a particle size of ~ 5 nm when compared to the particle size of carbon material which reveals a lot of agglomerates with no uniform distribution of Pt particles was observed.

The average particle size of Pt nanoparticles in Pt/TiO₂/ATV, and the Pt/TiO₂/G-PV were 4.3 ± 0.6 nm and 3.5 ± 1.2 nm, respectively. Despite the small differences in the particle size distribution between samples, the presence of TiO₂ does not adversely affect the dispersion of the catalyst nanoparticles in the TiO₂/carbon substrates, that in the case of TiO₂/G-PV could even be more favourable based on TEM results. The particle sizes are in good agreement with those estimated from the broadening of the Pt(111) peak in XRD analysis using the Debye-Scherrer equation (4 to 6 nm).

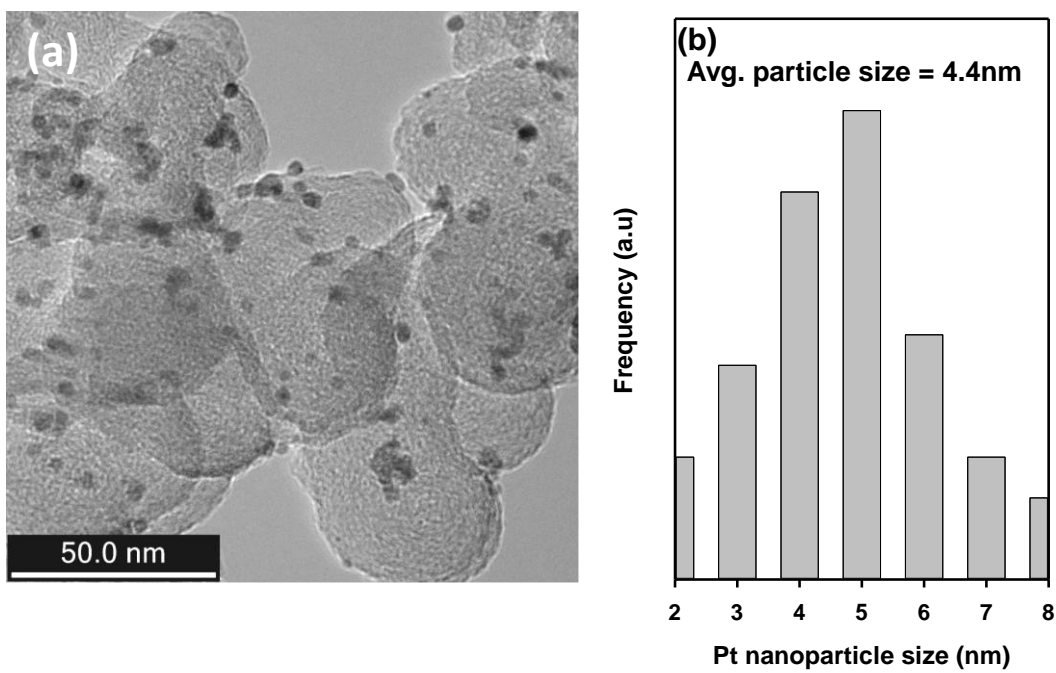
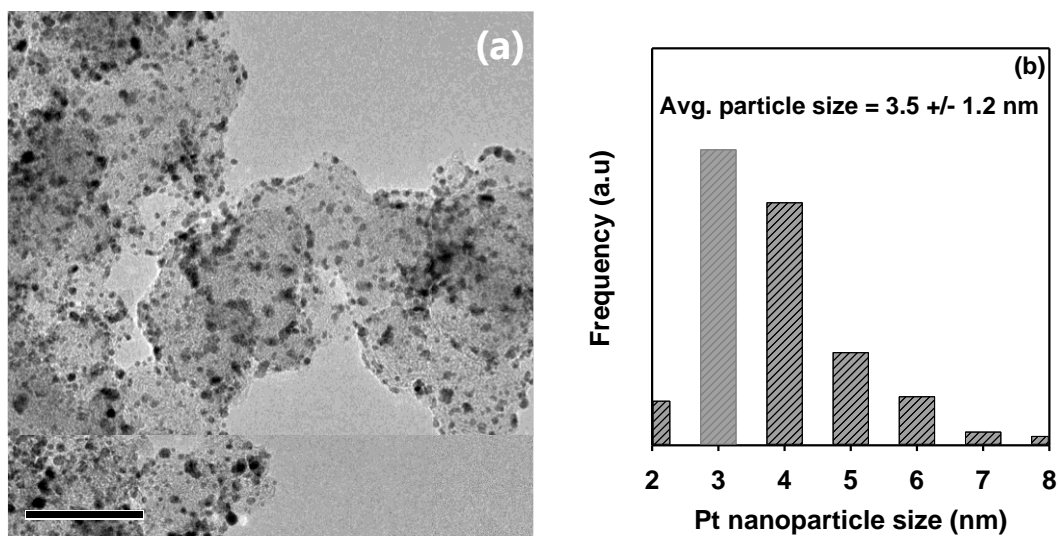


Figure 5.4: Transmission electron micrograph (a) and (b) Pt particle size distribution of Pt/PV catalyst.



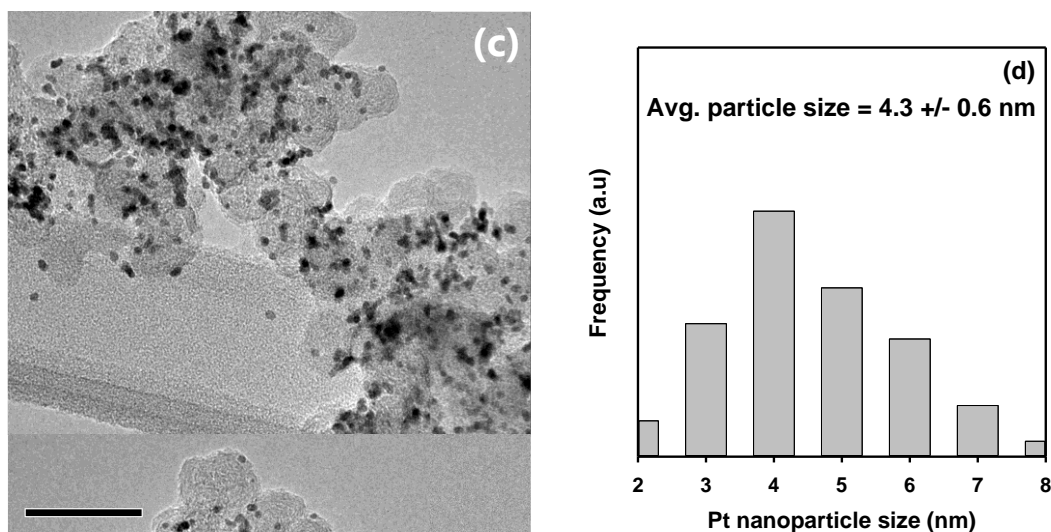
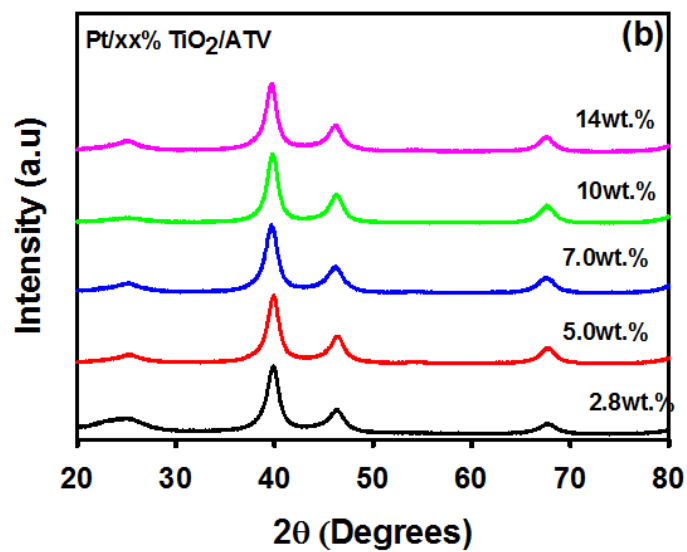
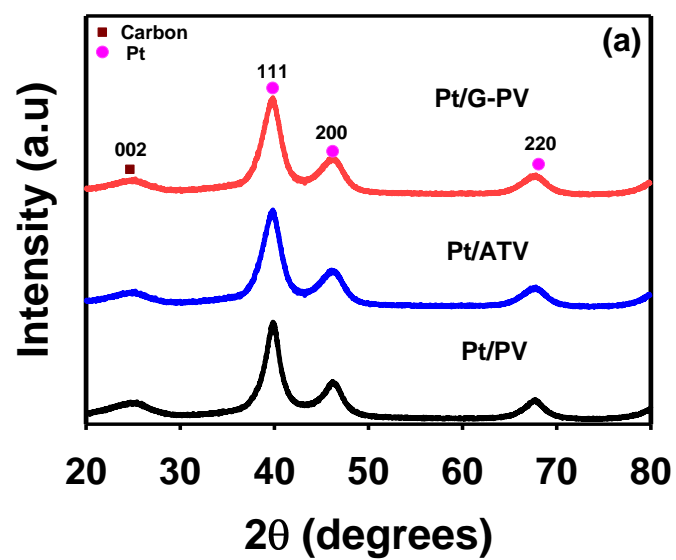


Figure 5.5: Transmission electron micrographs and Pt particle size distribution for: (a) and (b) 14 wt% TiO₂/GPV, (c) and (d) 14 wt% TiO₂/ATV

The particle size and crystallinity of supported Pt electrocatalyst employed in this study was investigated using XRD. Figure 5.6 shows the X-ray diffraction pattern of the catalysts on Vulcan carbon and composite supports recorded at recorded at 2θ range of 20-80°. The peak observed at 26° observed in all XRD pattern is attributed to the (002) reflection for graphitic carbon. Peak positions for the Pt metal are indicated by Miller indices. The peaks are consistent with face-centered cubic (fcc) structure for Pt, namely, the peaks at ca. 40°, 46°, 67.5°, 81.5°, and 86° were reflected from Pt(111), Pt(200), Pt(220) Pt(311), and Pt(220) planes, respectively. These diffractograms indicate that well crystallized Pt nano particles were well formed during the impregnation process. The average particle size and lattice parameter values are presented in Table 5.2 for Pt supported on carbon and oxide based supports. Composite supports appear to limit the growth of catalysts to a much greater extent when synthesized under the same conditions [22-23]. This may be attributed in part to the interaction between Pt and the electropositive transition metals used in the support, further suggesting support specific electrocatalysts effects.



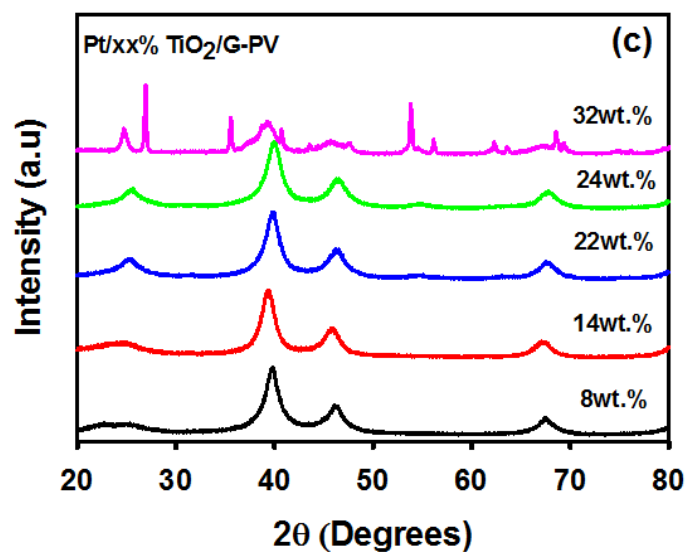


Figure 5.6: XRD patterns: (a) Pt on carbon supports(b) Pt/ wt%TiO₂/ATV (c) Pt/ wt%TiO₂/G-PV

Table 5.2: XRD average crystalline size of Pt in the synthesized catalyst materials.

Samples	Position (2θ)	Pt crystalline size (nm)
Pt/PV	39.811	4.6
Pt/ ATV	39.64	4.1
Pt/ G-PV	39.69	3.9
Pt/5%TiO ₂ /ATV	39.35	3.9
Pt/7.5%TiO ₂ /ATV	39.50	4.6
Pt/10%TiO ₂ /ATV	39.50	4.8
Pt/14%TiO ₂ /ATV	39.50	5.2
Pt/8%TiO ₂ / G-PV	39.64	3.9
Pt/14%TiO ₂ / G-PV	39.35	3.7

Pt/22%TiO ₂ / G-PV	39.76	4.2
Pt/24%TiO ₂ / G-PV	39.91	4.4
Pt/32%TiO ₂ / G-PV	40.07	4.9

XPS measurements were performed to understand the interactions of TiO₂ and Pt in the catalysts. In addition, XPS analysis was performed to evaluate if the addition of glucose resulted in changes in the electron structure of TiO₂ and Pt. The chemical states of O, Ti, C and Pt were investigated by XPS and the results are shown in Fig. 5.7, the binding energies (BE) and relative intensities are summarized in Table 5.3 along with reference values for prepared TiO₂, TiO₂ Degussa P25 [51] and Pt [10]. No significant differences were observed in the BE of O1s between Pt/TiO₂/G-PV (533.4 eV and 532.2 eV) and Pt/TiO₂/ATV (533.9 eV and 532.3 eV), but in the case of Ti, an appreciable shift of approximately 1 eV was observed in the Ti2p bands of the glucose doped substrate (TiO₂/G-PV) when compared with TiO₂ anatase. Similar changes in the BE of Ti2p in the case of c-doped TiO₂ deposited on CNT, 459.4 eV (Ti2p_{3/2}) and 465.1 eV (Ti2p_{1/2}), have been attributed to the substitution or intercalation of carbon in the crystal structure of TiO₂ [24].

In the composite with titania, the O1s peak was considerably diminished after Pt deposition which could be due to the interaction between Pt and Ti. The O1s peak in Pt/TiO₂/G-PV also show positive shift in BEs compared with pure TiO₂ and TiO₂/G-PV support. Similar shift in O1s was observed in Camaco's work [13], an indication of electronic interaction between carbon and TiO₂ particles. The latter observed shift can be ascribed to the mutual interaction between Pt and TiO₂ particles. The analysis of the Ti 2p peaks shows similar effect with respect to TiO₂ and TiO₂/G-PV however the peak positions remain essentially unchanged following Pt deposition. The fact that the Ti peaks do not change signifies that there is no formation alloy formation between the two elements.

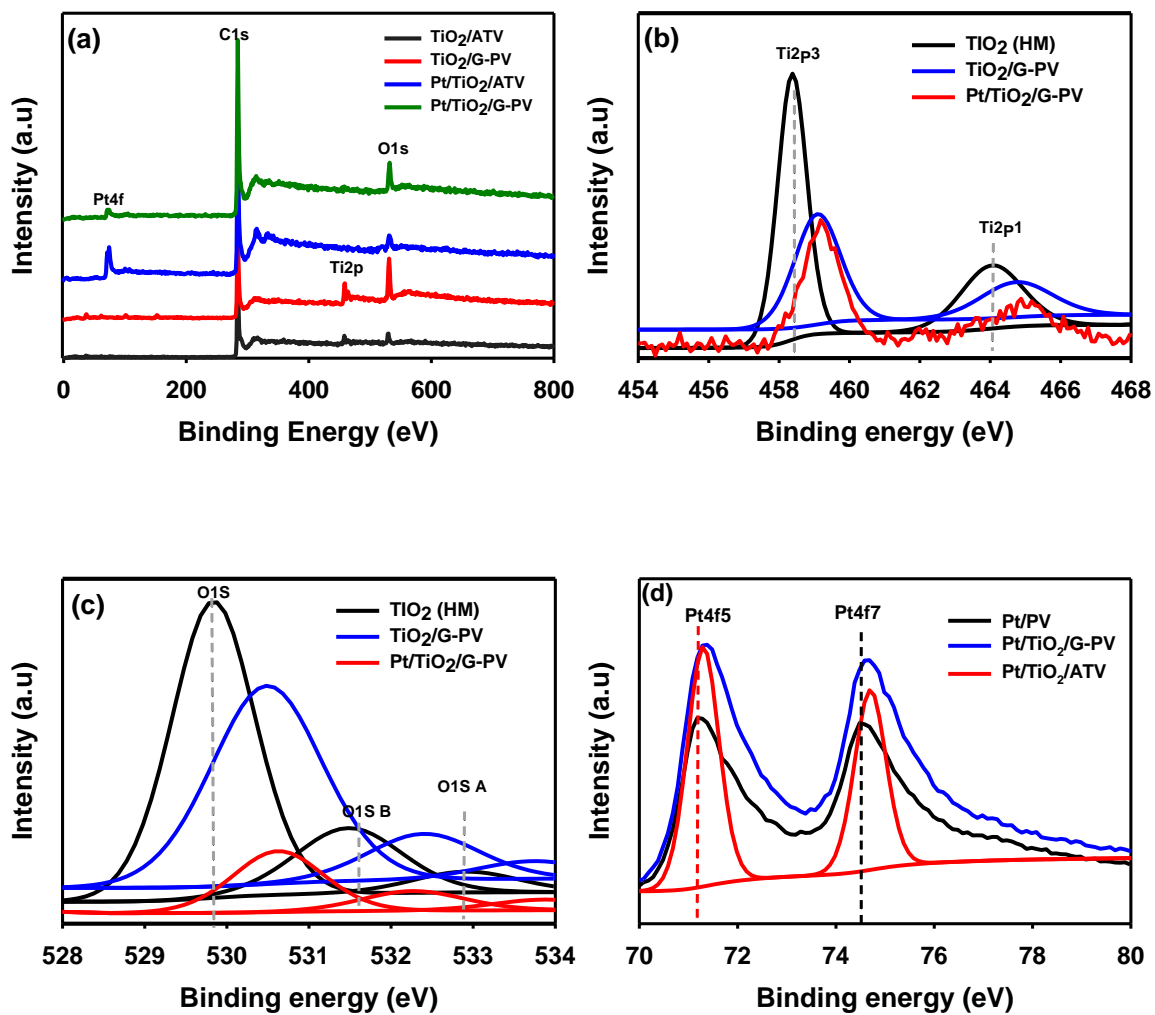


Figure 5.7: (a) XPS surface scan of C, Ti, O1s and Pt (b) Ti_2 peaks (c) O1s peaks and (d) Pt peaks scans for TiO_2 , $\text{TiO}_2/\text{G-PV}$ and $\text{Pt}/\text{TiO}_2/\text{G-PV}$ catalyst materials.

Table 5.3: XPS data for reference materials and prepared Pt/TiO₂/ATV and Pt/TiO₂/G-PV samples

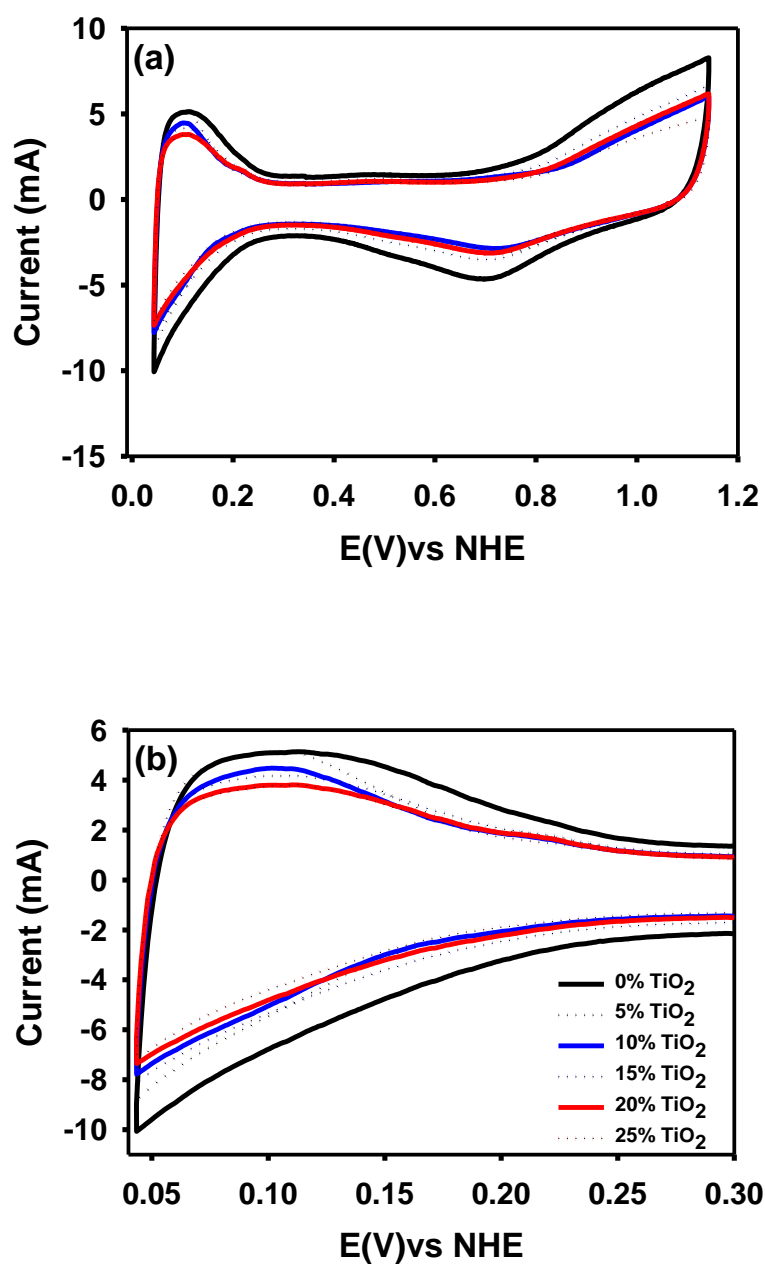
Catalyst	Species	Binding Energy (BE) /eV	Atomic %
TiO ₂ from ref. [22]	Ti2p3	458.3	
	Ti2p1	464.2	
TiO ₂ (Degussa) from ref.[10]	Ti2p3	458.5	
	Ti2p1	464.2	
Pt/14% TiO ₂ /ATV	Ti2p3	459.1	31.8
	Ti2p1	464.1	68.2
Pt/14% TiO ₂ /ATV	Pt4f7	71.3	44.1
	Pt4f7 B	73.6	23.4
	Pt4f7 A	72.1	32.5
Pt/14% TiO ₂ /G-PV	Pt4f7	71.3	48.5
	Pt4f7 B	73.5	24.5
	Pt4f7 A	72.2	27.1

5.4 Electrochemical characterization results

5.4.1 Ex-situ and In-situ Addition of TiO₂ NPs on standard Pt/C catalyst.

Preliminary studies of composite electrodes prepared using a range of TiO₂ compositions (5-25%) through mechanical mixing on 20 wt% Pt/C (JM), commercial catalyst was carried out in a three electrode system. The effect of TiO₂ loading in direct contact with the carbon support and platinum catalyst can be easily evaluated through this approach. The voltammograms are shown in Figure 5.8 and display

distinct Pt hydrogen absorption /desorption regions. The electrochemical surface areas decreased as more TiO_2 is added to the composite electrode. Agglomeration of the TiO_2 particles impaired Pt interaction with more electronically conductive carbon support resulting in blockage of catalyst layer with concomitant decreased in accessible surface area [25-26].



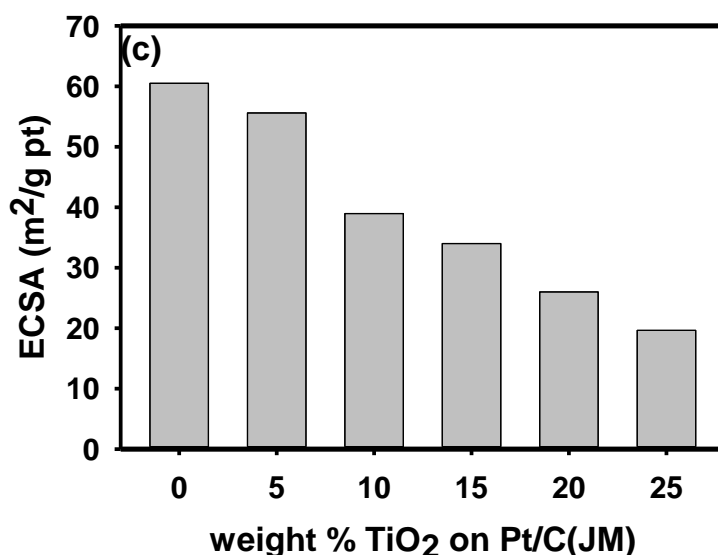


Figure 5.8: (a) Half-cell CV of mechanically mixed TiO₂ on Pt/C catalyst at different concentrations in N₂-saturated 0.5M H₂SO₄ solution at a scan rate of 50 mV/s, test temperature: 25 °C (b) Expansion of the hydrogen adsorption/desorption regions (c) Change in ECSA as a function of TiO₂ wt% loading.

EIS data was analysed to confirm changes in electrode resistance following incorporation of varied amount of TiO₂ as shown in Figure 5.9. This is done by constructing Nyquist plots to determine how resistivity, and therefore conductivity, varies in the catalyst layer. In addition, capacitance plots are also shown to follow changes in the electrode surface areas. Electrode resistivity increased with increased TiO₂ loadings, while the limiting capacitance decreased. Typically an increased limiting capacitance denotes a more available active area for electrochemical reaction. Conductivity and active area are lower at high TiO₂ concentrations due to covered platinum sites, blocked pores, and increased electronic resistance. The decreased capacitance reflects changes in the electrode surface area. This result is in agreement with pattern of changes in the catalyst active surface areas as depicted.

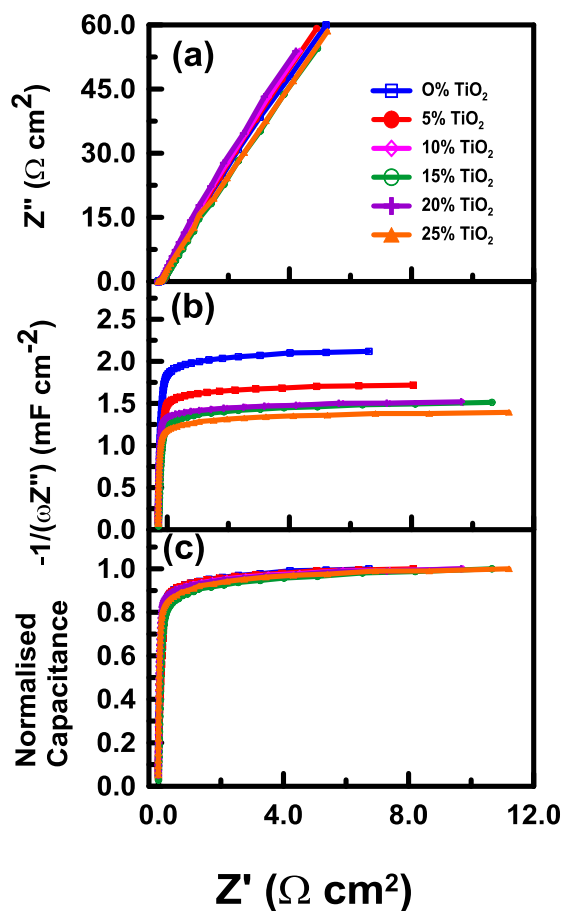


Figure 5.9: EIS characterization of mechanised mixed TiO_2 on Pt/C catalyst @ 0.425V biased potential in N_2 -saturated 0.5M H_2SO_4 solution (a) Nyquist plots (b) Limiting capacitance plots. (c) Normalised capacitance plots.

In order to maximise contact with composite catalyst elements, TiO_2 NPs of various weight % loadings were synthesized on Pt/C (JM, commercial catalyst). This sol-gel synthesis of TiO_2 particles on Pt based commercial catalyst was done *in situ* as a potential improvement over mechanically mixed composite materials. Thermal analysis showed that the TiO_2 loading ranged between 7-52 wt.% (not shown). In this case, the addition of TiO_2 NPs on Pt/C catalyst produced significant changes in the electrochemical performance. Fig 5.10 compares the CVs obtained with varying wt% TiO_2 . A gradual decrease in the double layer current as more TiO_2 is introduced into the catalyst. The peak hydrogen absorption – desorption regions also decreased sharply

as the electrode becomes more resistive. The charge due to hydrogen desorption almost disappeared at 52% TiO_2 loading. Thus, irrespective of the synthesis condition (mechanical vs *in situ* of TiO_2 on Pt/C electrode, a substantial loss in Pt surface areas was observed due to the increased resistance. In addition, both commercial and in-house synthesized TiO_2 produced similar results when added to the Pt/C electrode.

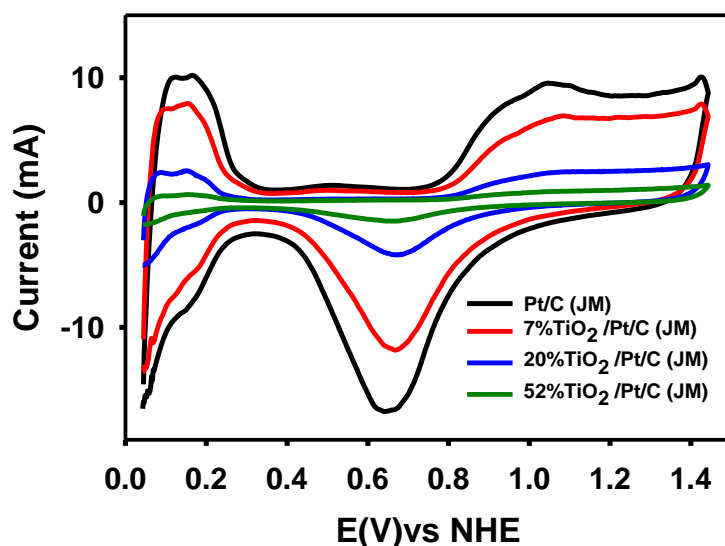


Figure 5.10: Half-cell CV of *in situ* deposited TiO_2 on Pt/C catalyst at different concentrations in N_2 -saturated 0.5M H_2SO_4 solution at a scan rate of 50 mV/s, test temperature: 25 °C

5.4.2 Electrochemical characterization of Pt/ TiO_2 /ATV catalysts

In a more practical approach, deposition of TiO_2 NPs onto the carbon support was done prior to Pt deposition. We expect better interfacial contact, perhaps even a core-shell like (TiO_2/C) material with carbon core and thin film TiO_2 NPs shell. However the formation of this composite configuration is often difficult due to segregation of TiO_2 NPs on the hydrophobic carbon substrate. Thus, the carbon substrate was functionalised in acid to

control nucleation growth of TiO_2 NPs on a more hydrophilic surface. With a more hydrophilic surface, there will be control growth of TiO_2 NPs on carbon surface with mutual contacts at the heterogeneous interface. The amorphous TiO_2 /ATV supports were heat treated in nitrogen to form a crystalline composite supports. The heat treatment was done at 500°C and 850°C for two hours prior to Pt deposition.

Typical voltammograms for the observed CVs in the proposed core shell Pt/ TiO_2 /ATV catalysts are depicted in Fig. 5.11 with metal oxide loadings varied from 2.8-10% weight composition of the electrode structure. Table 5.4 shows the corresponding ECSA values of the composite catalysts. Higher ECSA values are observed at lower TiO_2 loadings (up to 5wt %), a significant performance improvement in comparison to mechanically mixed composite catalysts. Higher accessible Pt surface areas may be ascribed to more synthetic control of TiO_2 NPs in the electrode material with more favourable interfacial contacts. A gradual decrease in ECSA value was also observed following increased TiO_2 loadings. The impedance response of these catalysts is shown in Figure 5.12. As expected electrode resistance will increased with loss of more conductive carbon content and consistence with the limiting capacitance plots.

In addition, we observed greater loss in ECSA value when supports are annealed at 850°C in inert condition. This is related to the growth of TiO_2 particles during phase transformation from anatase to rutile phase at the extreme temperature range. As a results, annealing condition was subsequently optimised for all prepared catalysts at 500°C .

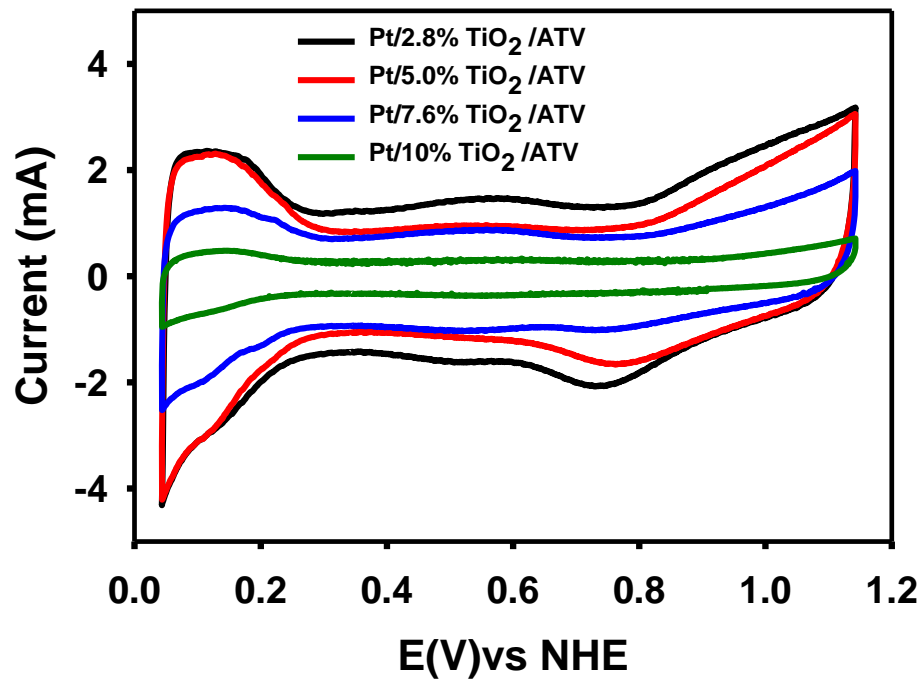


Figure 5.11: Half-cell CVs of Pt/TiO₂/ATV catalysts in N₂-saturated 0.5M H₂SO₄ solution at a scan rate of 50 mV/s test temperature: 25 °C

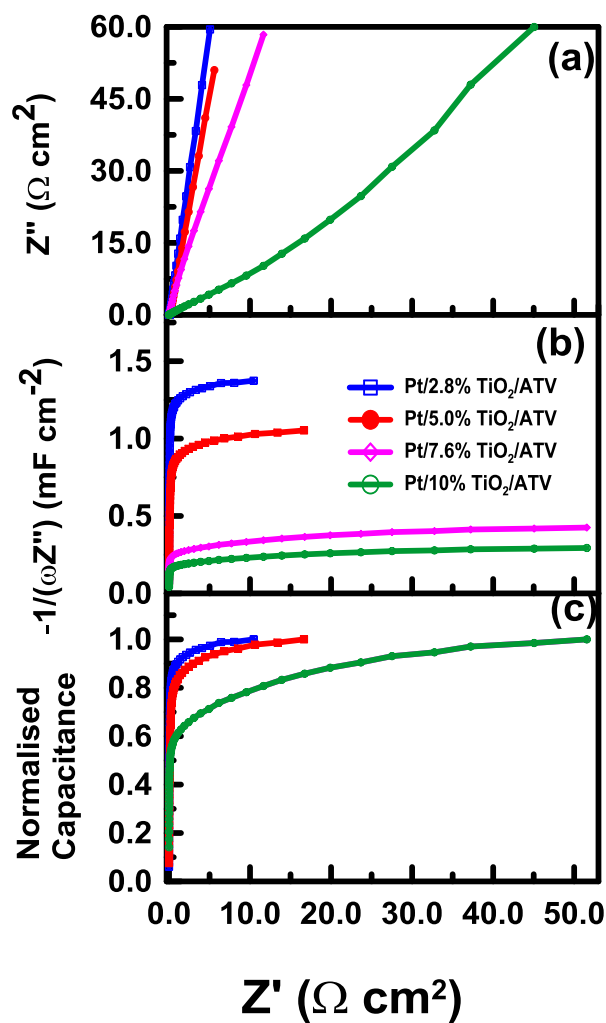


Figure 5.12: EIS characterization of Pt/TiO₂/ATV catalysts @ 0.425V biased potential in N₂-saturated 0.5M H₂SO₄ solution (a) Nyquist plots (b) Limiting capacitance plots. (c) Normalised capacitance plots.

Table 5.4: ECSA values of Pt/TiO₂/ATV catalysts.

Samples	TGA wt% TiO ₂	ECSA (m ² /g)
Pt/TiO ₂ /ATV	2.8	43.5 ± 6.4
Pt/TiO ₂ /ATV (500°C)	5	37.5 ± 3.8
Pt/TiO ₂ /ATV (850°C)	5	32.2 ± 2.7
Pt/TiO ₂ /ATV (500°C)	7.6	29.3 ± 3.1
Pt/TiO ₂ / ATV	10.3	23.2 ± 5.4
Pt/TiO ₂ / ATV	20	18.6 ± 1.8
Pt/TiO ₂ / ATV	20	16.9 ± 2.6

5.4.3 Electrochemical characterization of Pt/TiO₂/G-PV catalysts and comparison analysis with Pt/TiO₂/ATV catalysts.

In order to understand the impact of glucose on the activity and stability of Pt, different electrochemical measurements were carried out to determine the Pt specific surface area (m²/g Pt), the onset potential for the oxygen reduction reaction along with the mechanism of the reaction, and the kinetic current at 0.65V. Due to the relevance of the ECSA as characterization parameter in the field of PEMFCs, these studies will be discussed before the oxygen reduction reaction experimental kinetic data.

Typical CVs for four representative samples, Pt/ATV, Pt/G-PV, Pt/14 wt% TiO₂/ATV and Pt/14 wt% TiO₂/G-PV are shown in Fig.5.13 and after subjected to accelerate stress test for 4000 cycles. The most distinctive features in these samples are the presence of well-defined hydrogen adsorption/desorption peaks and a reduction on the quinone/hydroquinone peaks (0.4-0.8V) after the addition of TiO₂. The beginning of life

(BOL) ECSA values are summarized in Table 5.5 for the as prepared catalysts. As expected, the BOL-ECSA of the composite materials is strongly dependent on the TiO_2 loadings; a comparison between catalyst inks prepared using ATV and G-PV modified carbon with TiO_2 loadings between 7 and 14 wt% for TiO_2/ATV and between 8 and 32 wt% for $\text{TiO}_2/\text{G-PV}$, and Pt contents between 10wt% and 20.5%, is presented in Fig. 5.14. For the Pt/ TiO_2/ATV catalysts, there is a sharp decrease in ECSA after the addition of TiO_2 , a 57 % reduction on ECSA when compared with Pt/ATV at a TiO_2 loading of 14 wt%.

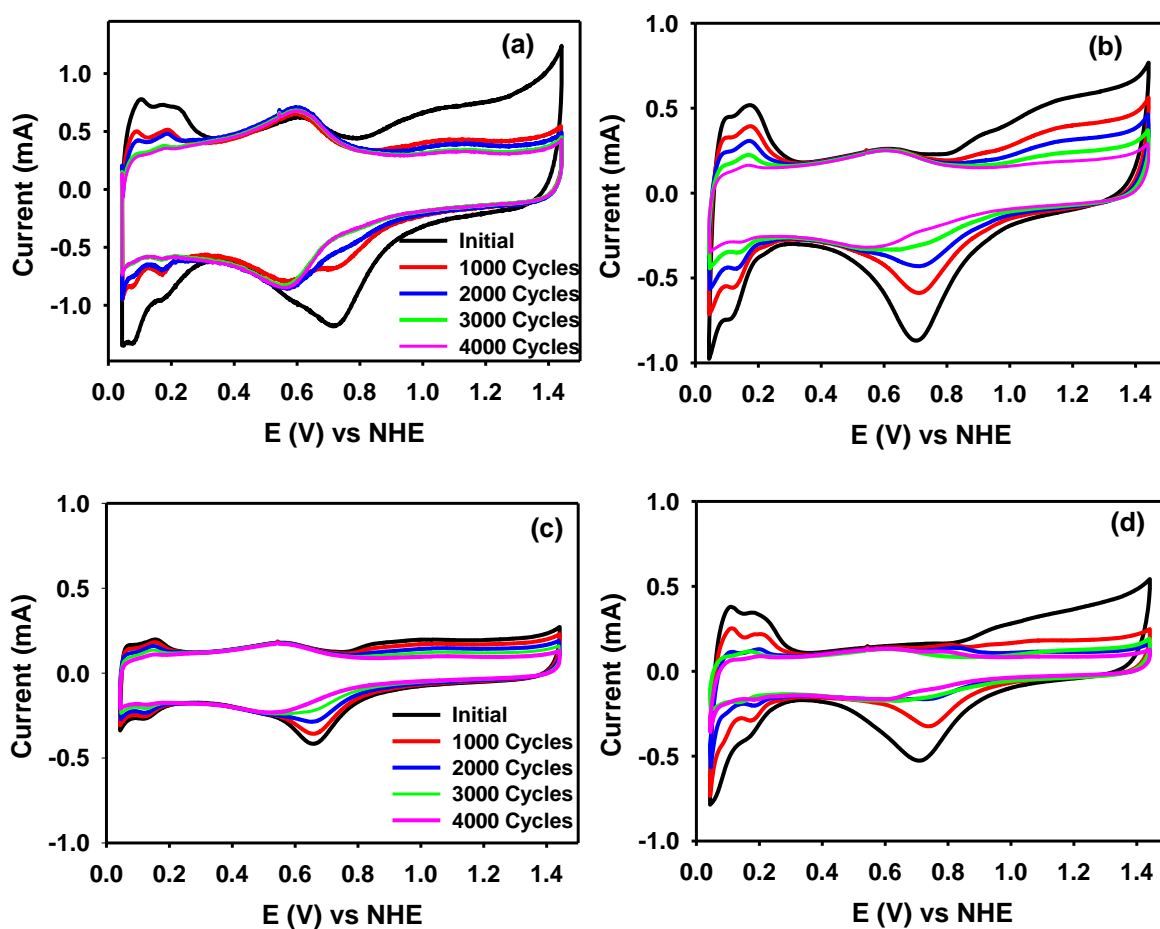


Figure 5.13: Half-cell CVs for: (a) Pt/ ATV, (b) Pt/ G-PV, (c) Pt/ 14 wt% TiO_2/ATV , and (d) Pt/ 14 wt% $\text{TiO}_2/\text{G-PV}$ catalysts in argon-saturated 0.5M H_2SO_4 solution at a scan rate of 50 mV/s. Aging conditions: 4000 potential cycles at 25 °C. Pt loading $0.05 \pm 0.01 \text{ mg/cm}^2$.

Table 5.5: Summary of electrocatalytic activity and stability

Samples	BOL ECSA (m ² /g Pt)	EOL ECSA (m ² /g Pt)	Onset Potential for ORR (V)	i _k (mA/cm ²)
Pt/ ATV	36.3 ± 4.8	0.6	0.90 ± 0.08	14.7 ± 0.6
Pt/G-PV	42.3 ± 2.2	4.9	0.92 ± 0.01	15.8 ± 1.8
Premetek (20%Pt /V)	64.2 ± 5.7	2.2	0.91 ± 0.6	16.1 ± 0.4
Pt/14% TiO ₂ /ATV	15.6 ± 1.6	3.7	0.92 ± 0.03	14.2 ± 2.1
Pt/14% TiO ₂ /G-PV	46.2 ± 5.4	7.6	0.94 ± 0.01	18.0 ± 1.1
Pt/22% TiO ₂ /G-PV	36.3 ± 2.4	9.7	0.95 ± 0.02	17.6 ± 1.7
Pt/24% TiO ₂ /G-PV	32.1 ± 6.1	7.4	0.96 ± 0.09	19.2 ± 0.9
Pt/32% TiO ₂ /G-PV	30.7 ± 3.9	4.3	0.94 ± 0.03	16.6 ± 2.3

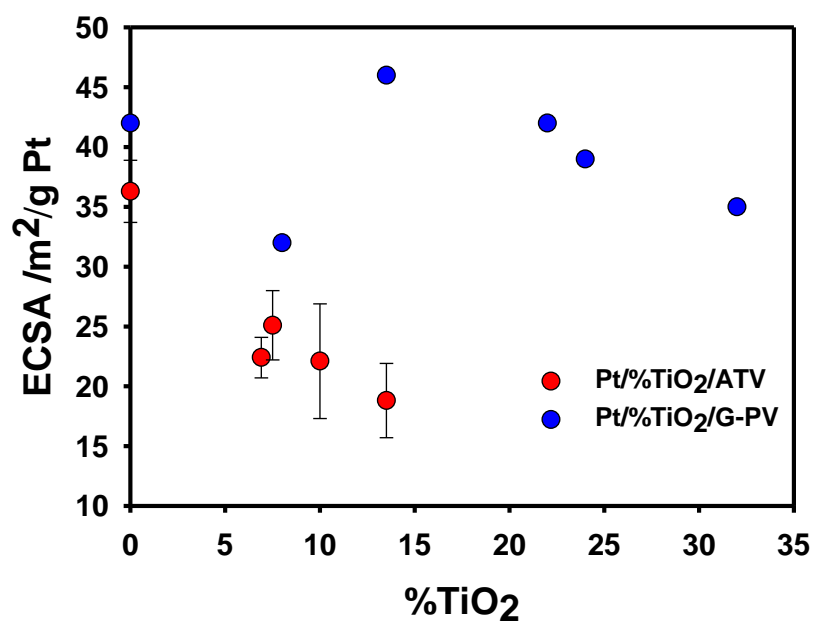
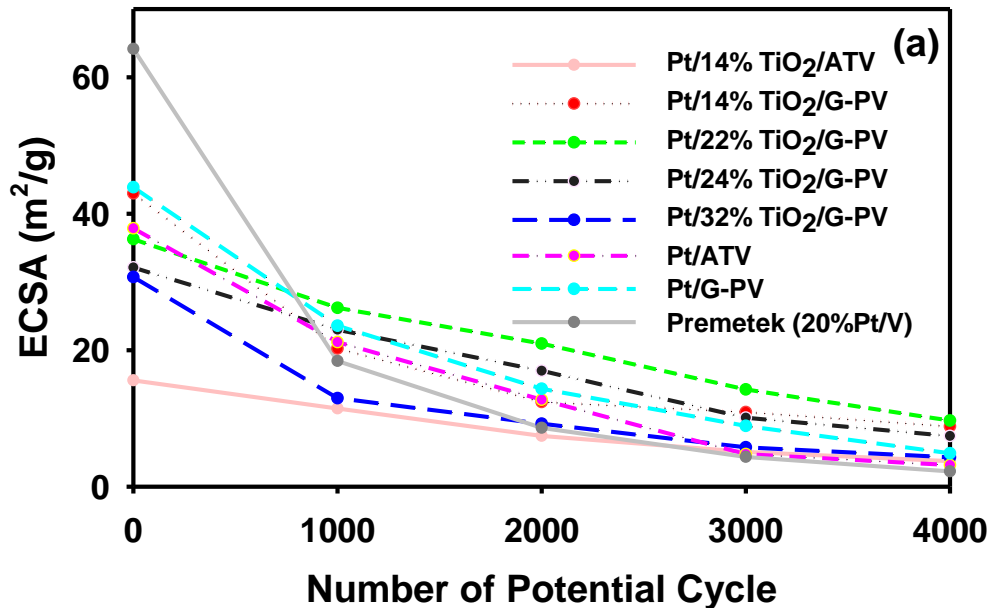


Figure 5.14: Beginning of Life (BOL) Electrochemical cell surface areas as a function of TiO_2 loadings for Pt/ TiO_2 /ATV and Pt / TiO_2 /G-PV.

Figure.5.15 shows the rate of Pt surface area loss is also dramatically slowed in the presence of TiO_2 . If we compare both catalysts that have 14 wt% TiO_2 , we see that the rate of decay is quite similar. However, at any point in time, the G-PV sample has twice the active surface area, indicating that this catalyst will perform better. The same applies for the Pt/G-PV catalyst for which excellent BOL-ECSA values were obtained. The difference cannot be explained by Pt grain sizes difference since both TEM and XRD measurements indicate that similar particle sizes and dispersion for both catalysts. The relatively higher ECSA when glucose doped carbon substrates are compared with acid treated substrates might be associated with the formation of a more conductive C-doped TiO_2 phase in the presence of glucose, as supported by the XPS results. A preferential deposition of Pt in a more stable location such as the interface between TiO_2 and carbon nanoparticles that can prevent Pt aggregation has been also proposed in other studies involving metal oxides [21].



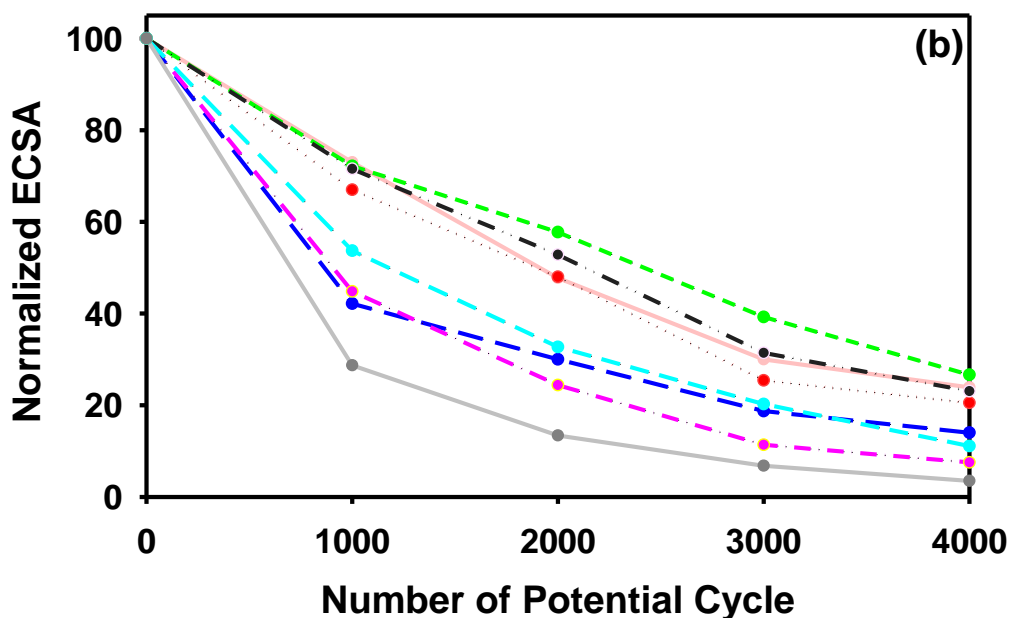


Figure 5.15: ECSA loss and normalized Electrochemical cell surface areas for different catalysts under stability assessment aging conditions.

The impedance responses of catalysts were also studied as a function of cycle number and are shown in Figures (5.16-5.18). In these figures, a, b and c represent Nyquist, capacitance and normalised capacitance plots for the different catalysts. The high frequency region represents the charge transfer process, protons in this case. From the Nyquist plots, we can see that there is a slight change in the ionic resistance profile. In addition, the variations in electrode resistivity can be better visualized through capacitance plots which allow visualization of conductivity within the CL and active area at once. The observed limiting capacitance is proportional to active surface area of the electrode material at beginning of life [27].

Figs. 5.16-18b show capacitance plots observed for representative samples following 4000 potential cycles. The decay pattern of these catalysts is consistent with the results obtained for other standard catalyst material [28]. There is zero difference overtime indicating more stable supports [29].

At the BOL, the limiting capacitance increases in the order of the observed ECSA values with Pt/G-PV showing highest value. For Pt/G-PV catalyst, the active area decreases moderately with increased cycle numbers. Decrease in proton conductivity of the Pt/G-PV electrode is observed under the cycling condition as shown by increasing less steep high frequency slopes. In comparison, composite based electrodes show an initial increase in proton conductivity, the slope remains constant until the EOL, indicating that virtually no change in the electrode resistivity occurred. In addition, there is a slight decrease in resistance over time with TiO_2 in the catalyst layer, leading to slightly higher limit capacitance. The capacitance plots were normalised by dividing them by the maximum capacitance value (Figs 5.16-18c) to show differences in CL resistance between samples.

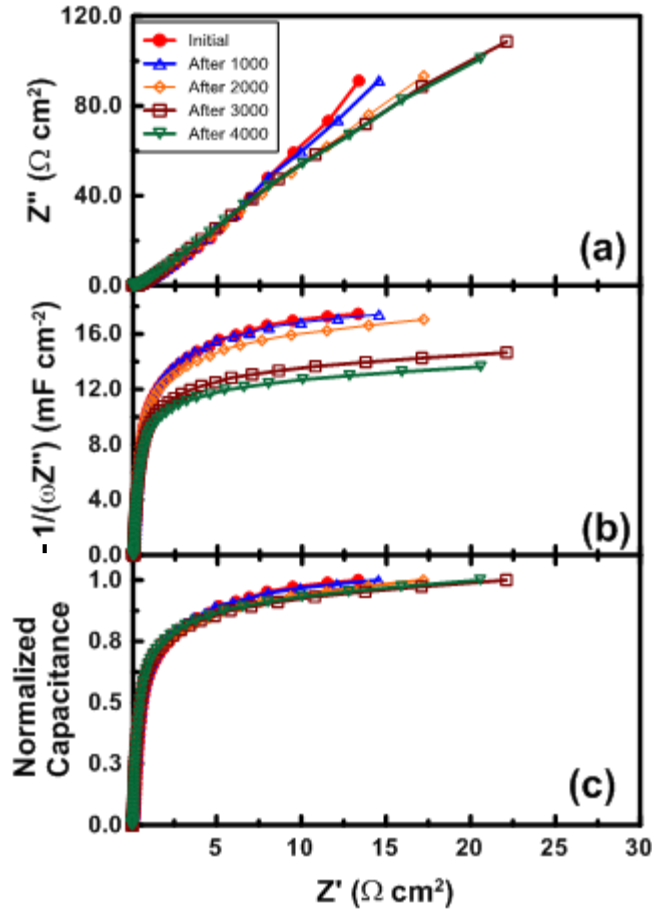


Figure 5.16: EIS characterization of Pt/G-PV catalyst @ 0.425V biased potential in N_2 -saturated 0.5M H_2SO_4 solution at various intervals under durability study (a) Nyquist plots (b) Limiting capacitance plots. (c) Normalised capacitance plots.

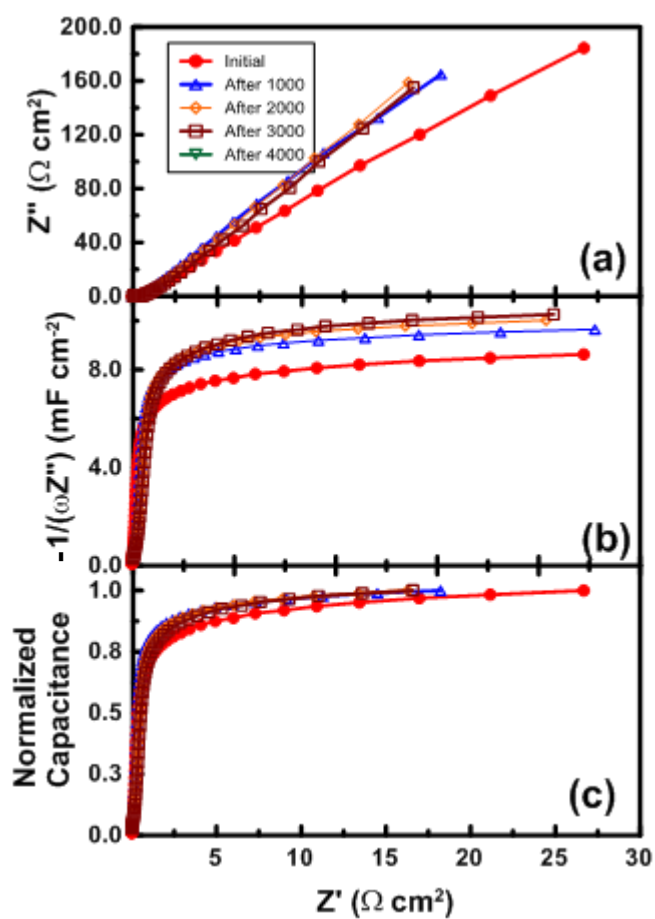


Figure 5.17: EIS characterization of Pt/ 14 wt% TiO₂/ ATV catalyst @ 0.425V biased potential in N₂-saturated 0.5M H₂SO₄ solution at various intervals under durability study (a) Nyquist plots (b) Limiting capacitance plots. (c) Normalised capacitance plots.

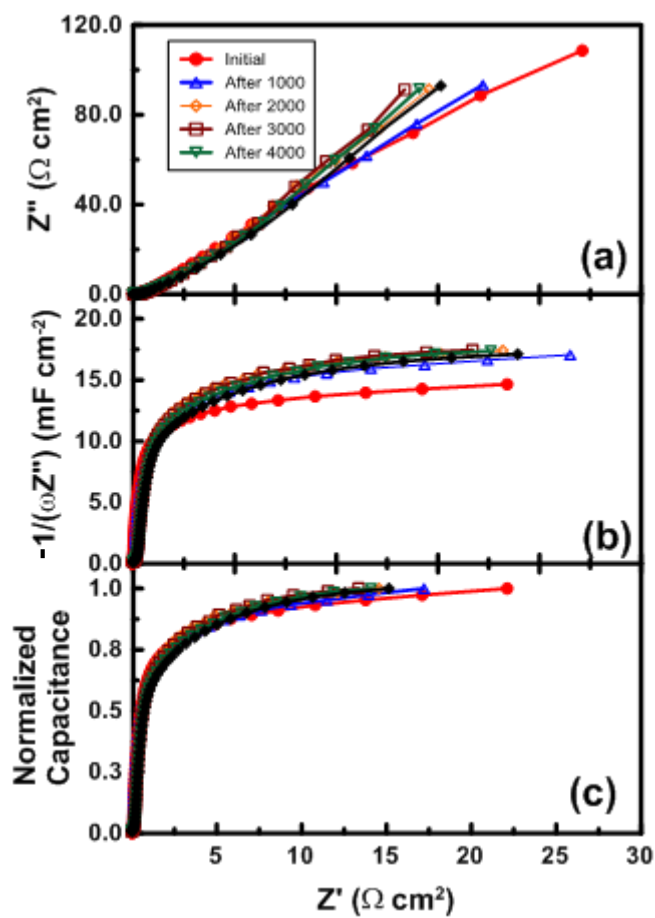


Figure 5.18 : EIS characterization of Pt/ 14 wt% TiO₂/ G-PV catalyst @ 0.425V biased potential in N₂-saturated 0.5M H₂SO₄ solution at various intervals under durability study (a) Nyquist plots (b) Limiting capacitance plots. (c) Normalised capacitance plots.

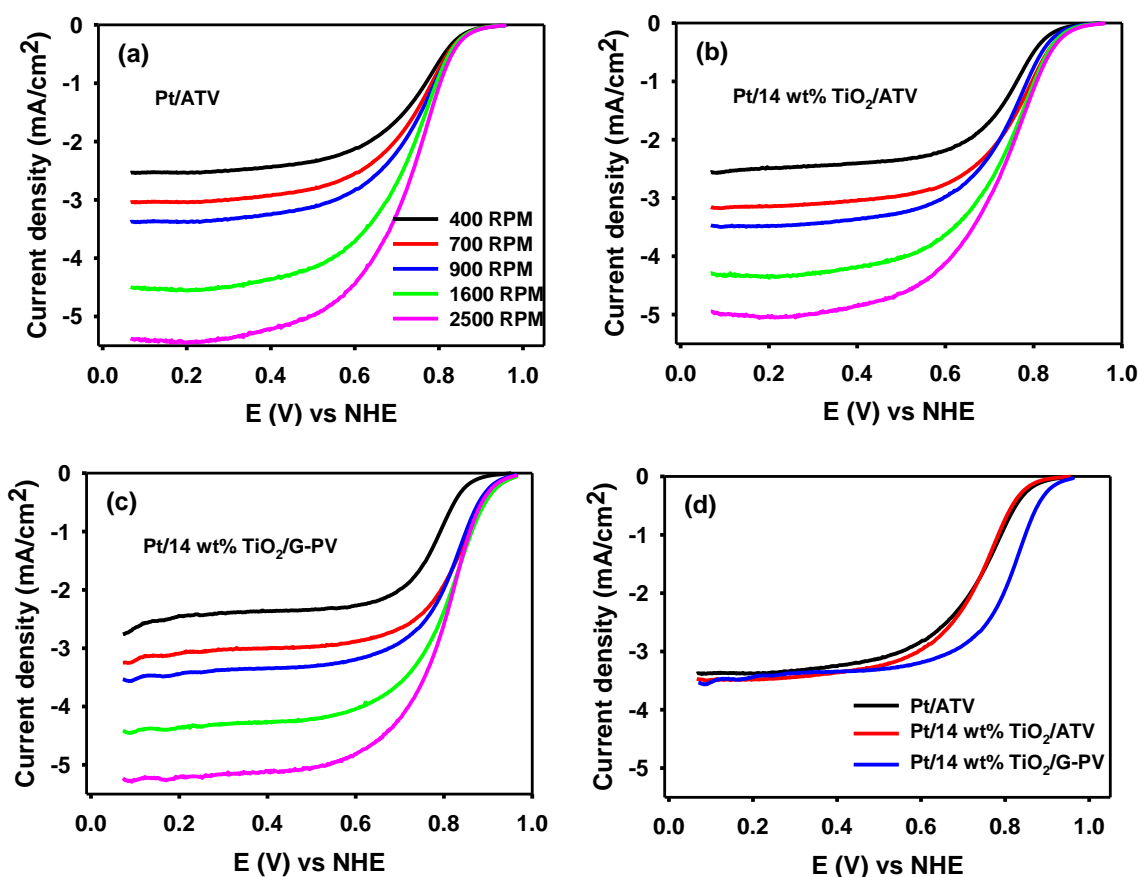
Table 5.6: Limiting capacitance BOL and EOL data following stability study

Samples	BOL Capacitance (mF/cm ²)	EOL capacitance (mF/cm ²)
Pt /G-PV	17.3	13.7
Pt/14% TiO ₂ /ATV	7.90	9.62
Pt/14% TiO ₂ /G-PV	13.2	15.6
Pt/22% TiO ₂ /G-PV	12.5	12.1
Pt/24% TiO ₂ /G-PV	8.72	9.10
Pt/32% TiO ₂ /G-PV	4.57	4.80

The platinum catalysts supported on carbon and TiO₂/C composites were evaluated for the molecular oxygen reduction reaction (ORR) in oxygen saturated sulfuric acid medium using the RDE. Fig. 5.19 contain representative RDE voltammetry data for Pt/ATV and two different carbon substrates with identical TiO₂ content (20% Pt/14 wt% TiO₂/ATV and 16.5% Pt/14 wt% TiO₂/G-PV). The kinetic currents and onset potentials for the ORR on Pt deposited on three different substrates: ATV, 14wt% TiO₂/ATV, 14 wt% TiO₂/G- PV at 0.65V are compared in Table 5.5.

Kinetic analysis of the composite catalysts towards the ORR shows a preferable 4-electron transfer process. From these results, it is clear that the glucose pre-treatment has a beneficial overall positive impact on the activity of Pt, with higher onset potential and kinetic current than those for the ATV support with and without glucose modification. The results could be associated with the presence of glucose pyrolysis products between carbon and the metal oxide film as observed in the case of hollow Pt/TiO₂-c nanotubes[21], the formation of a carbon film on top of the Pt/C/TiO₂ [30], or the formation of a more conductive carbon-doped TiO₂ material[24]. Any of these options would facilitate electron transport from the support to the catalyst.

These results are in agreement with other studies where in situ carbonization of glucose on Pt composite catalysts has been reported to extend the catalyst stability during potential cycling in half cell. However, our approach is different; glucose is used as a surface modifier to control the *in situ* deposition of TiO₂ (and Pt) nanoparticles on carbon substrates. In addition, the in situ carbonization of glucose on composite supports can minimize Pt particle size growth without the need for heat treating Pt based catalyst. Thus we demonstrate that incorporation of nanostructured metal oxide particles into conventional carbon electrode structure results in a core shell like catalyst material, which will facilitate electronic transport through synergetic effect.



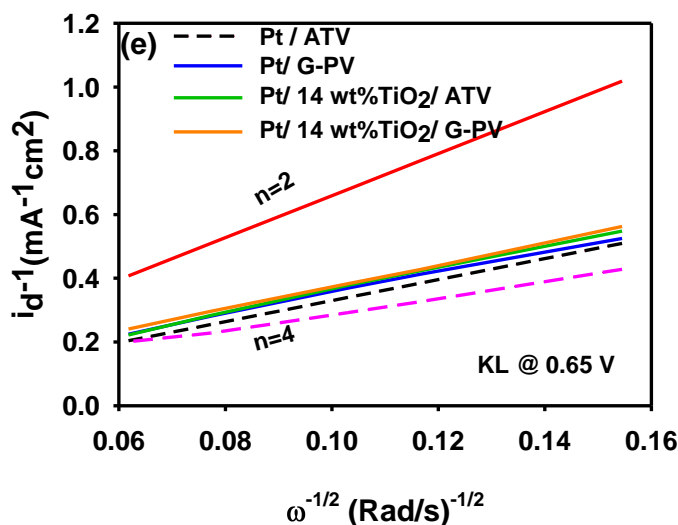


Figure 5.19: ORR curves: for different rotation speeds (400-2500RPM) at a scan rate of 5 mV/s for prepared catalysts (a) Pt/ATV (b) Pt/14 wt% TiO₂/ATV (c) Pt/14 wt% TiO₂/G-PV (d) Comparison at 900 RPM for tested catalysts (e) Koutecky-Levich plots at 0.65V vs. NHE. Measurements were carried out in O₂-saturated 0.5M H₂SO₄ at 25 °C. Current density based on the electrode geometric area (0.196cm²).

5.5 Conclusion and summary

The sol synthesis of TiO₂/C composite has been optimised based on the use of glucose as molecular seed for the controlled deposition of TiO₂ nanoparticles on “as received” carbon black that it can contribute to eliminating the need for acid treatment functionalization. For comparison, glucose doped (G-PV) and acid treated (ATV) Vulcan XC-72R carbon were coated with TiO₂ and used as substrates for the preparation of Pt/TiO₂/Vulcan carbon composites. The catalysts’ performance on these materials was evaluated using cyclic voltammetry and rotating disc electrode experiments in 0.5 M H₂SO₄ with and without dissolved oxygen. In general, The beginning of life-electrochemical active surface area (BOL-ESCA) varied with TiO₂ loadings on both ATV and G-PV.

- Presence of glucose leads to a larger amount of TiO₂ deposited onto carbon compared to samples prepared from the base carbon that was not glucose doped.

- Relatively uniform distribution and well defined spherical shapes of TiO₂ particles can be inferred on the glucose modified porous carbon substrate.
- Uniform dispersion of Pt nanoparticles was achieved on these composite catalysts.
- The ECSA values for glucose doped catalysts (Pt/x wt. % TiO₂/G-PV) are significantly higher compared with Pt/x wt. % TiO₂/ATV catalysts.
- Optimum ECSA of Pt on TiO₂/Vulcan glucose doped Vulcan[®] carbon (Pt/14wt. % TiO₂/G-PV) 46.2 m²/g Pt, was significantly higher than that of the two reference samples prepared with acid-treated carbon, Pt/ATV (36.3 m²/g Pt) and Pt/14 wt% TiO₂/ATV (16.8 m²/g Pt).
- Kinetic analysis of the composite catalysts towards ORR shows a preferable 4-electron transfer process and higher kinetic currents are observed on Pt/TiO₂/G-PV catalysts
- Composite catalysts are relatively stable in comparison to the in house fabricated Pt/ ATV and Pt/G-PV catalysts
- Composite catalysts show higher retention rates of electrochemical active surface areas following durability assessment in reference to commercial catalysts (E-20 (Etek) and JM-20)

The enhancements in ECSA of glucose doped composite catalysts can be ascribed to thinner films of TiO₂ that subsequently increased dispersion of Pt nanoparticles with minimal increase in catalyst layer resistance. This can be attributed to a more conductive supports, as well as, minimal TiO₂ segregation with better catalyst dispersion. Overall, glucose plays a significant role on the properties of the final product, the glucose pyrolysis products formed during the annealing step helped to improve the conductivity properties of TiO₂, resulting in an enhancement of Pt performance and stability. A similar beneficial effect was observed in the case of Pt deposited on glucose doped Vulcan.

5.6 References

- 1) Wang, S., Yu, D., and Dai, L. (2011). *Journal of the American Chemical Society*, 133(14), 5182-5185.
- 2) Debe, M. K. (2012). *Nature*, 486(7401), 43-51.
- 3) Shao, Y., Yin, G., Zhang, J., and Gao, Y. (2006). *Electrochimica Acta*, 51(26), 5853-5857.
- 4) Borup, R., Meyers, J., Pivovar, B., Kim, Y. S., Mukundan, R., Garland, N., and Zelenay, P. (2007). *Chemical reviews*, 107(10), 3904-3951.
- 5) Antolini, E. (2009). *Applied Catalysis B: Environmental*, 88(1), 1-24.
- 6) Yu, X., and Ye, S. (2007). *Journal of Power Sources*, 172(1), 133-144.
- 7) Franco, A. A., and Gerard, M. (2008). *Journal of The Electrochemical Society*, 155(4), B367-B384.
- 8) Ioroi, T., Siroma, Z., Fujiwara, N., Yamazaki, S. I., and Yasuda, K. (2005). *Electrochemistry Communications*, 7(2), 183-188.
- 9) Bauer, A., Song, C., Ignaszak, A., Hui, R., Zhang, J., Chevallier, L., & Rozière, J. (2010). *Electrochimica Acta*, 55(28), 8365-8370.
- 10) Beak, S., Jung, D., Nahm, K. S., and Kim, P. (2010). *Catalysis letters*, 134(3-4), 288-294.
- 11) Shanmugam, S., and Gedanken, A. (2007). *Small*, 3(7), 1189-1193.
- 12) Huang, K., Sasaki, K., Adzic, R. R., and Xing, Y. (2012). *Journal of Materials Chemistry*, 22(33), 16824-16832.
- 13) Camacho, B. R., Morais, C., Valenzuela, M. A., and Alonso-Vante, N. (2013). *Catalysis today*, 202, 36-43.
- 14) Vogel, W., Timperman, L., and Alonso-Vante, N. (2010). *Applied Catalysis A: General*, 377(1), 167-173.
- 15) Tiido, K., Alexeyeva, N., Couillard, M., Bock, C., MacDougall, B. R., and Tammeveski, K. (2013). *Electrochimica Acta*, 107, 509-517.
- 16) Wang, B., Xin, H., Li, X., Cheng, J., Yang, G., and Nie, F. (2014). *Scientific reports*, 4, 3729
- 17) Akalework, N. G., Pan, C. J., Su, W. N., Rick, J., Tsai, M. C., Lee, J. F., and Hwang, B. J. (2012). *Journal of Materials Chemistry*, 22(39), 20977-20985.

- 18) Zhang, L., Wang, L., Holt, C. M., Zahiri, B., Li, Z., Malek, K., and Mitlin, D. (2012). *Energy & Environmental Science*, 5(3), 6156-6172.
- 19) Xia, B. Y., Wang, B., Wu, H. B., Liu, Z., Wang, X., and Lou, X. W. D. (2012). *Journal of Materials Chemistry*, 22(32), 16499-16505.
- 20) Dogan, D. C., Hwang, S. M., Yim, S. D., Sohn, Y. J., Yang, T. H., and Park, G. G. (2013). *ECS Transactions*, 58(1), 1843-1847.
- 21) Jiang, Z. Z., Wang, Z. B., Chu, Y. Y., Gu, D. M., and Yin, G. P. (2011). *Energy & Environmental Science*, 4(3), 728-735.
- 22) Timperman, L., Feng, Y. J., Vogel, W., and Alonso-Vante, N. (2010). *Electrochimica Acta*, 55(26), 7558-7563.
- 23) Rigdon, W. A., and Huang, X. (2014). *Journal of Power Sources*, 272, 845-859.
- 24) Huang, K., Sasaki, K., Adzic, R. R., and Xing, Y. (2012). *Journal of Materials Chemistry*, 22(33), 16824-16832.
- 25) Sambandam, S., Valluri, V., Chanmanee, W., De Tacconi, N. R., Wampler, W. A., Lin, W. Y., and Rajeshwar, K. (2009). *Journal of Chemical Sciences*, 121(5), 655.
- 26) Von Kraemer, S., Wikander, K., Lindbergh, G., Lundblad, A., and Palmqvist, A. E. (2008). *Journal of Power Sources*, 180(1), 185-190.
- 27) Easton, E. B., & Pickup, P. G. (2005). *Electrochimica Acta*, 50(12), 2469-2474.
- 28) O'Rian, O. R., Saleh, F. S., and Easton, E. B. (2014). *ECS Transactions*, 61(23), 25-32.
- 29) Saleh, F. S., and Easton, E. B. (2012). *Journal of The Electrochemical Society*, 159(5), B546-B553.
- 30) Jiang, Z. Z., Wang, Z. B., Chu, Y. Y., Gu, D. M., and Yin, G. P. (2011). *Energy & Environmental Science*, 4(7), 2558-2566.

CHAPTER SIX

Photo-enhanced methanol oxidation and electrochemical stability: understanding the impacts of Pt and TiO₂ nanoparticles on the electrode performance.

Part of the work described in this chapter has been published in journal of applied catalysis b (ACB) as:

Christopher Odetola, Liliana N. Trevani, and E. Bradley Easton, Photo enhanced methanol electrooxidation: Further insights into Pt and TiO₂ nanoparticle contributions, Applied Catalysis B: Environmental, Volume 210, 5 August 2017, Pages 263-275, ISSN 0926-3373

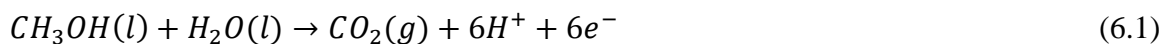
<http://doi.org/10.1016/j.apcatb.2017.03.027>

This chapter is focusing on the understanding how the interaction between Pt and TiO₂ influences the photo-enhancement of MOR. To aid in the understanding, I have performed HR-STEM with elemental mapping of the catalysts surface.

6.1 Introduction

This chapter is aimed to probing some fundamental questions on photo-electrocatalysis driven by UV-visible light on Pt/carbon and Pt/TiO₂/carbon catalyst materials and get further insights on the roles of Pt and TiO₂. The study is centered on methanol oxidation because it is a simple alcohol, and it has been extensively investigated in connection with its use in direct alcohol fuel cells (DAFCs). The thermodynamic equilibrium potential of the methanol oxidation reaction (MOR) is also close to that of the hydrogen oxidation [1] and without recourse to the engineering design challenge of illuminating a fuel cell stack that nowadays seems to be a major limitation, this study can contribute to the development of new generation light assisted energy conversion devices [2]. In addition, the photocatalytic and photoelectrochemical oxidation of organic pollutants in aqueous media represent two cost-effective approaches for the treatment of pharmaceuticals and industrial waste waters and environment remediation initiatives [3-4].

Direct methanol fuel cells (DMFCs) have been found useful in portable fuel cell applications due to their high energy density [5-6]. Platinum is the electrocatalyst by choice for methanol oxidation because it is known to be the best catalyst for breaking the C-H and O-H bonds in alcohols but developing catalysts with high activity and high resistance to surface poisoning still remains a research challenge for this application. For instance, it is difficult to carry out the complete oxidation of methanol on Pt in acid media (equation 6.1), because several reaction intermediates such as formaldehyde, formic acid and most especially carbon monoxide (CO) can be adsorbed on the surface and lead to a rapid deactivation of the Pt catalyst nanoparticles (PtNPs) thus, the achieved performance data of DMFC is not satisfying and material costs are too high [7-10].



The reaction network for electrochemical oxidation of methanol on platinum has been reviewed and summarized [11-12], the overall reaction pathway is presented below.

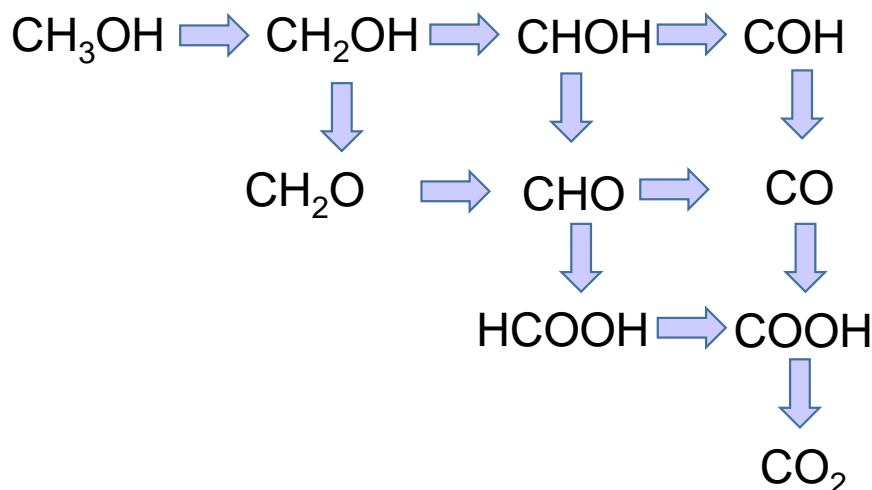


Figure 6.1: Network of reactions for methanol oxidation ¹¹

From Figure 6.1, series of intermediate steps can be formed in the complete oxidation of methanol to CO_2 involving several processes: (1) methanol adsorption in active site; (2) C-H bond activation; (3) O-H bond activation and (4) CO oxidation. Depending on the reaction conditions, this pathway can produce various intermediates. Complete oxidation of methanol on Pt take place via two processes that occurs at different potentials. The first process requires that methanol be adsorbed into platinum sites. Because methanol is not able to displace adsorbed H atoms, adsorption can only begin at potentials where sufficient Pt sites are free of H (around 0.2 V vs. NHE) [13]. The second process requires the dissociation of water, which provides the oxygen for the reaction. On platinum, interaction of water with the catalyst surface is only possible at potentials above 0.4 V vs. NHE [13]. The water separates according to equation 6.2,



The adsorbed CO reacts with OH adsorbed to produce CO_2 [16]. The reaction can be written as follows,



The high overpotential needed to disassociate water and provide the oxygen to oxidize CO provides a major difficulty to use platinum as catalyst alone. For that reason, researchers started experimenting adding various metals to platinum that can provide oxygenated species at much lower potentials for removal of CO adsorbed. Often Pt-based catalysts have been modified with other metals to maximize performance and reduce the Pt loading [14-15]. PtRu, one of the best catalysts for the MOR, proceeding by a bifunctional catalytic mechanism. Pt provides the main site for the dehydrogenation of methanol, and the electrocatalytic performance improves with the oxidation degree of the Ru surface atoms since the hydroxide (OH) group facilitates the oxidation of CO-like species to CO₂. However, PtRu catalytic activity is still far from optimal. Ru is also expensive, and its long-term stability during fuel cell operation is a concern [1].

Thus in addition to the search for Pt- alloy catalysts, other studies have involved the exploration of alternative carbon and metal oxide support materials [16-20]. Dispersing catalyst nanoparticles onto metal oxide supports has been shown to enhance both activity and durability for both anodic and cathodic fuel cell reactions. Within this group, TiO₂ is one of the most studied materials, mainly because of its inertness under oxidizing and acidic conditions. It has been used as Pt and Pt-alloy catalyst support for a number of different application, including the cathode of hydrogen fuel cells and the anode of methanol fuel cells [21]. In the case of the MOR, the presence of a metal oxide can decrease the adsorption energy of CO intermediates and convert them into CO₂ [22]. This enhances surface diffusion of CO to the places where the OH_{ads} partner is formed, thus improved methanol oxidation reaction. However, the low electronic conductivity of metal oxides complicate their usefulness in electrode structure. This, coupled with the challenge of evenly dispersing the metal oxide within the catalysts layer, limits the utilization of catalyst surface area. To overcome these issues, many groups have developed synthetic methods to deposit very thin layers of TiO₂ nanoparticles on carbon. In addition, other groups have prepared catalysts on different types of TiO_x suboxide-modified supports with a higher electronic conductivity [23].

Recently, it has been shown that the electrochemical oxidation of methanol on Pt/TiO₂/C can also be enhanced by illumination with UV light [24-25]. The most commonly accepted mechanism for this process is depicted in Fig. 6.2B. The mechanism

involves the creation of holes in the valence band of TiO_2 upon irradiation with UV light, which can enhance the oxidation of methanol molecules and produce a current through the photo-generated electrons [26]. The presence of Pt can suppress recombination of electron-hole pairs and enhance the photocatalytic activity [27-30]. Thus, if Pt can be evenly dispersed within the catalysts support, $\text{Pt/TiO}_2/\text{C}$ has the potential to be a highly active and highly stable photo-electrocatalysts for anodic fuel cell reactions.

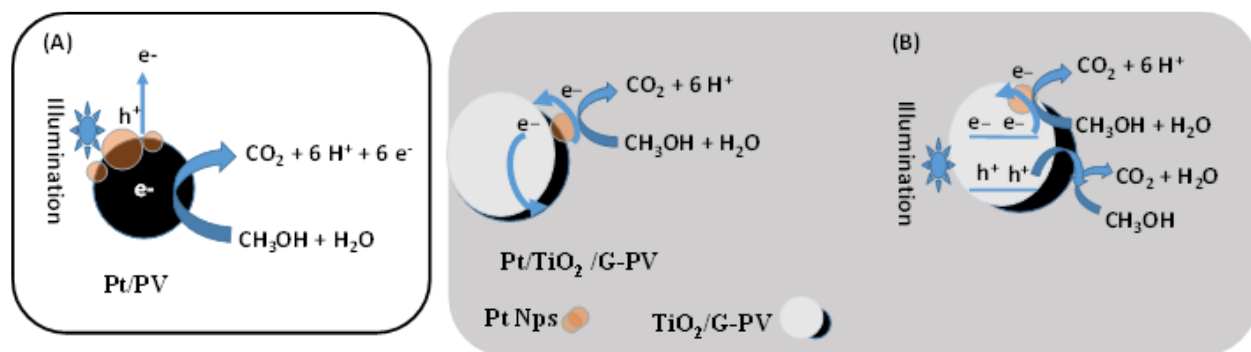


Figure 6.2: Schematic mechanism of methanol photo oxidation enhancement on (A) Pt/PV, and (B) $\text{Pt/TiO}_2/\text{G-PV}$ catalysts.

In contrast to this, recent studies have shown that the electrochemical oxidation of methanol on Pt/carbon can also be enhanced by illumination with UV light in the absence of TiO_2 . Li and co-workers [31] demonstrated significant enhancement of methanol oxidation on a 40 wt% Pt/C commercial catalyst upon irradiation with UV light. This enhanced activity was attributed to the formation of oxygen-containing species on Pt at lower potentials when irradiated that contribute to the electrooxidation and faster release of adsorbed CO [31-32]. A similar improvement in performance has been reported by Arulmani *et al.* [33] for Pt/C and PtRu/C commercial catalysts for which up to a five-fold enhancement was observed for the electrocatalytic oxidation of methanol when exposed to a broadband source of UV to near infrared light. However, the precise nature of the Pt/C photo-electrocatalysis catalysis mechanisms under visible and UV light have not been clarified thoroughly to date. Fig. 6.2A illustrates a possible mechanism for photoactivation on a Pt/C catalyst for methanol oxidation. In this model, Pt nanoparticles with inherent surface plasma resonance bands in the UV-visible region can absorb UV-visible light and

generate high-energy photoelectrons under illumination. The coherent excitation of these free conduction electrons induced by the electrical field of the incident light leaves holes in the inner d band of the Pt metal. The enhanced photochemical reaction takes place by the interaction of the energized charge-carriers from the optically excited nanoparticles and the adsorbed surface reactant molecules [34-35].

Given the fact that a photo enhancement effect occurs with Pt in the absence of TiO₂, one would reasonably assume that same pathway would also occur in the presence of TiO₂/G-PV. Furthermore, the presence of electronic interactions between Pt and TiO₂ supports can alter the electrocatalytic performance (in the absence of irradiation). Together, this leads us to hypothesize that the role of TiO₂ in photo enhancement on Pt/TiO₂/C systems is more complex than initially proposed. For this reason, there is a need to better understand the mechanism of photo enhancement of the MOR in the presence and absence of TiO₂.

To do this, we have prepared a series of Pt/C and Pt/TiO₂/C catalysts and examined their MOR activity in the presence and absence of UV-visible irradiation. The Pt/TiO₂/C catalysts studied here were made using a glucose modification process which controls the morphology and distribution of TiO₂ NPs on pristine Vulcan XC-72R carbon (G-PV) [36-37] so that high utilization of Pt is achieved. We have previously demonstrated that these Pt/TiO₂/G-PV catalysts have improved activity towards the oxygen reduction reaction (ORR) and are highly durable. The pre-adsorption of glucose on pristine Vulcan carbon is a more versatile method to introduce surface functionalities over covalent bonding upon strong acid treatment. This is because the acid treatment approach is often harsh and could induce defects (oxidized surface sites) that may affect the properties of the carbon substrate [38-39]. In addition, this approach provides little control over the nature, location, and quantity of the introduced functional groups and also seems to etch carbon surfaces. The use of glucose functional groups provides an excellent tool to control the size of the deposited TiO₂ particles with homogeneous coating and upon crystallization phase transformation, the glucose carbon will enhance conductivity of TiO₂/C composite. This TiO₂-modified catalyst used in this study has very similar electrochemical properties (Pt surface area, conductivity) to the Pt/C catalysts studied here, essentially creating an even playing field for comparison of photo enhanced activity.

Electrochemical impedance spectroscopy (EIS) and cyclic voltammetry were used to investigate the MOR on Pt deposited on pristine Vulcan XC-72 (Pt/PV) and Pt supported on 14 wt% TiO₂/G-doped Vulcan carbon (Pt/TiO₂/G-PV). EIS was used to study methanol oxidation and evaluate the charge transfer resistance (R_{CT}) on each prepared catalysts. To the best of our knowledge, this is the first report to examine the R_{CT} for the oxidation of methanol with and without illumination by EIS. These results were analyzed along with those obtained by CO stripping experiments to gain insight into the dominant mechanistic pathways during irradiation. As expected, a higher electrocatalytic activity toward the MOR can be achieved in the presence of TiO₂. However, a significant improvement in MOR activity was also observed under illumination for samples without TiO₂, which suggests the Pt pathway is relevant and cannot be ignored.

6.2 Materials characterization

HR-STEM micrographs were acquired using an FEI Titan 80-300 cubed TEM (FEI Company, Eindhoven, The Netherlands), operated at 300 kV. The instrument is equipped with a hexapole CEOS image and probe corrector (CEOS GmbH, Heidelberg, Germany). EELS maps were acquired using a Gatan Quantum GIF (Gatan Inc., Pleasanton, CA). The dispersion was set to 1 eV/channel, convergence angle was 19 mrad, and acceptance angle was 36 mrad. Gatan Digital Micrograph was used to extract elemental maps from the raw EELS data cubes.

6.3 Electrochemical and photoelectrochemical measurements

Electrochemical experiments were performed at room temperature (25 °C) in a three-electrode cell with an Hg/HgSO₄ reference electrode and a platinum wire counter electrode as discussed in chapter 2. A factor of 0.65V was used to convert reference electrode potential to NHE. Experiments with illumination were carried out in a 50 mL glass cell with a quartz window and thermostatic jacket (Adams & Chittenden Scientific Glass, PEC Cells 946500.7) and identical reference, counter and working electrodes.

The light of a 300 W Xenon lamp from a Solar Simulator (XPS-300TM) was used for illuminating the working electrode surface and placed less than 5 cm distance away from it. The spectrum of light emitted is flat, with almost equal intensities at all wavelengths throughout the UV and visible ranges. Undesirable heating was avoided with an optical filter at the lamp output for infrared and near-infrared radiation absorption. In this work, the surface area of Pt was estimated in an alternative way by CO stripping experiments in a 0.5 M H₂SO₄ solution. For this experiment, CO was pre-adsorbed on the electrode surface at a constant electrode potential (0.15 V vs. NHE) for 20 minutes. After adsorption, the excess of CO in the solution was removed by purging with N₂ gas. The surface area of Pt was estimated by using the charge density for the oxidation of an adlayer of CO on Pt to CO₂, 420 $\mu\text{C}/\text{cm}^2$, and taking into account that two electrons are involved in the oxidation reaction [33]. The electrocatalytic activity for the MOR was measured in N₂-purged 0.5 M H₂SO₄ and 0.5 M CH₃OH solutions from 0.3 V to 1.1 V at a sweep rate of 50 mV/s in the presence and absence of light.

6.4 Results and Discussion

6.4.1 Materials Characterization

The elemental mapping images of the composite support-TiO₂/G-PV and the Pt/TiO₂/G-PV catalyst are shown in Figs.6.3 and 6.4. Fig 6.3 allows to clearly identify the support component elements -C, O and Ti that are fairly uniform in agreement with the results of TEM analysis. The interface between metallic Pt nanoparticles and TiO₂ nanoparticles was observed from the latter. These images also confirm the presence of Pt and Ti nanoparticles with interface formation and minimal segregation on the carbon substrate. The mapping shows that Pt particles are observed in different environments, mostly in the TiO₂ nanoparticles region but a few distribution could be observed on uncoated carbon substrate, as well as, at the interface of the TiO₂-C support. It is consistently observed that Pt tends to locate in proximity to TiO₂ NPs in the dual phase support. It has been reported that Pt favorably nucleates at oxygen vacancies on titania and this likely leads to their preferred arrangement [40-41]. This reported experimental

approach produced a highly dispersed Pt/TiO₂/G-PV composite catalyst with a clear hybrid interface that will benefit charge transfer processes.

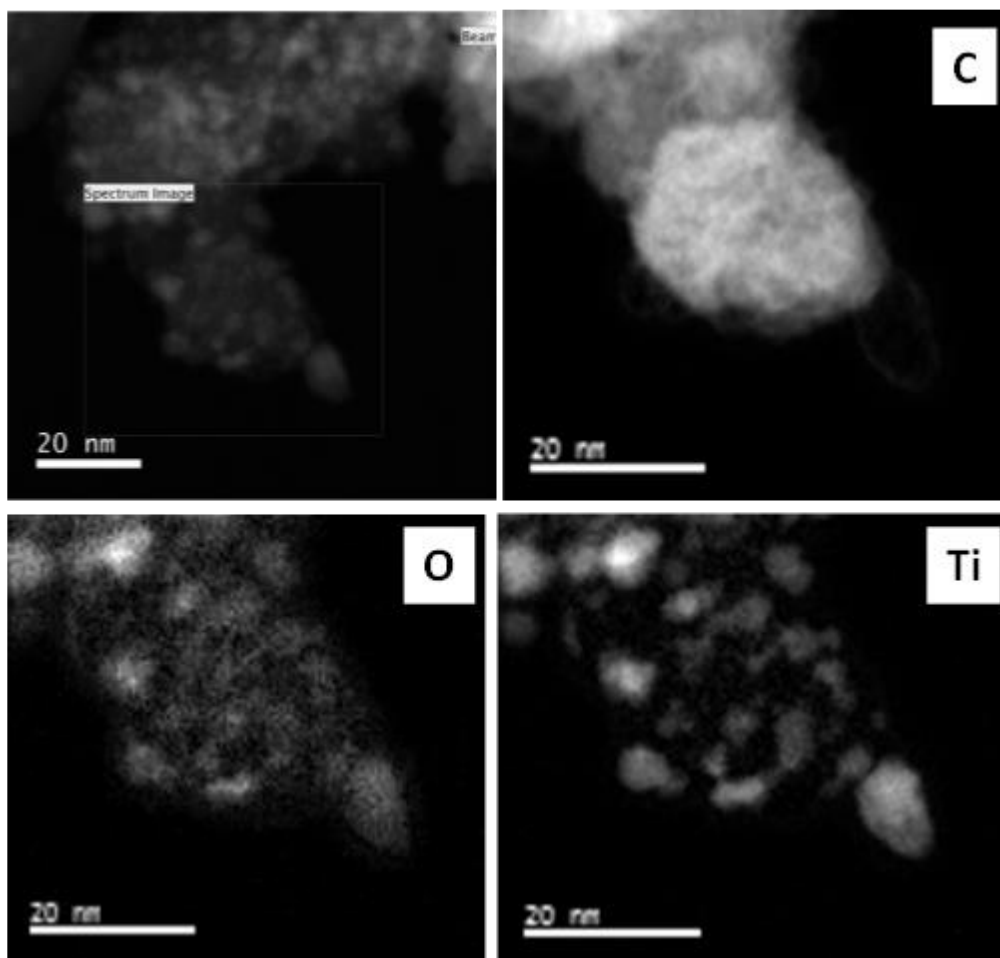


Figure 6.3: HR-STEM image of TiO₂/G-PV composite support and elemental mapping images of C, O and Ti.

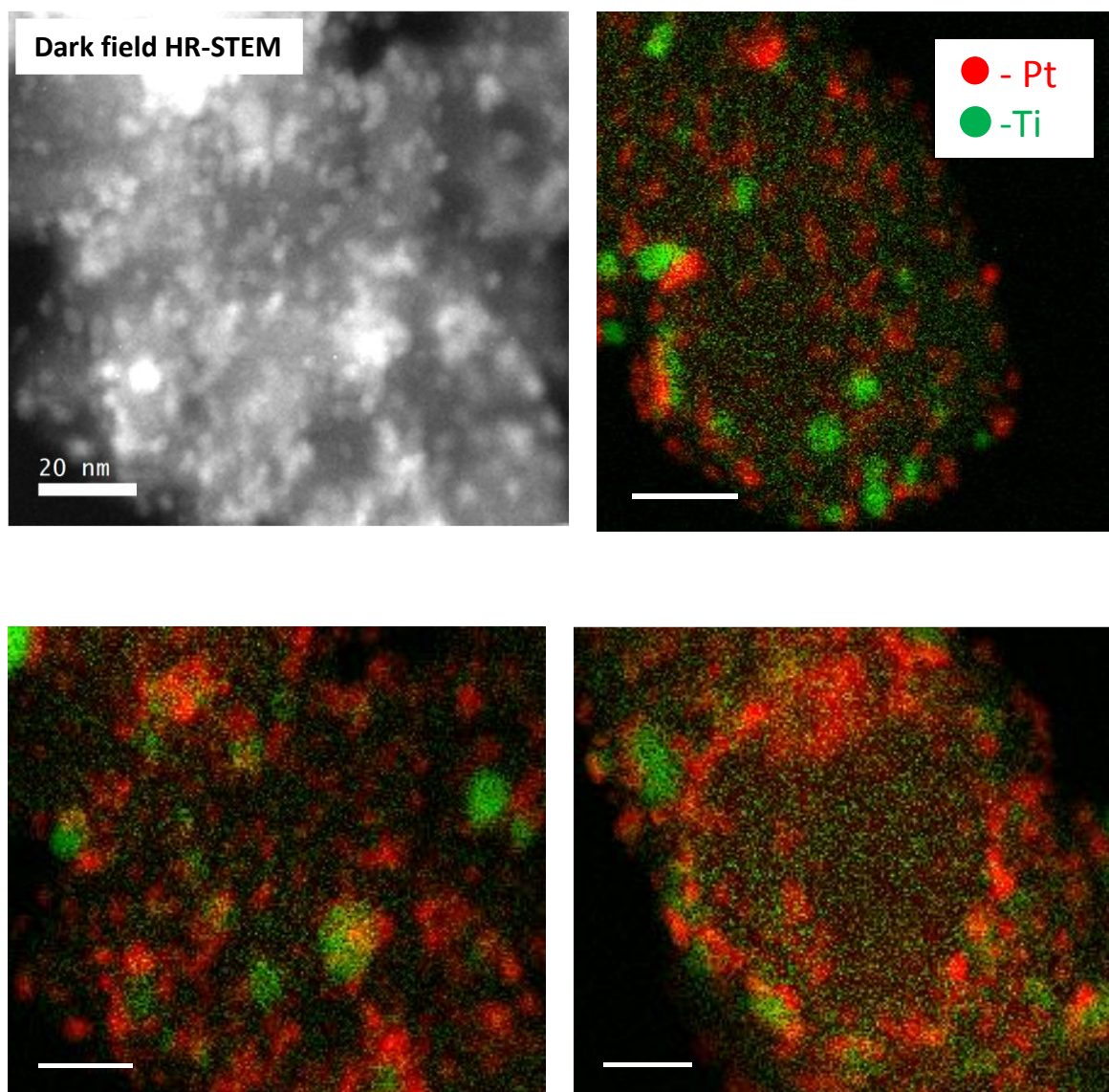


Figure 6.4: HR-STEM image of Pt/ TiO₂/G-PV catalyst and elemental mapping of Pt and Ti nanoparticles.

XPS was also used to evaluate changes in the composition and chemical bonding state of elements at the surface of these materials. As shown in Figs 6A and 6B, the O1s spectra of a pure TiO₂ (synthesized) reference sample and the TiO₂/GPV composite support show a major peak at ca. 530.1 eV and 530.0 eV, respectively. A minor peak is observed at higher binding energies ca. 532.3 eV, which arises from TiO₂ and OH functionalities, respectively. The other significant BE peak at 533.92 eV possibly originates from adsorbed H₂O [42].

Since the surface chemistry of the catalyst support can exert a potential influence on the behavior of the overlying metal NPs, it is of interest to explore the possible metal–support interactions between the PtNPs and the TiO₂ NPs in the catalyst composite material. Fig. 6C compares the binding energies (BEs) of Pt 4f between the Pt/TiO₂/G-PV and Pt/PV catalysts. The Pt 4f signals for both catalysts were deconvoluted into two pairs of doublets, which can be attributed to metallic Pt (ca. 71.2 eV), Pt (IV) (ca. 73.9 eV), and Pt(II) in PtO or Pt(OH)₂ species (ca. 71.3 eV). The deposition of PtNPs on the TiO₂/G-PV composite support shifted the BEs of Pt 4f to slightly higher values. A positive 0.2 eV shift for Pt/TiO₂/G-PV was detected compared to the Pt/PV catalyst. The shift in the BEs of Pt 4f may be ascribed to the so-called metal–support interactions arising from an increased electron density [43]. This kind of electronic interaction between Pt and the metal oxide support, that shifts the binding energies to higher values with respect to those for the PtNPs has already been reported [44-46]. Moreover, the reduction of Pt is more favorable on TiO₂/G-PV with 86% metallic Pt formed as compared with 76% on Pt/PV.

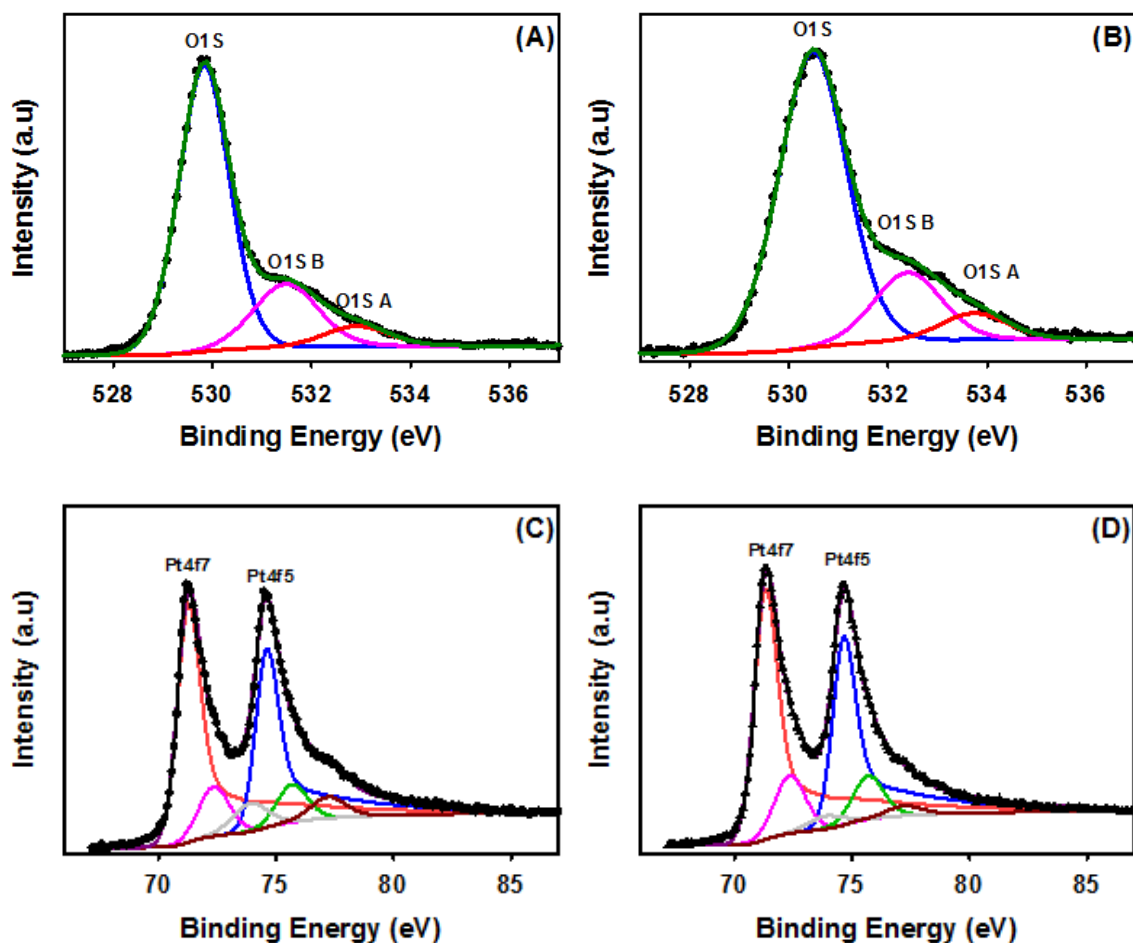


Figure 6.5: XPS spectra. High resolution spectra of O1s for (A) TiO₂, (B) TiO₂/G-PV catalyst supports. High resolution spectra of Pt4f for (C) Pt/PV and (D) Pt/ TiO₂/G-PV. Experimental data are represented by symbols.

6.4.2 Electrocatalytic Activity of Pt supported catalysts toward Methanol Oxidation

To measure the electrocatalytic activity of the various electrode materials, CV experiments for methanol oxidation were performed in a 0.5 M H₂SO₄ solution containing 0.5 M CH₃OH without illumination. The magnitude of the current density, and thus the magnitude of methanol oxidation, is greater in TiO₂ based support catalysts than Pt/PV when taking into account the metal content loading (Fig. 6.6). The Pt/14%TiO₂/G-PV

catalyst possesses the best electrocatalytic activity for MOR as evidenced by the order of the maximum forward peak current $\text{Pt}/14\% \text{TiO}_2/\text{G-PV} > \text{Pt}/24\% \text{TiO}_2/\text{G-PV} > \text{Pt}/32\% \text{TiO}_2/\text{G-PV} > \text{Pt}/22\% \text{TiO}_2/\text{G-PV} > \text{Pt}/8\% \text{TiO}_2/\text{G-PV} > \text{Pt}/\text{PV}$. The presence of TiO_2 in the catalyst layer improved methanol oxidation current. These results are comparable to literature data for PtNPs deposited on carbon and carbon-coated TiO_2 fibers [47], despite the fact that the PtNPs are not in direct contact with TiO_2 in this study, but on a mesoporous carbon film.

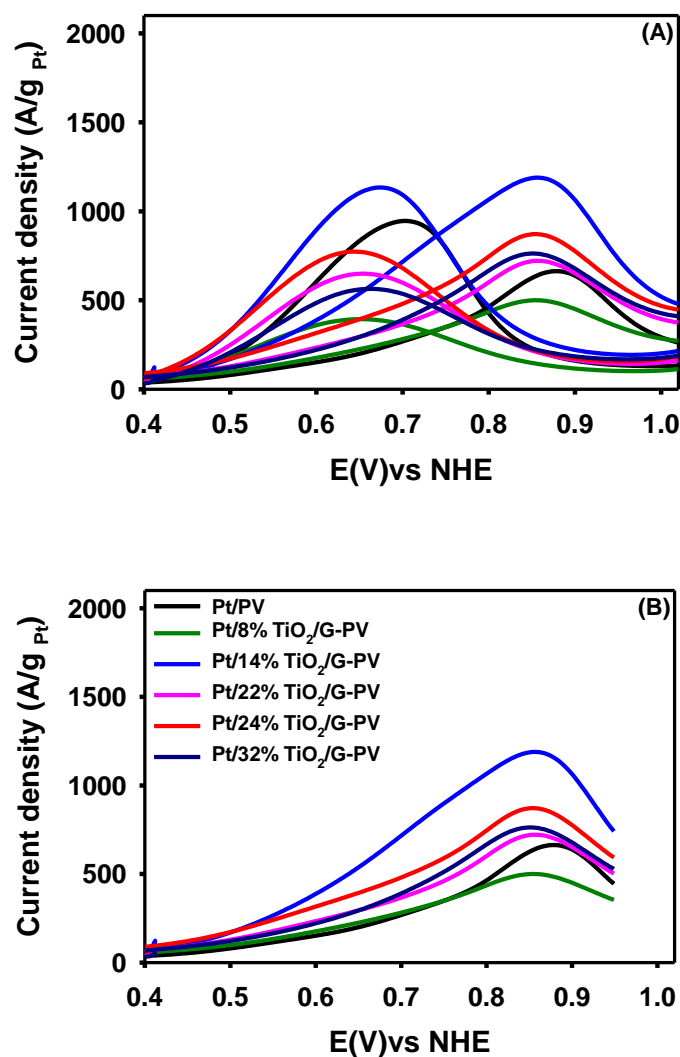


Figure 6.6: Methanol Oxidation Reaction (A) Mass normalized current density CVs and (B) Forward peak current density in N_2 -saturated 0.5M CH_3OH + 0.5M H_2SO_4 solution scan rate of 50 mV/s test temperature: 25 °C

The forward peaks show differences in onset potentials with a slight negative shift for methanol oxidation in the presence of TiO_2 on the catalyst layer. This further substantiates the fact that the electrocatalytic activity occurs more favorably in the composite catalysts. The oxidation kinetics of CO and other intermediate oxidation species formed during MOR is governed by the binding strength of adsorbed CO and presence of OH functional group on a metal surface [48]. The presence of TiO_2 -OH surface groups on Pt/ TiO_2 /G-PV will facilitate the MOR even in the absence of light [49]. Thus, the intrinsic catalytic activity and surface area effect of the composite support promotes overall a significant enhancement in electrocatalytic activity.

Moreover, the peak current density of Pt/14 TiO_2 /G-PV catalyst is also much higher than Pt/PV catalyst. These results state clearly that the optimized composite catalyst is approximately 14% TiO_2 loading, and is a suitable catalyst support, probably due to a good balance between the overall resistance and the available surface area of the catalyst layer. A good electrocatalysts must fulfill at least two requirements: 1) high current density and 2) lower onset potential for the corresponding electrochemical process. According to this, Pt/14% TiO_2 /G-PV presents the highest methanol electro-oxidation activity and was further analysed in this thesis as Pt/ TiO_2 /G-PV.

In order to evaluate methanol concentration impact on electrode performance, CVs were collected at varying concentrations in electrolyte solution as shown in Fig 6.7. Methanol is completely absorbed as there are no visible presence of hydrogen adsorption/desorption peaks within the concentration interval. We observed that increasing methanol concentration gives rise to increasing trend in peak current for both forward and reverse reactions [50]. The forward peak current is enhanced at increasing methanol concentration but the effect becomes less pronounced at the peak methanol concentrations. This behavior may be explained by a shift from a diffusion-controlled reaction at low methanol concentration to reaction, which is inhibited by adsorbed reaction intermediates at higher concentrations and insufficient availability of OH^- in the solution [51]. A positive shift of both forward and reverse oxidation peak potential was also observed. This may be as a result of deactivation of the electrode surface by poisoning species that are produced at higher methanol concentration.

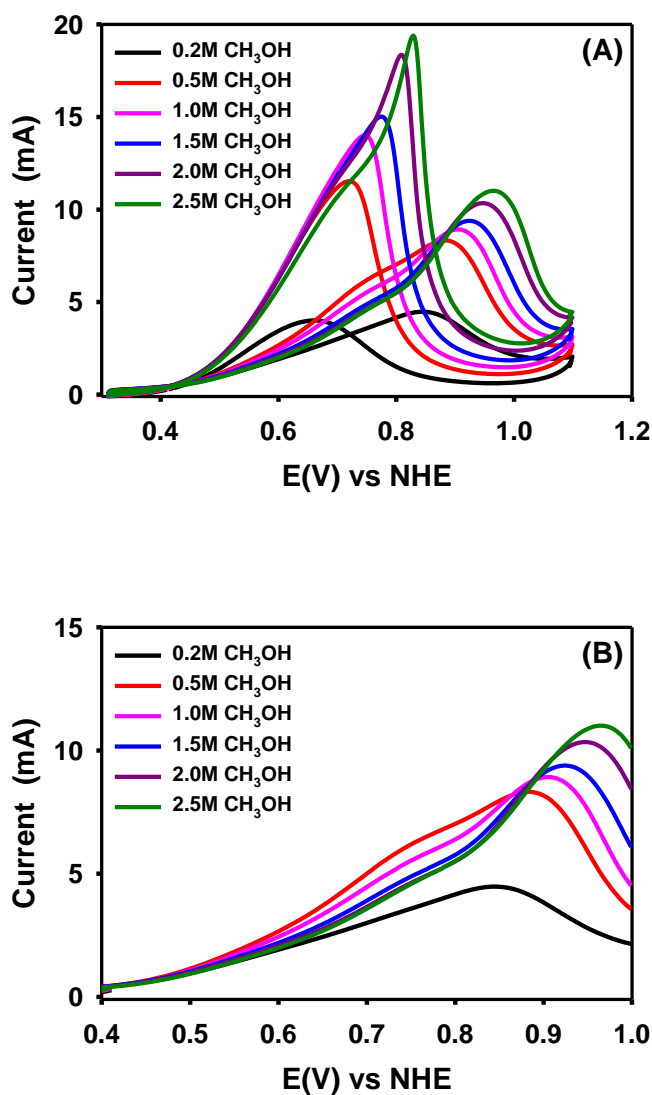
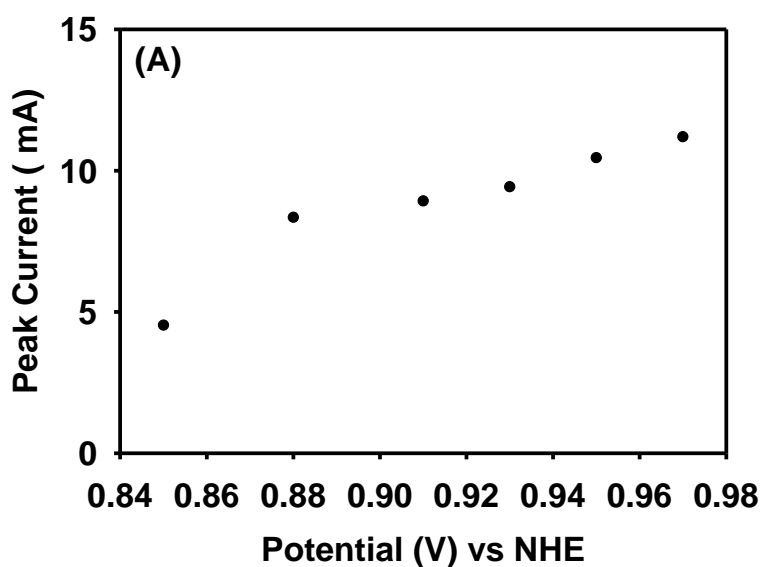


Figure 6.7: Methanol oxidation at electrolyte concentrations on Pt/TiO₂/G-PV (A) CVs (B) forward reaction in N₂- saturated 0.5M CH₃OH + 0.5M H₂SO₄ solution scan rate of 50 mV/s test temperature: 25 °C

Fig. 6.8 shows the peak current densities at various methanol concentrations from 0.2 M to 2.5 M of catalyst in the forward scan. The plot reveals that methanol oxidation peak current increases sharply with increasing methanol concentration up to 0.5 M, after which gradual peak increase was observed. At a higher concentrations, it is expected that the trend will shift toward a constant value independent of the concentration. This effect may be assumed due to the saturation of active sites on the surface of the electrode. The

adsorption of oxidation products at the electrode surface causes hindrance to further oxidation. At higher concentration of methanol, diffusion control reaction can no longer occur, and the reaction is inhibited by adsorbed reaction intermediates. Diffusion control reaction with respect to methanol occurs when OH^- ions are available in excess and chemisorbed methanol species is insufficient. The plot mimics the Langmuir adsorption model within the methanol concentrations used in this study, where the current density is dictated by the surface coverage of the alcohol and hydroxyl adsorbates [52]. The dependence of anodic peak potential of methanol oxidation on the bulk concentration of methanol is shown in Figure 6.7A and follows similar trend.



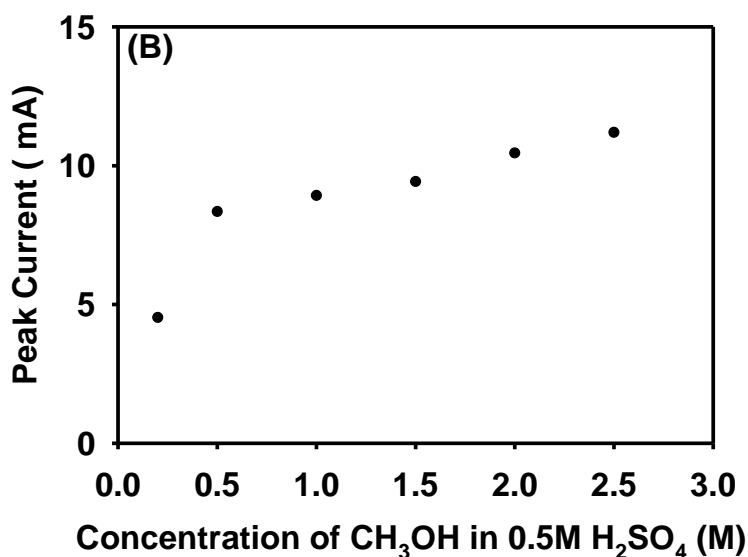


Figure 6.8: Methanol oxidation (A) Peak current vs onset potential and (B) Peak currents vs electrolyte concentration Activity

6.4.3. Photo-Electrocatalytic Activity toward Methanol Oxidation with and without UV-Visible Light

Fig. 6.9 shows the MOR activity of PV, TiO₂ and TiO₂/G-PV support with and without illumination as a control experiment. The bare TiO₂ has negligible electrocatalytic ability toward methanol oxidation. A slight increase in methanol oxidation current was observed under illumination at ~ 0.70V. This is not unexpected for a semiconductor material, but electron-hole recombination will be more favorable in samples without PtNPs. The unplatined supports (PV and TiO₂/G-PV) were also evaluated for methanol oxidation (Fig. 6.9A and C). Higher capacitive currents were obtained in the presence of methanol on these more conductive supports compared with bare TiO₂. For the TiO₂/G-PV, a slightly higher current density was observed when compared with PV support. Overall methanol oxidation activity on these supports is low.

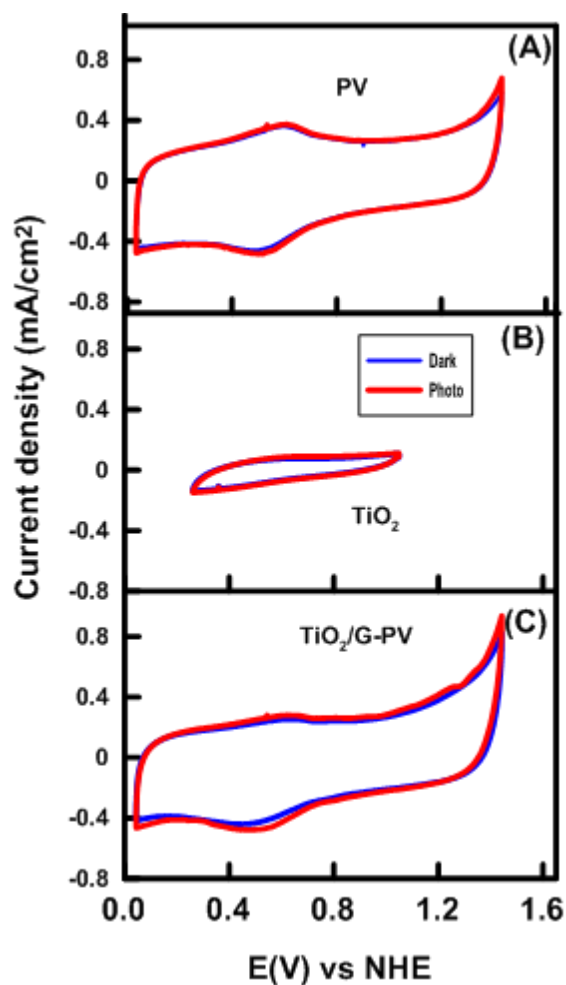


Figure 6.9 : Methanol oxidation activity at 25 °C of (A) PV, (B) TiO_2 (homemade) and (C) $\text{TiO}_2/\text{G-PV}$ supports with and without irradiation in N_2 - saturated 0.5 M CH_3OH + 0.5 M H_2SO_4 solution at a scan rate of 50 mV/s. Currents normalized by glassy carbon electrode area = 0.196 cm^2 .

The MOR activity of the platinized samples (Pt/PV and Pt/ $\text{TiO}_2/\text{G-PV}$) was investigated. The CV curves, with and without illumination, are shown in Fig. 6.10. The fact that the maximum currents densities (I_{max}) normalized by either Pt mass or ECSA do not show any significant difference trend between samples rules out Pt utilization as the reason for the enhanced activity. The normalized currents for the Pt/PV and Pt/ $\text{TiO}_2/\text{G-PV}$ samples start to increase at ~ 0.46 V vs. NHE for both dark and under illumination. The shape of the curves for the forward process are also similar to each other.

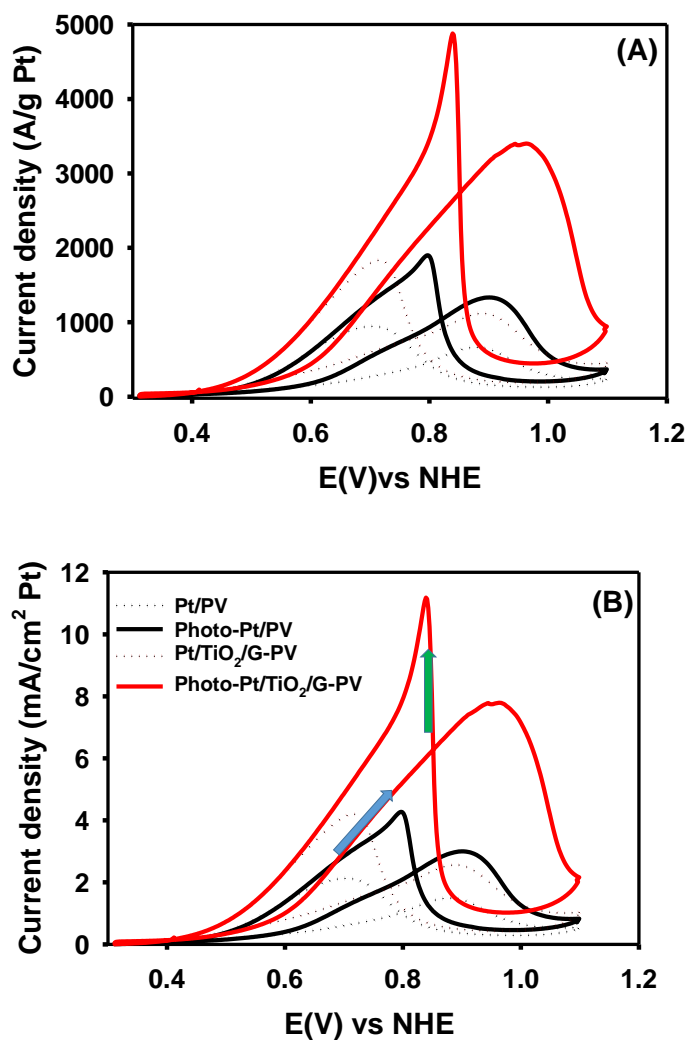


Figure 6.10: Methanol oxidation on platinized supports at 25 °C. (A) Mass activity and (B) Specific activity with and without irradiation in N₂-saturated 0.5 M CH₃OH + 0.5 M H₂SO₄ solution at a scan rate of 50 mV/s.

The moderate enhancement observed under illumination in the case of PtNPs deposited on a carbon substrate, Pt/PV, is quite interesting, and it was found in the past by other groups [31]. However, the presence of TiO₂ on G-PV clearly leads to a greater enhancement in photoelectrocatalytic activity. The total current density for the MOR and the enhancement observed under illumination, $(I_{\text{total-forward max (light)}} - I_{\text{total-forward max (dark)}}) * 100 / I_{\text{total-forward max (dark)}}$, are summarized in Table 6.1.

Table 6.1: Total peak current density and current contributions for methanol oxidation at 0.8 V vs NHE with and without illumination

Sample	Illumination	$I_{\text{total-forward max}}$ (A/g Pt)	Enhancement [#]
Pt/PV	No	678	100
	Yes	1357	
Pt/TiO ₂ /G-PV	No	1214	171
	Yes	3293	
Pt-TiO ₂ /C (Ref. 42)	No	1043	149
	Yes	2597	
[#] $(I_{\text{total-forward max (light)}} - I_{\text{total-forward max (dark)}}) * 100 / I_{\text{total-forward max (dark)}}$			

In the absence of illumination, the forward peak current density on Pt/TiO₂/G-PV for methanol oxidation (1214 A/g Pt) is 1.8 higher than that of Pt/PV (678 A/g Pt). The presence of TiO₂–OH surface groups on Pt/TiO₂/G-PV will facilitate the MOR even in the absence of light [49], because the oxidation kinetics of CO and other intermediate oxidation species formed during MOR is governed by the binding strength of adsorbed CO and presence of OH functional group on the metal surface [48]. The results are in good agreement with the behavior reported for PtNPs deposited on carbon and carbon-coated TiO₂ fibers [47], despite the fact that in these cases the PtNPs are not in direct contact with TiO₂, but on a mesoporous carbon film.

In the presence of UV-visible light illumination, the enhancement observed for the oxidation of methanol on Pt/TiO₂/G-PV (3293 A/g Pt) is 2.4 times higher than that of Pt/PV (1357 A/g Pt). Thus, the intrinsic photocatalytic activity of TiO₂ and surface area effect of the composite support promotes overall a significant enhancement in electrocatalytic

activity. Also, the formation of O-containing species on Pt under illumination on the Pt/PV catalyst at lower potentials can facilitate electrooxidation reaction of adsorbed CO intermediate formed [31].

Chronoamperometry with intermittent illumination in repeated off–on cycles was used for studying the contribution of the photocurrent to the current density. These curves were obtained by polarizing the electrodes at 0.85 V. As shown in Fig. 6.11, with the light off, a remarkable decrease in current density can be observed in the polarization curves for the repeated cycles. The significant enhancement in photocurrents on base metal catalysts and composite catalyst indicates the synergetic effects of the catalyst components following illumination in good agreement with the behavior observed on other Pt/TiO₂/C catalysts [47, 53]. In addition, this type of enhancement on metal supported catalyst is comparable to literature data where ~ 3 fold improvement in a photocurrent was observed on Pt/C catalyst using a solar simulator as a light source [31]. This indicates that MOR was improved by irradiation via a photochemical reaction.

However, given the fact that photo-enhancement occurs in the presence and absence of TiO₂, EIS measurements were carried out to evaluate how charge transfer kinetics of methanol oxidation are altered in the presence of illumination.

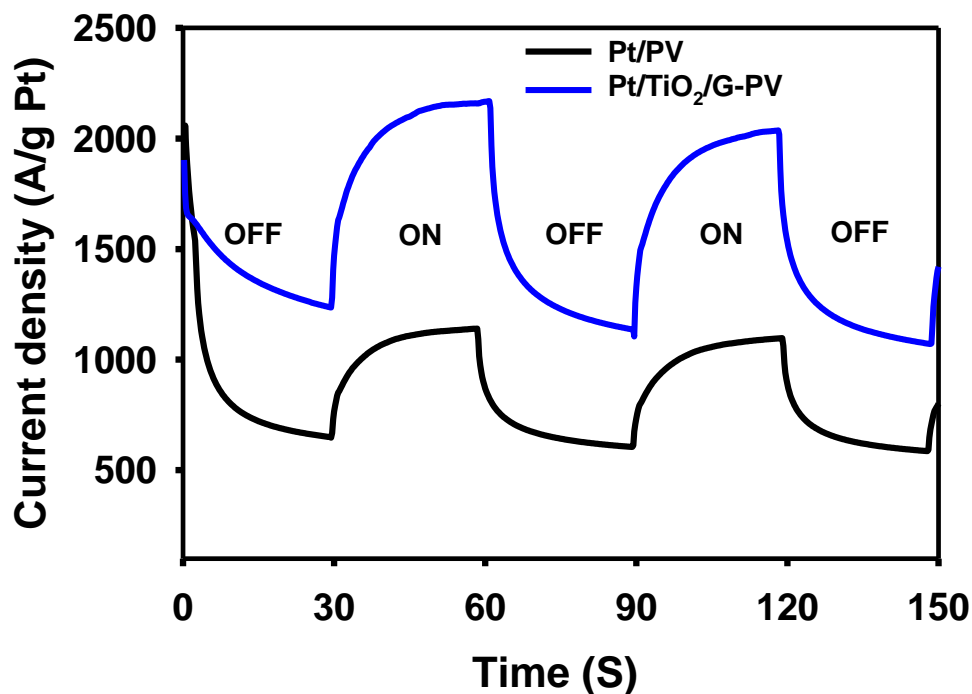


Figure 6.11: Chronoamperometry intermittent irradiation of catalyst materials at 25 °C and 0.85V in N₂-saturated 0.5 M CH₃OH + 0.5 M H₂SO₄ solution.

An intermediate direct current (DC) bias potential of 0.55 V was chosen to compare the reactivity of prepared catalysts [54] and modeled with an equivalent circuit [55], representing the impedance behavior (Fig. 6.12A). The equivalent circuit includes the solution resistance (R_s) between the working electrode and the reference electrode, a constant phase element (CPE), representing the double layer capacitance of the absorbed methanol, the charge transfer resistance (R_{CT}), inductance (L), related to the methanol dehydrogenation and the intermediates adsorption reactions. The methanol oxidation process at the catalyst interface can be treated as a parallel model of CPE and a resistor (R_2).

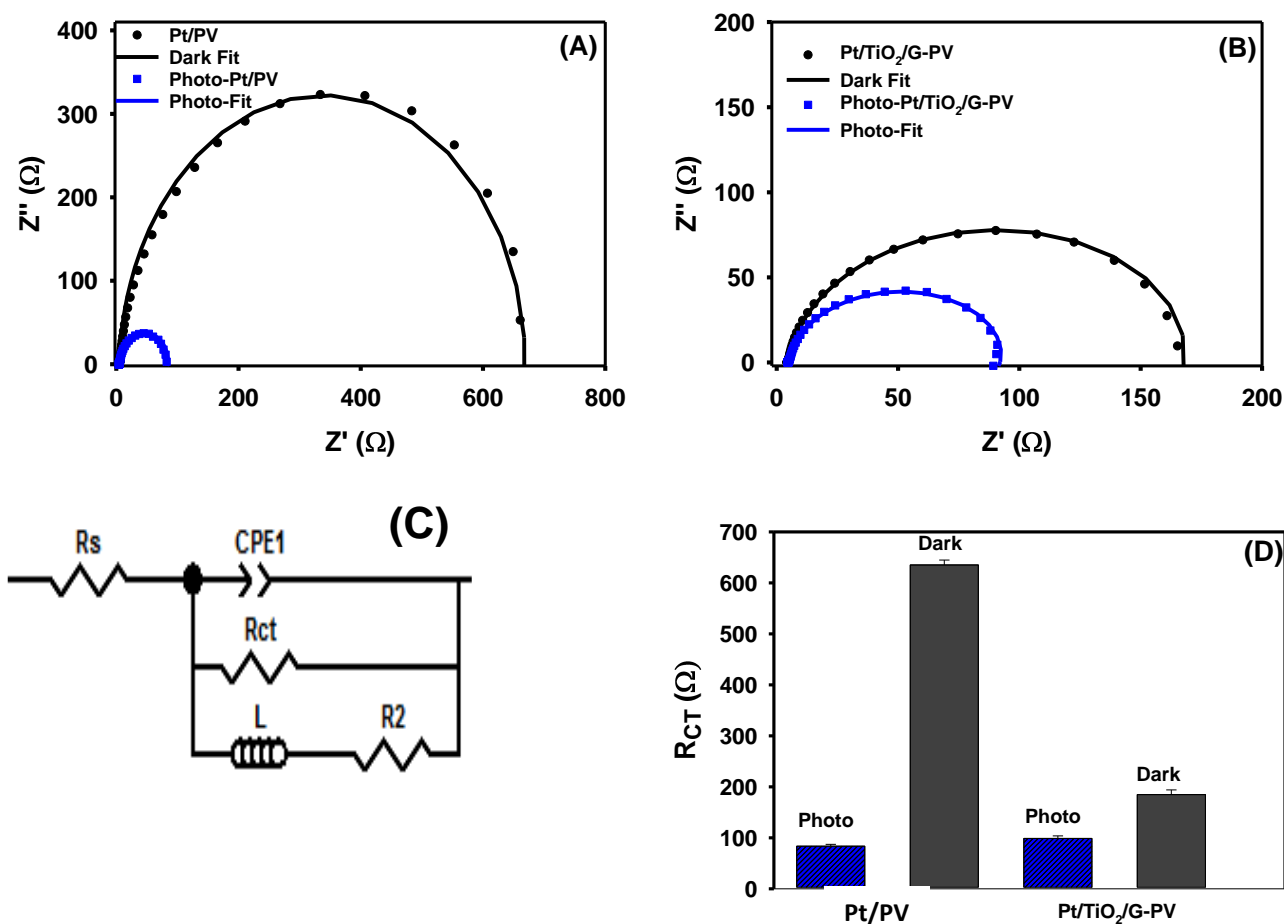


Figure 6.12: Nyquist plots at 25 °C and 0.55V for (A) Pt/PV and (B) Pt/TiO₂/G-PV with corresponding fittings from the equivalent circuit; (C) Equivalent circuit for fitting impedance data, in N₂- saturated 0.5 M CH₃OH + 0.5 M H₂SO₄ solution; (D) Charge transfer resistance with and without irradiation from fitting impedance data to equivalent circuit.

The Nyquist plots consist mainly of semi-circles, whose diameters are associated with the charge transfer resistance for MOR [56-57]. The Nyquist plots obtained for each catalyst in the presence and absence of irradiation are shown in Fig. 6.12 (A-B). The expected semi-circle response was observed in all cases, with a clear reduction in the diameter when UV irradiation is present. Each spectrum was readily fit to the equivalent

circuit model; the values of R_{ct} obtained from fitting each spectrum are listed in Table 6.2. The Nyquist plot of Pt/PV catalyst is similar that observed for EIS studies of methanol oxidation on a Pt/C thin film electrode Pt electrode and the resistance of charge transfer is in agreement with literature data obtained at similar potential region [58].

The exchange current density, j_o , was determined using the values of R_{CT} and the linearized form of the Butler-Volmer equation [59]:

$$j_o = \frac{RT}{nFAR_{CT}} \quad [6.4]$$

where R corresponds to the ideal gas constant, T corresponds to the cell temperature, F is Faraday's constant, A is the geometric area of the electrode (0.196 cm²), and n is the number of electrons transferred in the reaction (n = 6 for MOR).

Table 6.2: Charge Transfer Resistance (R_{CT}) and exchange current density (j_o) obtained from EIS data for Pt/PV and Pt/TiO₂/G-PV catalysts

Samples	R_{CT} (Ω)	j_o (mA/cm ²)
Without illumination		
Pt/ PV	635 \pm 10	0.034
Pt/TiO ₂ /G-PV	185 \pm 9	0.12
With illumination		
Photo-Pt/PV	83.6 \pm 3.5	0.26
Photo-Pt/TiO ₂ /G-PV	98.7 \pm 5.0	0.22

In the absence of irradiation, R_{ct} was ca. 3-times higher for Pt/PV compared to Pt/TiO₂/G-PV. This indicates that TiO₂ has a favorable influence on MOR kinetics in the absence of irradiation. In the presence of UV irradiation, the charge transfer resistance was considerably lower for each catalyst leading, to observed enhancement in MOR kinetics.

However, it is worth noting that the measured value of R_{CT} and j_o for each catalyst were very similar in the presence of UV irradiation, with the kinetics slightly more favorable on Pt/PV. This striking similarity implies that the photo enhancement should be given by changes in the Pt-CO binding energy and separation efficiency of the photogenerated electron-hole pairs due to surface-plasmon-induced charge separation in PtNPs in contact with TiO_2 [60]. To further understand this phenomenon, we examined the influence of illumination on the activity of each catalyst towards CO stripping.

6.4.4. CO Oxidation and Stripping Experiments with and without UV-Visible Light

Fig. 6.13 shows the CO stripping voltammograms on Pt/PV and Pt/ TiO_2 /G-PV catalysts in 0.5 M H_2SO_4 solution at 50 mV/s. We observed that illumination leads to a reduction in the onset potential of ca. 40-50 mV for both catalysts, indicating that illumination does indeed alter energetic around CO removal from the Pt surface. The presence of TiO_2 NPs also has a beneficial effect, showing lower onset potentials. This further implies that TiO_2 is also influencing the kinetics of CO removal on the electrode surface. The presence of pre-wave/shoulder on Pt/ TiO_2 /G-PV catalyst is likely due to the presence of domains of a different surface phase as it was observed in the case of PtRu catalysts [61]. Also, the onset potential of CO_{ad} oxidation for Pt/ TiO_2 /G-PV (0.78 V) catalyst shifted negatively compared to the Pt/PV (0.85 V) in the dark. This further indicates that a more conductive composite support accelerates the oxidative removal of CO adsorbed on the Pt active sites and was consistent with the results of methanol oxidation and EIS measurements and the higher ECSA of the Pt/ TiO_2 /G-PV catalyst determined by both H_2 adsorption/desorption and CO stripping experiments.

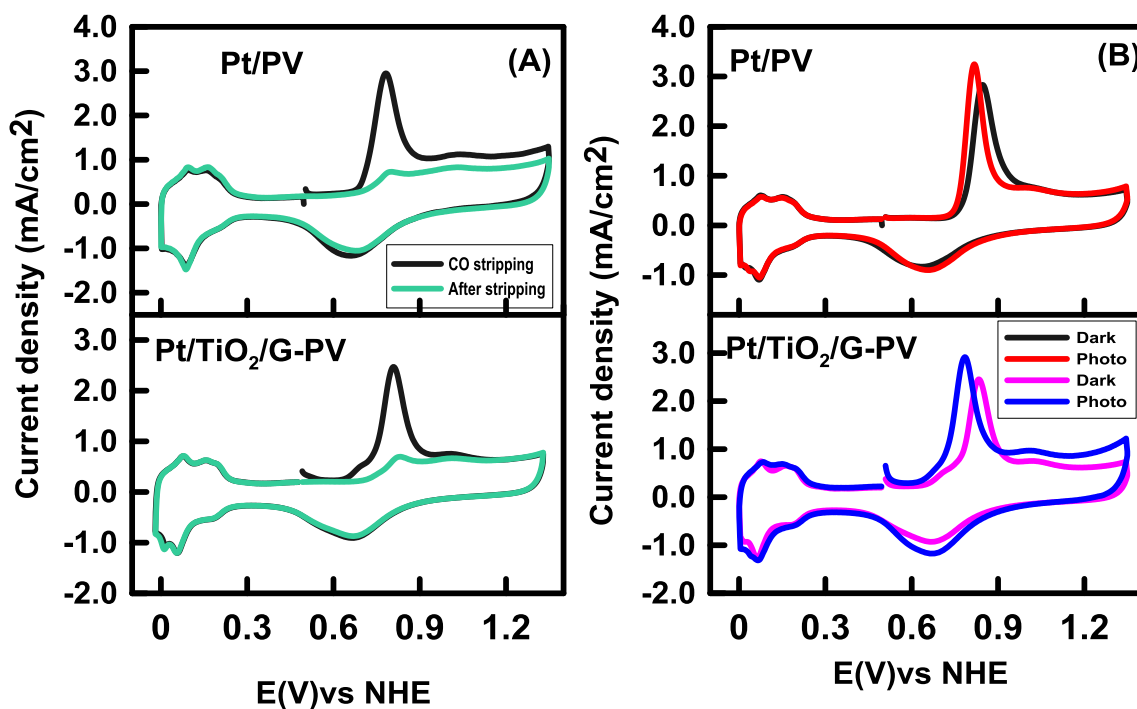
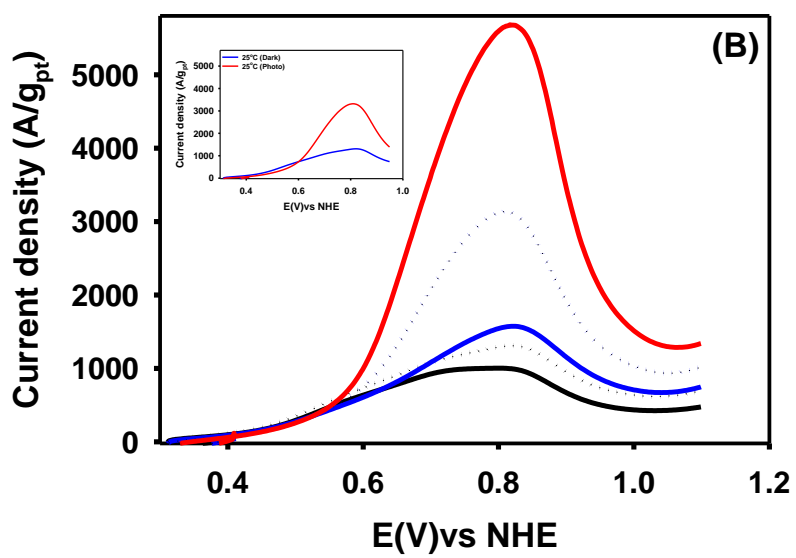
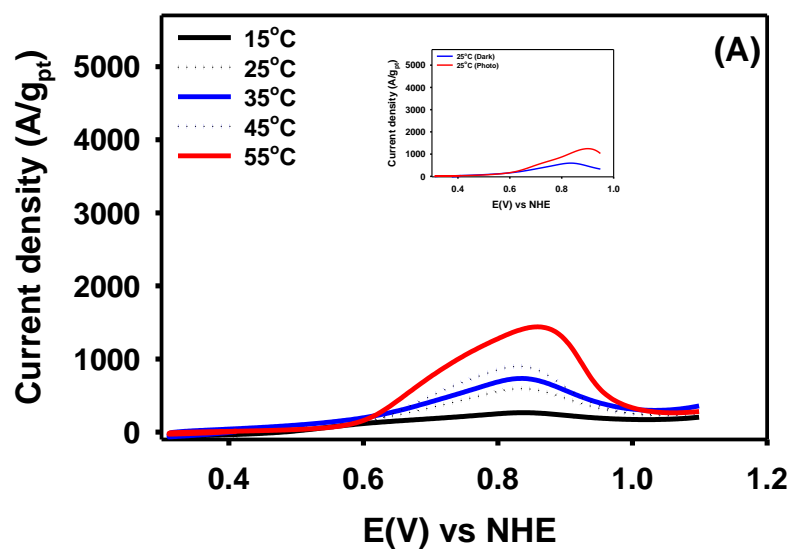


Figure 6.13: (A) CO oxidation and stripping without illumination and (B) CO oxidation with and without illumination in 0.5 M H₂SO₄ solution at a scan rate of 50 mV/s and 25 °C. Currents normalized by glassy carbon electrode area = 0.196 cm².

To rule out any temperature effect on the observed behaviour, the CVs of methanol electro-oxidation at a scan rate of 50 mV/s were recorded at temperatures ranging from 15 to 55 °C without illumination. As shown in Fig.6.14 A and B, the MOR current on Pt/PV and Pt TiO₂/G-PV increase with temperature, but the onset potential and the peak potential did not vary significantly with temperature increase.



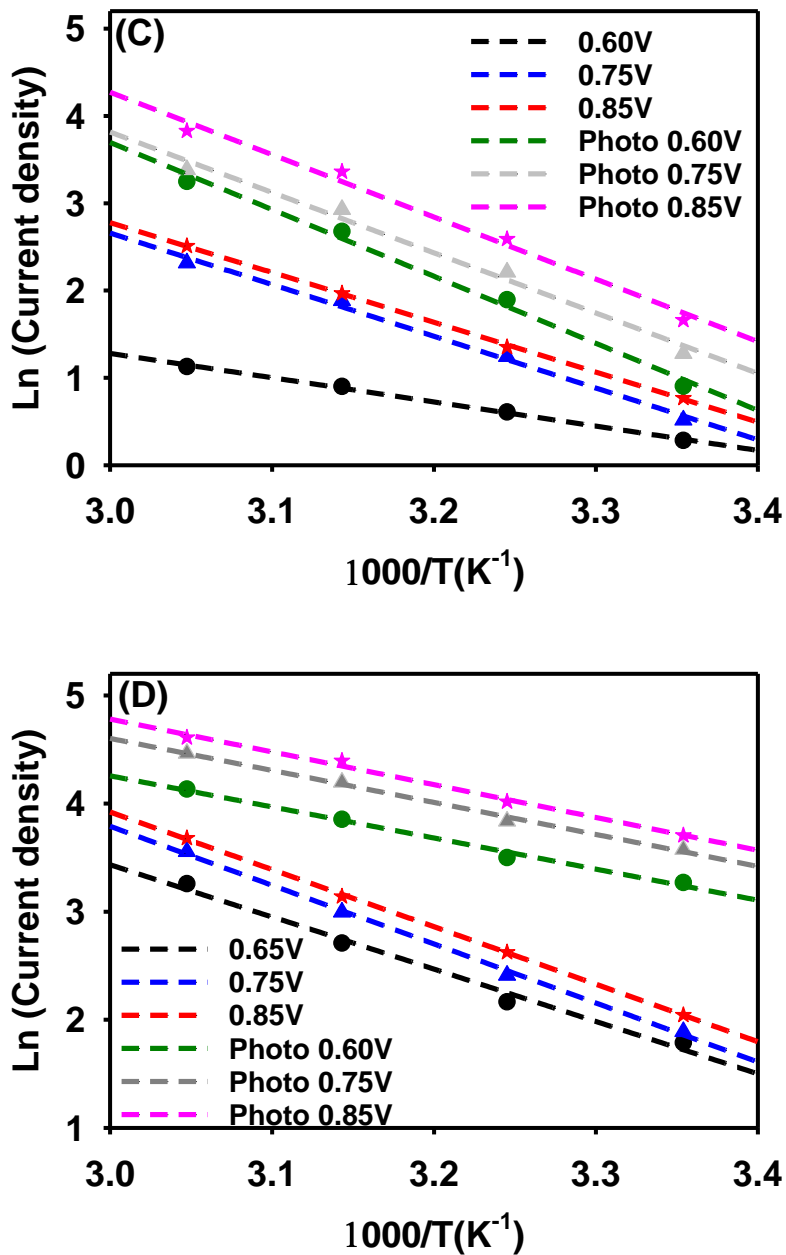


Figure 6.14: Methanol oxidation platinized supports (A) Pt/PV and (B) Pt/TiO₂/G-PV catalysts at different temperature without irradiation in N₂-saturated 0.5 M CH₃OH + 0.5 M H₂SO₄ solution at 50 mV/s. Insets show methanol oxidation currents with and without irradiation at 25 °C. Corresponding Arrhenius plots of methanol oxidation at various temperatures with and without illumination for (C) Pt/PV and (D) Pt/TiO₂/G-PV catalysts.

The apparent activation energy, E_a^{app} , values for the MOR obtained from the slope of the Arrhenius plots, $\ln(\text{current})$ vs $1/T$, at several constant potentials (Fig.6.14 C and D) are summarized in Table 6.3. It is clear that the potential dramatically affects the E_a^{app} values, thus limiting the comparisons that can be made between different catalyst materials. Nevertheless, at 0.85 V (~ peak potential for both samples) and in the absence of irradiation, the E_a^{app} are significant different; 73.0 and 52.8 kJ/mol for Pt/PV and Pt/TiO₂/G-PV, respectively. With illumination, E_a^{app} values obtained for Pt/PV and Pt/TiO₂/G-PV are in the order of 49.7 and 25.2 kJ/mol, respectively. This corresponds to 32 % reduction in E_a^{app} in the case of the Pt/PV, and a 52% reduction in the case of Pt/TiO₂/G-PV. While heating of the electrode surface upon irradiation cannot be totally discarded, the significant different between samples with and without TiO₂, reinforces the idea that the observed enhancement is mostly due to a photocatalytic effect on the MOR kinetics. In this work, the obtained E_a^{app} values fall within the activation energy reported in the literature that varies from 16 to 95 kJ/mol depending on the test condition [62-63].

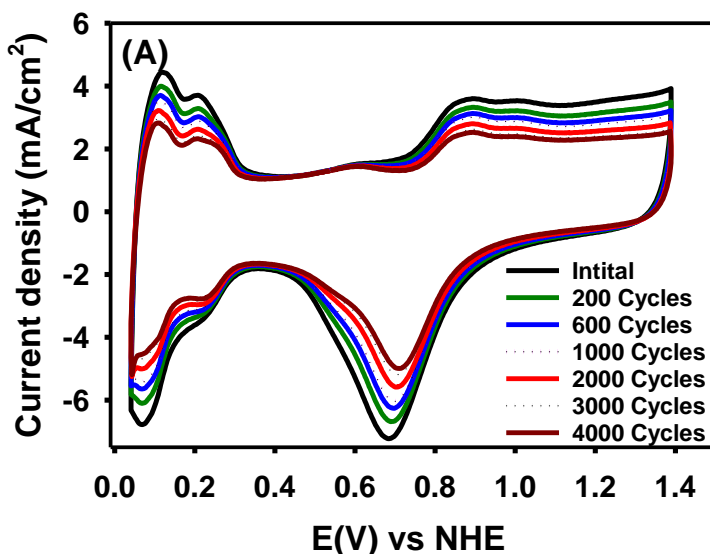
Table 6.3: Activation energies (E_a) obtained from methanol oxidation at differential potentials for Pt/PV and Pt/TiO₂/G-PV catalysts with and without illumination.

Catalyst	E(V) vs NHE	Slope (E_a^{app} /R)	E_a^{app} (Dark) (kJ/mol)	E_a^{app} (Photo) (kJ/mol)
Pt/PV	0.60	6291	52.3	42.0
	0.75	8552	71.1	43.4
	0.85	8780	73.0	49.7
Pt/TiO ₂ /G-PV	0.60	5930	49.3	21.4
	0.75	6303	52.4	22.4
	0.85	6351	52.8	25.3

6.4.5. Influence of Pt surface area on photo-enhancement.

In order to further probe the role of the PtNP, one can manipulate their surface area and examine its influence on the extent of photo-enhancement. This can be accomplished *in situ* by employing a typical accelerated stress test (AST) protocol which will cause the dissolution/aggregation of PtNPs [59-60]. The method we employed involved performing a large number of CVs up to high potentials with periodic assessment of ECSA. This AST method has been previously shown to only Pt surface area loss and not carbon corrosion for these catalysts [36-37]. In addition to modulating and periodically assessing ECSA in an N_2 -purged 0.5 M H_2SO_4 , we also examined the MOR activity of each catalyst in the presence and absence of UV light.

As reported in a previous work [37], the ECSAs of Pt/PV and Pt/TiO₂/G-PV are reduced with the number of CV cycles over the 4000 cycling period (Fig. 6.15A and B), but the rate of decay is faster in the Pt/PV catalyst. After 4000 cycles, the Pt/C ECSA was found to be 96 % smaller than the initial value compared with 68 % for the Pt/TiO₂/G-PV catalyst. These results indicate that Pt/TiO₂/G-PV will perform better when used as fuel cell catalyst.



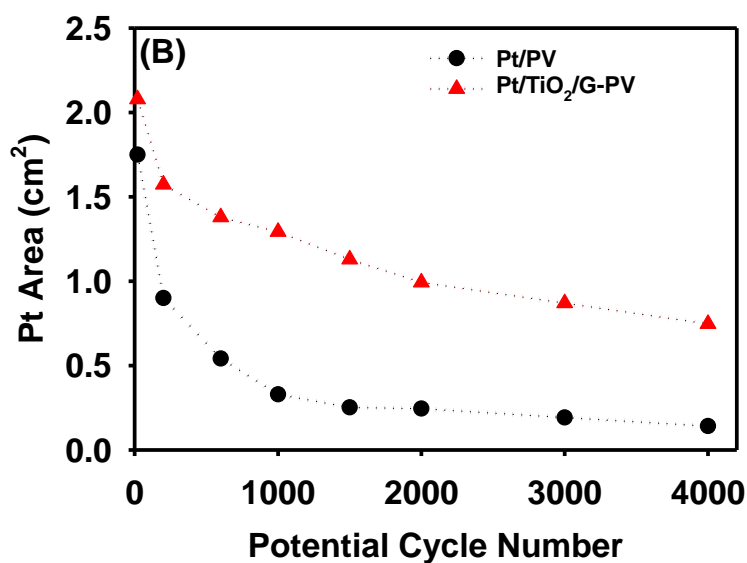


Figure 6.15: Durability study (A) CVs of Pt/TiO₂/G-PV based on the electrode geometric area (0.196cm²), and (B) Pt active area as a function of cycle number carried out in N₂-saturated 0.5 M H₂SO₄ at 25 °C and a scan rate of 50 mV/s.

The loss of Pt active surface area as a function of methanol electrooxidation forward peak current is shown in Fig. 6.16. When catalyst surface areas were compared with peak methanol currents, it can be seen that there is a close resemblance in decay rates with and without illumination. From these plots, the peak current losses scale substantially well with Pt area loss. Even though higher methanol oxidation peak currents are observed with photo excitation, the performance loss is faster in comparison to the activity loss in the dark within the same cycling period. Under photo irradiation, the Pt/PV catalyst shows that ca 7 % of the initial oxidation activity is maintained after 4000 cycles which correspond to 95 % surface area loss. Under the same experimental conditions, Pt/TiO₂/G-PV retains 32 % of its initial value methanol activity in line with the available catalyst surface area. The fact that catalyst performance is approximately proportional to the catalyst surface areas substantiates the inevitable role of PtNPs during photo-electrooxidation of methanol in this study since the TiO₂ support area is expected to be essential unchanged by potential cycling.

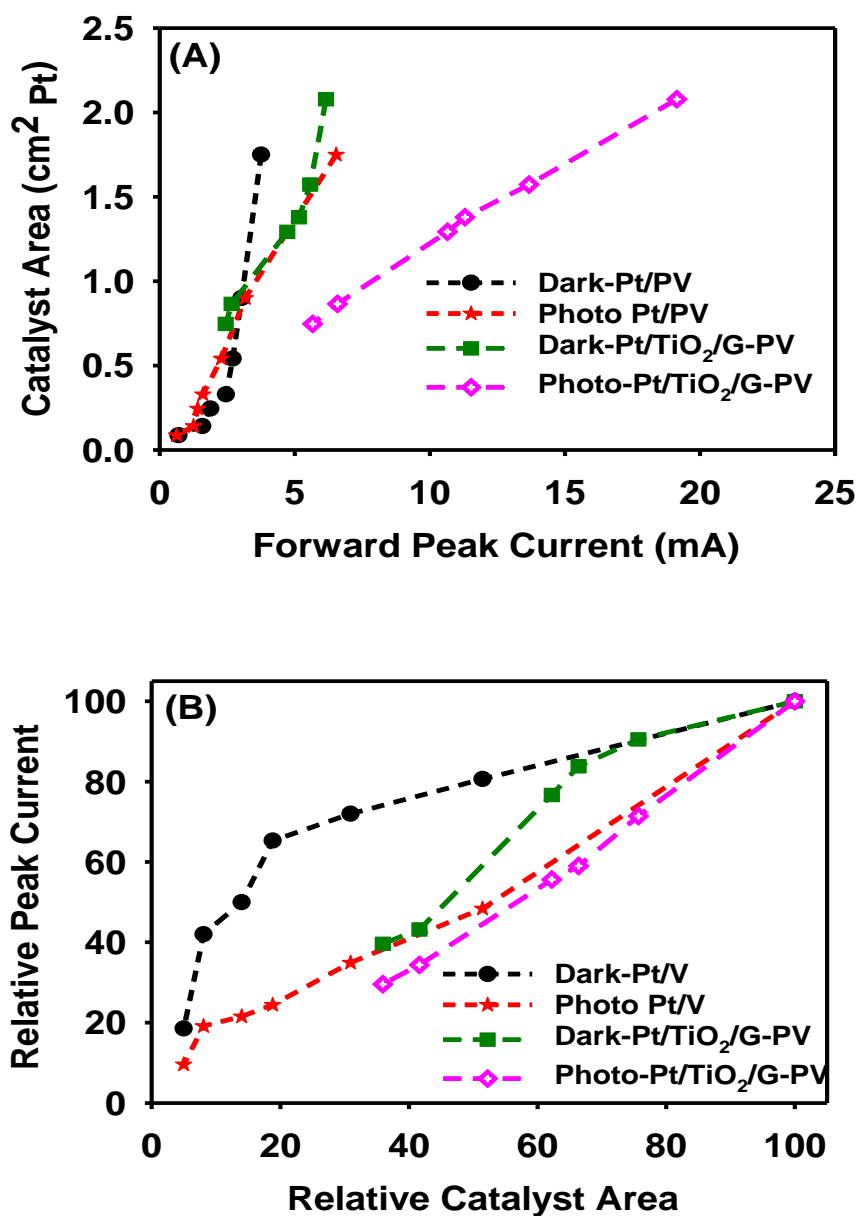


Figure 6.16: (A) Pt surface area as a function of methanol oxidation peak currents in N₂-saturated 0.5 M CH₃OH + 0.5 M H₂SO₄ at different cycling intervals following during durability study in 0.5 M H₂SO₄ and (B) Normalized data for the catalysts with and without illumination.

Based on the overall results, the improvement observed on the MOR on Pt/TiO₂/G-PV without illumination can only be due to two main factors: (i) the oxophilic nature of TiO₂

NPs in the catalyst layer. The presence of -OH groups and other oxygen-containing species can facilitate the conversion of adsorbed CO species on Pt to CO₂ during methanol oxidation and (ii) the interaction between the PtNPs and TiO₂ NPs that can reduce the electron density of the d band of Pt with a consequently weakening of the binding energy between CO and Pt atoms, and making them easier to oxidize [66-67].

Moreover, we observed that the electrocatalytic performances of Pt/PV, as well as TiO₂ modified catalyst (Pt/TiO₂/G-PV) for the oxidation of methanol, are distinctly improved with illumination. As described earlier, this photo enhancement on Pt/PV catalyst may be ascribed to the plasmonic effect of PtNPs under illumination, with resulting charge carriers that eventually promote the oxidation of methanol molecules. On the other hand, the methanol oxidation current on the Pt/TiO₂/G-PV electrode can be enhanced by several different modes: (i) electron-holes pair created on the TiO₂NPs surface during illumination that could independently oxidize methanol and produce a photocurrent by absorption of UV light. The energy of the TiO₂- valence band (VB) would easily allow the oxidation of methanol to an hydroxymethyl radicals, which can donate an electron to the conduction band (CB) of the semiconductor with the formation of formaldehyde, which can subsequently be converted to CO₂ [62]. ; (ii) the surface area of the Pt catalyst layer may be altered through electron-hole pairs induced under UV-visible illumination with an increase in methanol oxidation current [31]; and (iii) a current produced through a synergistic effect of the catalyst components, Pt, C and porous TiO₂ NPs under illumination which may result in a strong photoabsorption capacity [68-69].

Even though TiO₂ has a cooperative effect under illumination, leading to a much higher photocurrent on Pt/TiO₂/G-PV, similar charge transfer resistances were obtained for catalysts with and without TiO₂ under illumination.

6.5 Conclusions

In conclusion, we have evaluated performances of in-house catalysts Pt/PV and Pt/TiO₂/G-PV catalysts toward methanol oxidation reaction (MOR). The method used to prepare the Pt/TiO₂/G-PV composite catalyst as described in ref. 37 results in materials with a higher electrocatalytic activity than Pt/PV catalyst in the absence of illumination due to strong metal-support interaction. This improved performance is consistent with an observed negative shift in onset potential of CO oxidation on Pt/TiO₂/G-PV. With illumination, higher methanol oxidation currents are observed on these electrodes even in the absence of TiO₂ NPs.

Pt/PV show moderate enhancement in catalytic activity under illumination ($(I_{\text{peak}}^{\text{illumination}} - I_{\text{peak}}^{\text{dark}}) * 100 / I_{\text{peak}}^{\text{dark}} \sim 100 \%$) that can be attributed to a significant reduction in the charge transfer resistance (R_{ct}) when the electrode is illuminated (635 Ω (dark) vs 84 Ω (illumination)) as determined by electrochemical impedance spectroscopy (EIS). The photo enhancement observed in the case of PtNPs deposited on TiO₂/G-PV is more impressive, ($(I_{\text{peak}}^{\text{illumination}} - I_{\text{peak}}^{\text{dark}}) * 100 / I_{\text{peak}}^{\text{dark}} \sim 171 \%$) even though the change in the R_{ct} (185 Ω vs. 99 Ω) is not as pronounced as in the Pt/PV sample. Illumination leads to a reduction in the onset potential of ca. 40-50 mV for each catalyst, indicating that it does indeed alter energetic around CO removal.

This photo-assisted electrocatalytic process could remarkably enhance the oxidation efficiency toward methanol oxidation and can be utilized in outdoor fixtures where single stack cells can be spread to capture sunlight. Taking into account the engineering design constraint of fuel cell stack illumination, these electrode materials can be used as a tool to design disposable and portable electrochemical sensors for environmental monitoring such as water quality tests, organic compound analyses, heavy metals detection and gas pollutants. This light sensitive electrode can as well provide a breakthrough in developing a liquid methanol concentration sensor. More studies will be required to quantify individual contributions to the observed photocurrent from photo-generated holes in TiO₂ electrode and electron-hole pairs produced by the synergetic effect of the catalyst components.

6.6 References

- 1) Corti H. R., and Gonzalez E. R. (2014). In *Direct Alcohol Fuel Cells* (pp. 1-32). Springer Netherlands.
- 2) Kruth A., Todd M. J., Macphee D. E., and Wells R. P. K. (2011). Fuel cell: Google Patents
- 3) Ryu, J., and Choi, W. (2007). *Environmental science & technology*, 42(1), 294-300.
- 4) Li, D., Haneda, H., Hishita, S., and Ohashi, N. (2005). *Chemistry of Materials*, 17(10), 2596-2602.
- 5) Freitas, R.G., Santos, M.C.D., Oliveira, R.T.S., Bulhões, L.O.S. and Pereira, E.C., (2006). *Journal of Power Sources*, 158(1), 164-168.
- 6) Zhou X., Xie X, and Ishikawa M, (2012). *Advanced Materials Research* 347, 3281–3285.
- 7) Qian W., Wilkinson, D. P., Shen J., Wang H., and Zhang J. (2006). *Journal of Power Sources*, 154(1), 202-213.
- 8) Fukunaga, H., Ishida, T., Teranishi, N., Arai, C., and Yamada, K. (2004). *Electrochimica Acta*, 49(13), 2123-2129.
- 9) Chen, Y. X., Miki, A., Ye, S., Sakai, H., and Osawa, M. (2003). *Journal of the American Chemical Society*, 125(13), 3680-3681.
- 10) Parsons, R., and VanderNoot, T. (1988). *Journal of electroanalytical chemistry and interfacial electrochemistry*, 257(1-2), 9-45.
- 11) Zainoodin, A. M., Siti Kartom Kamarudin, and Wan Ramli Wan Daud. "Electrode in direct methanol fuel cells." *International Journal of Hydrogen Energy* 35, no. 10 (2010): 4606-4621.
- 12) Hamnett, A. (1997). *Catalysis Today*, 38(4), 445-457.
- 13) Vielstich, W., Yokokawa, H., and Gasteiger, H. A. (2009). *Handbook of fuel cells: fundamentals technology and applications*. John Wiley & Sons.
- 14) Cui, Z., Li, C. M., and Jiang, S. P. (2011). *Physical Chemistry Chemical Physics*, 13(36), 16349-16357.

- 15) Lee, Y. W., Ko, A. R., Han, S. B., Kim, H. S., and Park, K. W. (2011). *Physical Chemistry Chemical Physics*, 13(13), 5569-5572.
- 16) Yu X.W., and Ye S.Y. (2007), *Journal of Power Sources*, 172, 145.
- 17) Zhao, X., Yin, M., Ma, L., Liang, L., Liu, C., Liao, J., and Xing, W. (2011). *Energy & Environmental Science*, 4(8), 2736-2753.
- 18) Cao, M., Wu, D., and Cao, R. (2014). *ChemCatChem*, 6(1), 26-45.
- 19) Huang, H., and Wang, X. (2014). *Journal of Materials Chemistry A*, 2(18), 6266-6291.
- 20) Yao, Z., Zhu, M., Jiang, F., Du, Y., Wang, C., and Yang, P. (2012). *Journal of Materials Chemistry*, 22(27), 13707-13713.
- 21) Chen, J. M., Sarma, L. S., Chen, C. H., Cheng, M. Y., Shih, S. C., Wang, G. R., and Hwang, B. J. (2006). *Journal of power sources*, 159(1), 29-33
- 22) Hepel, M., Kumarihamy, I., and Zhong, C. J. (2006). *Electrochemistry communications*, 8(9), 1439-1444.
- 23) Esfahani R.A.M., Monteverde Videla A.H., Vankova S., Specchia S., (2015). *International Journal of Hydrogen Energy*, 40(42), 14529-14539.
- 24) Wang, Y. Q., Wei, Z. D., Gao, B., Qi, X. Q., Li, L., Zhang, Q., and Xia, M. R. (2011). *Journal of Power Sources*, 196(3), 1132-1135.
- 25) Ye L., Li Z., Zhang L., Lei F., Lin S., (2014). *Journal of Colloid Interface Sci.*, 433, 156-162.
- 26) Vinodgopal, K., Hotchandani, S., and Kamat, P. V. (1993). *The Journal of Physical Chemistry*, 97(35), 9040-9044.
- 27) Li, X., Zhuang, Z., Li, W., and Pan, H. (2012). *Applied Catalysis A: General*, 429, 31-38.
- 28) Xu A. W., Gao Y., Liu H. Q. (2002). *Journal of Catalysis*, 207(2), 151-157
- 29) Xia, B. Y., Wu, H. B., Chen, J. S., Wang, Z., Wang, X., and Lou, X. W. D. (2012). *Physical Chemistry Chemical Physics*, 14(2), 473-476.
- 30) Zhai, C., Zhu, M., Ren, F., Yao, Z., Du, Y., and Yang, P. (2013). *Journal of hazardous materials*, 263, 291-298.
- 31) Li, P., Li, Z. P., and Liu, B. H. (2012). *Journal of Power Sources*, 199, 146-149.
- 32) Fukutani K., Song M.B., Murata Y., (1995). *J. Chem. Phys.*, 103(6), 2221-2228.

- 33) Arulmani D. V., Eastcott J. I., Mavilla S. G., Easton E. B. (2014). *Journal of Power Sources*, 247, 890-895.
- 34) Linic, S., Aslam, U., Boerigter, C., and Morabito, M. (2015). *Nature materials*, 14(6), 567-576.
- 35) Brongersma, M.L., Halas, N.J., Nordlander, P., (2015). *Nature Nanotechnology*, 10(1), 25-34.
- 36) Odetola, C., Easton, E. B., and Trevani, L. (2016). *International Journal of Hydrogen Energy*, 41(19), 8199-8208.
- 37) Odetola C., Trevani L., and Easton E. B. (2015). *Journal of Power Sources*, 294, 254-263.
- 38) Han K. I.; Lee J. S.; Park S. O.; Lee S. W.; Park Y. W.; and Kim H. (2004). *Electrochim. Acta*, 50, 791-794.
- 39) Sebastian D.; Suelves I.; Moliner R.; and Lazaro M. J. (2010). *Carbon*, 48, 4421-4431.
- 40) Çakır, D., and Gulseren, O. (2012). *The Journal of Physical Chemistry C*, 116(9), 5735-5746.
- 41) Dulub, O., Hebenstreit, W., and Diebold, U. (2010). *Physical Review Letters*, 84(16), 3646.
- 42) Park, J. H., Kim, S., and Bard, A. J. (2006). *Nano letters*, 6(1), 24-28.
- 43) Bonanni, S., Aït-Mansour, K., Brune, H., and Harbich, W. (2011). *Acs Catalysis*, 1(4), 385-389.
- 44) Horsley, J. A. (1979). *Journal of the American Chemical Society*, 101(11), 2870-2874.
- 45) Awaludin, Z., Suzuki, M., Masud, J., Okajima, T., and Ohsaka, T. (2011). *The Journal of Physical Chemistry C*, 115(51), 25557-25567.
- 46) Awaludin, Zaenal, James Guo Sheng Moo, Takeyoshi Okajima, and Takeo Ohsaka. *Journal of Materials Chemistry A* 1, no. 46 (2013): 14754-14765.
- 47) Li, W., Bai, Y., Li, F., Liu, C., Chan, K. Y., Feng, X., and Lu, X. (2012). *Journal of Materials Chemistry*, 22(9), 4025-4031.
- 48) Marković, N. M., and Ross, P. N. (2002). *Surface Science Reports*, 45(4), 117-229.

- 49) Chen, C. S., and Pan, F. M. (2009). *Applied Catalysis B: Environmental*, 91(3), 663-669.
- 50) Pournaghi-Azar, M. H., and Habibi-A, B. (2005). *Journal of Electroanalytical Chemistry*, 580(1), 23-34.
- 51) Yu, E. H., Scott, K., Reeve, R. W., Yang, L., and Allen, R. G. (2004). *Electrochimica acta*, 49(15), 2443-2452.
- 52) Wang, Y., Alsmeyer, D. C., and McCreery, R. L. (1990). *Chemistry of Materials*, 2(5), 557-563.
- 53) Li, W., Bai, Y., Liu, W., Liu, C., Yang, Z., Feng, X., and Chan, K. Y. (2011). *Journal of Materials Chemistry*, 21(18), 6718-6724.
- 54) Wu, G., Li, L., and Xu, B. Q. (2004). *Electrochimica Acta*, 50(1), 1-10.
- 55) Seland F., Tunold R., and Harrington D. A. (2006). *Electrochim. Acta*, 51(18), 3827-3840.
- 56) Hirschorn, B., Orazem, M. E., Tribollet, B., Vivier, V., Frateur, I., and Musiani, M. (2010). *Journal of The Electrochemical Society*, 157(12), C452-C457.
- 57) Ma, B., Bai, J., and Dong, L. (2013). *Journal of Solid State Electrochemistry*, 17(11), 2783-2788.
- 58) Hsing I. M., Wang X., and Leng Y. J. (2002). *Journal of The Electrochemical Society*, 149(5), A615-A621.
- 59) Newman J., and Thomas-Alyea K. E. (2004). *Electrochemical systems*, 3rd Edition, Wiley Interscience.
- 60) Clavero, C. (2014). *Nature Photonics*, 8(2), 95-103.
- 61) Jusys Z., Kaiser J., and Behm R. J. (2002). *Electrochim Acta*, 47(22), 3693-3706.
- 62) Cohen, J. L., Volpe, D. J., and Abruna, H. D. (2007). *Physical Chemistry Chemical Physics*, 9(1), 49-77.
- 63) Gasteiger, H. A., Marković, N., Ross, P. N., & Cairns, E. J. (1994). *Journal of the Electrochemical Society*, 141(7), 1795-1803.
- 64) Saleh F.S., and Easton E.B., *Journal of The Electrochemical Society*, 159 (2012) B546-B553.
- 65) O'Rian O.R., Saleh F.S., and Easton E.B. (2014). *ECS Transactions*, 61(23), 25-32

- 66) Fampiou, I., and Ramasubramaniam, A. (2013). *The Journal of Physical Chemistry C*, 117(39), 19927-19933.
- 67) Yoo S. J., Lee K. S., Cho Y. H., Kim S. K., Lim T. H., and Sung Y. E. (2011). *Electrocatalysis*, 2(4), 297-306.
- 68) Colbeau-Justin, C., Kunst, M., and Huguenin, D. (2003). *Journal of materials science*, 38(11), 2429-2437.
- 69) Eppler A. M., Ballard I. M., and Nelson J. (2002). *Physica E: Low-dimensional Systems and Nanostructures*, 14(1), 197-202.

CHAPTER SEVEN

Summary and Future Directions

7.1 Summary and Future Directions

The development of Pt/TiO₂-modified carbon electrocatalysts and trying to understand the interplay between the 3 components has been a goal of this research. The degradation of electrocatalysts is a major cause of operational performance loss and affects the durability of its various components. The corrosion of carbon based catalyst support constitutes major concern to electrocatalyst longevity. Instead of totally replacing carbon with a more stable non transition metal oxide material, this thesis has explored a composite consisting of both carbon and TiO₂ to support platinum catalysts. Carbons and stable metal oxides have become a popular material selection for catalyst supports in many recent publications, but their design lacks a fundamental understanding.

TiO₂/C supports for Pt were able to better preserve catalyst performance than a control without TiO₂ under half- cell electrochemical condition. Choice of glucose as a dopant on carbon surface prior to TiO₂ deposition was used in an approach to modify the structure and electronic properties of the TiO₂/C composites. The presence of TiO₂ promotes electronic interactions through junctions formed with the catalyst. These metal-support interactions enhanced catalyst bonding characteristics extended from the support. Thus, a synergy between electrochemical performance and durability was realized by design of conductive composite supports.

TiO₂ based composite catalysts were extensively evaluated as possible fuel catalysts through materials and electrochemical characterization. Specifically, it was focused on the fabrication and characterization of composite materials as catalyst supports for use as oxygen reduction and methanol oxidation reactions. Electrode compositions were prepared by depositing Pt NPs on TiO₂ modified Vulcan carbon XC-72 via the sol-gel process. Enhancement of the surface properties of pristine Vulcan carbon was accomplished through two treatment approaches, the acid treatment and glucose doping to increase hydrophilic functional groups for particle dispersion.

In chapter 3, the influence of carbon surface was examined by treating pristine carbon material with nitric acid. This treatment induced surface functional groups with subsequent loadings of TiO₂ NPs in a range of 3-14 wt.% . With this treatment, hydrophilic functional groups are formed that provide attractive interactions with the

titanium sol [1-2]. However, with this approach, we observed little control over the nature, location and quantity of the introduced functional groups, [3]. Pt NPs were deposited on the resultant composite catalyst support, TiO₂/ATV following heat treated in inert medium. These materials were characterized physically and electrochemical in a half-cell set-up using CV and EIS. These analysis show that with respect to the carbon substrate, the BET surface areas and ECSA values were substantially decreased as more TiO₂ is added. This could be due to a detrimental effect on the pore structure of the substrate material. The presence of the TiO₂ aggregates on the carbon substrate could have restricted pore size. TEM analysis confirmed less desirable particle segregates on the substrate and thus the treatment does not enhance TiO₂ particle growth during sol-gel synthesis.

A more desirable sol-gel synthesis route was developed to deposit highly dispersed TiO₂ nanoparticles (NPs) on glucose doped carbon substrates (TiO₂/G-ATV and TiO₂/G-PV). These materials prepared through glucose pre-adsorption on carbon solutions present higher BET surface areas compared with TiO₂/ATV composites counterpart for the same TiO₂ loading. This higher surface area is an important contribution due to their mesoporosity. In comparison to the base carbon support, lower surface areas were observed on TiO₂ based support as a result of heat treatment procedure needed to form crystalline material and the highly dense TiO₂ particles on the carbon surface.

The XPS analysis of the TiO₂/ATV and TiO₂/G-PV confirms both are nanocomposites and consist of carbon material with TiO₂ particles. This mode of synthesis allowed better oxide dispersion with an intimate contact with carbon surface particles as revealed by TEM analysis. TEM analysis showed that TiO₂ NPs are uniformly deposited on carbon substrate with a narrow size distribution and the average particle size is estimated to be 5–10 nm. This dispersion of TiO₂ NPs promotes contact areas with carbon substrate.

Pt NPs were also well dispersed on the TiO₂/G-PV composite support with a high degree of dispersion. In addition it can be seen that majority of the Pt NPs are in close contact with TiO₂ NPs. This indicates that the TiO₂ NPs on modified carbon have an important effect on the deposition of the Pt NPs. More interestingly, it was observed that some Pt NPs are anchored at the interface between TiO₂ and carbon instead of on the carbon alone thus forming the Pt/TiO₂/G-PV -component interface. Thus, the addition of TiO₂ to

catalyst had positive effect on reducing the particle size and improving the dispersion of obtained Pt nanoparticles on the support.

ORR testing by RDE revealed higher kinetic currents were observed on the TiO_2 based catalyst materials. Kinetic analysis of the ORR data also showed a more preferential 4 electron transfer process suggesting no mechanism change in the catalyst activity. The durability under accelerated stress tests in the Pt-dissolution potential and support oxidation showed significantly better retention of ECSA for $\text{Pt/TiO}_2/\text{G-PV}$ based catalysts compared to Pt/C . The more enhanced performance is attributed to electronic interaction and modified electronic structure of Pt, on the glucose treated carbon. Thus, the glucose doping method is shown created a catalysts structure that maximizes the beneficial support interactions while maintaining the critical level of electronic conductivity required to have a high utilization of Pt surface area.

Furthermore, this same $\text{Pt/TiO}_2/\text{C}$ catalysts system was also evaluated for its activity towards the methanol electrooxidation reaction (MOR). The strong electronic interaction between TiO_2 and Pt was also beneficial for this reaction, weakening the adsorption of CO and facilitating its removal from Pt active sites. Electrochemical measurements showed that the $\text{Pt/TiO}_2/\text{G-PV}$ catalyst had higher catalytic activity and better stability for methanol electrooxidation compared to Pt/C .

Moreover, in this thesis, the electrocatalytic performance of TiO_2 modified catalyst ($\text{Pt/TiO}_2/\text{G-PV}$) for the oxidation of methanol, was distinctly improved with illumination. As described earlier, this photo enhancement may be due to several effects such as: (i) electron-holes pair created on the TiO_2NPs surface during illumination that could independently oxidize methanol and produce a photocurrent by absorption of UV light ; (ii) the surface area of the Pt catalyst layer may be altered through electron-hole pairs induced under UV-visible illumination with an increase in methanol oxidation current and (iii) a current produced through a synergistic effect of the catalyst components, Pt, C and porous TiO_2 NPs under illumination which may result in a strong photoabsorption capacity .

Taken together, my research suggests that modified Vulcan carbon show tremendous promise for increasingly functional fuel cell catalyst material. A more facile,

non-acid treatment approach with controlled nucleation of TiO₂ particles and improved conductivity with glucose carbon endows these exciting materials with even more remarkable properties. The ECSA values are generally higher for Pt/TiO₂/G-PV catalysts than Pt/TiO₂/ATV catalysts despite use of the same TiO₂ and Pt deposition methods. The critical features of this method (compared to conventional TiO₂ modification) are the improved electronic conductivity and porous nature of these materials allows for better access to catalytic sites.

This research supports ongoing efforts towards rapid optimization of the synthesis conditions in producing high surface area and more porous composite supports with a complete core-shell structure. Future prospect may include doping with other transition elements to reduce the band gap and improve electronic conductivity of the TiO₂ particles; specifically the addition of niobium [4]. When TiO₂ is appropriately doped with niobium it is far more conductive than nondoped material [5]. The doping of niobium into the TiO₂ lattice will add electrons into the highest nonoccupied orbitals of TiO₂ effectively reducing the band gap and improving the electrical conductivity. The enhanced conduction mechanism has been proposed to involve partial substitution of Ti⁴⁺ with Nb⁵⁺ leaving some oxygen vacancies in the crystal structure that form shallow electron donor sites. In addition, niobium dopant could enhance phase stability of the anatase by increasing the rutile phase transformation temperature and retarding grain growth [6].

Developing nanostructures to increase the specific surface area of TiO₂ based support is another area of interest; TiO₂ nanobelts, previously used for photocatalysis in water treatment [7-8] can be use in electrocatalyst supports for Pt nanoparticles. Do et al. used an electrospinning technique to obtain high aspect ratio fibers and high surface area Nb doped TiO₂ and reported mass activity comparable to traditional carbons [9]. Other variants as catalyst support include TiO₂ embedded in polymer nanofibres [10], (i) TiO₂ nanotube arrays [11] and TiO₂ nanotube arrays produced via sacrificial CNT templates [12].

Studying the physio-chemical properties of the Pt/TiO₂/G-PV interface with a setup that will accommodate *in situ* characterization techniques such as X-ray diffraction and *infrared* spectroscopy will be needed in future studies, so that we can monitor different things in real time while the electrochemical process is taking place [13-14]. This approach

will shed more light into the beneficial aspects of TiO_2 in boosting the performance of Pt catalyst

In addition, this synthesis approach may be useful to modify other forms of carbon material as electrocatalyst support. The use of other advance carbon materials may be beneficial to further improve the performance of Pt/ TiO_2 /C catalysts. These advanced catalyst supports such as carbon nanotube possess unique graphitic contents, surface areas, and differing level of surface functionalization [15-19].

All of my work was done in carefully controlled 3-electrode cell configuration. These half-cell performances are promising for the development of low temperature fuel cell catalysts. So, one of the most logical next steps would be to evaluate the single-cell fuel cell performance. It is anticipated that a new student will perform these single cell tests in the near future.

For use in direct alcohol fuel cells, further research is needed to identify and quantify the actual products from the oxidation of small organic molecules like methanol and ethanol and to correlate the electrochemical behavior with theoretical predictions. In order to gain more information from the fundamental studies of methanol oxidation on these materials, collaboration with a theorist could help deepen the level of understanding of these systems and why they work at the fermi level. Electrochemical information like CO coverages, and spectroscopic information of adsorbed intermediates would aid a theorist in uncovering new information about these systems and guide alternate structures and compositions.

In situ studies of by product formation could be studied using direct electrochemical mass spectroscopy [20-21]. A study such as this would provide detailed analysis of the catalytic enhancement of composite materials. The effluent from fuel cell operation could also be useful in determining by products from the incomplete oxidation of these small organic molecules. This may lead to a better understanding of the catalytic oxidation mechanism of the materials described in this dissertation.

The newly developed TiO_2 /C support may provide a new opportunity to design and synthesize Pt alloy catalysts for instance Pt-Ru and Pt-Pd for electrooxidation of small organic molecules to boost performance of low temperature fuel cell with and without

illumination [22-24]. This approach will greatly minimize the use of precious metals without loss of activity and can also minimize poisoning effect.

Lastly, the optimised Pt/TiO₂/C catalyst can also be a promising candidate for photocatalytic and photoelectrochemical oxidation of organic pollutants in aqueous media, as a cost-effective approach for the treatment of pharmaceuticals and industrial waste waters and environment remediation initiatives processes using UV-visible light. This can also be extended to hydrogen production by splitting of water [25-26].

7.2 References

- 1) Gomathi, A., Vivekchand, S. R. C., Govindaraj, A., and Rao, C. N. R. (2005). *Advanced Materials*, 17(22), 2757-2761.
- 2) Yan, X. B., Tay, B. K., and Yang, Y. (2006). *The Journal of Physical Chemistry B*, 110(51), 25844-25849.
- 3) Salzmann, C. G., Llewellyn, S. A., Tobias, G., Ward, M. A., Huh, Y., and Green, M. L. (2007). *Advanced Materials*, 19(6), 883-887.
- 4) Liu, Y., Szeifert, J. M., Feckl, J. M., Mandlmeier, B., Rathousky, J., Hayden, O., and Bein, T. (2010). *ACS nano*, 4(9), 5373-5381.
- 5) Zhang, X., Zhou, M., and Lei, L. (2005). *Carbon*, 43(8), 1700-1708.
- 6) Tao, J., Pan, H., Wong, L. M., Wong, T. I., Chai, J. W., Pan, J., and Wang, S. J. (2014). *Materials Research Express*, 1(1), 015911.
- 7) Hu, A., Liang, R., Zhang, X., Kurdi, S., Luong, D., Huang, H., and Servos, M. R. (2013). *Journal of Photochemistry and Photobiology A: Chemistry*, 256, 7-15.
- 8) Yang, Z., Du, G., Meng, Q., Guo, Z., Yu, X., Chen, Z., and Zeng, R. (2012). *Journal of Materials Chemistry*, 22(12), 5848-5854.
- 9) Do, T. B., Cai, M., Ruthkosky, M. S., and Moylan, T. E. (2010). *Electrochimica Acta*, 55(27), 8013-8017.
- 10) Kedem, S., Schmidt, J., Paz, Y., and Cohen, Y. (2005). *Langmuir*, 21(12), 5600-5604.
- 11) Yang, L., Luo, S., Liu, S., and Cai, Q. (2008). *The Journal of Physical Chemistry C*, 112(24), 8939-8943.

- 12) Hungria, A. B., Eder, D., Windle, A. H., and Midgley, P. A. (2009). *Catalysis Today*, 143(3), 225-229.
- 13) Vogel, W., Timperman, L., and Alonso-Vante, N. (2010). *Applied Catalysis A: General*, 377(1), 167-173.
- 14) Morris, D., Dou, Y., Rebane, J., Mitchell, C. E. J., Egdell, R. G., Law, D. S. L., ... and Casarin, M. (2000). *Physical Review B*, 61(20), 13445.
- 15) Wang, X., Li, W., Chen, Z., Waje, M., and Yan, Y. (2006). *Journal of Power Sources*, 158(1), 154-159.
- 16) Shao, Y., Yin, G., Gao, Y., & Shi, P. (2006). *Journal of the Electrochemical Society*, 153(6), A1093-A1097.
- 17) Liu, H., Zhang, Y., Li, R., Sun, X., and Abou-Rachid, H. (2012). *Journal of Nanoparticle Research*, 14(8), 1016.
- 18) Chen, Y., Wang, J., Liu, H., Li, R., Sun, X., Ye, S., and Knights, S. (2009). *Electrochemistry communications*, 11(10), 2071-2076.
- 19) Chen, Y., Wang, J., Liu, H., Banis, M. N., Li, R., Sun, X., and Knights, S. (2011). *The Journal of Physical Chemistry C*, 115(9), 3769-3776.
- 20) Chen, W., Cai, J., Yang, J., Sartin, M. M., and Chen, Y. X. (2017). The kinetics of methanol oxidation at a Pt film electrode, a combined mass and infrared spectroscopic study. *Journal of Electroanalytical Chemistry*.
- 21) Tao, Q., Chen, W., Yao, Y., Yousaf, A. B., and Chen, Y. X. (2014). *Chinese Journal of Chemical Physics*, 27(5), 541-547.
- 22) Arulmani, D. V., Eastcott, J. I., Mavilla, S. G., and Easton, E. B. (2014). *Journal of Power Sources*, 247, 890-895.
- 23) Drew, K., Girishkumar, G., Vinodgopal, K., and Kamat, P. V. (2005). *The Journal of Physical Chemistry B*, 109(24), 11851-11857.
- 24) Lee, Y. W., Ko, A. R., Han, S. B., Kim, H. S., and Park, K. W. (2011). *Physical Chemistry Chemical Physics*, 13(13), 5569-5572.
- 25) Mohapatra, S. K., Misra, M., Mahajan, V. K., and Raja, K. S. (2007). *The Journal of Physical Chemistry C*, 111(24), 8677-8685.
- 26) Fan, K., Zhang, W., Peng, T., Chen, J., and Yang, F. (2011). *The Journal of Physical Chemistry C*, 115(34), 17213-17219.

CHAPTER EIGHT

Appendices

Request for Permission to Reproduce or Re-Publish ECS Material

Please fax this form to: The Electrochemical Society (ECS), Attn: Permissions Requests, 1.609.730.0629.
You may also e-mail your request to: copyright@electrochem.org. Include all the information as required on this form. Please allow 3-7 days for your request to be processed.

I am preparing a (choose one): ☐ paper ☐ chapter ☐ book ☒ thesis

entitled: Synthesis and characterization of glucose doped Pt/TiO₂/C composite catalysts for fuel cell applications

to be published by: University of Ontario Institute of Technology

in an upcoming publication entitled: Christopher Odetola Ph.D Dissertation

I request permission to use the following material in the publication noted above, and request nonexclusive rights for all subsequent editions and in all foreign language translations for distribution throughout the world.

Description of material to be used—Indicate what material you wish to use (figures, tables, text, etc.) and give the full bibliographic reference for the source publication. You may attach a separate list, organized by ECS title.

Figure 1 : García, B.L., Fuentes, R. and Weidner, J.W., 2007. Low-Temperature Synthesis of a PtRu/NbO. 1TiO. 9O2 Electrocatalyst for Methanol Oxidation. Electrochemical and Solid-State Letters, 10 (7), pp.B108-B110.

Signature: _____



Date: 10/02/2017

Name: Christopher Odetola

Address: University of Ontario Institute of Technology, 2000 Simcoe Street North, Oshawa, Ontario L1H7K4 Canada.

Telephone: 289-939-5341

Fax: _____

E-mail: christopher.odetola@uoit.ca

Permission is granted to reproduce the above-referenced material. Please acknowledge the author(s) and publication data of the original material, and include the words: "Reproduced by permission of The Electrochemical Society."

Date

Annie Goedkoop, Director of Publications Production

Request for Permission to Reproduce or Re-Publish ECS Material

Please fax this form to: The Electrochemical Society (ECS), Attn: Permissions Requests, 1.609.730.0629.
You may also e-mail your request to: copyright@electrochem.org. Include all the information as required on this form. Please allow 3-7 days for your request to be processed.

I am preparing a (choose one): ☐ paper ☐ chapter ☐ book ☒ thesis

entitled: Synthesis and characterization of glucose doped Pt/TiO₂/C composite catalysts for fuel cell applications

to be published by: University of Ontario Institute of Technology

in an upcoming publication entitled: Christopher Odetola Ph.D Dissertation

I request permission to use the following material in the publication noted above, and request nonexclusive rights for all subsequent editions and in all foreign language translations for distribution throughout the world.

Description of material to be used—Indicate what material you wish to use (figures, tables, text, etc.) and give the full bibliographic reference for the source publication. You may attach a separate list, organized by ECS title.

Figure 1 : Sasaki, K., Takasaki, F., Noda, Z., Hayashi, S., Shiratori, Y., and Ito, K. (2010). ECS Transactions, 33(1), 473-482.

Signature: _____

Date: 10/02/2017

Name: Christopher Odetola

Address: University of Ontario Institute of Technology, 2000 Simcoe Street North, Oshawa, Ontario L1H7K4

Telephone: 289-939-5341

Fax: _____

E-mail: christopher.odetola@uoit.ca

Permission is granted to reproduce the above-referenced material. Please acknowledge the author(s) and publication data of the original material, and include the words: "Reproduced by permission of The Electrochemical Society."

Date

Annie Goedkoop, Director of Publications Production